

マス・フォア・インダストリ研究 No.8



Practical inverse problems based on interdisciplinary and  
industry-academia collaboration

Institute of Mathematics for Industry  
Kyushu University

編集 藤原 宏志  
滝口 孝志

九州大学マス・フォア・インダストリ研究所





About the Mathematics for Industry Research

The Mathematics for Industry Research was founded on the occasion of the certification of the Institute of Mathematics for Industry (IMI), established in April 2011, as a MEXT Joint Usage/Research Center – the Joint Research Center for Advanced and Fundamental Mathematics for Industry – by the Ministry of Education, Culture, Sports, Science and Technology (MEXT) in April 2013. This series publishes mainly proceedings of workshops and conferences on Mathematics for Industry (Mfi). Each volume includes surveys and reviews of Mfi from new viewpoints as well as up-to-date research studies to support the development of Mfi.

October 2014

Yasuhide Fukumoto

Director

Institute of Mathematics for Industry

**Practical inverse problems based on interdisciplinary and  
industry-academia collaboration**

Mathematics for Industry Research No.8, Institute of Mathematics for Industry, Kyushu University

ISSN 2188-286X

Editors: Hiroshi Fujiwara, Takashi Takiguchi

Date of issue: 20 February 2018

Publisher:

Institute of Mathematics for Industry, Kyushu University

Motooka 744, Nishi-ku, Fukuoka, 819-0395, JAPAN

Tel +81-(0)92-802-4402, Fax +81-(0)92-802-4405

URL <http://www.imi.kyushu-u.ac.jp/>

Printed by

Social Welfare Service Corporation Fukuoka Colony

1-11-1, Midorigahama, Shingu-machi Kasuya-gun, Fukuoka, 811-0119, Japan

TEL +81-(0)92-962-0764 FAX +81-(0)92-962-0768



**Practical inverse problems based on interdisciplinary and  
industry-academia collaboration**

**Organized by  
Hiroshi Fujiwara (Kyoto University)  
Takashi Takiguchi (National Defence Academy of Japan)**



# Preface

These are the proceedings of the workshop “Practical inverse problems based on interdisciplinary and industry-academia collaboration”, held at IMI, Kyushu University, from October twenty fourth to October twenty seventh, 2017. During the workshop, the following investigations were reported and lively discussions were had on them. We had the following talks during the workshop. Remark that the following comments are brief explanations of the talks, not the titles.

- Dr. Kenji Hashizume : Original inspection techniques for expressways developed by West Nippon Expressway Engineering Shikoku Company Limited, and some unsolved problems for maintenance of the expressways.
- Prof. Yoshifumi Saijo : Ultrasonic medical imaging in relation with non-destructive inspection for concrete structures.
- Prof. Hiroshi Fujiwara : How to realize multiple-precision arithmetic on MATLAB.
- Prof. Takashi Ohe : Theoretical and numerical research in an inverse problem to determine moving wave sources by boundary measurements.
- Prof. Cheng Hua : How to give mathematical representation of the crack propagation in viscoelastic composite material.
- Prof. Yuko Hatano : Mathematical representation of the long-term concentration of Cs-137 in Fukushima area and its prediction.

On the first day of the workshop, Doctor Kenji Hashizume gave a talk to introduce the inspection techniques for the expressways developed by West Nippon Expressway Engineering Shikoku Company Limited. It is surprising that his talk necessarily contains new technology developed by West Nippon Expressway Engineering Shikoku Company Limited every year. He also proposed several open problems in the maintenance of the tunnels, the bridges and the expressways, which have a lot to do with integral geometry, propagation of cracks in viscoelastic bodies and so on, some of which are under investigation by interdisciplinary and industry-academia collaboration organized by the organizing committee of this workshop.

On the second day, in the morning, Professor Yoshifumi Saijo introduced medical imaging techniques applying ultrasound. He is a medical doctor as well as a researcher to develop non-invasive medical imaging techniques. Based on his talk, we discussed how to apply non-invasive ultrasonic medical imaging techniques to non-destructive inspection for concrete structures.



In the afternoon, Professor Hiroshi Fujiwara talked about how to transplant the multiple-precision arithmetic interface, exflib which he developed, onto MATLAB. Numerical implementation is a must for practicalization of theoretical research. He demonstrated how powerful exflib is even on MATLAB by showing some examples, which are included in these proceedings as well as their programs.

In the morning on October 26th, Professor Takashi Ohe presented his recent result to identify moving wave sources and dipoles by boundary measurements. In his talk, he, himself, asked a question on his treatment of generalized functions, which was discussed by participants to be concluded that his treatment is good. Since his research has many potential applications, a number of questions were asked on the future development.

In the afternoon, Professor Cheng Hua gave a talk on the problem “How to give a mathematical representation of the crack propagation in viscoelastic composite materials”, which may be a key research to predict when and where a pothole on the expressway happens. He proposed a new idea to modify CED method, which is known as a method to analyze elastic cracks, for viscoelastic crack propagation, not modification of  $K$ - or  $J$ -integral method. During his talk, many questions are asked on the future development of the modification of CED method and lively discussions were had on this problem.

On the final day, Professor Yuko Hatano give a talk on important problems. She introduced some mathematical models to describe the migration of radionuclides, Cs-137, near Fukushima area, for which what is called Richardson’s law is applied. She also introduced her recent results on the long-term prediction on the concentration of Cs-137 near Fukushima area. We are very sorry that it is only the abstract to report her talk in these proceedings. For its compensation, a reference material has been appended.

We wish that we would have more opportunities to hold such workshops to discuss important problems in practical inverse problems based on interdisciplinary and industry-academia collaboration. We also hope that such collaboration be much more popular.

At the end of Preface, we would express our gratefulness to Ms. Kazuko Ito, the secretary of this workshop, for her faithful help.

February 20,2018

Takashi Takiguchi  
Hiroshi Fujiwara

# Practical inverse problems based on interdisciplinary and industry-academia collaboration

October 24-27, 2017

IMI, Ito Campus, Kyushu University  
C513 Middle lecture room(W1-C-513)  
744 Motooka, Nishi-ku Fukuoka 819-0395, Japan

## October 24, Tuesday

13:50 Opening

(Chair: C. Hua)

14:00-15:30 Kenji Hashizume (West Nippon Expressway Engineering Shikoku Company Limited, Japan)

Development of the devices and the methods for inspection of bridges, tunnels and pavement

15:30-16:30 Discussion

## October 25, Wednesday

(Chair: T. Ohe)

11:00-12:30 Yoshifumi Saijo (Tohoku University, Japan)

Ultrasound Imaging in Medicine and Biology

12:30-14:00 Discussion over lunch

14:00-15:30 Hiroshi Fujiwara (Kyoto University, Japan)

Multiple-Precision Arithmetic on MATLAB for reliable computation of numerically unstable problems

15:30-16:30 Discussion

## October 26, Thursday

(Chair: H. Fujiwara)

11:00-12:30 Takashi Ohe (Okayama University of Science, Japan)

Identification of moving wave sources from boundary measurements

12:30-14:00 Discussion over lunch

14:00-15:30 Cheng Hua (Fudan University, China)

A mathematical study for mixed-mode loading crack problem in viscoelastic composite material

15:30-16:30 Discussion

**October 27, Friday**

(Chair: T. Takiguchi)

11:00-12:30 Yuko Hatano (Tsukuba University, Japan)

Richardson's law and the concentration of Cs-137 in Fukushima

12:30-14:00 Discussion over lunch

14:00 Closing

**Organizers:**

Hiroshi Fujiwara (Kyoto University, Japan)

Takashi Takiguchi (National Defense Academy of Japan)

**Supported by:**

IMI, Kyushu University

JSPS Grant-in-Aid for Scientific Research Research (C) 26400198

# Table of contents

<b>1. Development of the devices and the methods for inspection of bridges, tunnels and pavement .....</b>	<b>1</b>
<i>Kenji Hashizume (West Nippon Expressway Engineering Shikoku Company Limited)</i>	
<b>2. Ultrasound Imaging in Medicine and Biology .....</b>	<b>45</b>
<i>Yoshifumi Saijo (Tohoku University)</i>	
<b>3. Multiple-Precision Arithmetic Environment in MATLAB and Its Application to Reliable Computation of Fractional Order Derivatives .....</b>	<b>83</b>
<i>Hiroshi Fujiwara (Kyoto University)</i>	
<b>4. Identification of moving wave sources from boundary measurements .....</b>	<b>121</b>
<i>Takashi Ohe (Okayama University of Science)</i>	
<b>5. A mathematical study for mixed-mode loading crack problem in viscoelastic composite material .....</b>	<b>189</b>
<i>Cheng Hua (Fudan University)</i>	
<b>6. Richardson's law and the concentration of Cs-137 in Fukushima .....</b>	<b>231</b>
<i>Yuko Hatano (Tsukuba Unibersity)</i>	







# Development of the devices and the methods for inspection of bridges, tunnels and pavement.

**Kenji Hashizume**

West Nippon Expressway Engineering Shikoku Company Limited  
3-1-1 Hanazono-cho, Takamatsu-shi, Kagawa 760-0072, Japan  
Email: kenji.hashizume@w-e-shikoku.co.jp

In this talk, our company's development of the devices and the methods for inspection of expressways is introduced. Here we would like to propose the method of the inspection of bridges, tunnels, and pavement by using cameras seeking for their objective evaluations and keeping their records properly, for which we have also developed new devices for inspection.

**Key Words:** inspection, non-destructive, infrared, visual image

## 1. Introduction

It requires a large amount of resources and expenses to develop and rehabilitate infrastructure. The followings are also essential for the resource utilization and social sustainability: (i) maintaining, repairing, and rehabilitating the existing infrastructure more efficiently and effectively. (ii) realizing the society where we can live safe and sound by reducing serious accidents triggered by deterioration and damages of infrastructure.

Accordingly the efficient and effective inspection and repairing would be very important. For the given purpose, the efficient and effective inspections and maintenance practice shall be necessary. The inspection method using cameras for the bridges, tunnels, and pavements inspections with objective evaluations and keeping their records is now proposed.



## 2. New devices for inspection

### 2.1 Bridge Inspections

We now explain the “J-System” (Figure-1) for the inspection method using the infrared cameras. The reinforced concrete fulfill its role with the joint functioning of rebar and concrete for the concrete structure. When the rebar gathers rust in the concrete, cracks appear on the concrete surface along the rebar, the surface concrete spalls, and so its durability is to be reduced. We have been inspecting the cracks triggered by the concrete delaminations along the rebar through the hammering. The infrared cameras inspection is the new one detecting the damaged areas such as concrete delaminations and cracks through photographing the concrete surface by using infrared cameras from remote palaces, and keeping the records of the concrete surface conditions using digital cameras. The inspections of bridges surface by infrared cameras are done by the passive method, and the followings are the important elements;



figure -1 J-system

#### i. Cameras Quality (Is the cameras suitable for the inspection environment?)

Inspections are done basically during night, so it is important to extend the surveillance hours of the day and increase the annual surveillance days by using the camera with a short- wave type which has no the environmental reflections during night and with a enforcing-cooling-system type with a small thermal resolution.

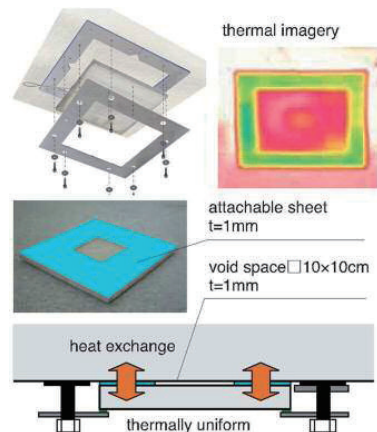


figure -2 J-system EM(S)

#### ii. Judgment on time zone of the day when inspections can be done (Do we inspect at a suitable time ?)

We implement the night- time inspection basically, because there are various bridge types and bridge members which are not suitable to inspect during daytime. The time zone of the day when inspection is possible is based on data

of the EMS (Environment Measuring System)(Figure-2) mounted on the inspection bridges.

**iii. Simple and Objective Evaluation Method (Is it possible and easy to evaluate objectively?)**

There could be, for individuals, differences among the inspection judgments because it is sometime impossible to judge the damage evaluation such as delamination and spalling for the bridge members and damaged parts only by looking at the infrared images. It is also impossible to judge the crack's depth along the rebar. However, the red, yellow, and blue cracks' judgment- images at the 1, 2, 3 cm depth from the surface are shown at the camera monitor (Figure -3).



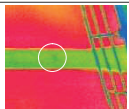
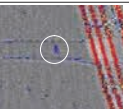


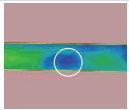
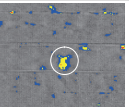


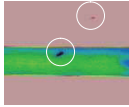
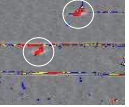
Damage grade	Visible image	Infrared image	3 level indication
Observation Abnormal sound 			
Caution Possibility of falling down near future 			
Warning Require emergency measure 			

figure -3 J-System Monitor Image

**2.2 Tunnel and Pavement Inspection**

**2.2.1 Tunnel and Pavement Inspection**

We now explain the “L & L System” (Figure-4) inspection method which uses the Line Censor Camera and Laser Marker. Line Censor cameras mount the visual image sensors, and can photograph seamless and continuous imageries. They can also be applied for the tunnel and pavement inspections. Light Cutting method is photographing the laser marker images from a upper and oblique position by using the laser which is irradiated vertically down on measuring surfaces and obtain the object shape. This method is used for road surface profile measuring.



figure -4 L&L System

### i. Tunnel Inspection

It is possible to obtain the fine and colorful continuous images (Figure-5) of tunnel lining by using Line Censor cameras mounted on the inspection cars with high speed (less than 100km/h). The cracks of tunnel lining can be detected up to 0.2mm, and water leakage and lime isolation can be also found. The damage spreading drawings and their diagonal charts can easily be produced based on the captive pictures, and so we inspect only the areas where further close

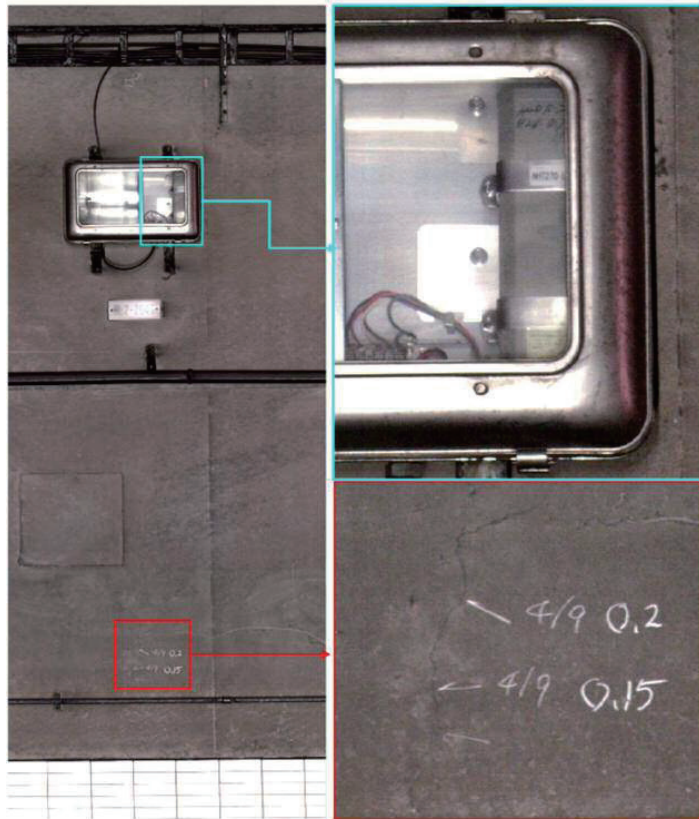


figure -5 Visual image with cracks and the accessories

and detail investigations are necessary. And we can clearly watch the conditions of rusted accessories in tunnels, and so it is now possible to apply them for the accessories inspections.

### ii. Pavement Inspection

We can inspect the pavement conditions such as cracks and potholes, and conditions of bridge expansion joints by using Line Censor cameras mounted on the vehicle with high speed (less than 100km/h). At the same time, we can also measure rutting, bumps, and upheaval through using laser cameras, and measure road surface profile such as height, and also evaluate the evenness, bump and IRI values.

We can also display the grade evaluation for the cracks, rutting, bumps,

evenness, and IRI values obtained by the road surface measurements, and we can also easily sort and extract some of the data with abnormal ranges which show more than a certain threshold (Figure-6). Thus, the repairing and renewal plans of road pavement and the bumps will be made easier.

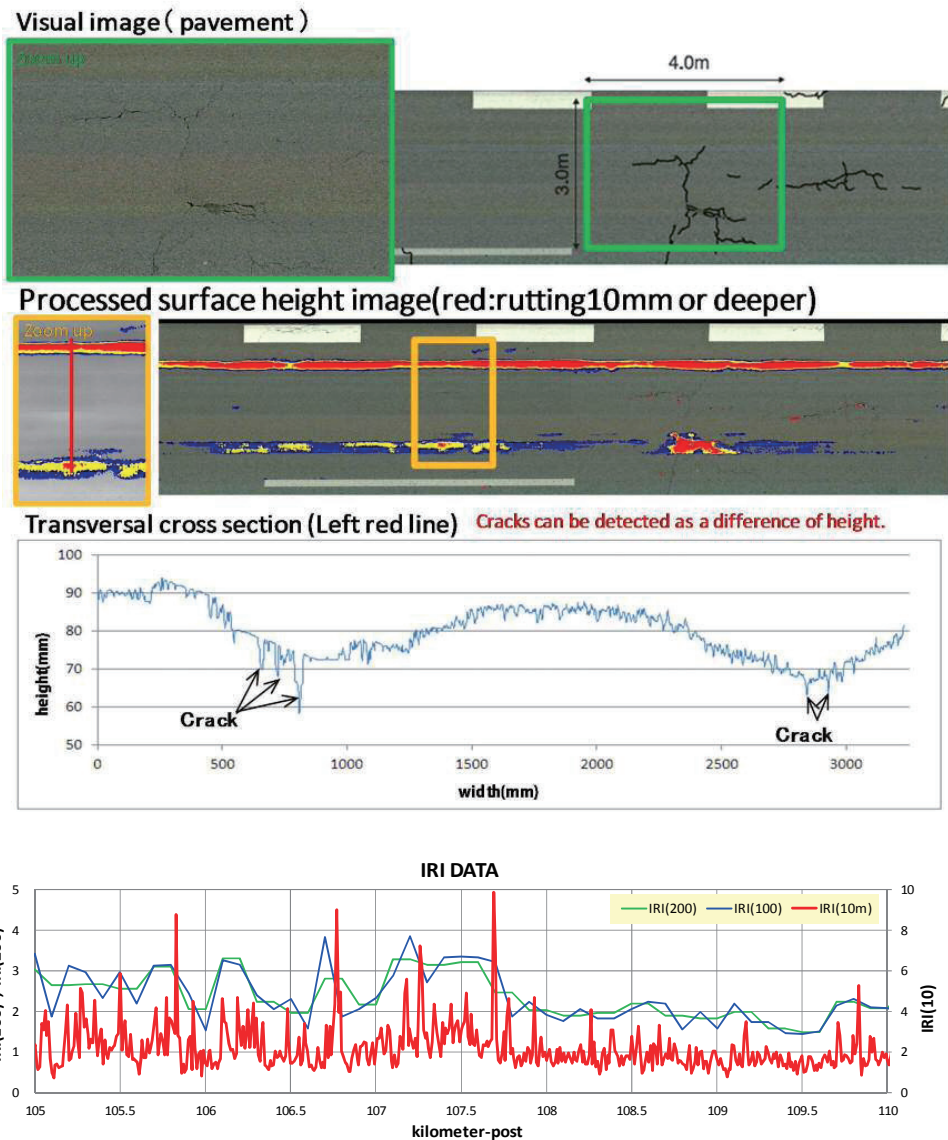


figure -6 Pavement evaluation

### 3. Conclusion

The bridges, tunnels, and pavement inspections by cameras can be used for the assistances for the on-site inspections or their alternatives, and we can maintain the objective evaluations and predict the future damages through their annual transitions. Also the repairing plan can be made easily and efficiently.

The proposed inspection method using the cameras makes it possible to use, select and combine those inspection tools economically and effectively in accordance with budges and utilizations patterns of each organization based on their different road structure maintenance and repairing standards.

This work is partially based on the discussions at 2017 IMI Joint Use Research Program Workshop (II) "Practical inverse problems based on interdisciplinary and industry-academia collaboration"

### Reference

- 1) A study for detection accuracy improvement in the infrared thermography method, J.JCI, vol.34, No.1, 1696-1701, 2012
- 2) Predictive probability of the concrete delamination and damage by an infrared thermography method, J.JCI, vol.35, No.1, 1813-1818, 2013
- 3) Study of the infrared thermography method automatic diagnosis support system using the co-occurrence matrix, J.JCI, vol.36, No.1, 2002-2007, 2014
- 4) One approach of the forecasting method for the pot-hole occurred by the deterioration of deeper than binder course on porous asphalt pavement, J.JSCE, Ser.E1, vol.70, No.3, I\_17-I\_24, 2014

# Development of the devices and the methods for inspection of bridges, tunnels and pavement.



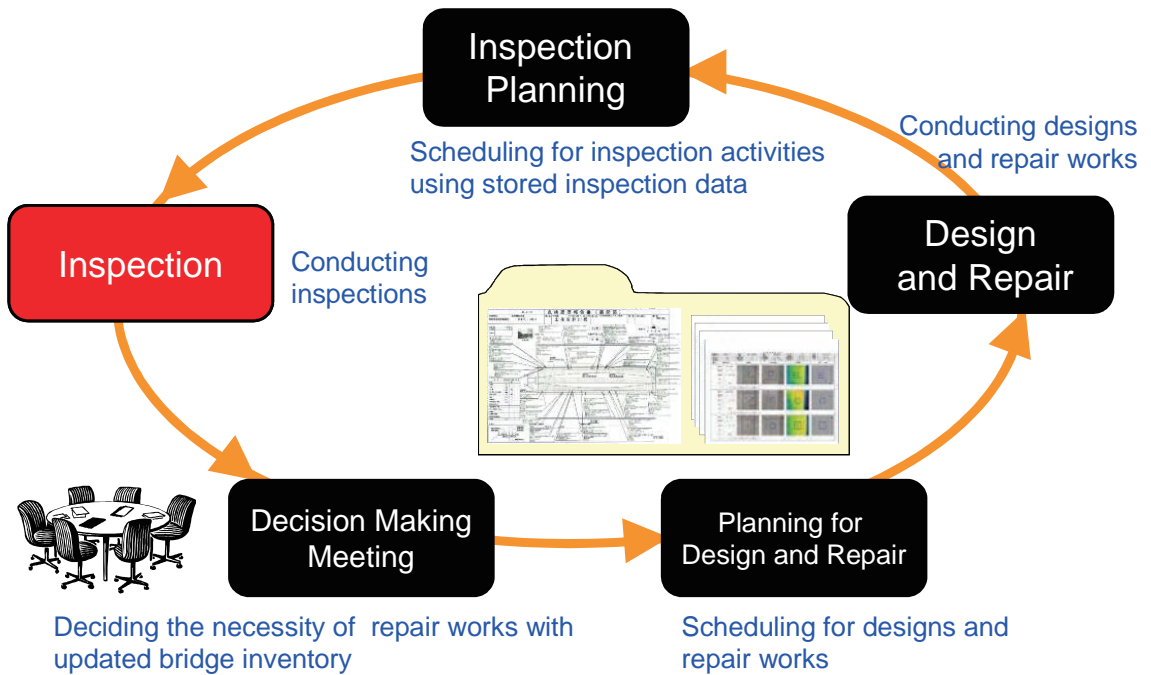
West Nippon Expressway Shikoku Company Limited.

## The NEXCO-West Group Policy




# 100% Safety and Reliability



# Operation and Maintenance Management



## Inspection Types

Type	Procedure	Frequency
Daily Inspection 	Visible unusual conditions and deformations of structures are daily inspected behind the wheels.	Once every two days to Once every four days (Dependent on traffic volume)
Routine Inspection 	The safety of the structure is regularly confirmed by distant visual inspection, cross visual inspection and hammering test.	More than once a year
Detailed Inspection 	The safety of the structure is understood by cross visual inspection and hammering test more in detail.	Once every five years

## Proposal of our technology



J-System

- We developed this technology to gain effective inspection in order to comply Road Management rule
- After analyzing accumulated data we propose an Evaluation Indicator that related in order to understand deterior mechanism of Architectural structure and to do a preventive action



Eagle

### **【Our approachment】**

Not just hand over a complete system, but we submit a proposal by finding out the needs from user and design the machine based on measurement accuracy as needed and customize soft ware that easy to use

## Contents

### I . Approach and issues for preventing concrete accident flaking

#### I -1. Bridge

( reinforced concrete structure)

#### I -2. Tunnel

(unreinforced concrete structure)

### II . Approach and issues for identity of pavement damages



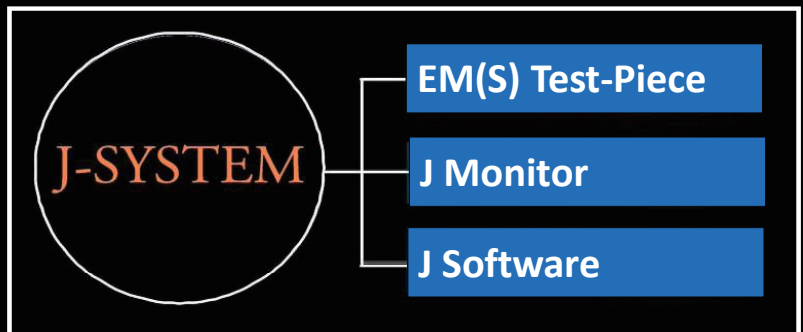


# Bridge Inspection

## J -SYSTEM



A new concrete inspection and assessment method with safer manipulating, higher performance, and lower cost based on infrared thermography technology.

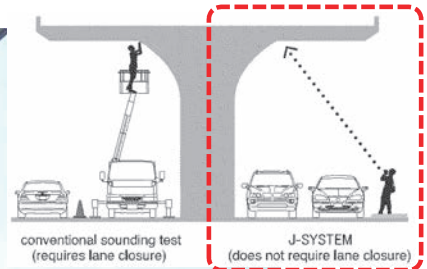


## Sounding inspection for prevention measure against flaking



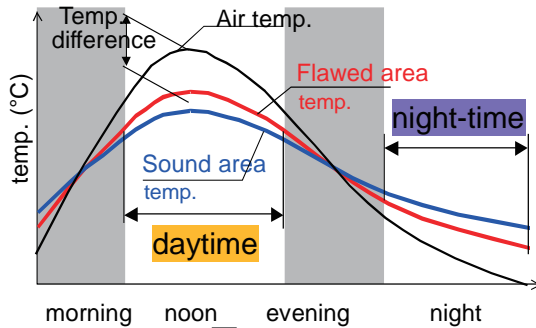
Present method needs a lot of costs and time

## Infrared inspection situation

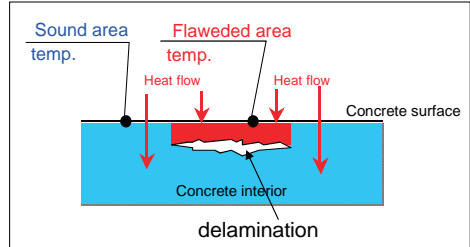


# Basic Theory of Infrared Thermography

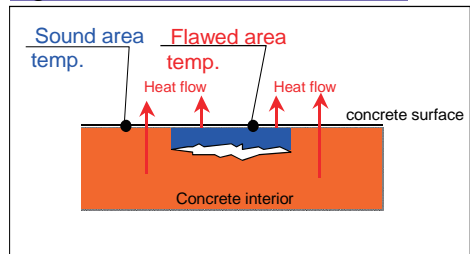
Inspection must be done when the temperature difference between air and concrete is large enough.



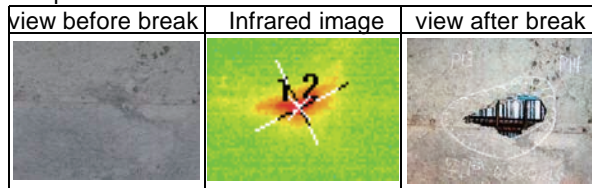
daytime : sound < flawed < air



night-time : sound > flawed > air



Temp. differences creates thermal anomalies



## Relationship between Inspection time, and bridge type or part

Direction of heat flow and temperature in damage part

Section	Surface to be inspected	Direct effect	Indirect effect
All bridges			
Metal bridge		Surface to be inspected is not directly exposed to sunlight	
Box beam bridge		Surface to be inspected is not directly exposed to sunlight	

Inspection time should be selected by bridge type or part

# Inspection time period of each bridge type

Seto Inland Sea climate during summer/autumn

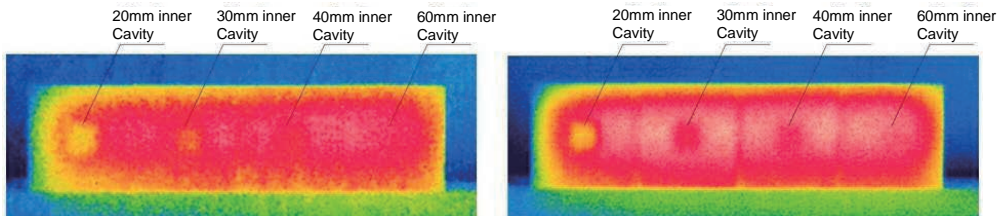
Inspection time period

Bridge type	Section	Time											
		6	8	10	12	14	16	18	20	22	24	2	4
All bridges	Wall balustrade		█	█	█	█		█	█	█	█	█	█
RC bridge	Overhang								█	█	█	█	█
	Floor slab			█	█	█	█			█	█	█	█
Me bridge	Overhang	█							█	█	█	█	█
	Floor slab	█							█	█	█	█	█
Box beam bridge	Overhang	█							█	█	█	█	█
	Floor slab									█	█	█	█
PC bridge	Overhang	█							█	█	█	█	█
	Girder			█	█	█	█			█	█	█	█
	Floor slab	█							█	█	█	█	█

Almost all bridge types and bridge sections can be investigated during night time.

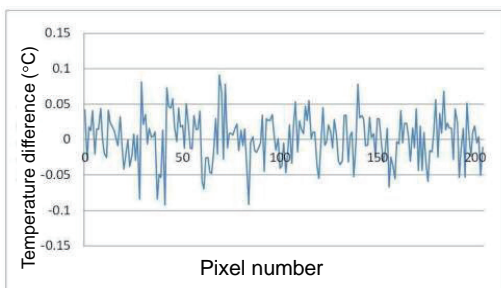
## Images of damage from different minimum detected temperatures

Thermal images of different minimum detected temperatures (NETD)  
(Daily range = 10°C: photographed at 0 a.m.)

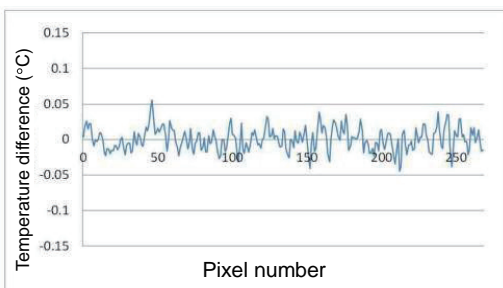


a) Thermal image photographed by Camera A

b) Thermal image photographed by Camera B



a) Temperature variation of Camera A

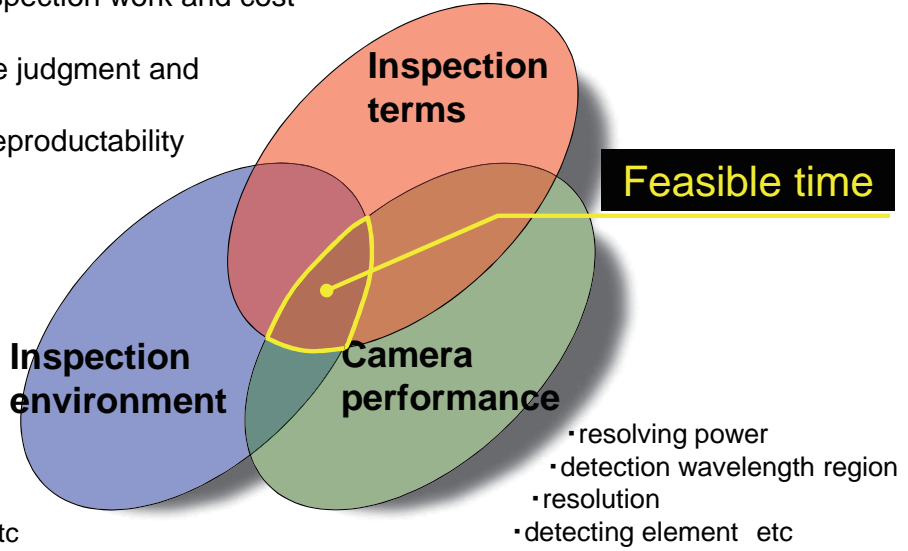


b) Temperature variation of Camera B

# Issues for accurate infrared inspection

- clarification of inspection depth
- quality guarantee and prevention of missing damage
- high efficient inspection work and cost performance
- efficient damage judgment and objectivity
- recording and reproductability

- kind of bridge, part
- detection depth
- photographing distance etc



- daily range
- solar radiation
- wind and rain etc

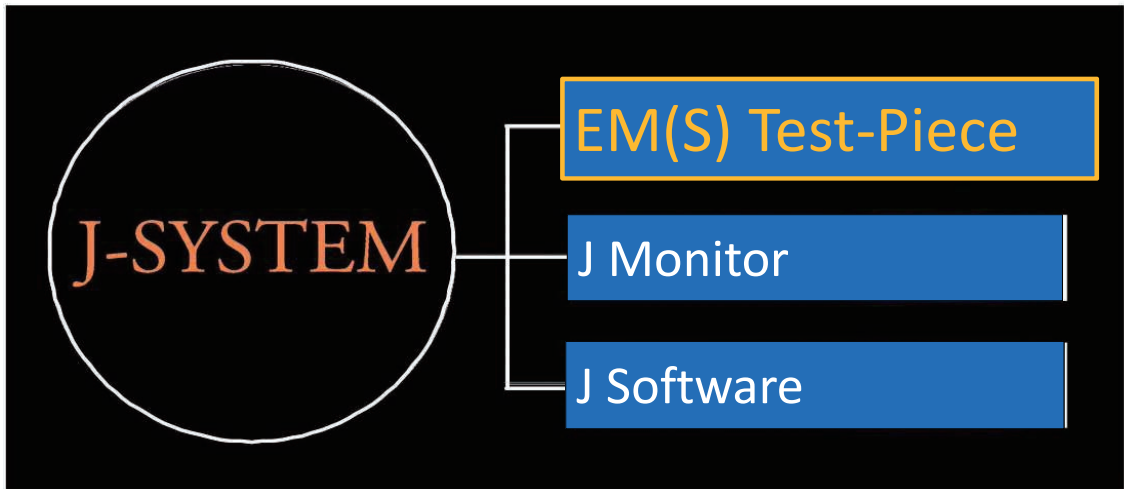
- resolving power
- detection wavelength region
- resolution
- detecting element etc

# J -SYSTEM

A new concrete inspection and assessment method with safer manipulating, higher performance, and lower cost based on infrared thermography technology.

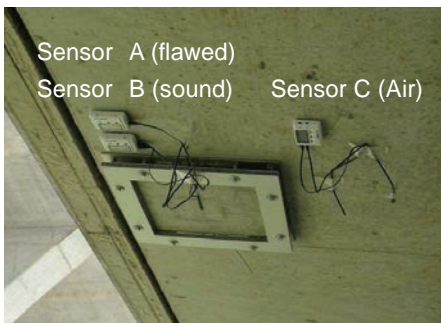
The diagram shows a person in a white protective suit and helmet holding a device. To the right, a white-bordered box contains a circle labeled 'J-SYSTEM' connected to three blue rectangular boxes: 'EM(S) Test-Piece', 'J Monitor', and 'J Software'.

# EM(S): On-the-spot Test Piece

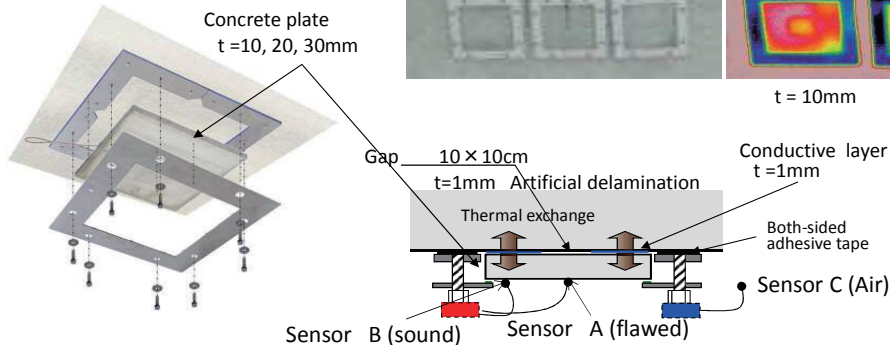
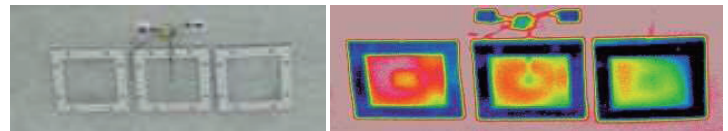
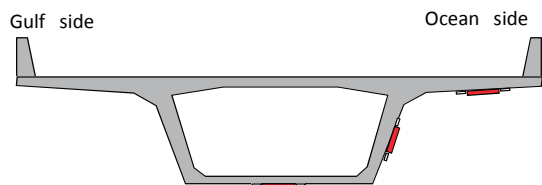


To ensure thermal condition of real structure for infrared testing before and during infrared inspection

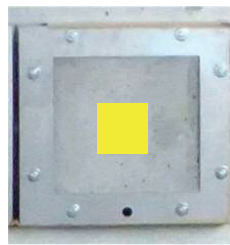
# EM(S) : On-the-spot Test-Piece



To obtain real temperature data under actual conditions element by element

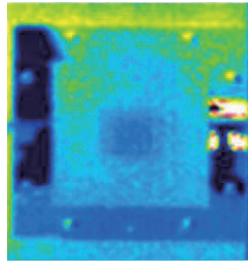


# Do we inspect at a suitable time ?

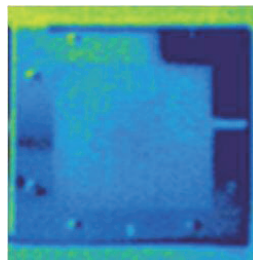


EM(S)

Checking  
central Void



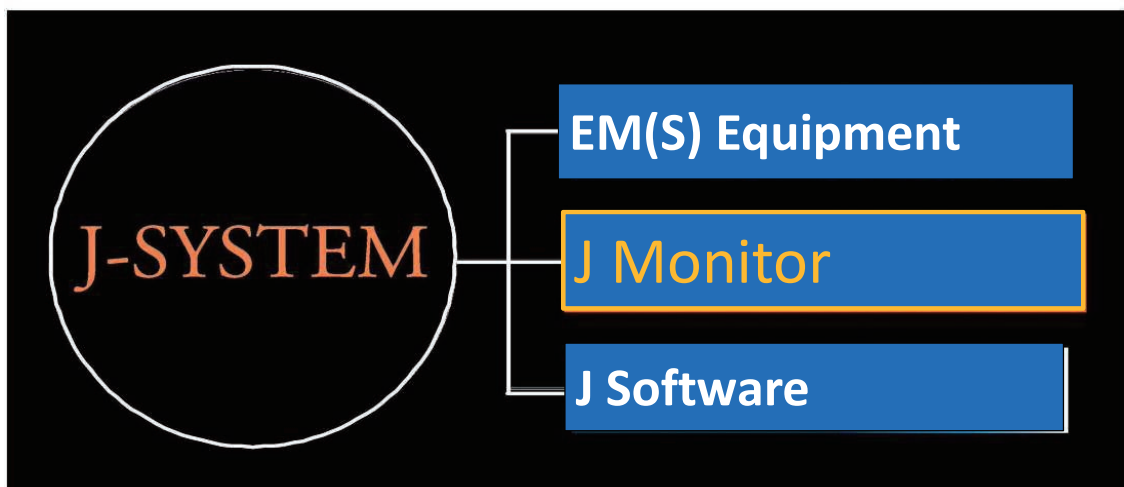
IR Image  
Central cavity is  
observed.  
『OK』



IR Image  
Cavity is not observed.  
『NG』

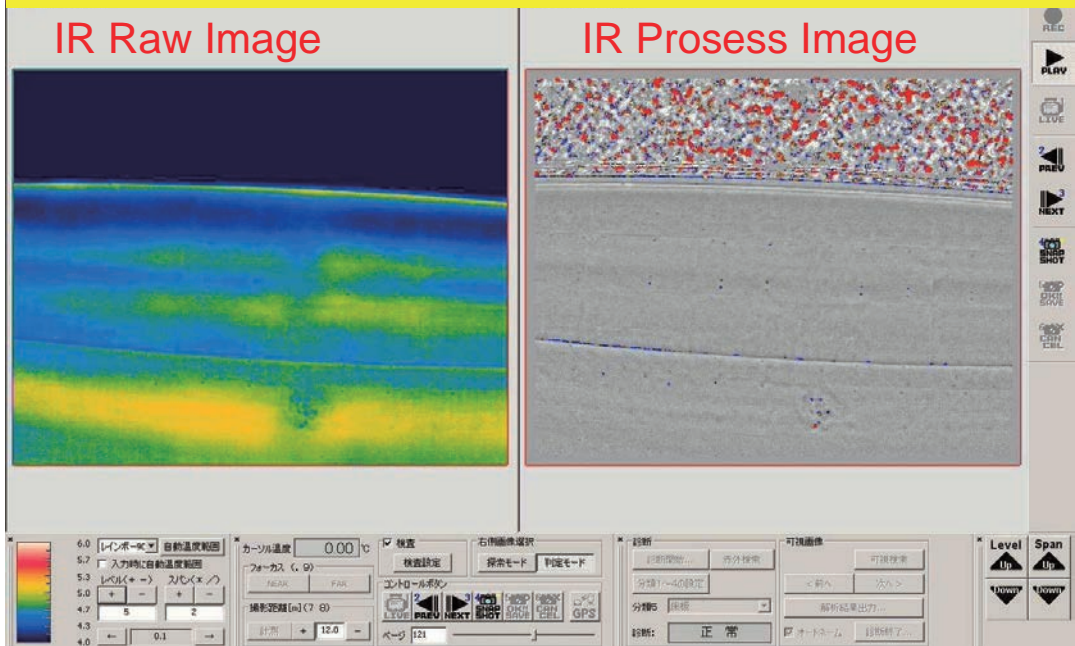
The thermal environment should be precisely obtained by an EM(S) device before any investigation

## J Monitor: A Display for IR images in Real Time

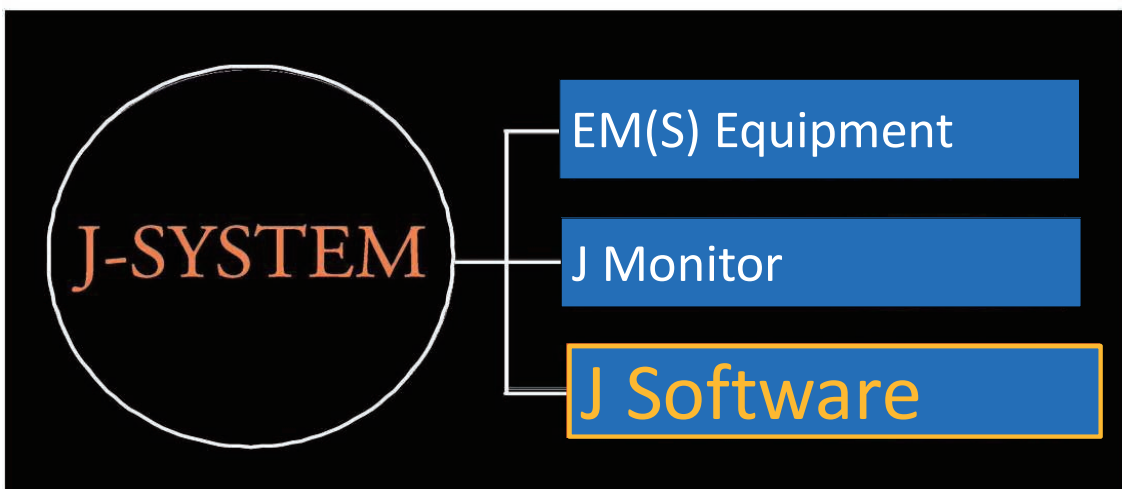


# J Monitor

## J Monitor

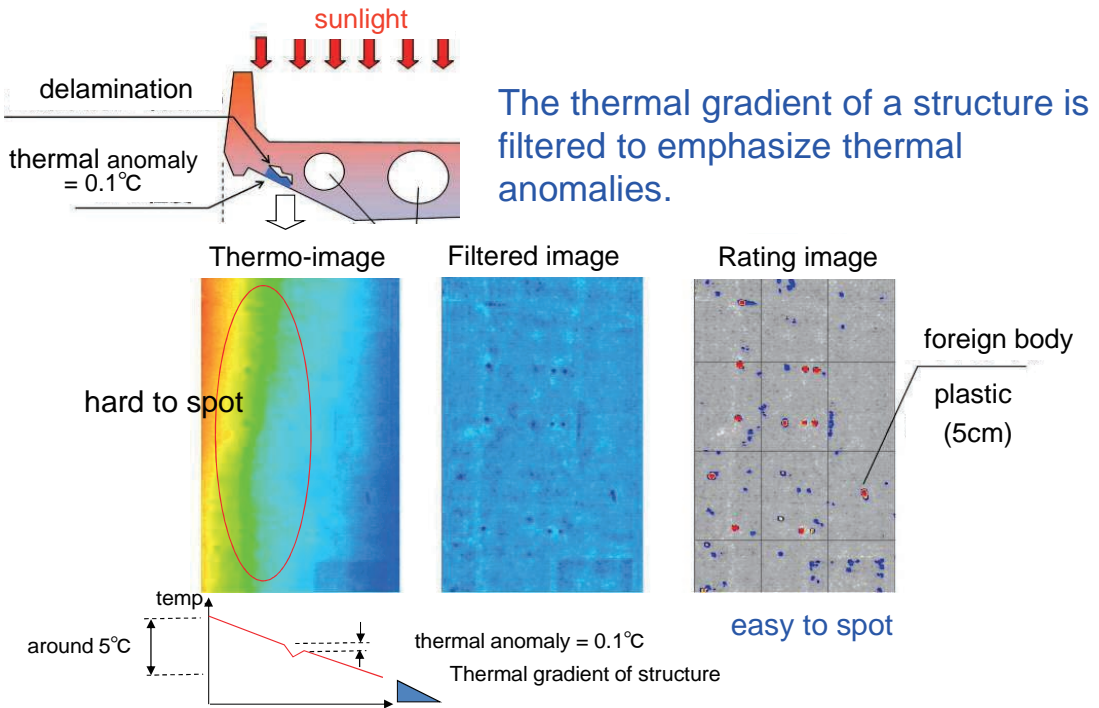


## J Software: Infrared Image Processing Software





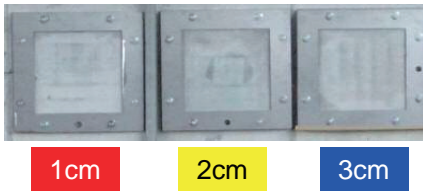
# Image Emphasizing Thermal Anomalies



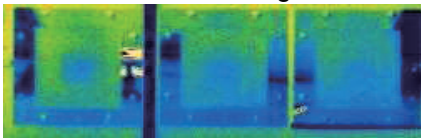
# J Software: Damage Ratings

Temperature distribution is interpreted into damage ratings by using a comprehensive database of temperature patterns.

Visible image: EM(S) test-piece



IR raw image

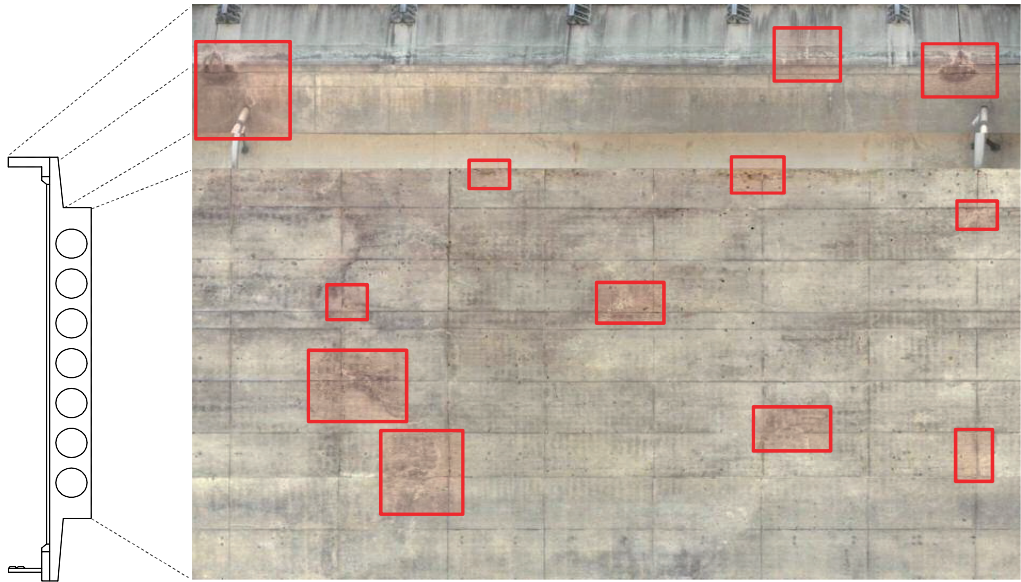


IR Process image

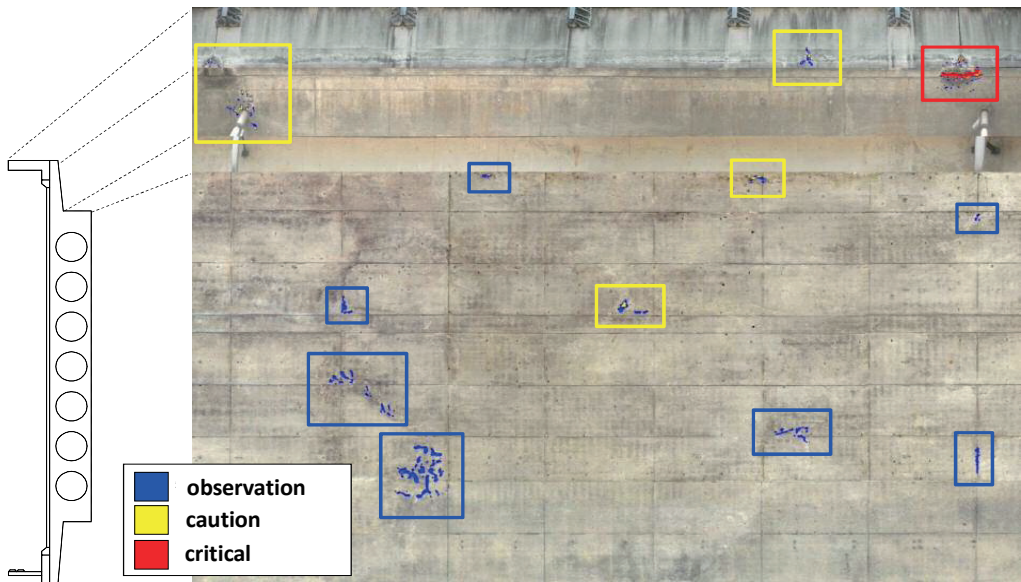


Damage level	
Damage pattern	indication
	<p><b>Observation (Insignificant)</b></p>
	<p><b>Caution</b></p>
	<p><b>Critical</b></p> <p>Emergency measures required</p>

# Comparison Between New and Conventional



## Is it possible and easy to evaluate objectively?



Your resources can be focused on the areas that need the most work.

# J-System Features

Proper investigable time can be assessed.

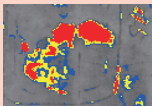

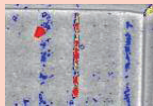

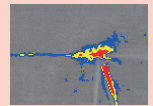
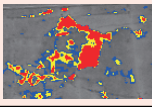
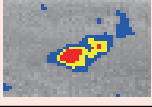
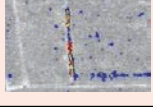






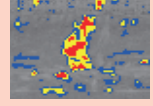




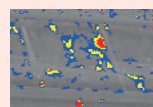
Damage depth can be obtained in real time

Absolute quality assurance

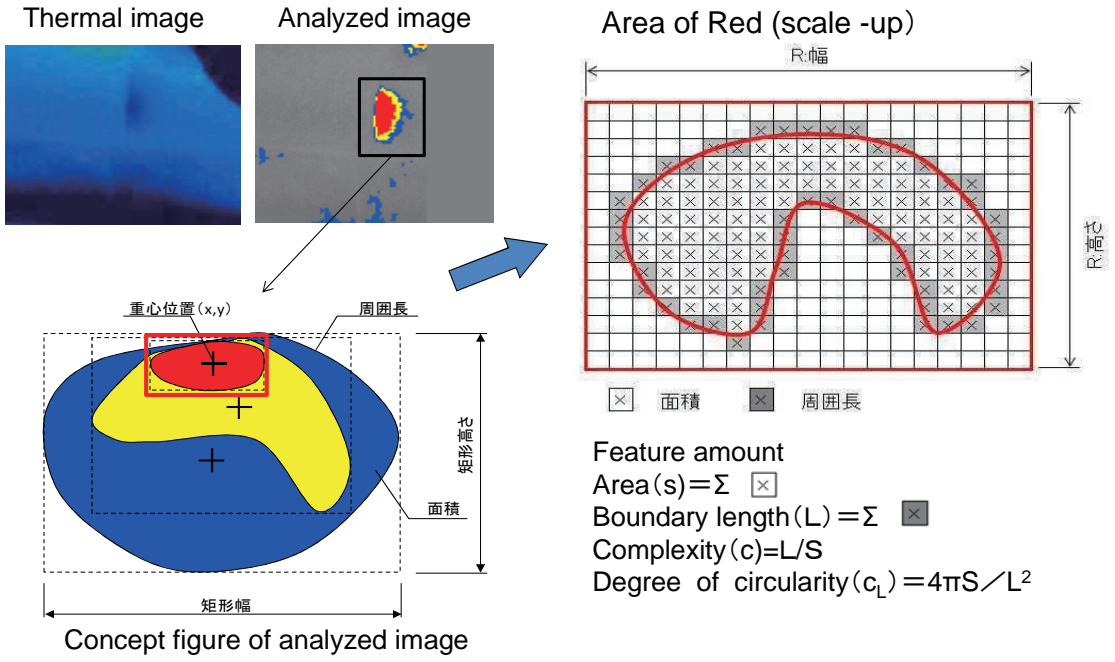
& Oversight prevention

**“J-System” supports investigations conducted by customers**

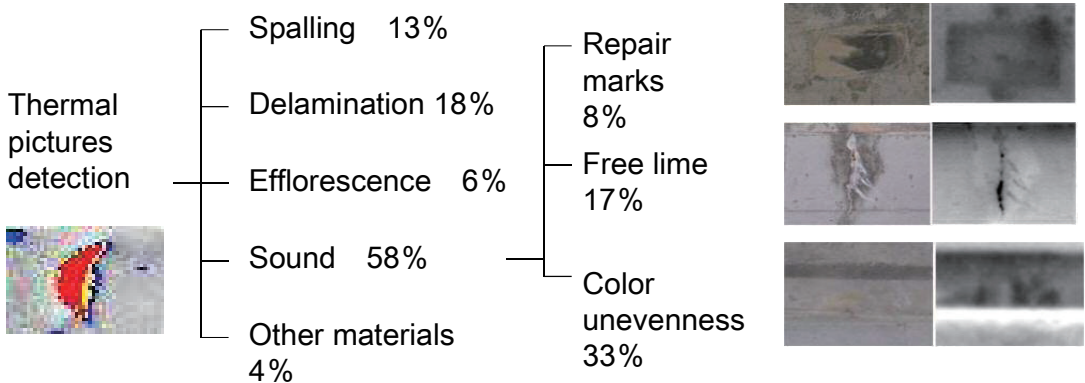
Features analyzed image by results of hammering sound

removal or flaking	Cavity	Slag	Foreign substances	Normal
				
				
				
				
Surrounding form is complexity, Red is out of center.	Surrounding form is smooth, Red is in the center.	Form is long thin, surrounding form is complexity.	Form is square, Red occupancy is high.	Yellow occupancy is high, Red's barycenter is in the midst.

# Extraction of feature amount on analyzed image



# Increasing prediction accuracy ( reclassification)



60% of sound parts

Redistribution of sound parts = repair marks, free lime, and color unevenness

Examining algorithm of classifying 7 categories

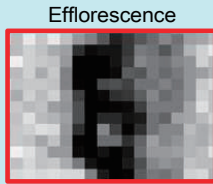


Utilizing thermal pictures textures

# Situations of thermal pictures textures

## Thermal recording of foreign substances

Surface adhesion

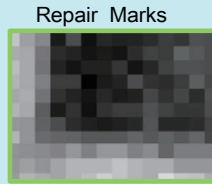


Efflorescence



Free Lime

Lacing



Repair Marks



Foreign substance lacing

## Measuring thermal movement through detection

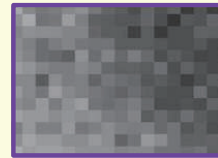
Sound ( color unevenness )



Spalling Area



Delamination Area



With contrast  
( even )



Local contrast

With contrast  
( uneven )

## Texture Analysis by Gray-Level Co-occurrence Matrix

### Texture Analysis by GLCM

(GLCM : Gray-Level Co-occurrence Matrix)

Method of inspecting colorful density location of remote two-pixel pair at certain area

### Computing GLCM



Computing 14 different character values

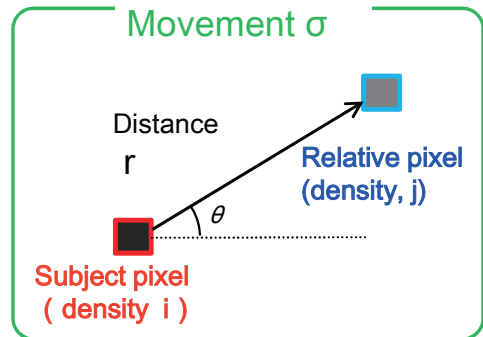


Effective character value for evaluating damage level

# Texture Analysis by GLCM

## GLCM ( Probability Matrix )

Probability  $P_{\delta}(i, j)$  where a relative pixel's density is  $j$  at a distance  $\delta = (r, \theta)$  from a subject pixel density  $i$



Enlarged thermal picture

1	2	0	3
1	2	2	3
2	0	3	2
1	3	0	2

$$P_{\delta} = \begin{matrix} & \rightarrow j \\ & 0 & 1 & 2 & 3 \\ \begin{matrix} 0 \\ 1 \\ 2 \\ 3 \end{matrix} \downarrow i & \begin{bmatrix} 0 & 0 & 1 & 2 \\ 0 & 0 & 2 & 1 \\ 2 & 0 & 1 & 1 \\ 1 & 0 & 1 & 0 \end{bmatrix} \end{matrix}$$

$(r, \theta) = (1, 0^\circ)$

Converting the probability of movement appearance frequency

## Character value arising from GLCM

	Character value	Significance probability
1	Angular Second Moment	0.405
2	Contrast	0.000 ※※
3	Correlation	0.108
4	Sum of Square:variance	0.000 ※※
5	Inverse Difference Moment	0.109
6	Sum Average	0.000 ※※
7	Sum Variance	0.000 ※※
8	Sum Entropy	0.140
9	Entropy	0.374
10	Difference Variance	0.160
11	Difference Entropy	0.135
12	Information Measure of Correlation1	0.045 ※
13	Information Measure of Correlation2	0.871
14	Maximal Correlation Coefficient	0.621

# Tunnel Inspection

## Background

Conventional visible inspection adds damage conditions of tunnel linings concrete , such as flaking concrete to be caused critical accident, adopted camera technical and developed vehicle to inspect higher accurate

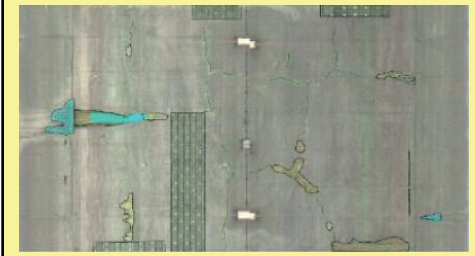


# Flow chart for tunnel inspection

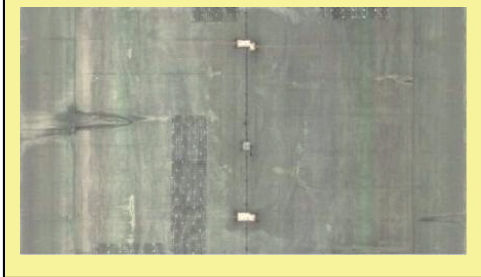
I . The captured image of the tunnel



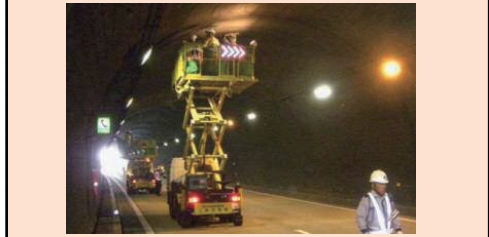
III. Analyzing



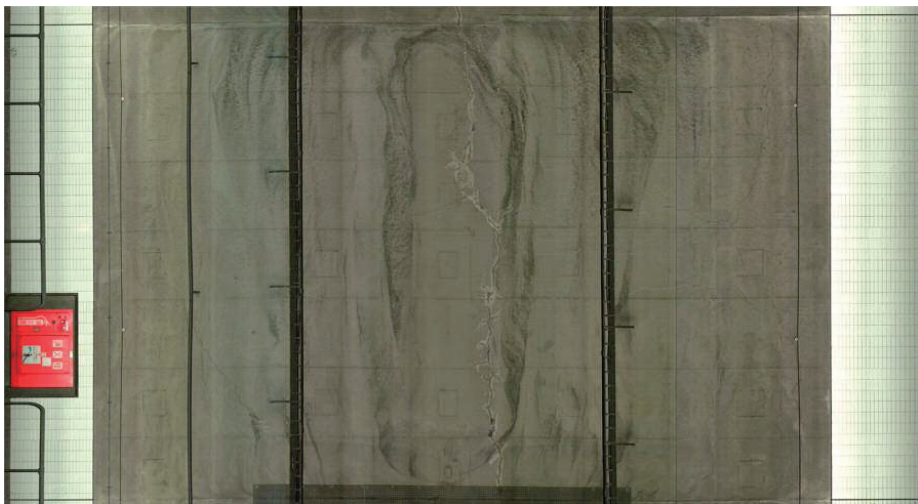
II . Creating an image of the tunnel



IV. Inspection



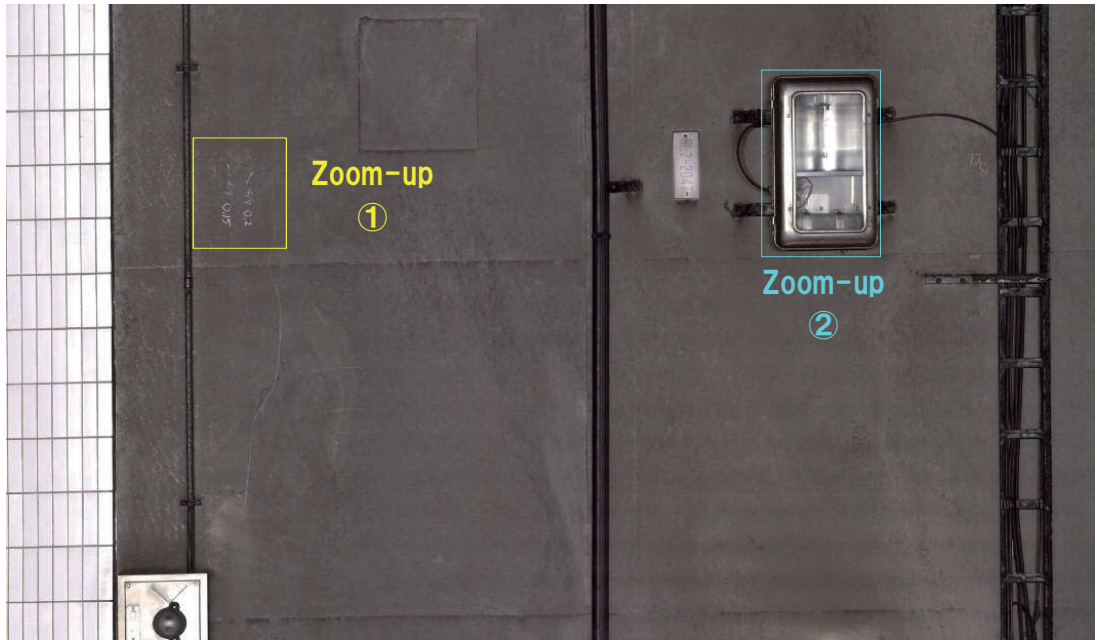
## Investigation of cracking and other damages



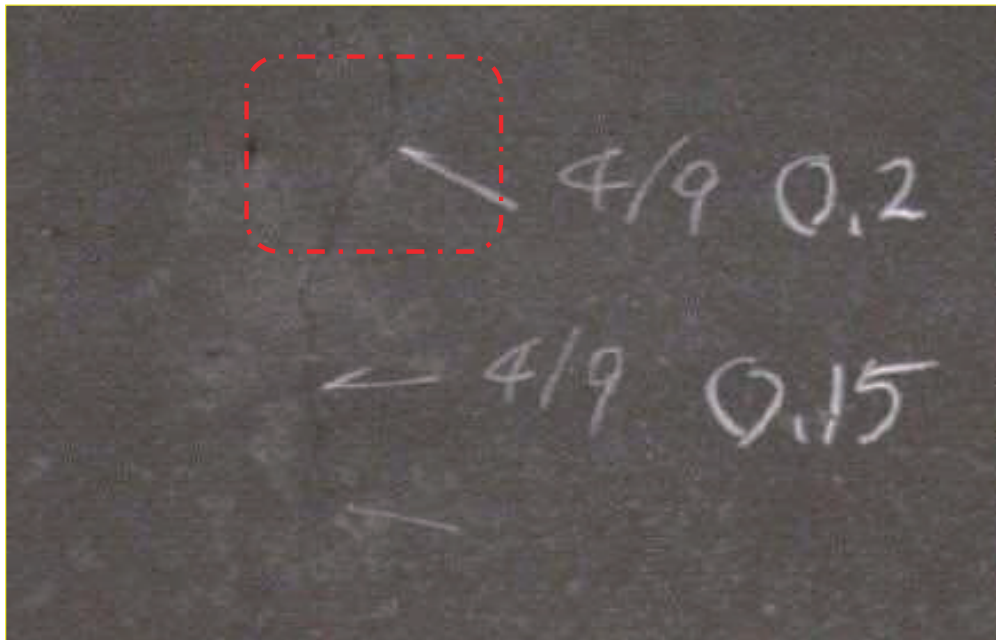
- The width, length, and number of cracks, efflorescence, and water leakage can be investigated with high precision.
- Color images allow the inspection of corrosion and damage to the accessories attached to the tunnel lining.
- High-precision photography/analysis enables a comparison between the previous investigation and the current damage progress.



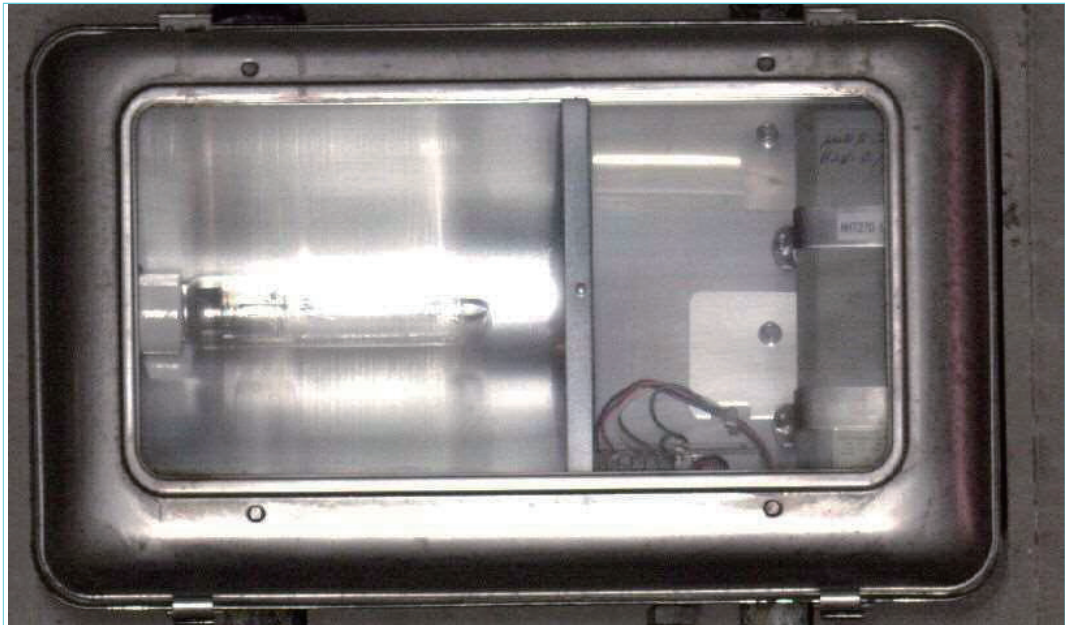
# Visual image ( tunnel )



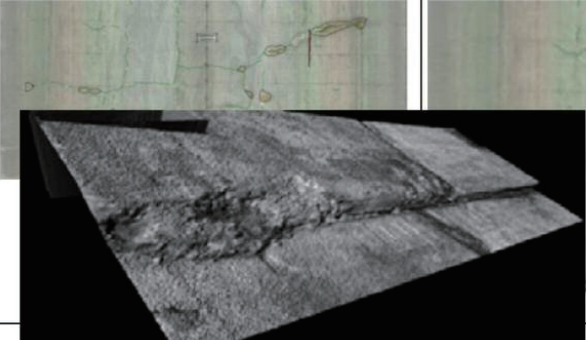

# Zoom-up visual image (Cracks )



# Zoom-up visual image (tunnel lighting )



## Current of Issues (improvement)

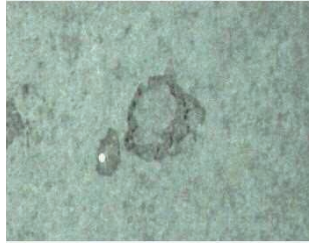
Current problems	New technique
<p data-bbox="175 1199 606 1392">No judging by the front of image whether the crack may be falling or not</p> 	<p data-bbox="621 1199 1190 1340">Detecting flaking point by obtaining height data of tunnel lining surface.</p> 

# Measurement of tunnel conditions by height data

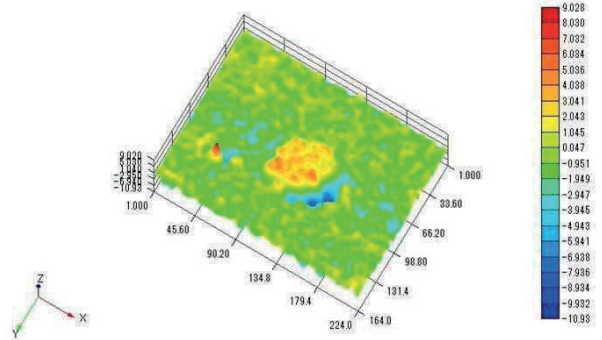
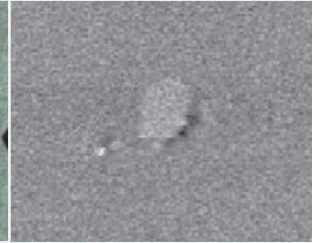


Damage of inside tunnel for verification (photo-shooting by digital camera)

Visual Image

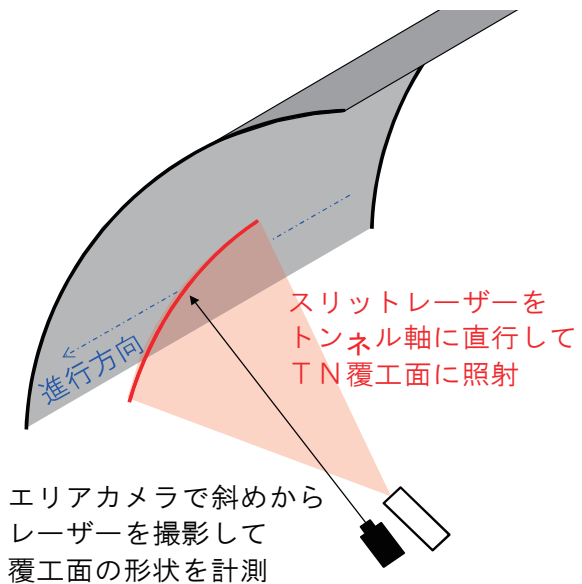


Height Image



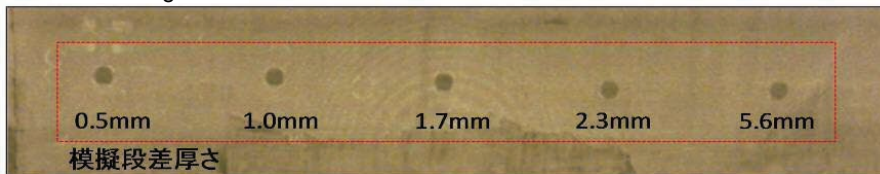
## Overview of proposed measuring technology ①

- ✓ Measuring tiny shapes of tunnel linings with vehicle speed of 50km/h
- ✓ Extracting local shapes' changes automatically through analyzing shape information, and identifying potential delaminating parts



# Overview of proposed measuring technology ②

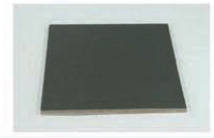
① Visual image



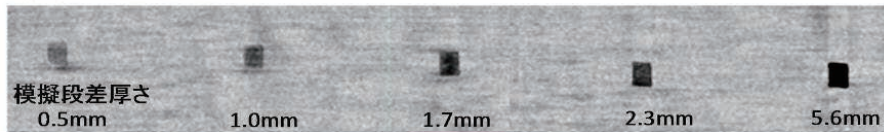
Simulate gap

□100×100mm

Thickness 0.5~5.6mm



② Height image

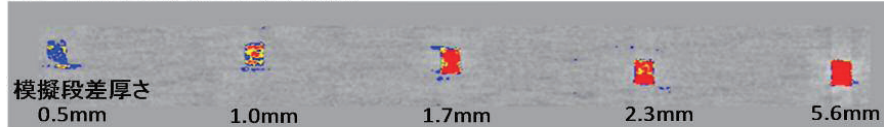


凡例



Black  
=Large gap

③ Process image



■ observation

■ caution

■ critical

# Pavement Inspection

# Inspection Methods

Daily Inspection (Behind the wheel)



Detailed Inspection pavement investigation

《Our product》

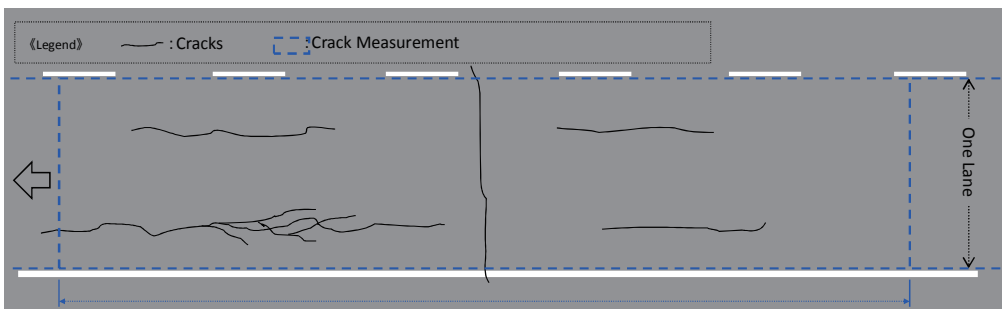


## Control Item

### Maintenance Target Values of Pavement

Rutting (mm)	Difference in Level (mm)		Coefficient of Sliding Friction ( $\mu$ V)	Flatness IRI (mm/m)	Cracking Ratio (%)
	Bridge Mounting	Crossing Structure Mounting			
25	20	30	0.25	3.5	20

### Cracks Evaluation (Conceptual Diagram)



Evaluation Unit: 100m

# Data Acquisition by Periodic Inspection

## Road Surface Measurement (3 Elements)

Company-owned vehicle



Cracks



Ruts

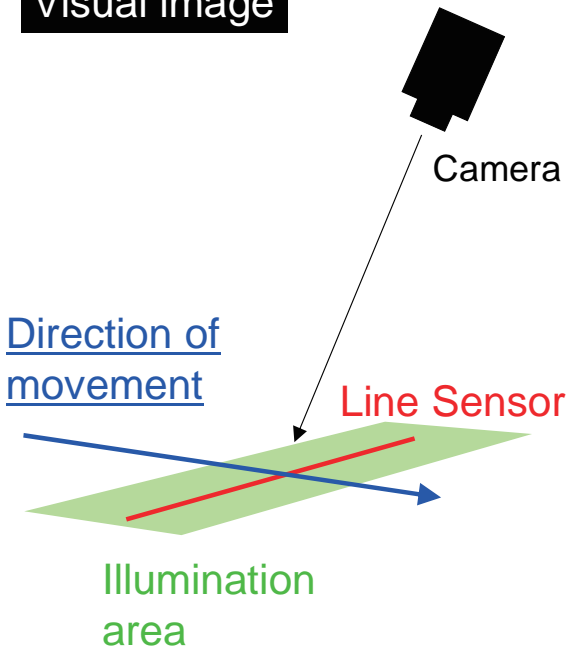


Flatness



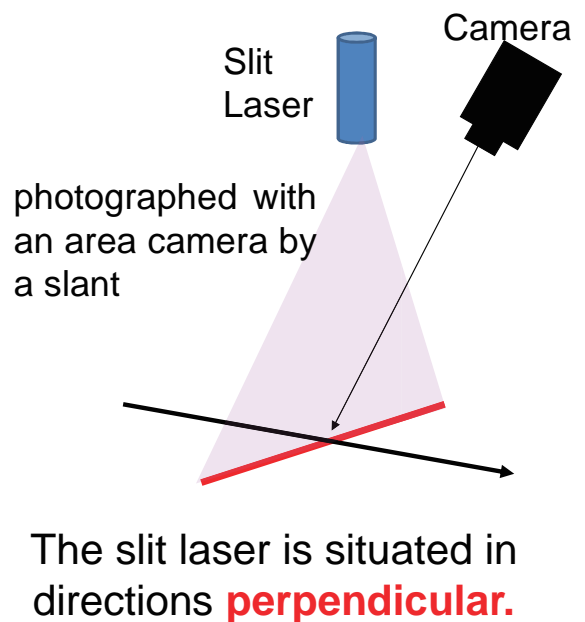
## L&L System

Visual image



Height image

Width profile



## Visual image ( pavement )



Accuracy at a speed of 100km/h

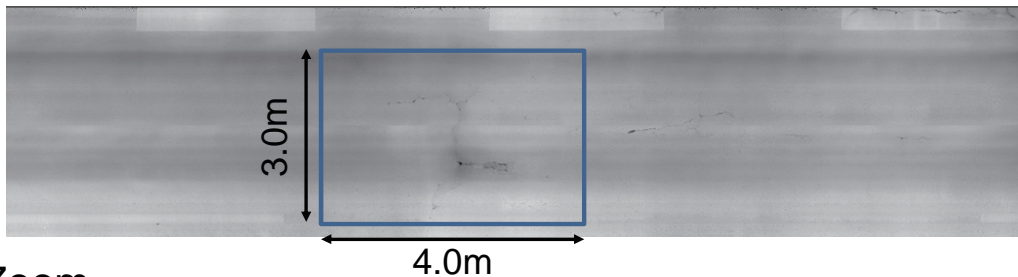
~Detecting cracks~

Shooting width=4.5m(Color image)

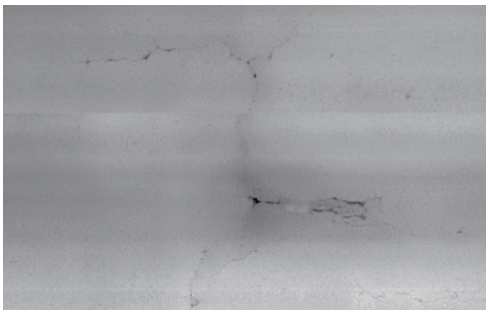
Resolution 0.8mm x 0.8mm/pixel

## Height image

Surface height image



Zoom



Accuracy at a speed of 100km/h

~Rutting Measurement~

Shooting width=4.4m

Dimension of rutting:1mm or less

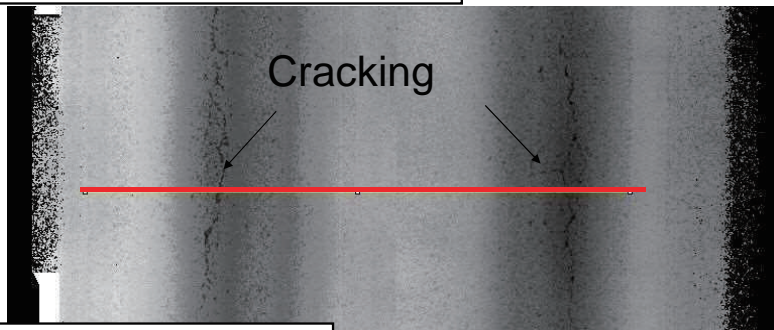
Resolution 1.68mm(Transversal)

5.60mm (Longitudinal)

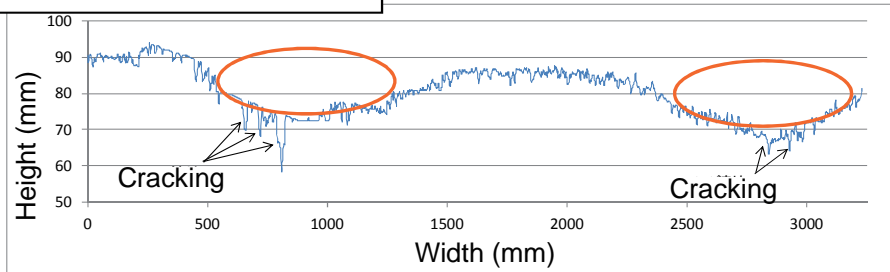
0.50mm (Depth)

# Ruts

Height image (Black part is low.)

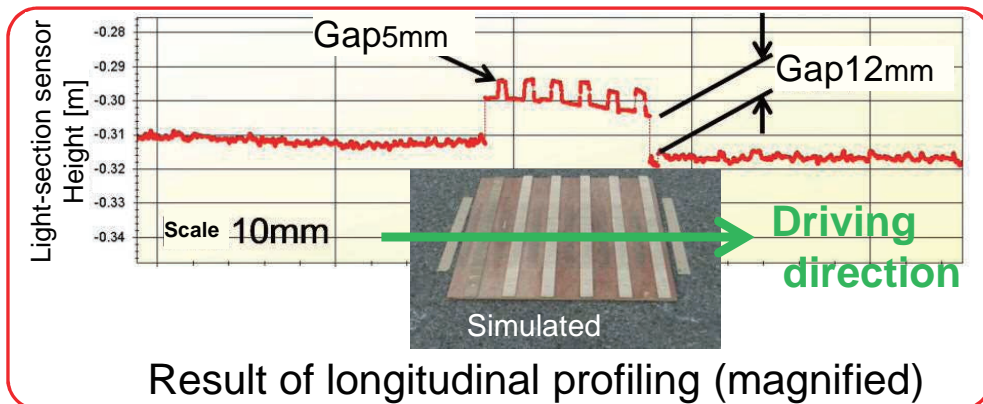
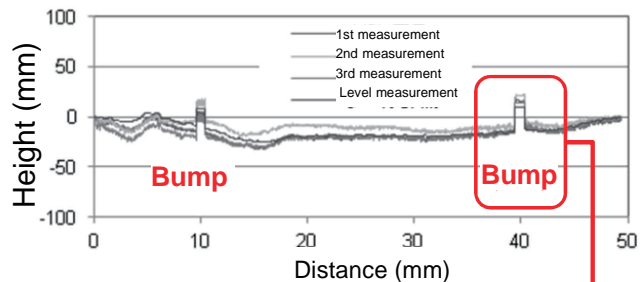


Ruts on the red line above



# Flatness (Longitudinal profiling)

High-resolution allows us to accurately profile the longitudinal shape of a microscopic bump.





# Analyzing highly accurate longitudinal profile

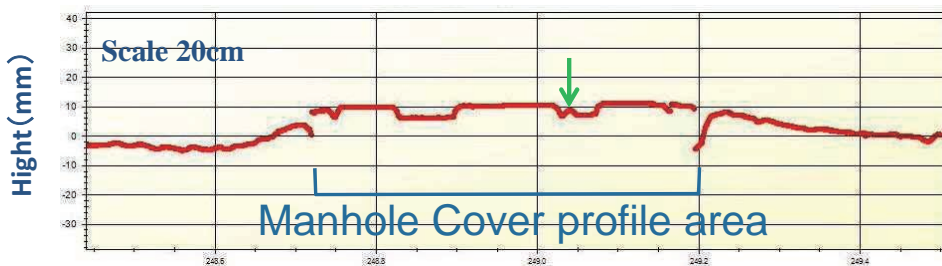
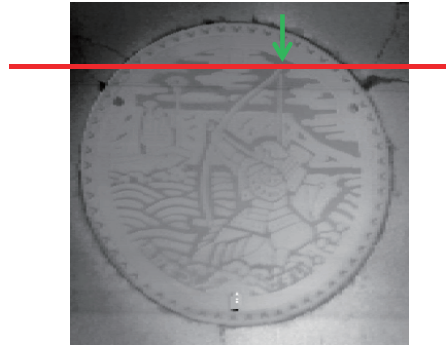


# Analyzing highly accurate longitudinal profile

Visual image



Surface height image



# Pavement analyzing

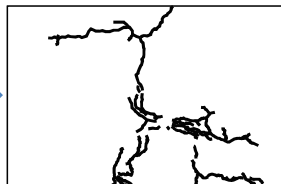
## To suggest a new pavement evaluation

### Bumps Analyzing

Detecting cracks Abstracting cracks from visual image

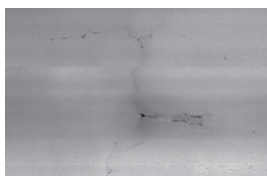


Visual image

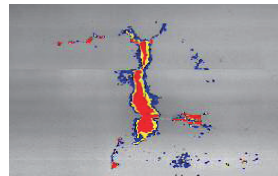


Abstracting crack image

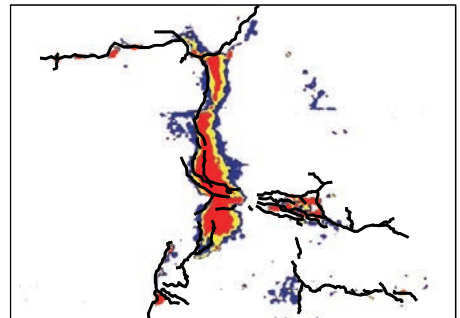
Detecting rutting Abstracting rutting from visual image



Surface height image



Processed surface height image

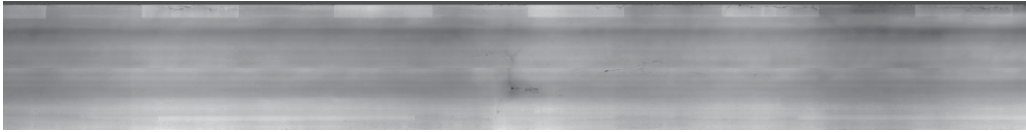


Crack+Processed image  
(red:bumps 5mm or deeper)

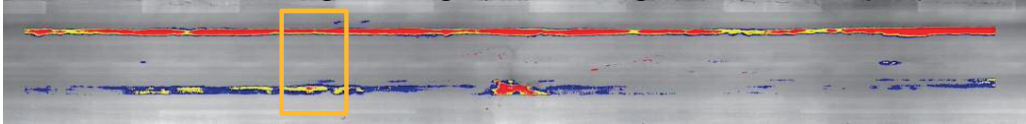
Depth of a rutting is contrasted through special software, called J-soft.

# Rutting Area Analysing

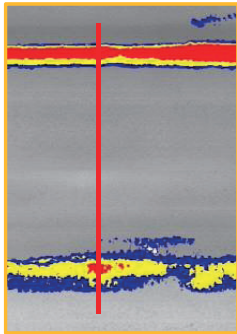
Surface height image



Processed surface height image (red: rutting 10mm or deeper)

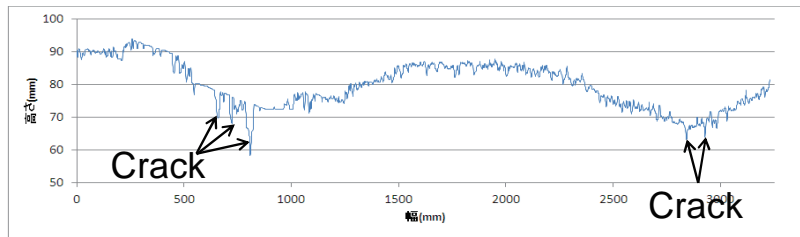


Zoom



Transversal cross section  
(Left red line)

Cracks can be detected as a difference of height.



# New proposal using image analysis (Blistering)



Visible image

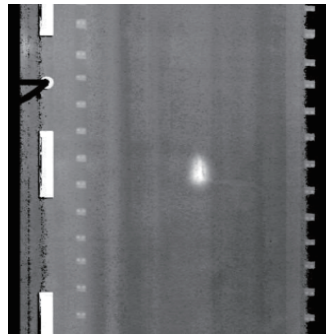
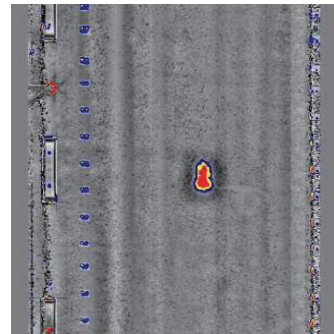
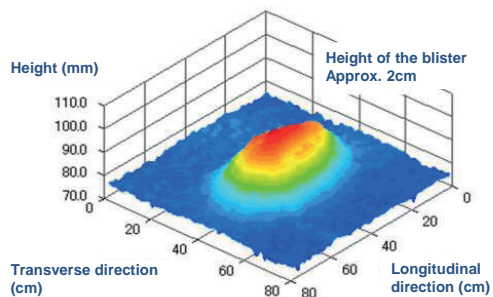


Image of road surface height

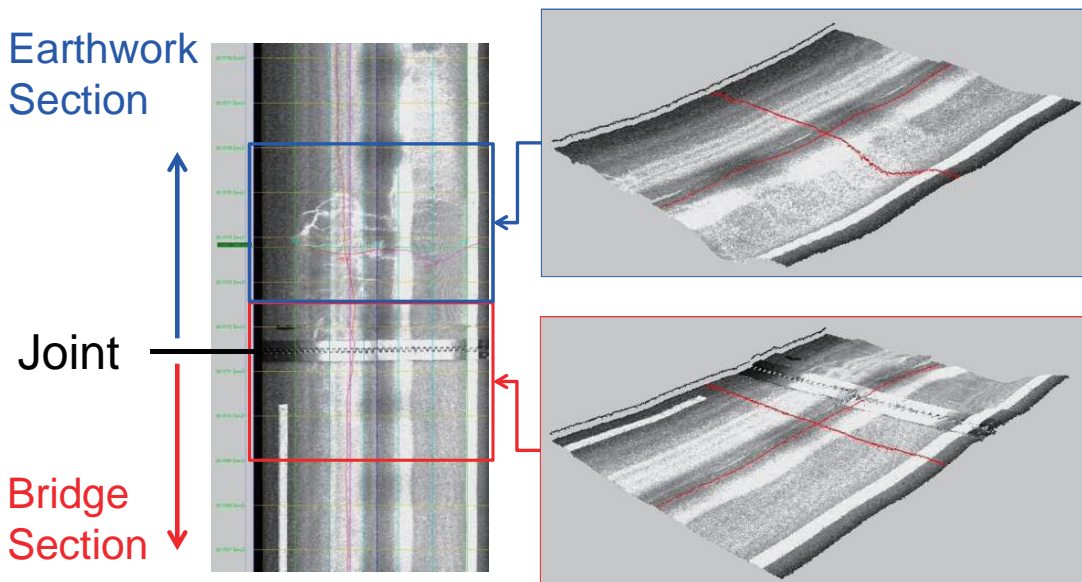


Analyzed image

The form of partial damage such as blistering can be replicated.

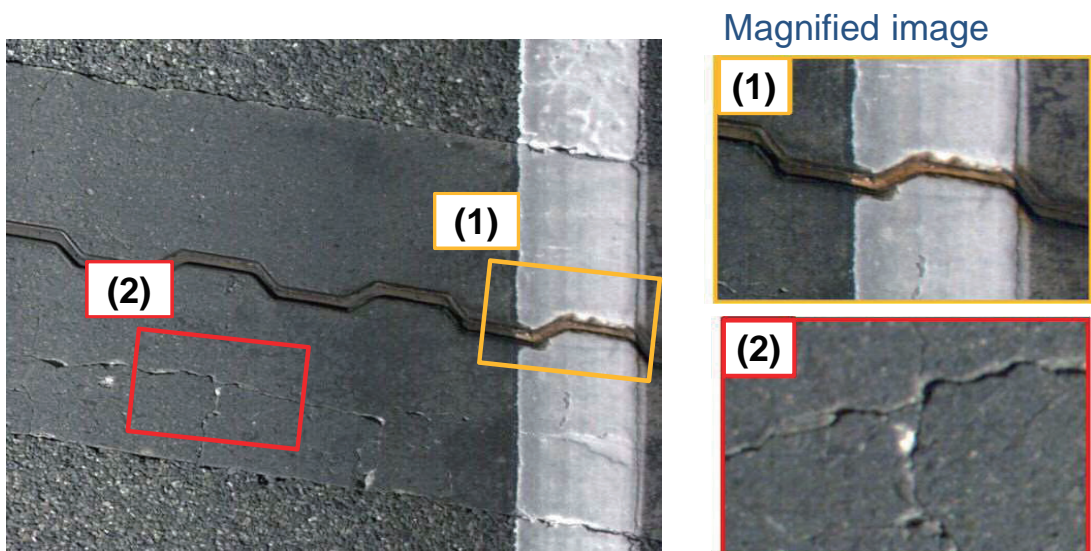


## Bumps height analysis image (3D display)



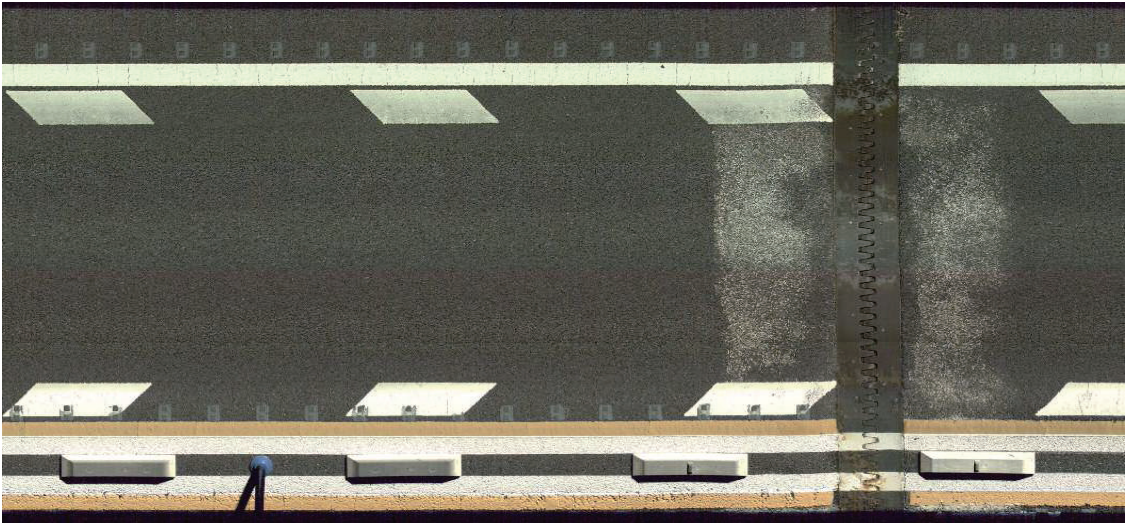
Visualizing the state of subsidence in an embankment at the back of an abutment

## Investigation using color images (Joint)



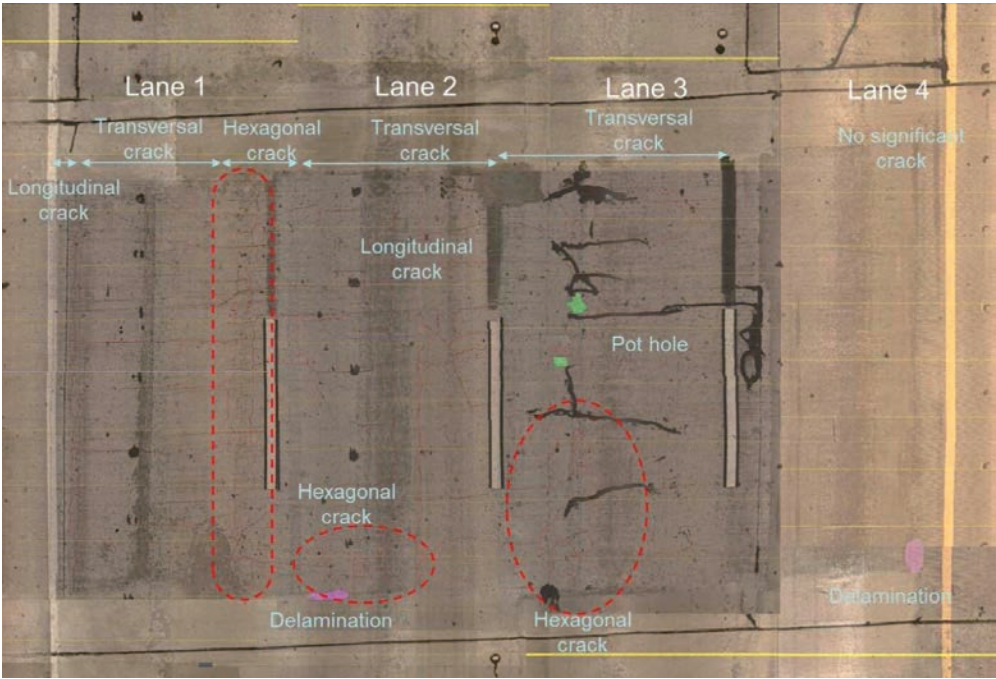
- (1) The degree of concrete corrosion and filling of fine materials can be identified.
- (2) Small cracks in the protective post-placed concrete cover can be photographed.

## Investigation using color images (Lane markings)



The adhesion status of lane marking paint to the road surface can be confirmed.

## Investigation using color images (Concrete Pavement)



# Proposal of a new evaluation method (Aggregate scattering) (1)

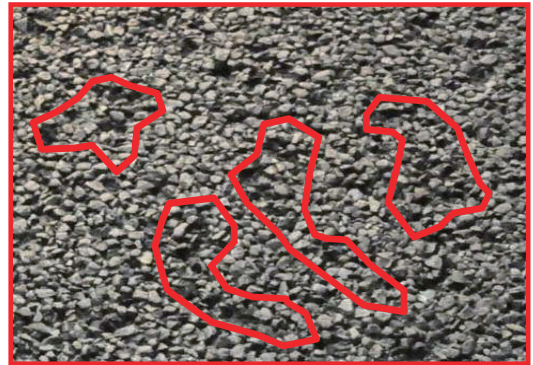
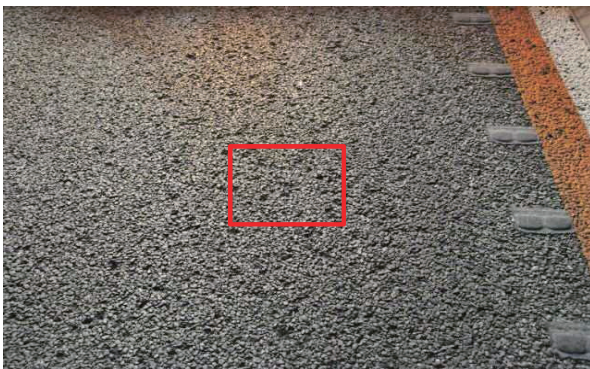
## ■ Current issues

Due to the spread of Porous asphalt-related road surfaces, problems caused by aggregate scattering have increased.

(1) Less noise reduction functionality

(2) Less driving safety and comfort

⇒ A quantitative evaluation method has not been established.



## Proposal

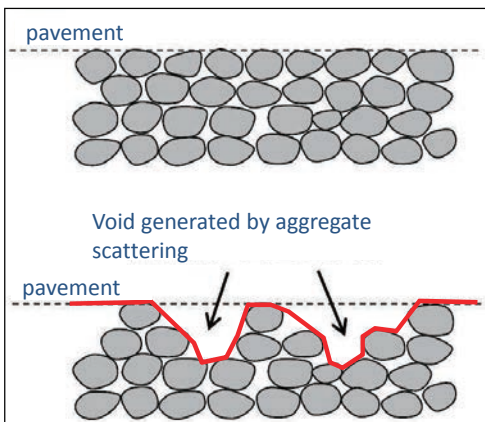
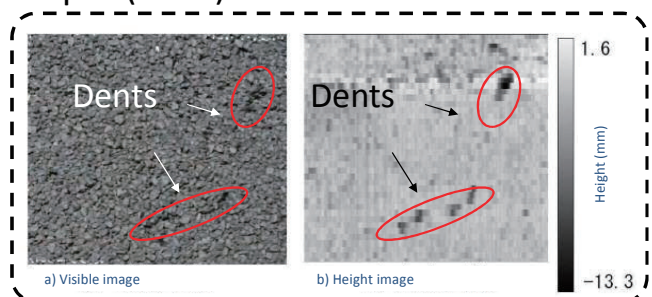


Image of aggregate scattering

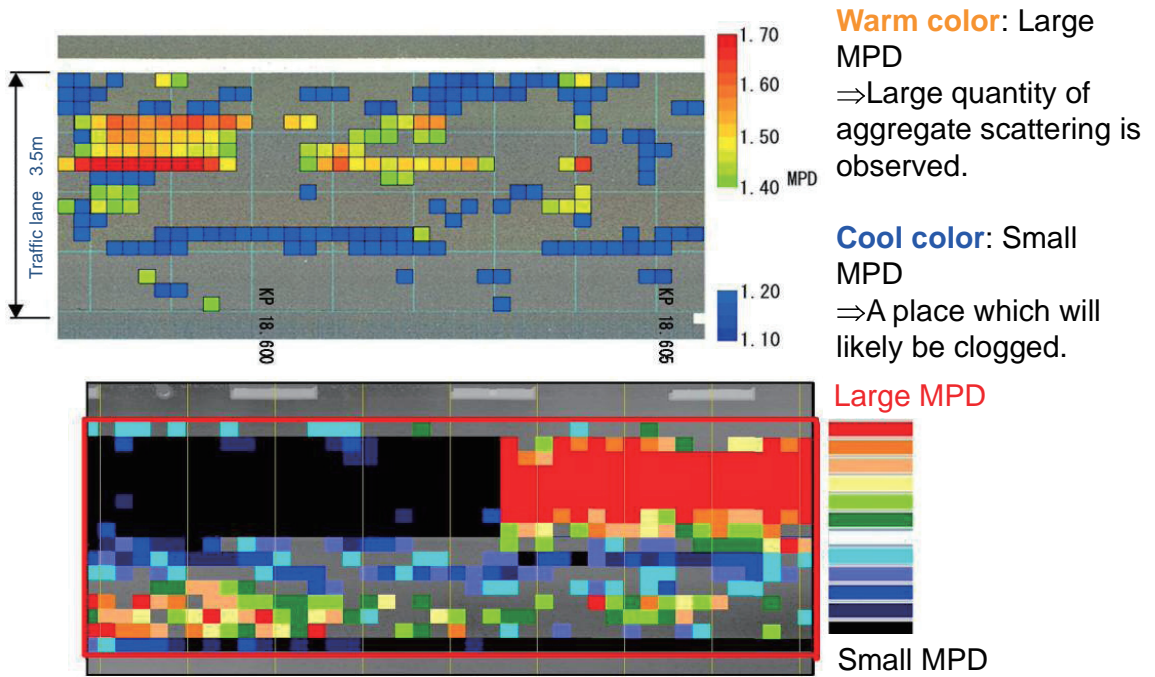
3D shape measurement by Light-Section Method allows us to measure the form of a pavement with high precision.



We focus on the relationship between aggregate scattering and mean profile depth (MPD).

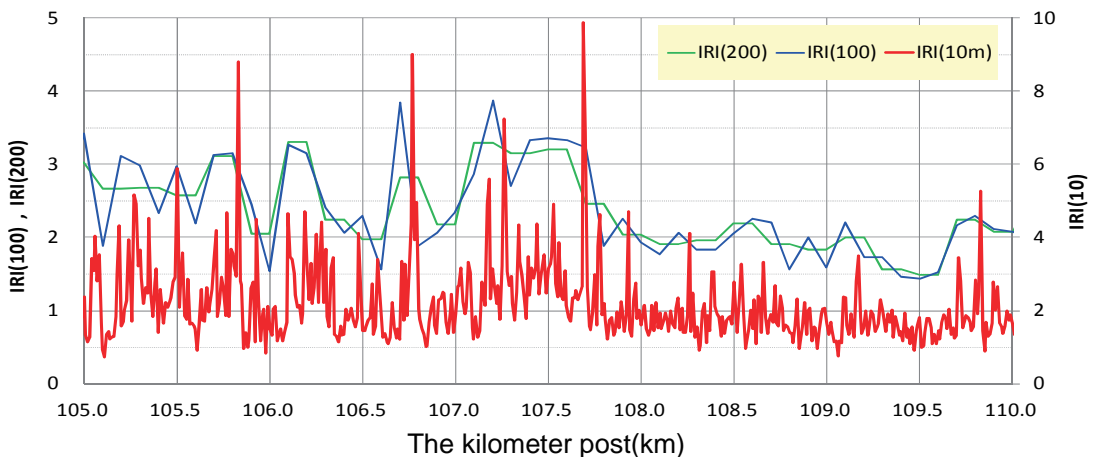


# Superficial (MPD) quantitative evaluation of aggregate scattering



# Analyzing highly accurate longitudinal profile

Future: IRI can be measured thanks to no speed dependanc



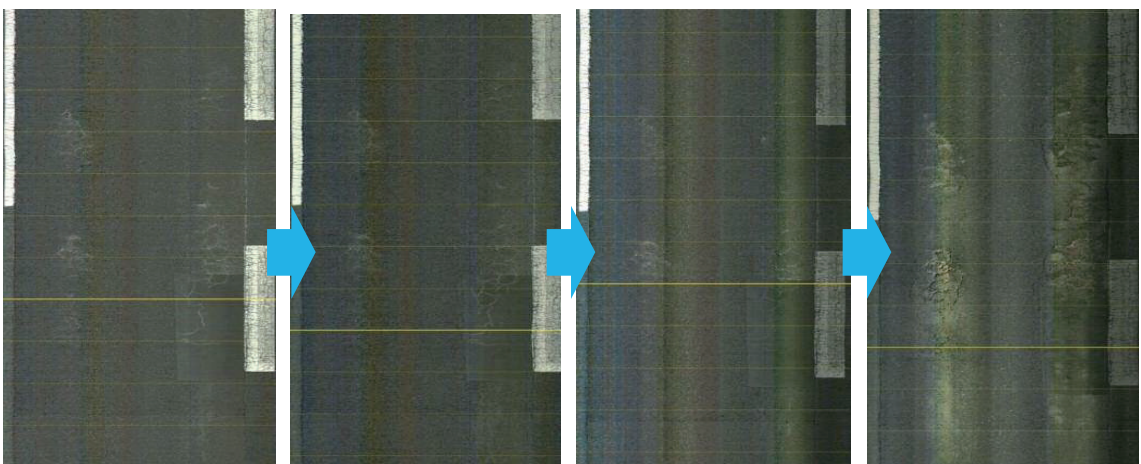
## Developmental event of pothole on Porous asphalt pavement

Done to review the objective of preventive maintenance

- Proposal new evaluation indicator to apply for Porous asphalt pavement
- Proposal method of predicting of occurrence of pot hole

## Data from periodic measurement

Visual image



Oct. 2013

Nov. 2013

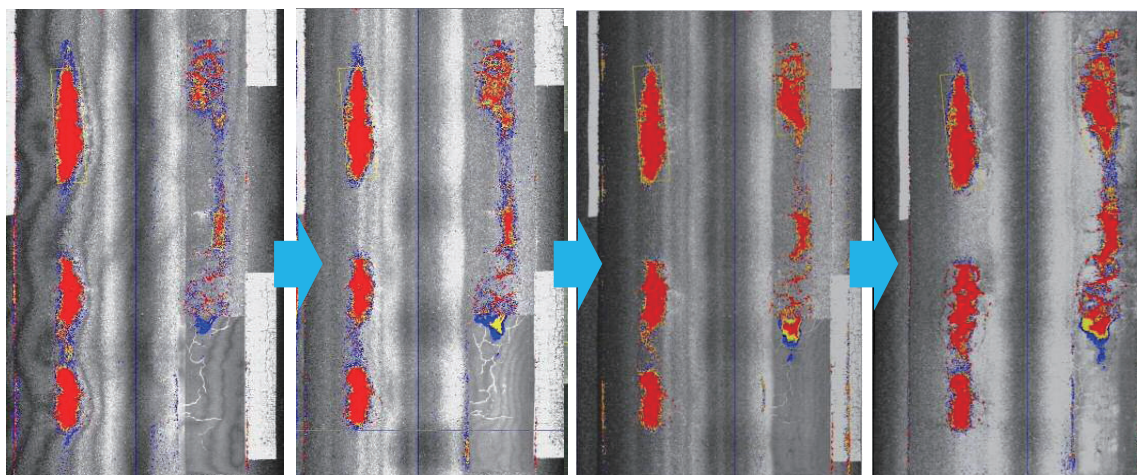
Dec. 2013

Jan. 2014



# Data from periodic measurement

## Height image



Oct. 2013

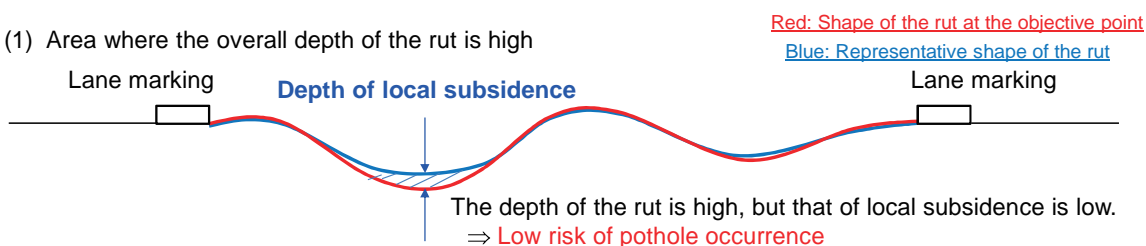
Nov. 2013

Dec. 2013

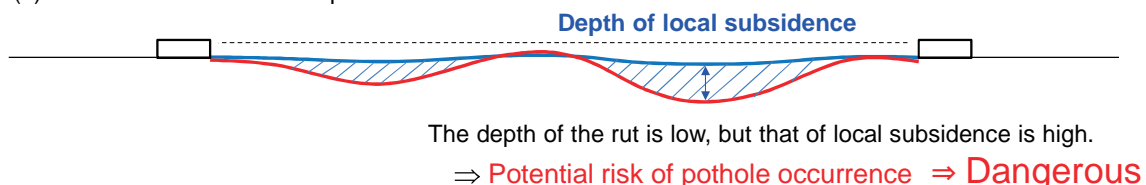
Jan. 2014

## Proposal of a new evaluation indicator

(1) Area where the overall depth of the rut is high



(2) Area where the overall depth of the rut is low



### Proposal method [Evaluation based on the depth of local subsidence]

The relative depth of local subsidence is calculated as the depth of local subsidence by calculating the difference between the rut depth of the objective point and the representative rut depth which is the central value of the maximum rut depth in a vicinity of 10m.

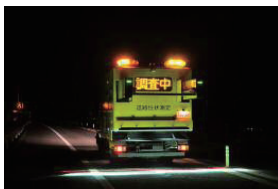
# Inspection of Airport

## Concept

Discover blistering by attaching J-system to Eagle and investigating the runway



J-System



Eagle





# **Ultrasound Imaging in Medicine and Biology**

**Yoshifumi Saijo**

Biomedical Imaging Laboratory  
Graduate School of Biomedical Engineering  
Tohoku University  
4-1 Seiryomachi, Aoba-ku, Sendai 980-8575, JAPAN  
saijo@bme.tohoku.ac.jp

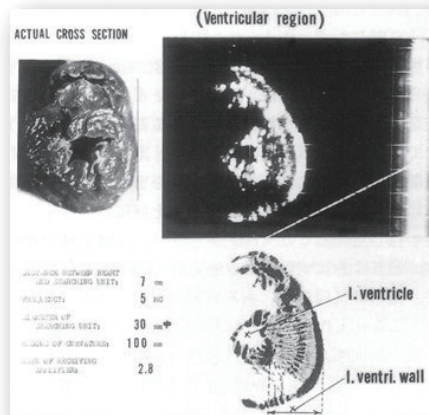
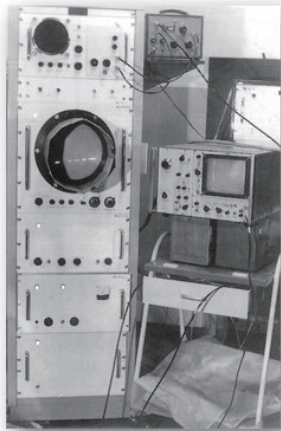
## **Abstract**

Ultrasound imaging is the most popular clinical imaging modality except conventional X-ray and usually characterized as easy, portable and safe imaging. Not only that, it has achieved temporally and spatially highest resolution imaging in clinical situations. Ultrasonic transducer is made of piezo-electric material and it sends ultrasonic signal into body and receives the reflected signal to form a tomographic image. Besides the conventional morphology imaging, ultrasound can provide functional information such as blood flow or biomechanical properties.

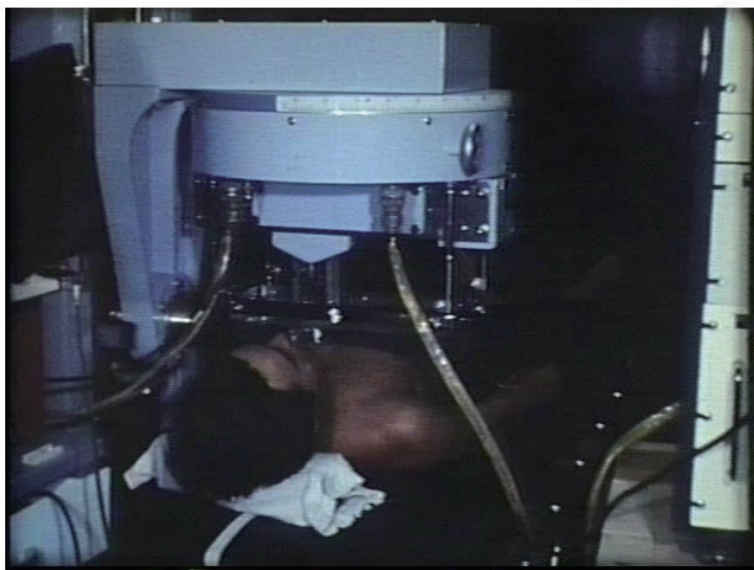
## Collaboration of medicine and engineering at Tohoku University

### ■ World's first cardiac tomogram

- Motonao Tanaka, MD, Institute of Tuberculosis (currently Institute of Development, Aging and Cancer)
- Yoshimitsu Kikuchi, PhD, Research Institute of Electric Communication



## Ultrasonic cardiac tomography (1965)



## Ultrasonic cardiac tomogram



## Medical imaging modalities in japan

### ■ Marketing of medical imaging modalities in FY 2014

- Medical CT: 1,286 (8,000 in use)
- MRI: 548 (4,400 in use)
- Angiography: 330
- PET-CT: 46
- Diagnostic ultrasound: 12,075 (uncountable use)



CT

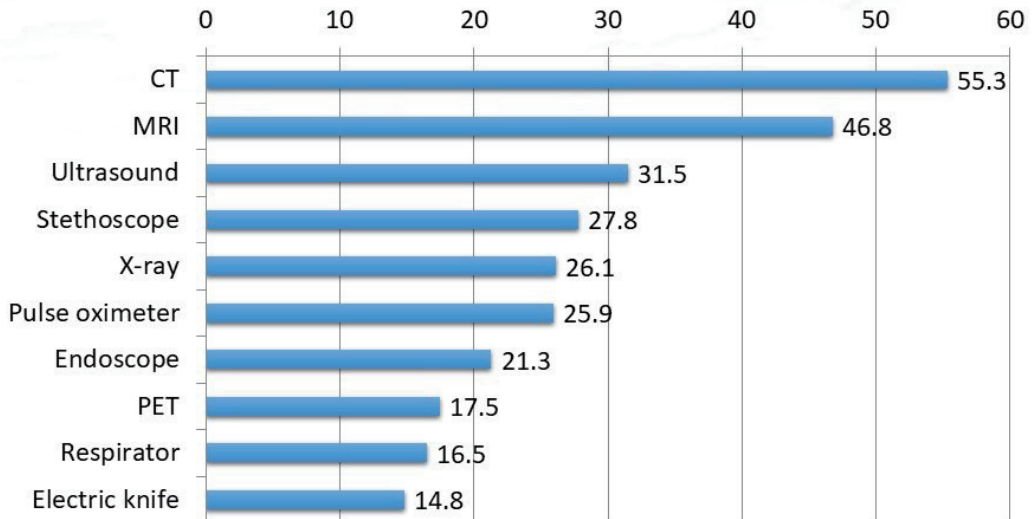


MRI



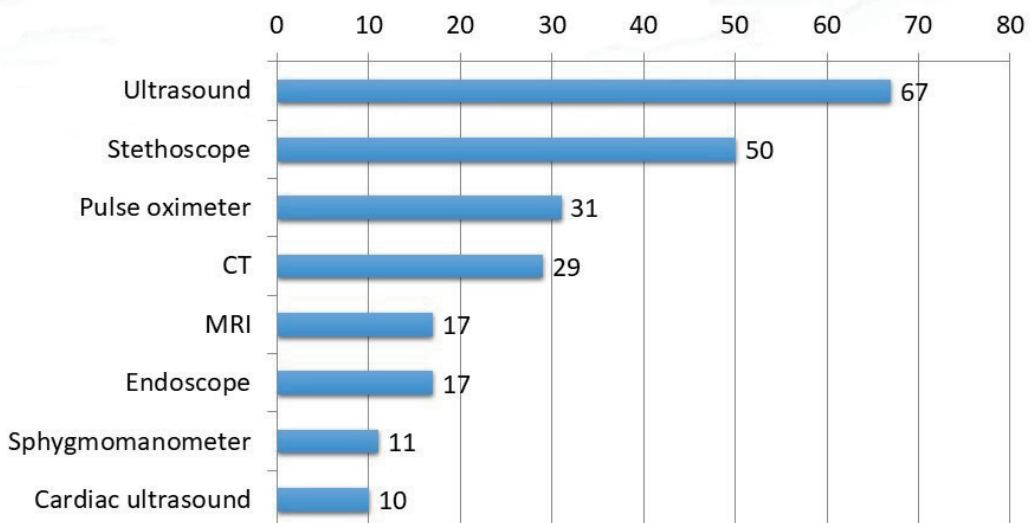
Angiography

## Question for doctors: Innovative medical device to develop medicine?



*Nikkei Medical Online 2011*

## Question for doctors: Favorite medical device in daily practice?



*Nikkei Medical Online 2011*

## Clinical features of ultrasound diagnosis

### ■ Easy

- Easy and repeatable examinations
- Switch on → image acquired by just placing probe

### ■ Portable

- Smaller than CT or MRI → Available at bedside and operation room
- More portable devices (390~725 g) in market

### ■ Safe

- No radiation exposure
- No accidents in more than 50 years

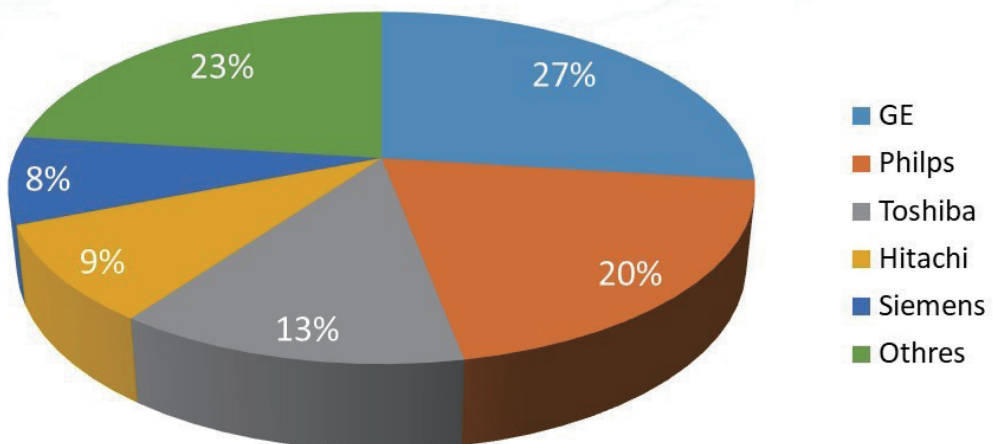


Siemens P10



GE Vscan

## World share of ultrasound devices

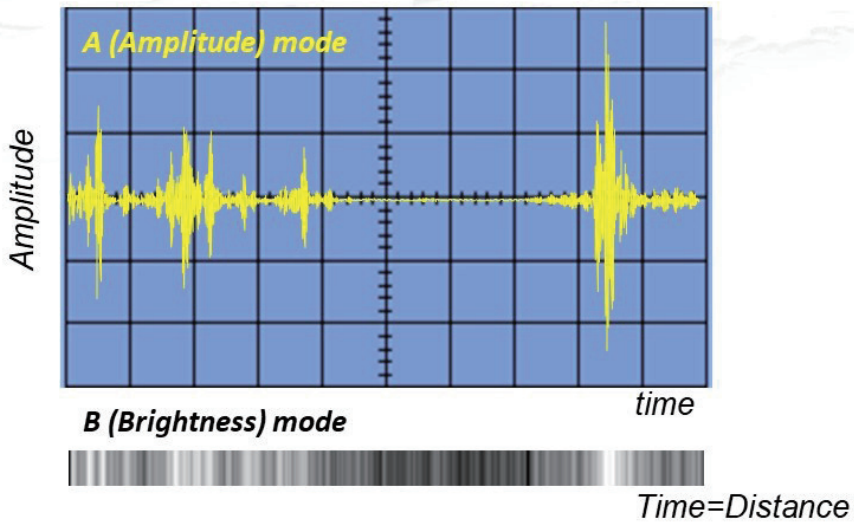


**Total: 57.7 billion USD**

Mitsubishi Tokyo UFJ Bank, Oct 1, 2013



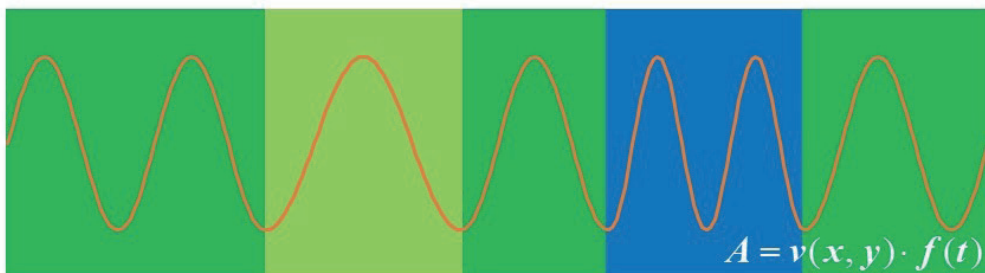
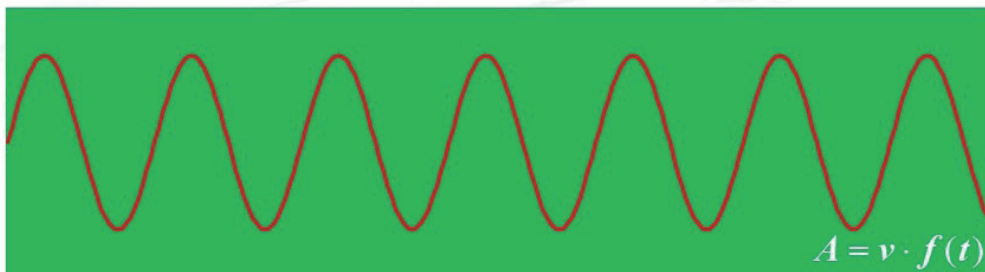
## A-mode and B-mode



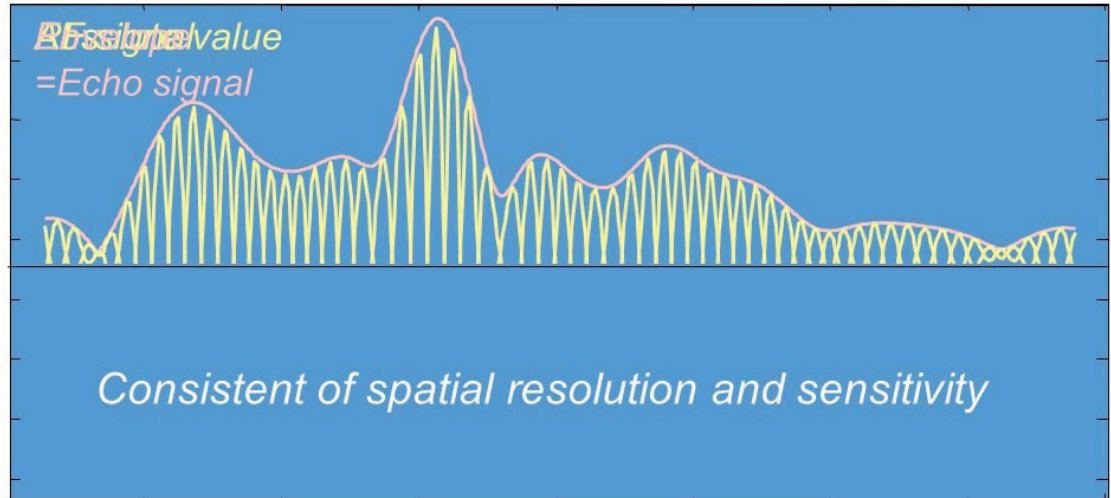
Amplitude of received signal at each time  
 → Brightness of each distance

**Note that sound speed is assumed to be constant (1530 m/s)**

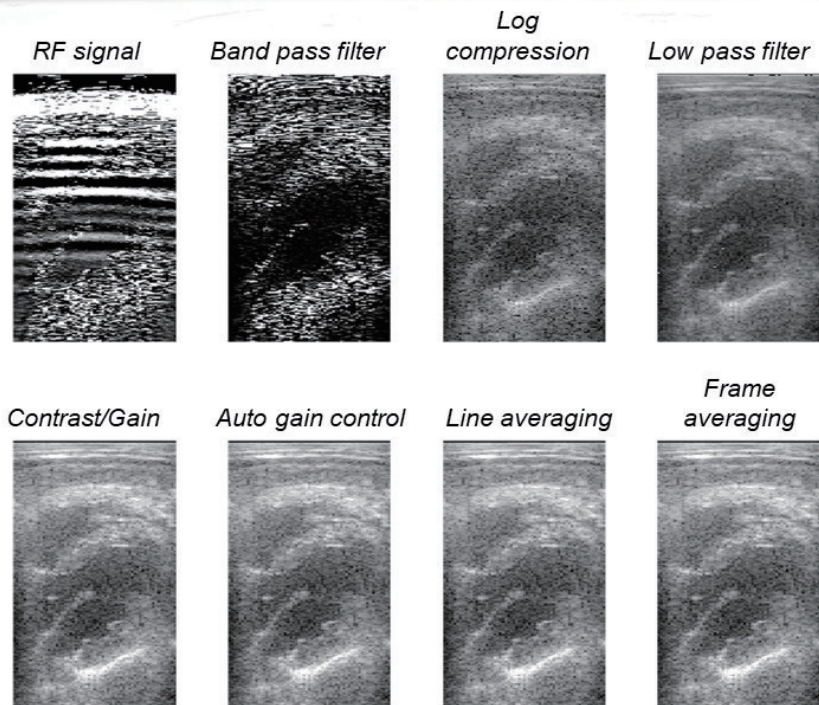
## Sound speed distribution and received signal



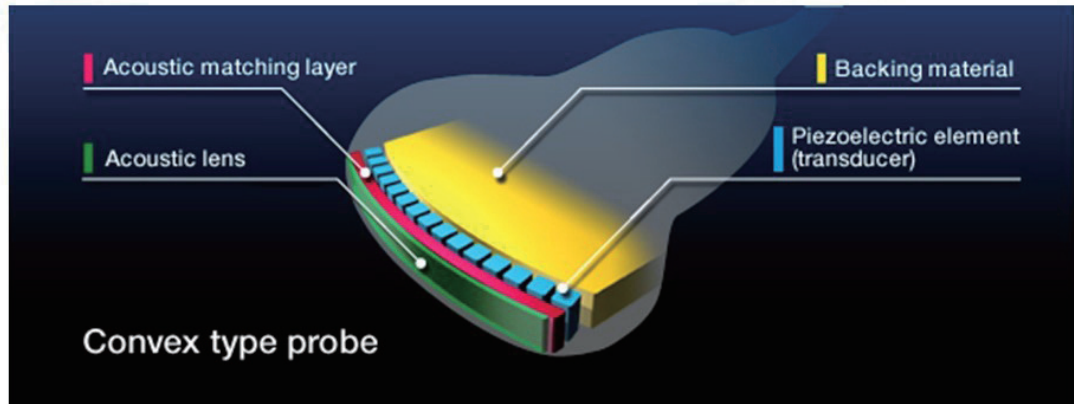
## Conversion from RF signal to echo signal



## Example of image processing

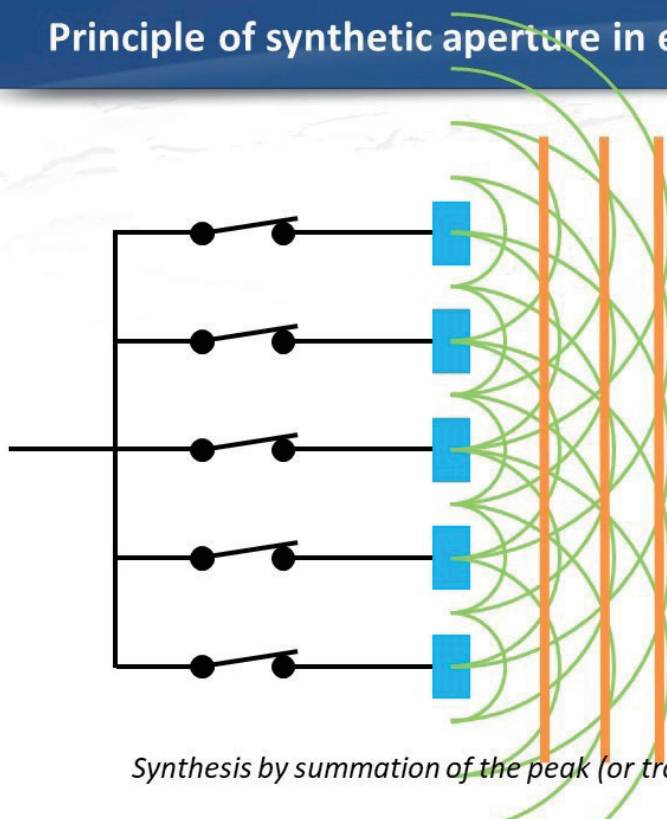


## Structure of electric scan probe

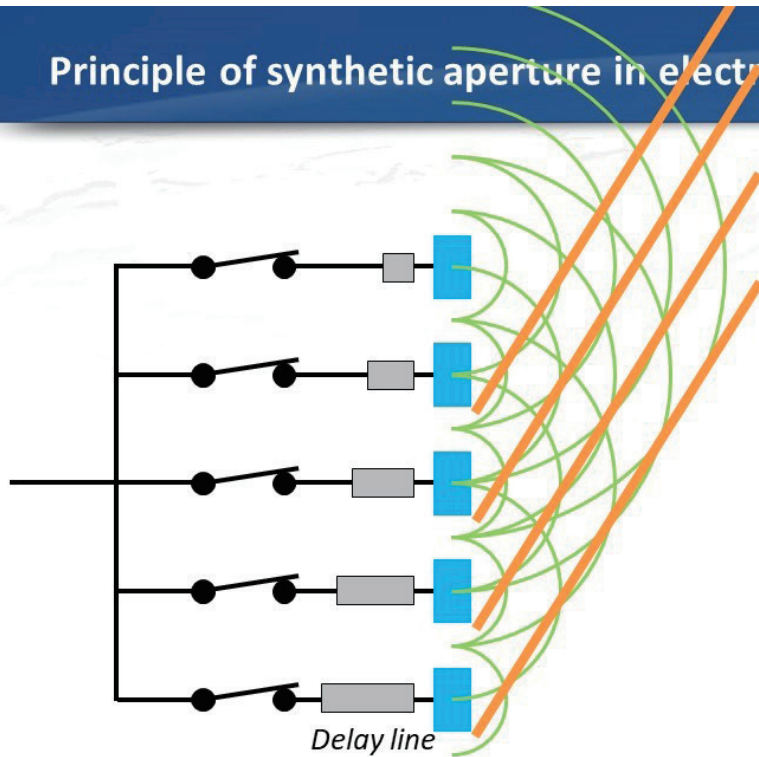


<http://www.ndk.com/jp/sensor/ultrasonic/basic02.html>

## Principle of synthetic aperture in electronic scan

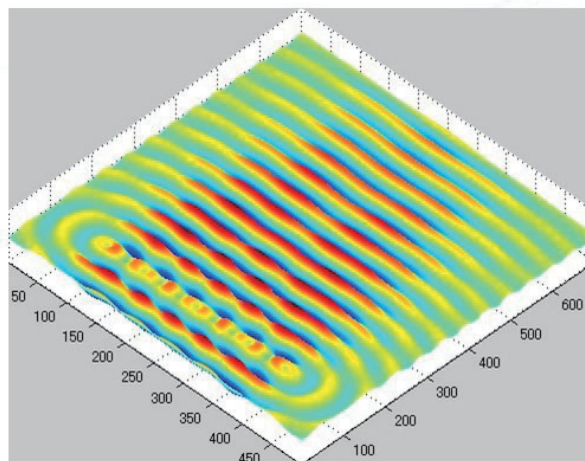


## Principle of synthetic aperture in electronic scan

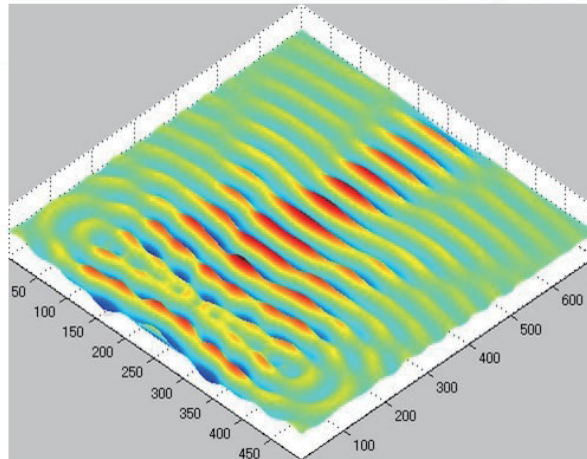


*Synthesis of oblique wave front formation by delay lines*

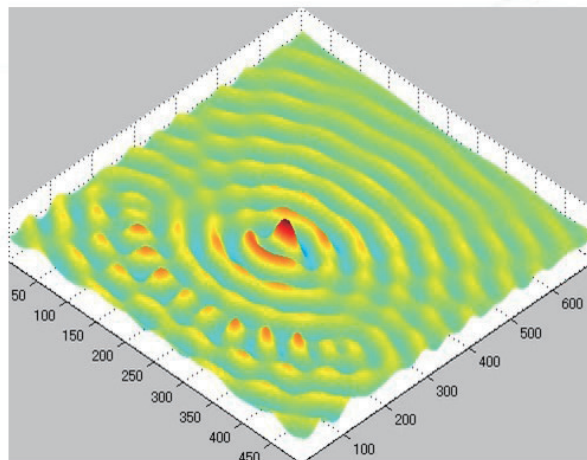
## Acoustic field: Simultaneous transmission from the linearly arranged transducers



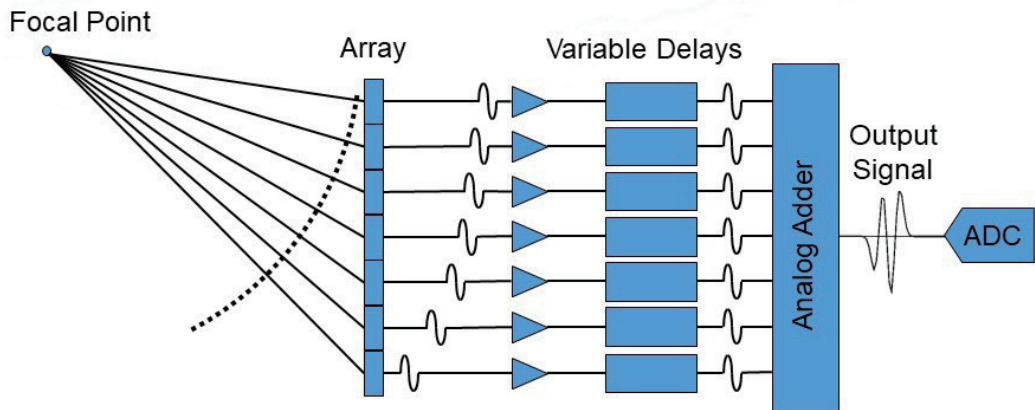
## Acoustic field: Delayed transmission from the linearly arranged transducers



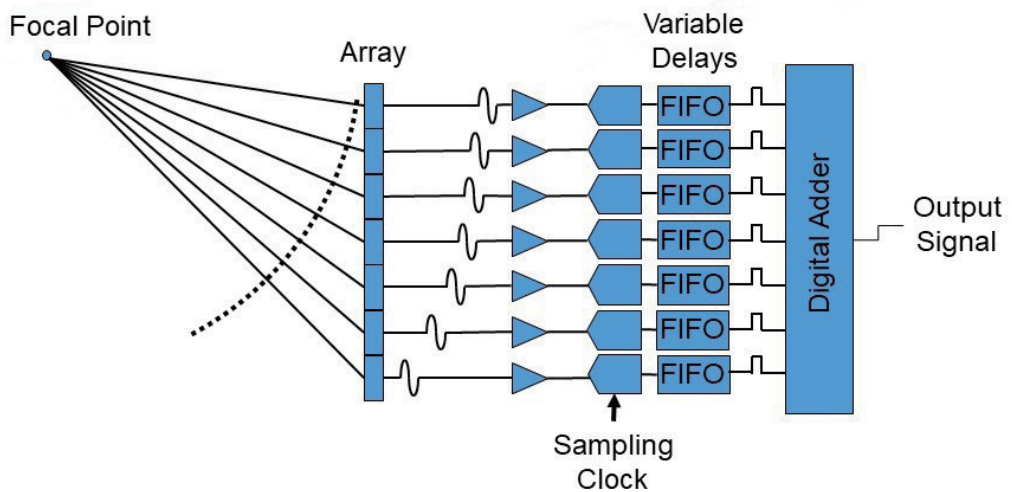
## Acoustic field: Simultaneous transmission from the concave arranged transducers



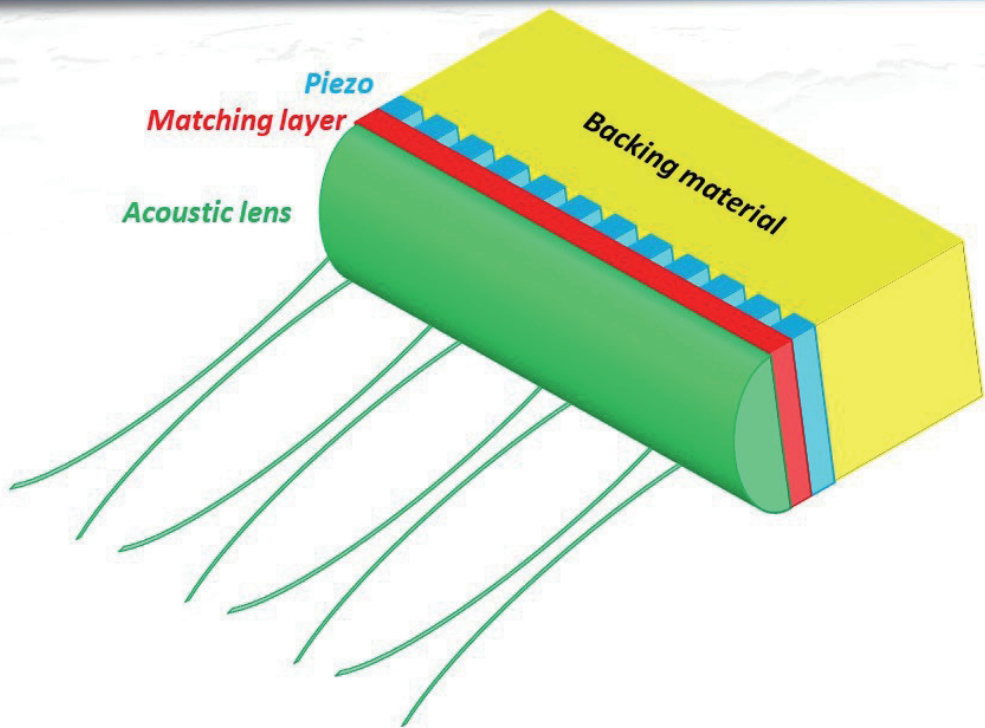
## Synthetic aperture (Analog)



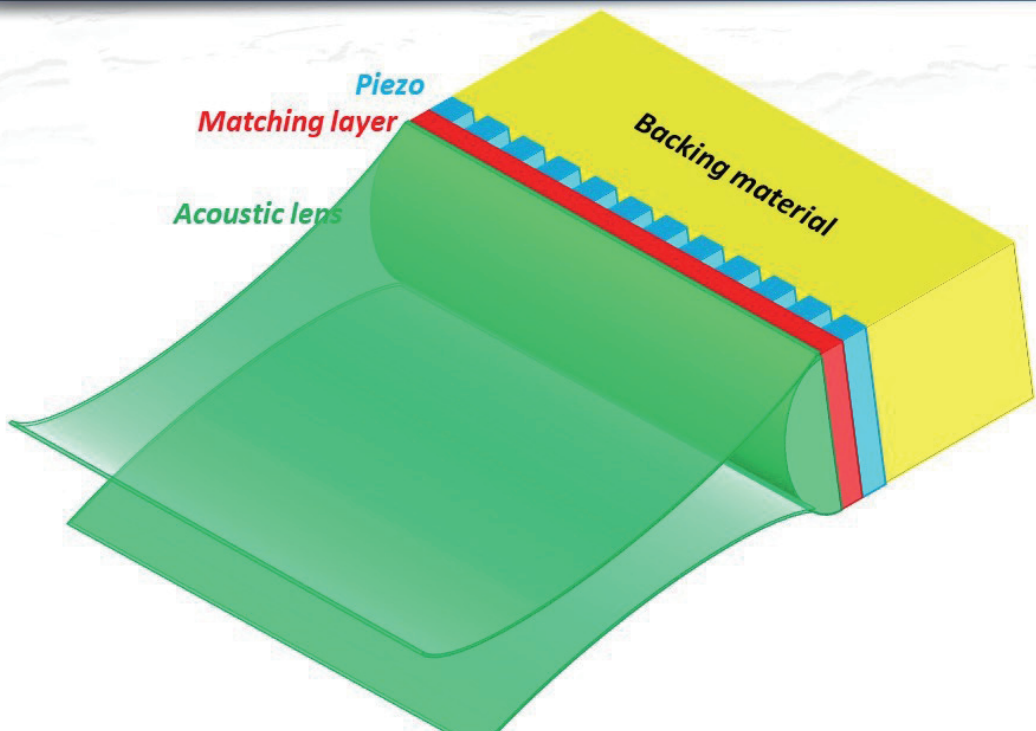
## Synthetic aperture (Digital)



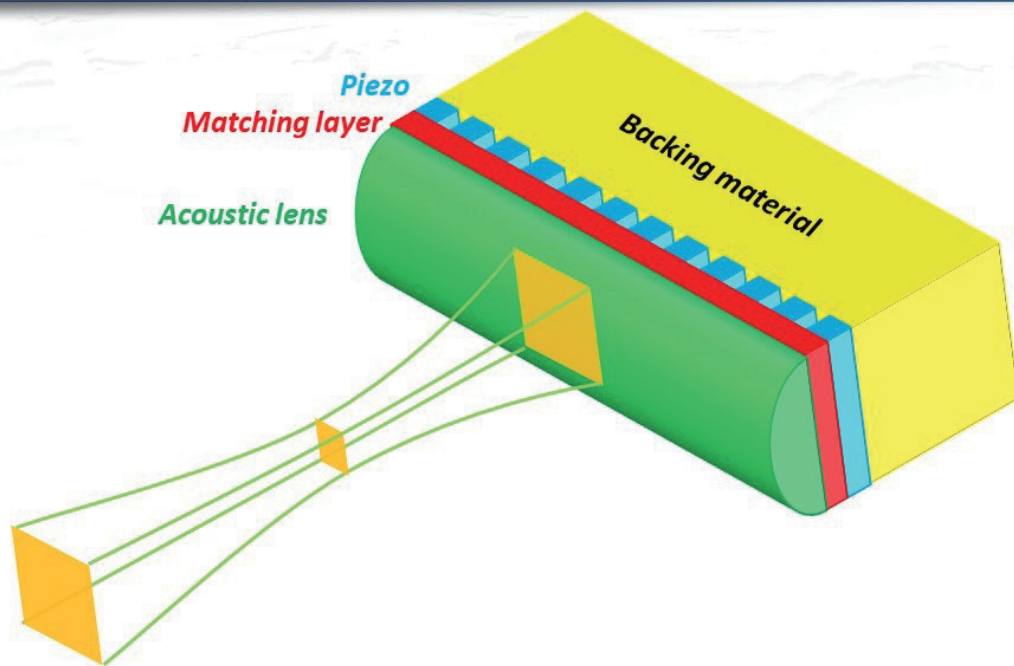
## Focusing in scanning plane



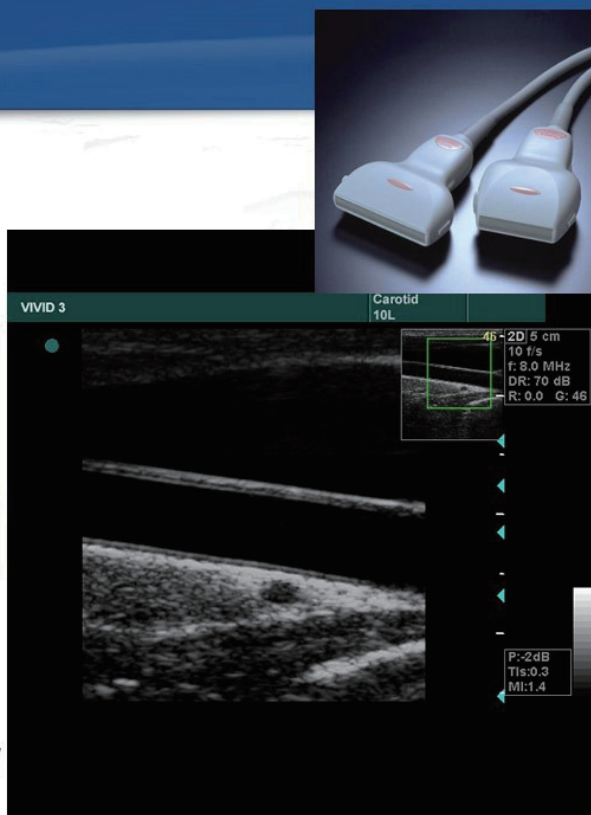
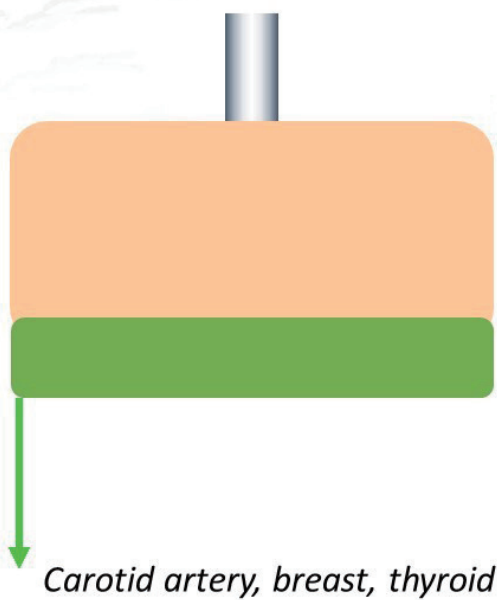
## Focusing in slicing plane



# Focusing

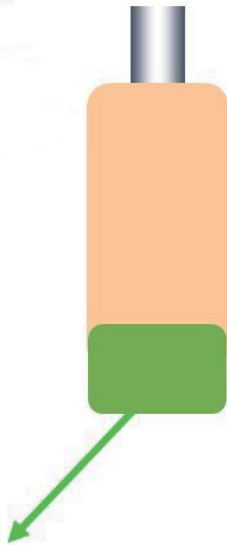


# Linear probe

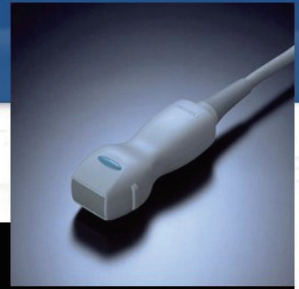




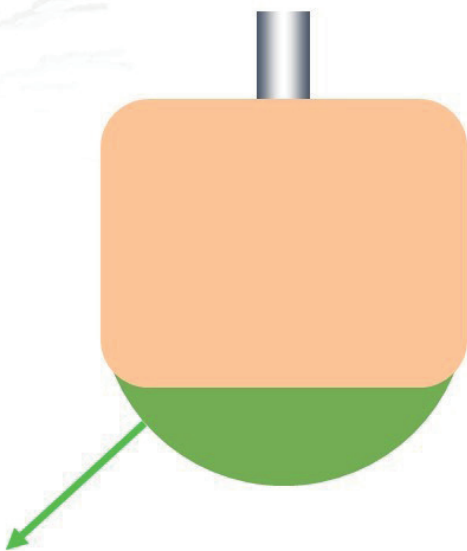
## Sector probe



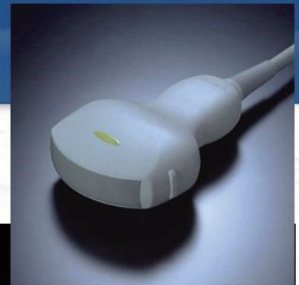
*Echocardiography*



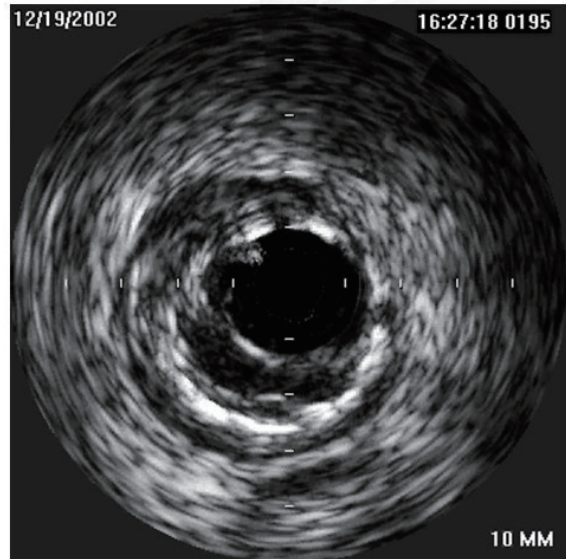
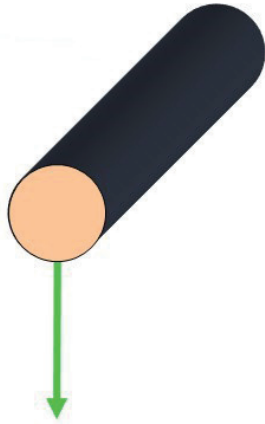
## Convex probe



*Abdominal US*

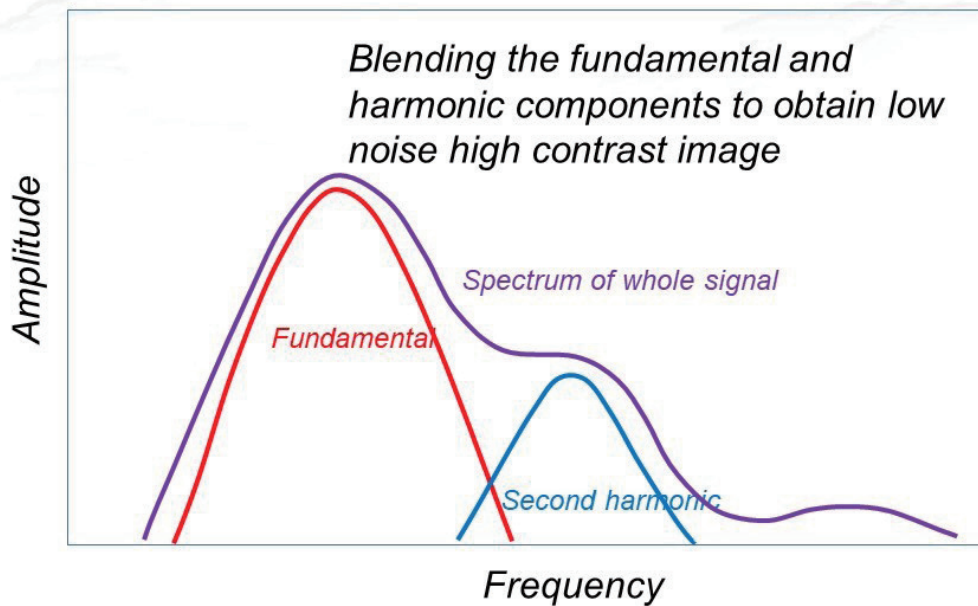


## Radial scan

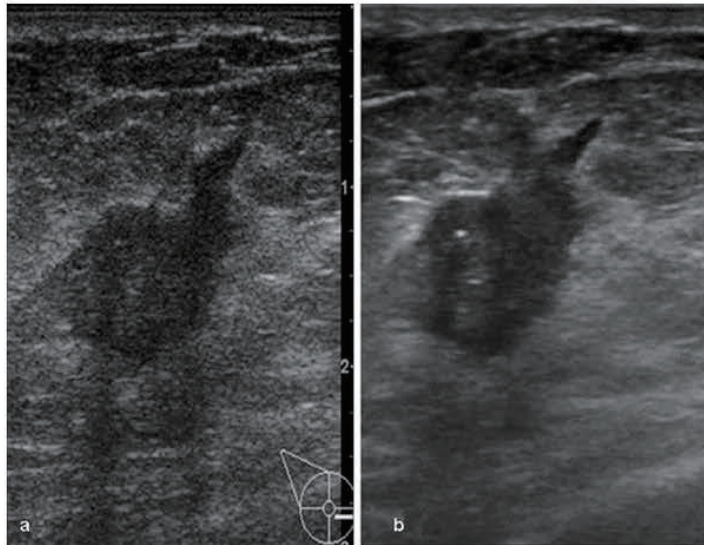


*Endoscope, intravascular ultrasound*

## Harmonic echo



## Harmonic echo

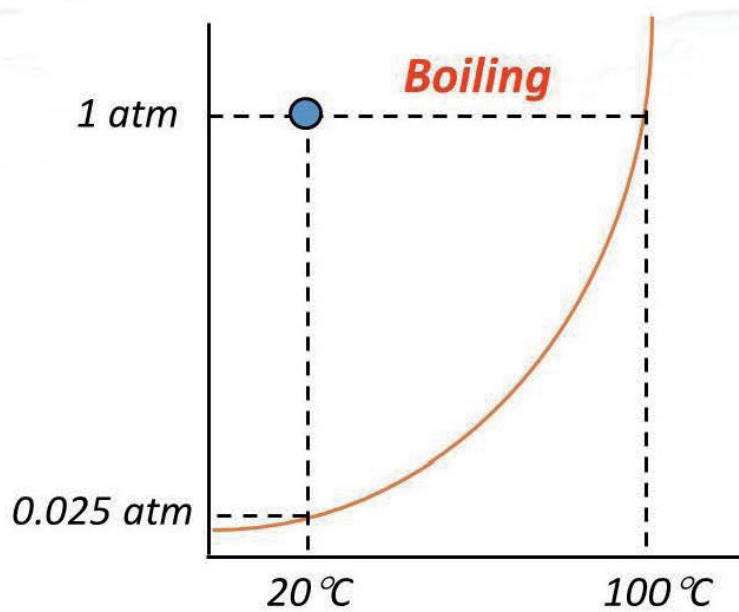


*Fundamental*

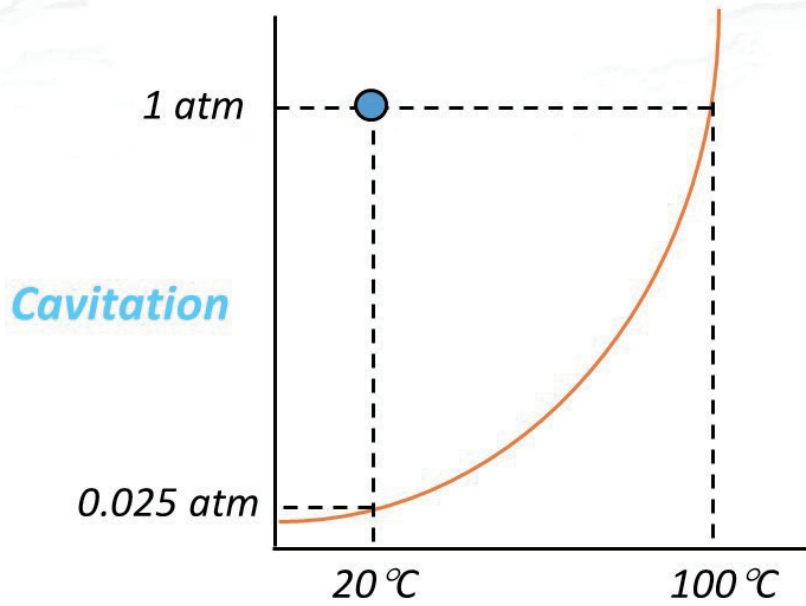
*Harmonic*

*Eur J Rad. 2007, 17 :1*

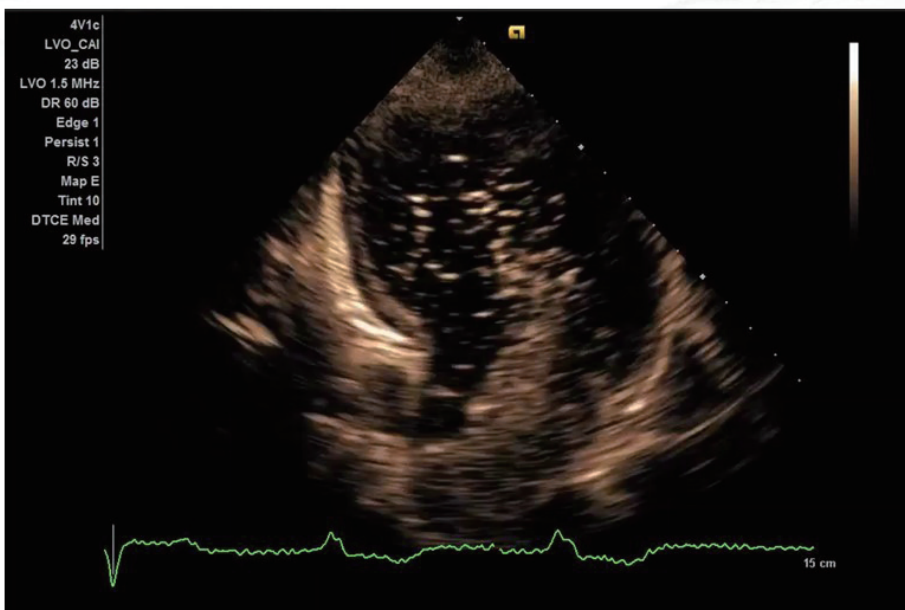
## Boiling and cavitation



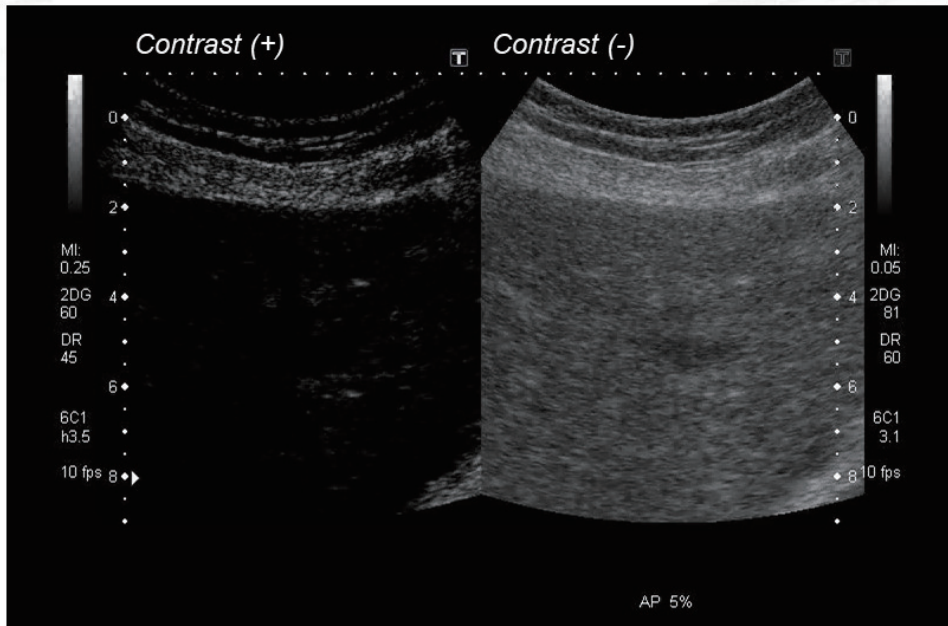
## Boiling and cavitation



## Contrast echocardiography



## Sharpening of hepatic cancer by contrast enhancement

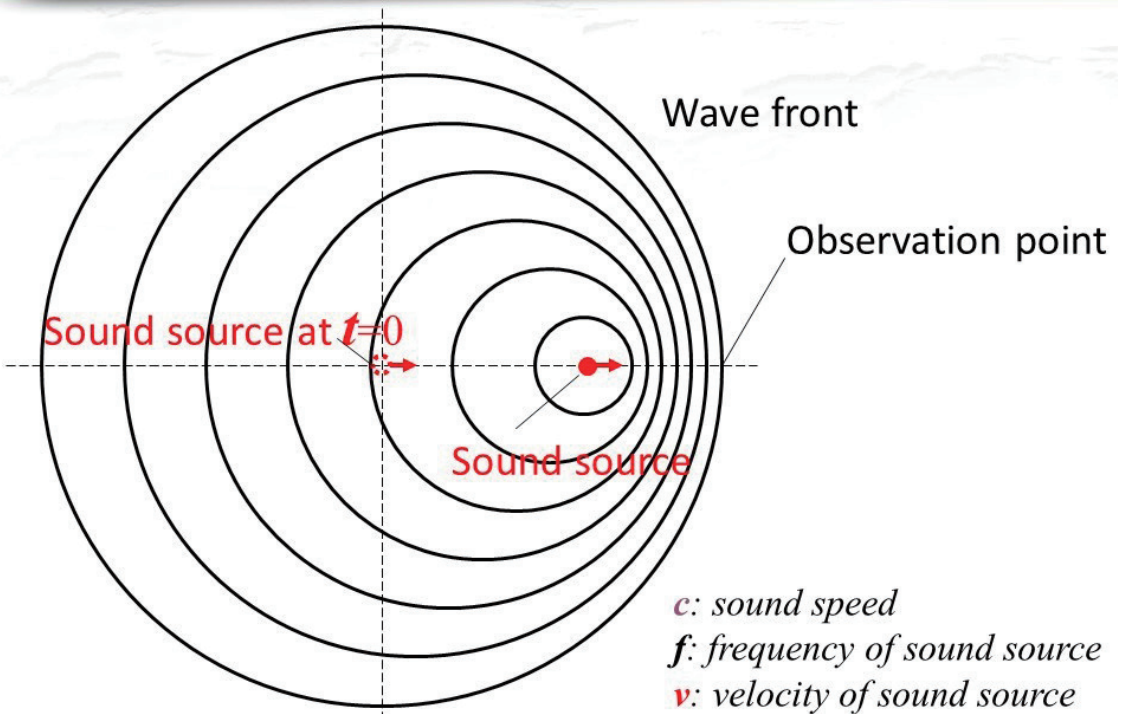


## Doppler effect

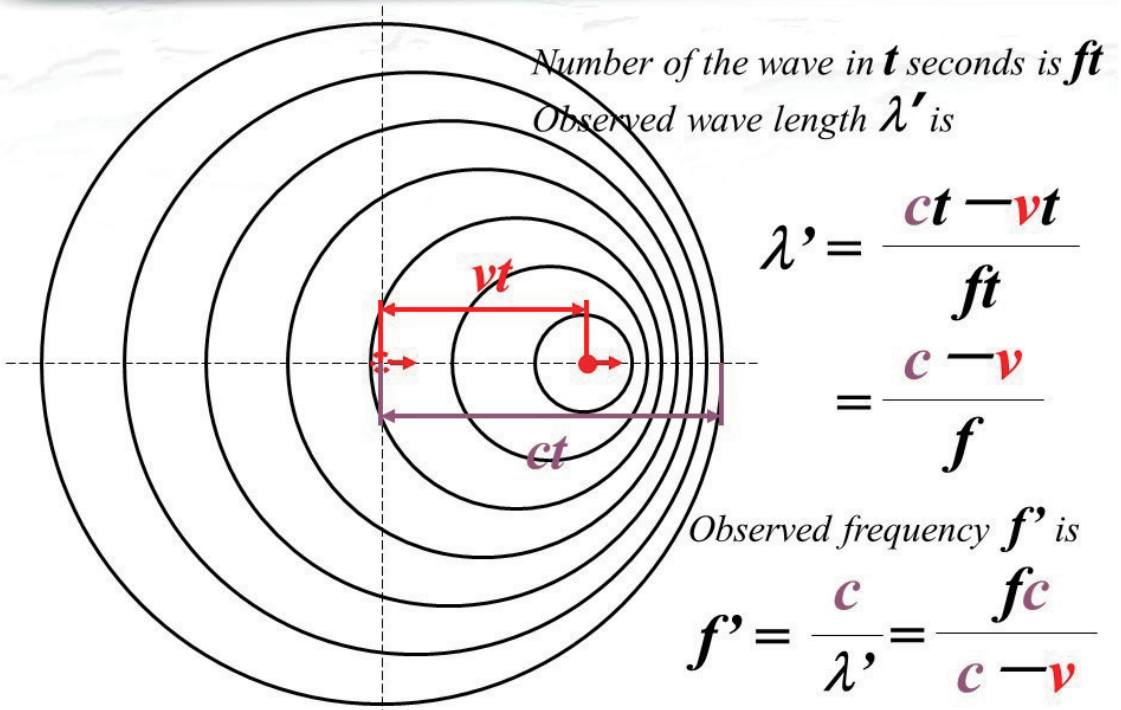
- Siren of the ambulance car
  - Approaching → high frequency
  - Going away → low frequency



## Principle of Doppler effect



## Principle of Doppler effect

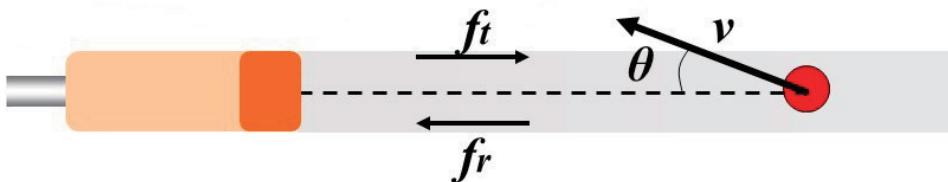


## Sound source velocity obtained by frequency shift

$$f_r = f_t \cdot \frac{c}{c - v}$$
$$v = \frac{f_r - f_t}{2 f_r} \cdot c$$

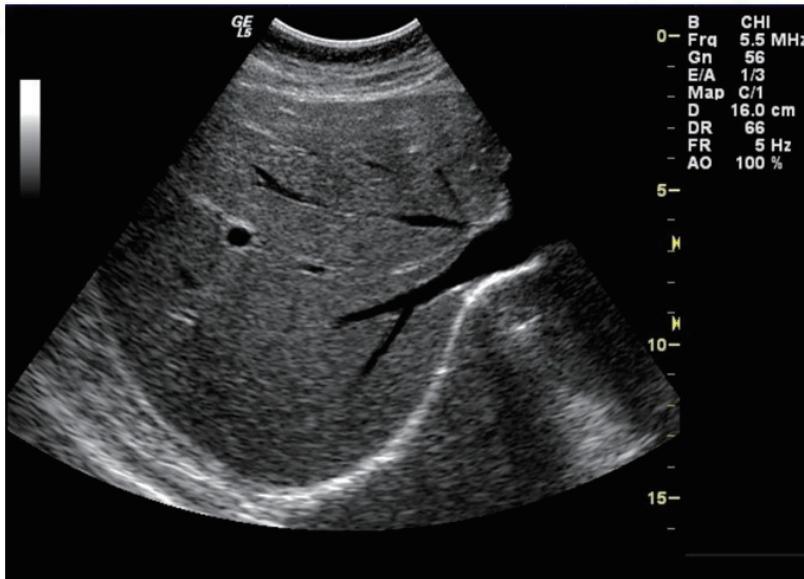
$f_t$ : transmitted frequency  
 $f_r$ : received frequency  
 $c$ : sound speed  
 $v$ : velocity of sound source

## Doppler measurement of blood flow velocity

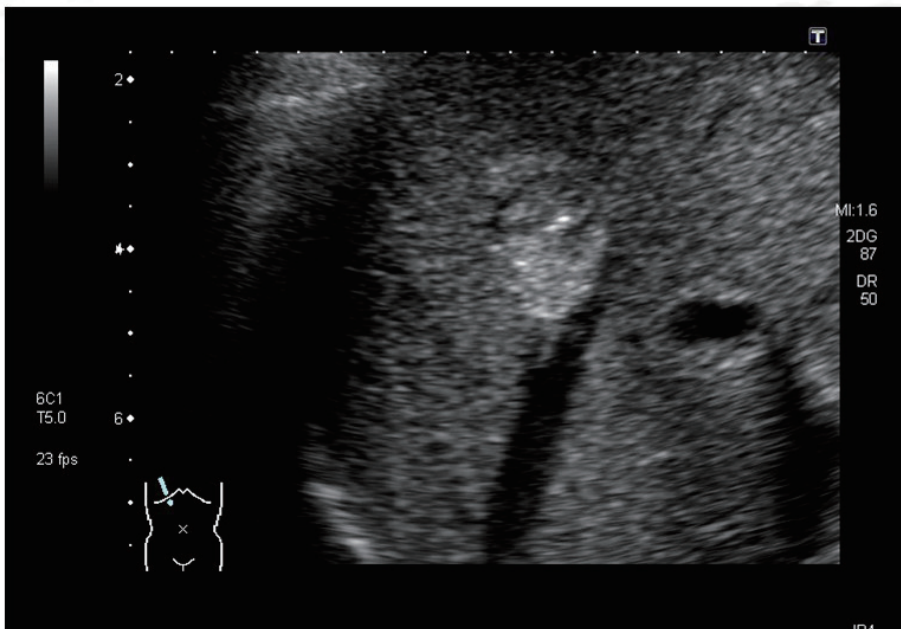


$$v = \frac{f_r - f_t}{2 f_r \cos \theta} \cdot c$$

# Normal liver



# Liver hemangioma

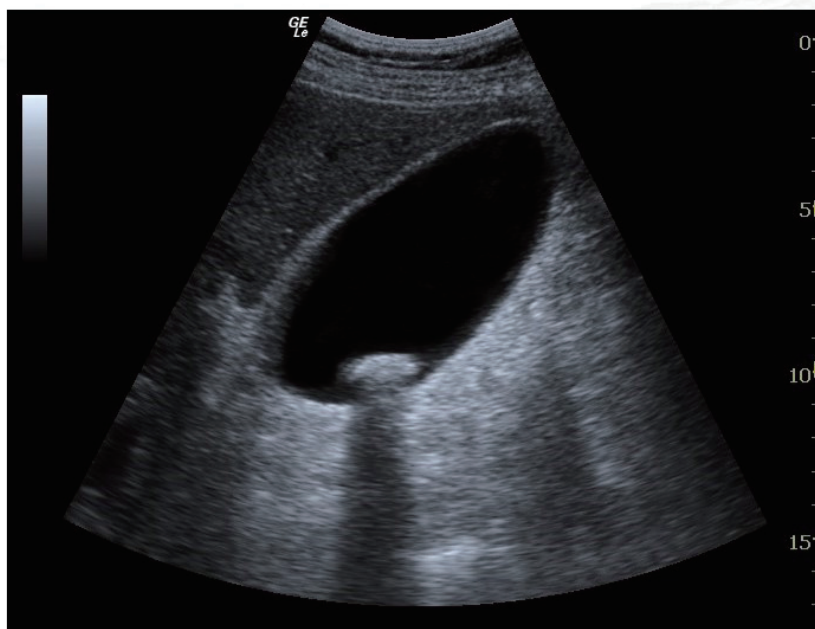




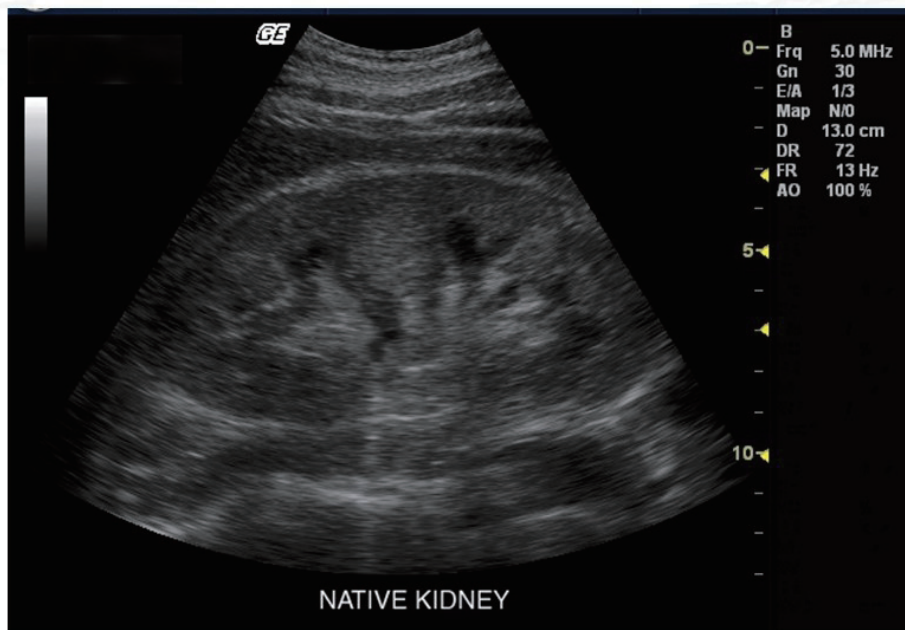
## Early liver cancer



## Gall stone: Acoustic shadow



## Normal kidney



## Vasculature in the kidney (Power Doppler)

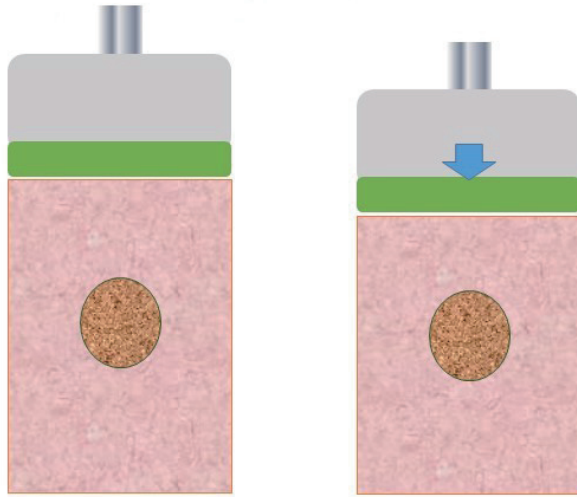


# Elastography

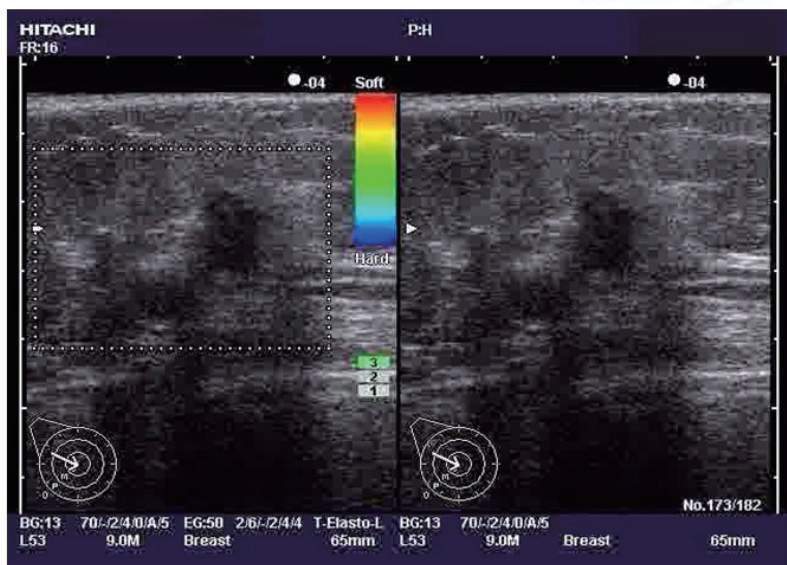
- Slightly push the tissue and imaging of the small displacement

- Targets

- Breast
- Thyroid
- Arteries

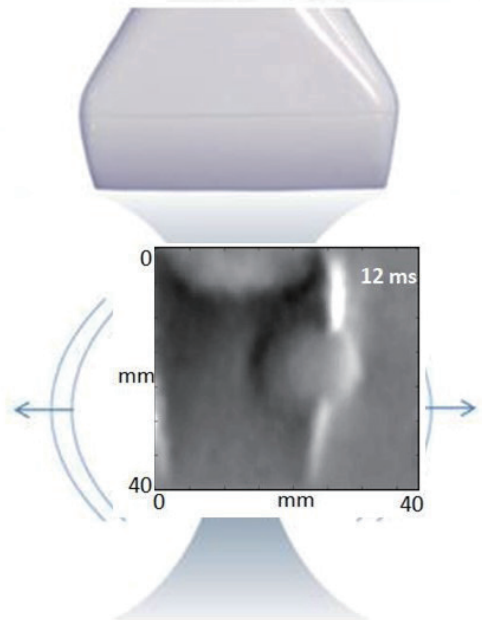


## Elastography (Invasive mammary gland cancer)

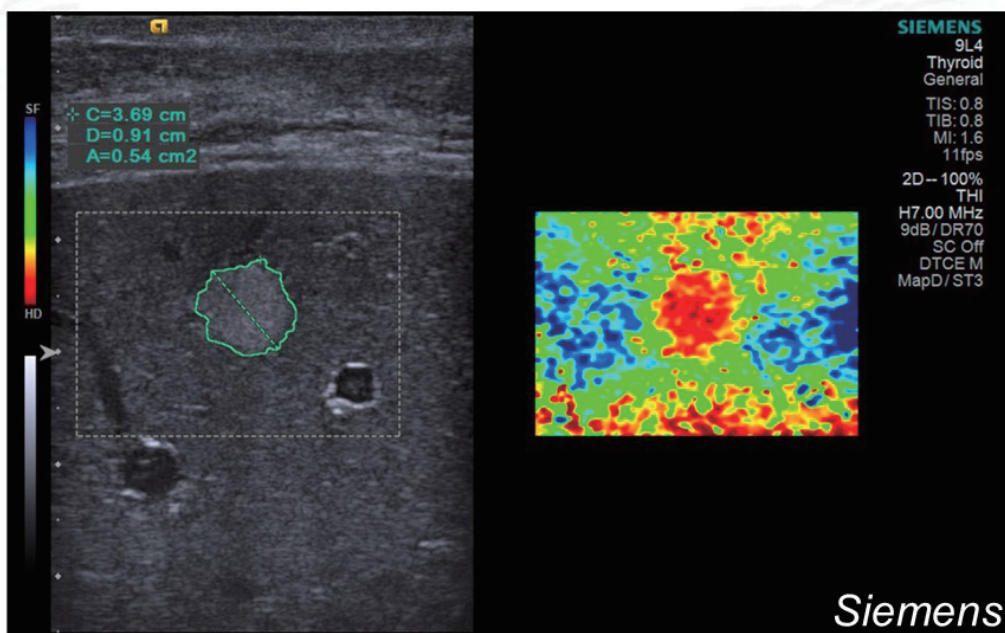


## Shear Wave Elastography

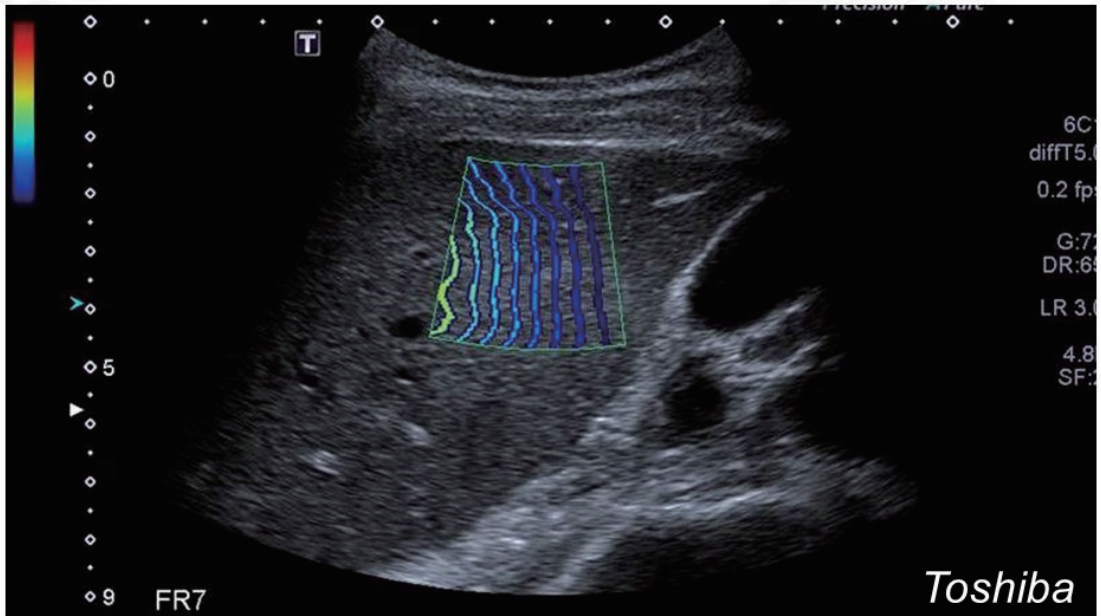
- Focused ultrasound pushes the tissue (push beam) to the beam propagation
- Shear wave is generated perpendicular to the push beam



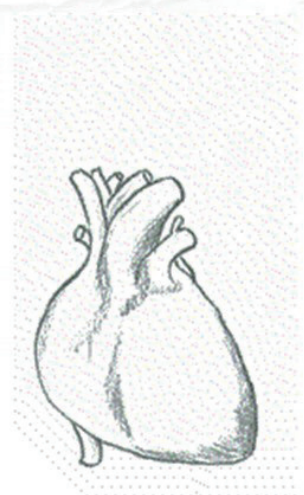
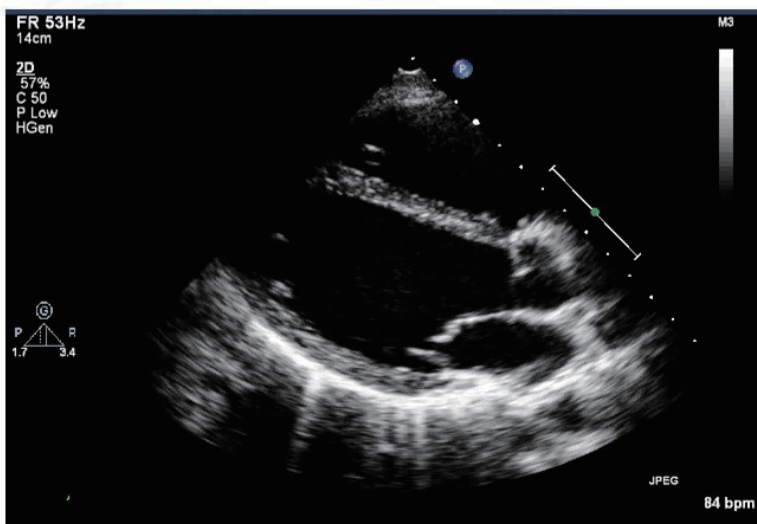
## Shear Wave Elastography



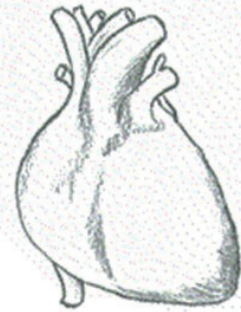
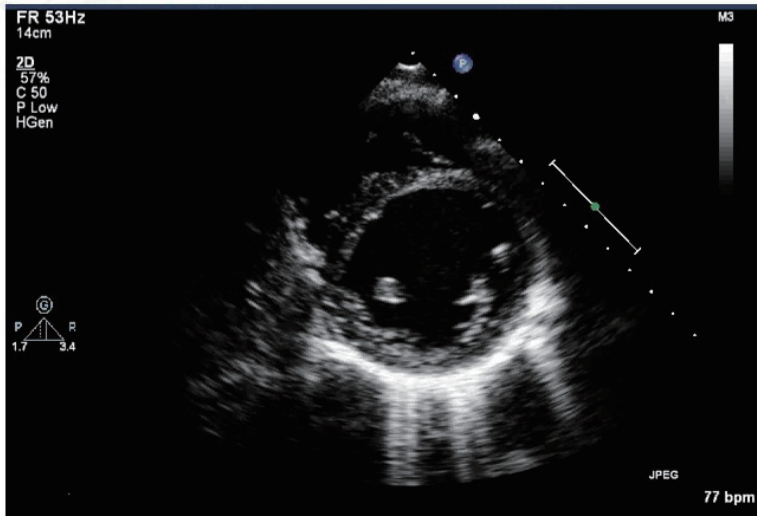
# Shear Wave Elastography



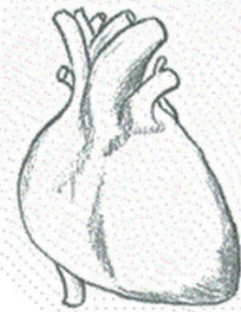
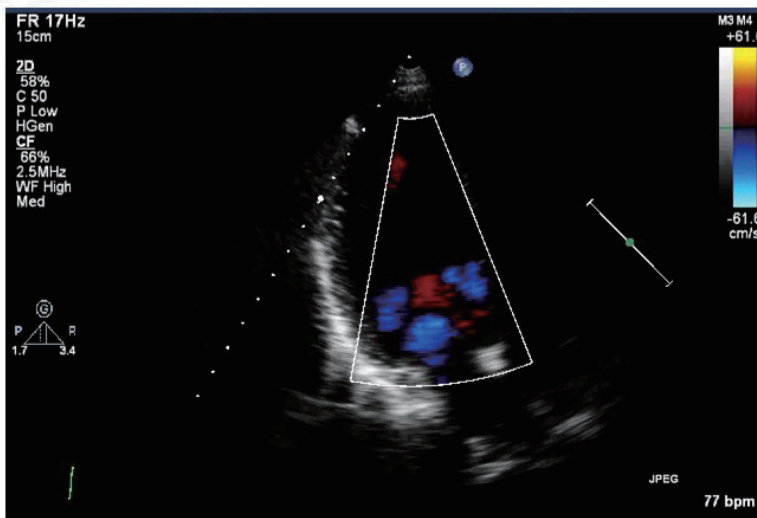
# Parasternal long axis view



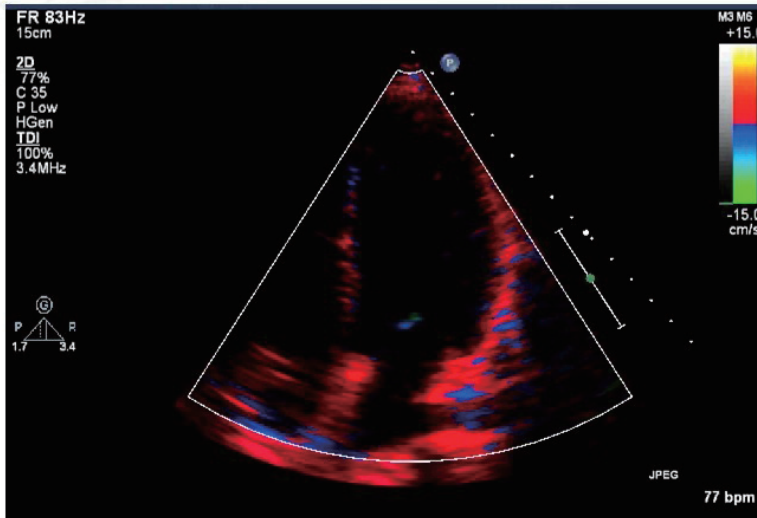
## Parasternal short axis view



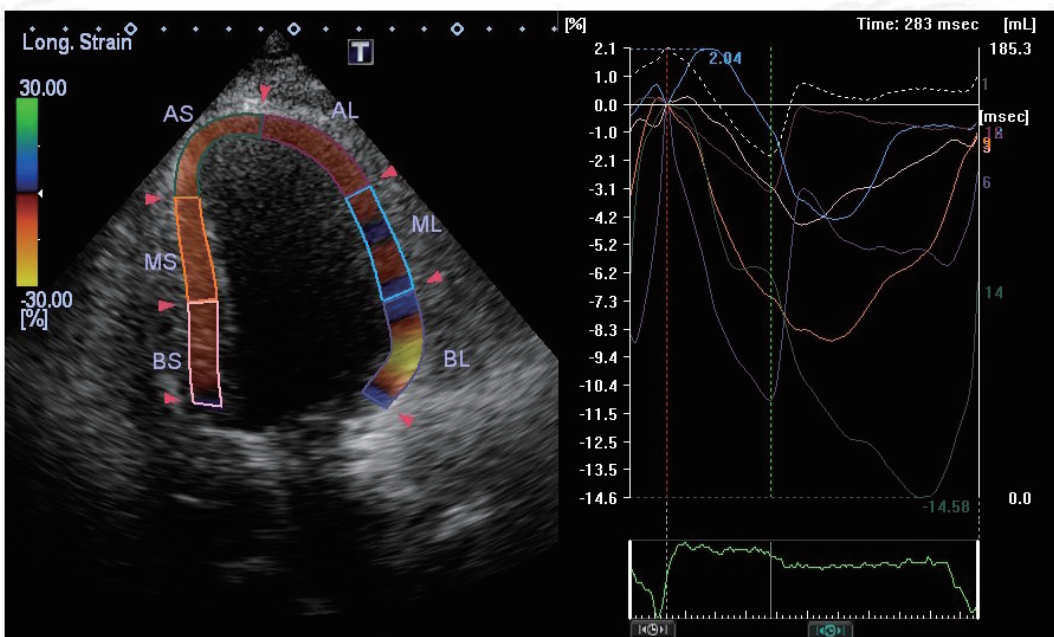
## Apical 3 chamber view (Color Doppler)



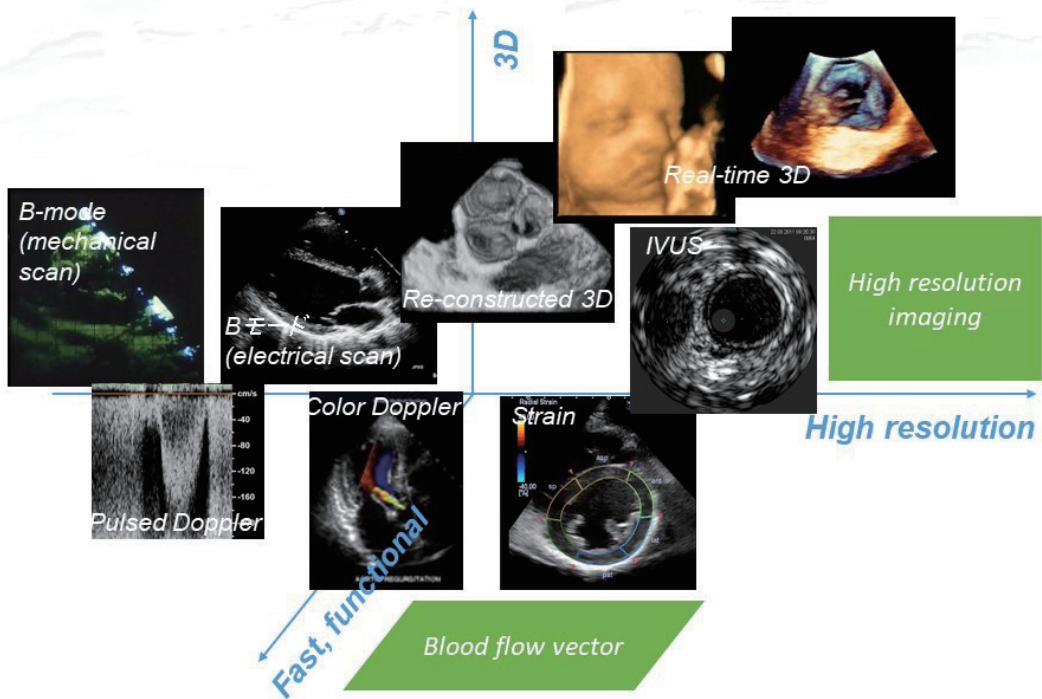
# Apical 4 chamber view (Tissue Doppler)



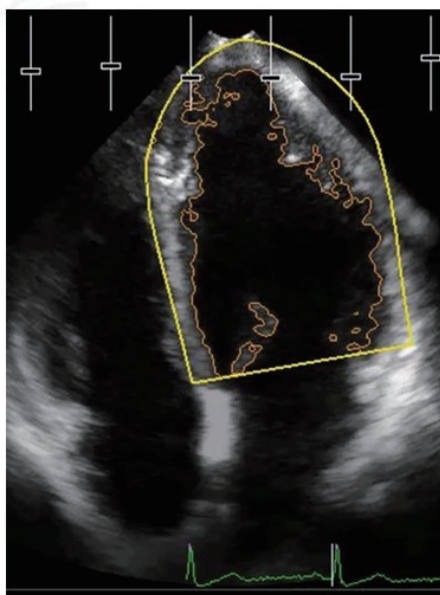
# Longitudinal strain rate imaging



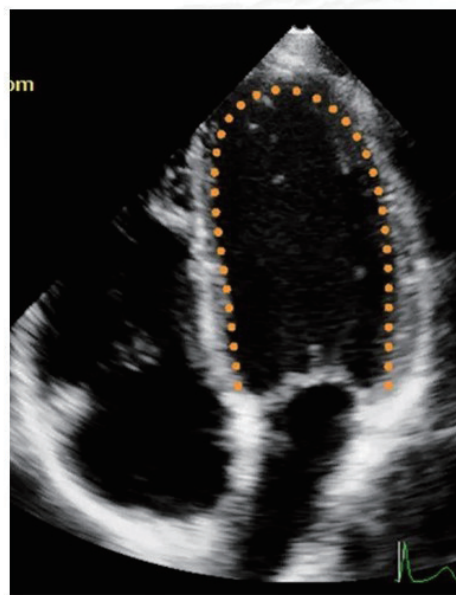
## Progress of ultrasound imaging



## Comparison of border detection



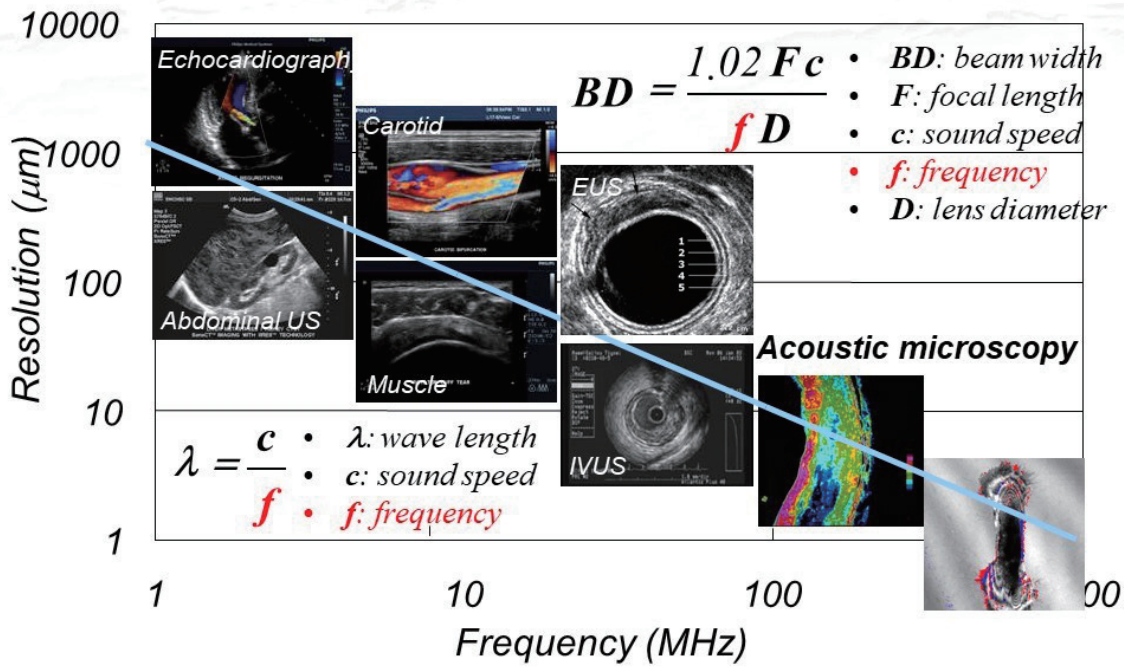
*Difference of reflection*



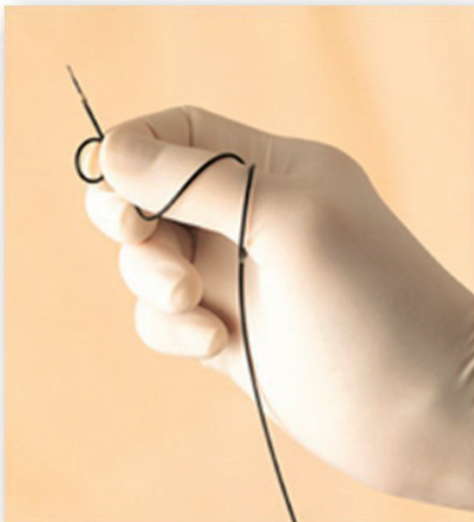
*Learning of human expert data*



# Resolution and Ultrasonic Frequency

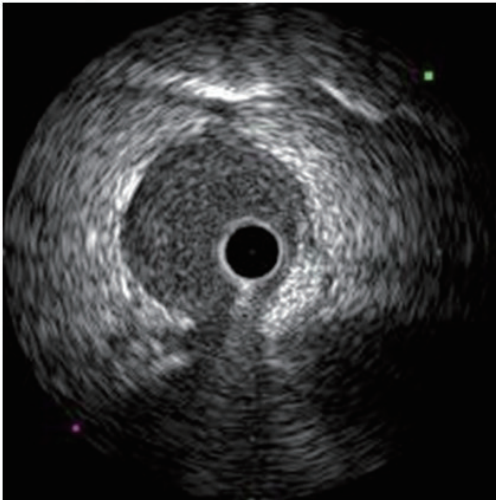


# IVUS (Intravascular Ultrasound)

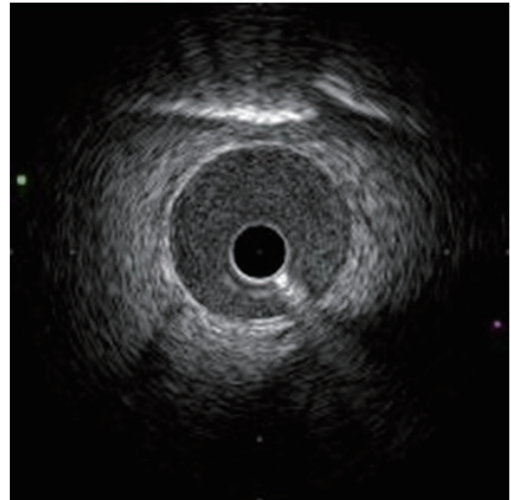


## Recent development of IVUS

- Improvement of image quality by increasing the ultrasonic frequency



*Conventional (40 MHz)*

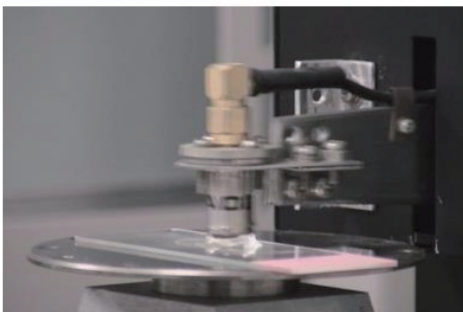


*New (60 MHz)*

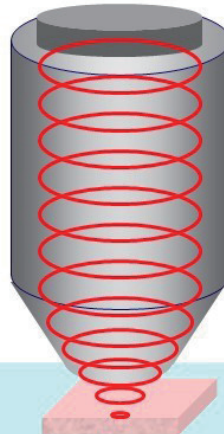
## C-mode scan of classical acoustic microscopy

### *Transducer*

- ZnO
- Central frequency: 170 MHz
- Sapphire lens



### *Planar transducer*



### *Acoustic lens*

## Acoustical parameters and biomechanical properties of the tissue

### ■ Elasticity

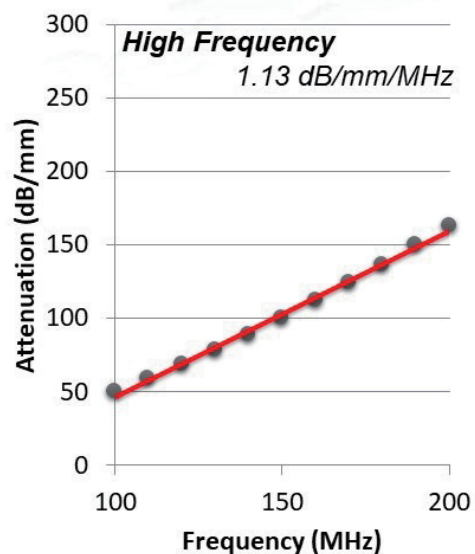
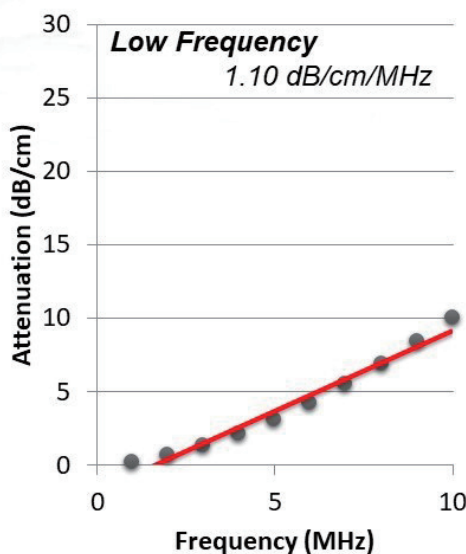
$$E = \frac{(1 - \sigma)\rho c^2}{(1 + \sigma)(1 - 2\sigma)}$$

### ■ Viscosity

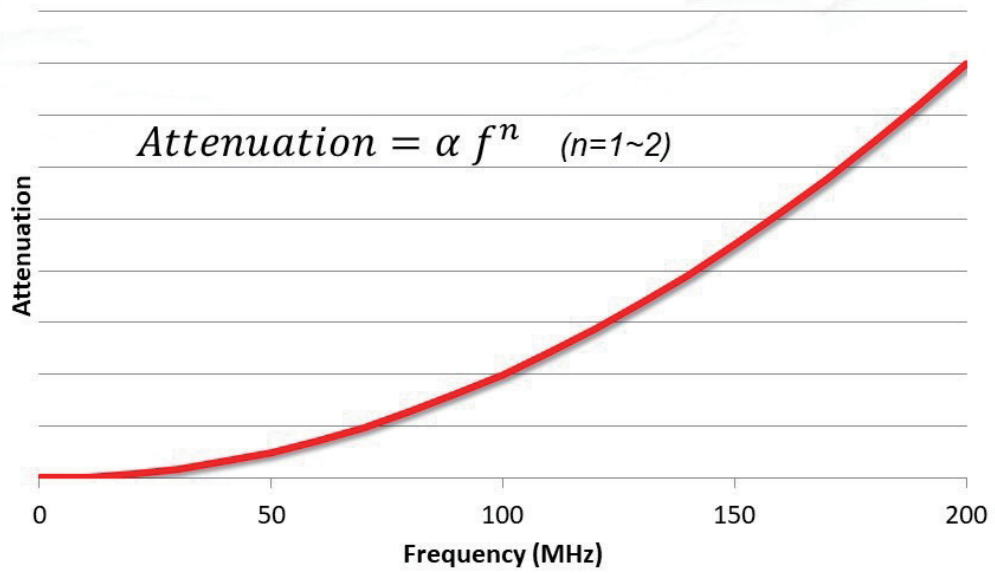
$$\alpha = \frac{2f^2\pi^2}{3\rho c^3} \left( \eta_v + \frac{4}{3}\eta_s \right)$$

- $c$ : sound speed
- $\rho$ : density
- $Z$ : acoustic impedance
- $R$ : reflection coefficient
- $E$ : Young's modulus
- $\sigma$ : Poisson's ratio
- $\alpha$ : absorption
- $f$ : frequency
- $\eta_v$ : volumetric viscosity
- $\eta_s$ : shear viscosity

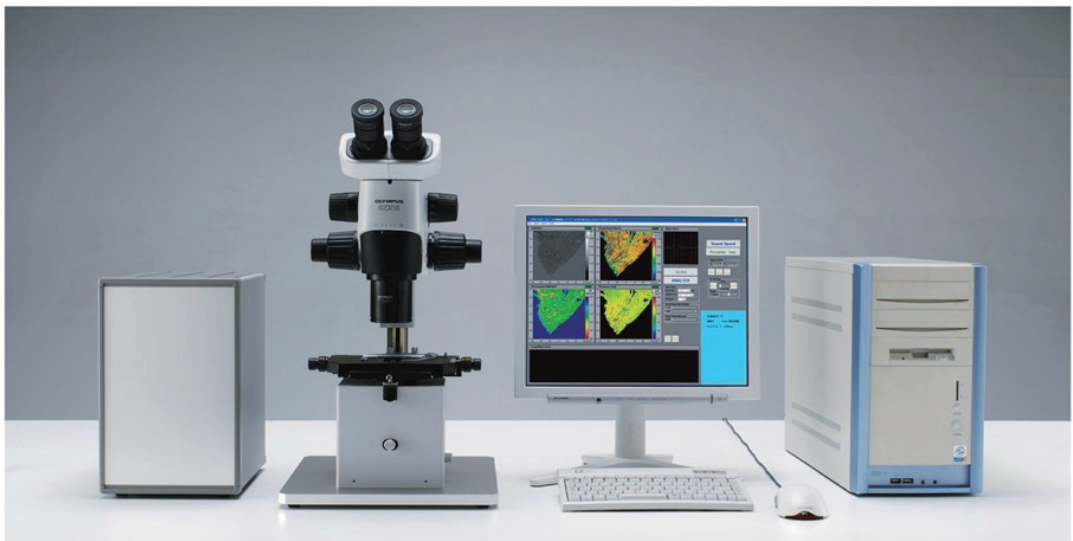
## Attenuation Coefficient of Myocardium in Low Frequency and High Frequency



## Frequency Dependence of Attenuation of Whole Frequency Range



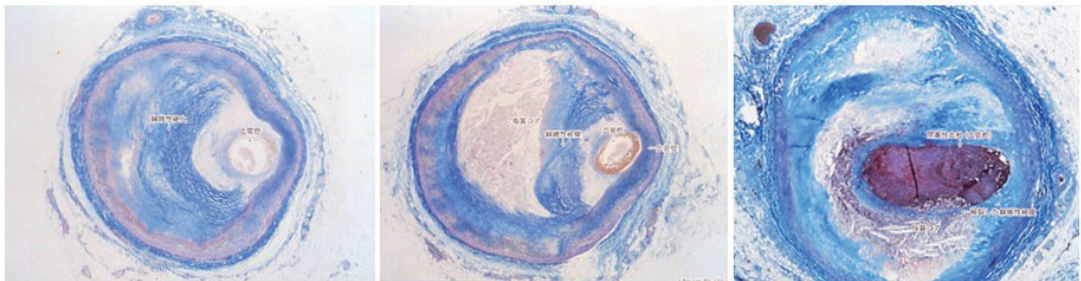
## Ultrasound / impedance microscope



## Atherosclerosis (Vulnerable plaque)

- **Plaque rupture depends on tissue character of the plaque rather than stenosis rate.**

- Falk E, Shah PK, Fuster V. Coronary plaque disruption. *Circulation*. 1995 Aug 1;92(3):657-71

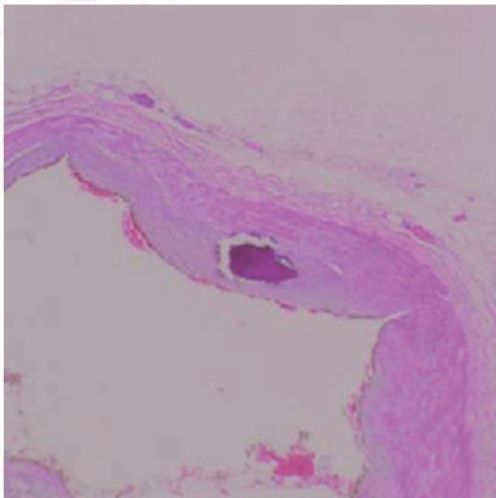


*Stable plaque*

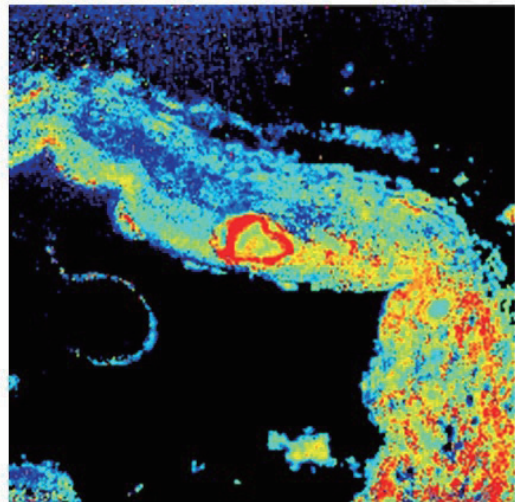
*Vulnerable plaque with lipid core*

*Ruptured plaque with thrombosis*

## Thickening of the intima in stable plaque

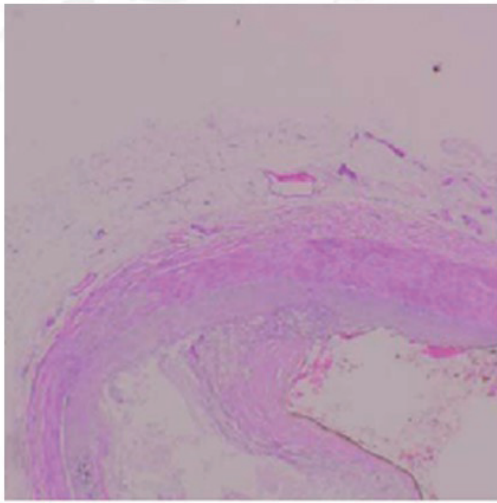


*Optical microscopy (HE)*



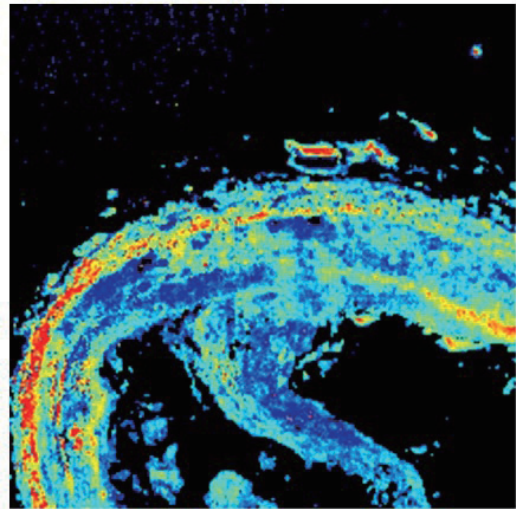
*Acoustic microscopy (Sound speed)*

## Thin fibrous cap in vulnerable plaque



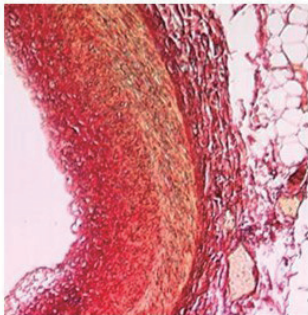
1.0mm

*Optical microscopy (HE)*



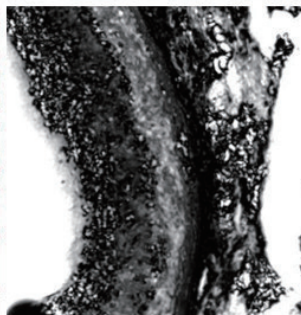
*Acoustic microscopy  
(Sound speed)*

## Resolution in different frequencies



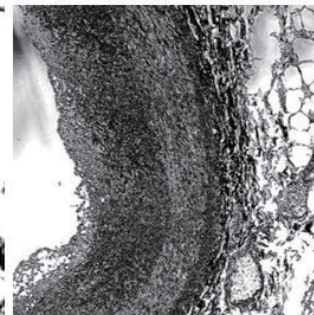
0.2mm

*Optical microscopy*



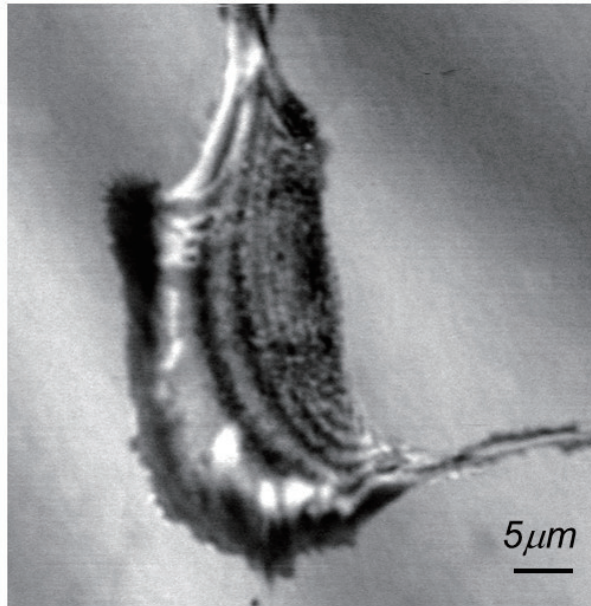
200 MHz

*Acoustic microscopy*

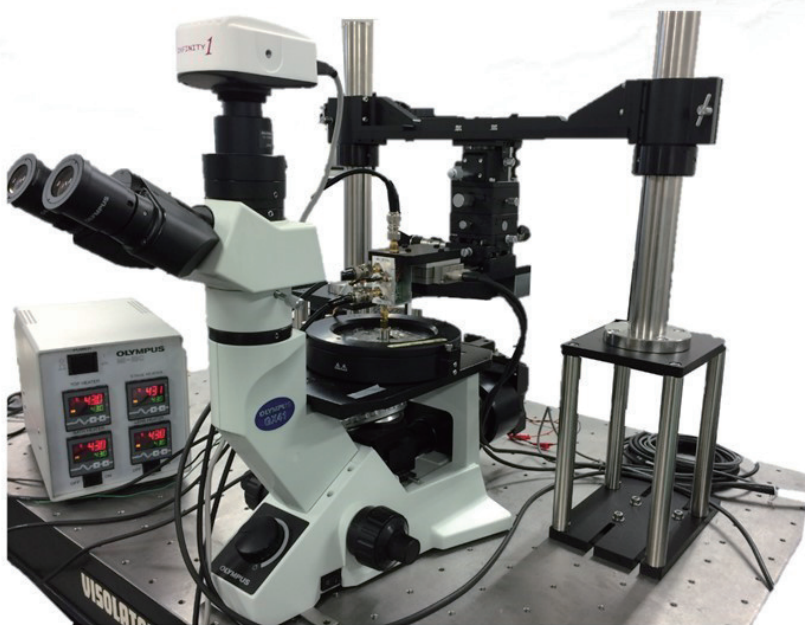


1.1 GHz

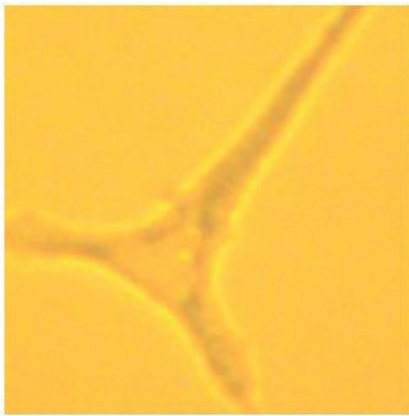
## Renal vascular smooth muscle cell (1.2GHz)



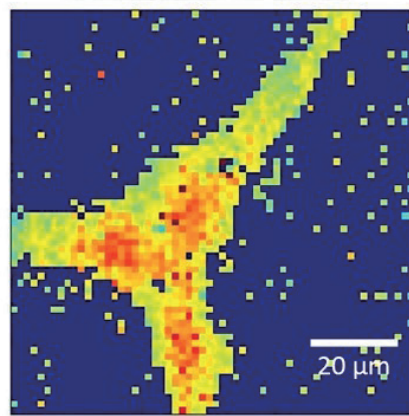
## Ultrasound-optical hybrid microscopy



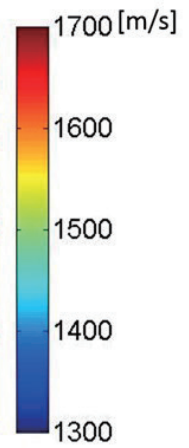
## 3T3-L1 fibroblast



*Optical microscopy (100x)*



*Ultrasound microscopy  
(sound speed)*







# Multiple-Precision Arithmetic Environment in MATLAB and Its Application to Reliable Computation of Fractional Order Derivatives

Hiroshi Fujiwara

Graduate School of Informatics, Kyoto University

## Abstract

This technical note introduces a new multiple-precision arithmetic environment in MATLAB based on *exflib*. We also show its effective application to reliable numerical computation of fractional order derivatives.

## 1 Introduction

In collaborations between mathematical science and industry, numerical computations play an essential role for understanding each other. From the view points of numerical analysis and computational science, we should pay attention to (i) qualitative reliability of numerical schemes, (ii) quantitative accuracy of numerical results, and (iii) practicality in computational time and resources. This talk presents a new strategy for (ii) which realizes accurate and reliable numerical results.

In representation of real numbers and their arithmetic on digital computers, the double precision arithmetic defined in IEEE754 [1] are commonly used in scientific and engineering computations, and it has approximately 16 decimal digits precision. Advanced theory and technologies sometimes involve unstable processes, and require accurate numerical results beyond the standard precision, and rounding errors caused by approximation of real numbers sometimes give serious influences. For instance, most of inverse problems are ill-posed in the sense of Hadamard, and it yields rapid growth of computational errors in their numerical treatments.

To overcome the problems caused by rounding errors, we develop fast multiple-precision arithmetic environment *exflib* [2], which works with the programming language C++ and FORTRAN95. In this talk we introduce user-friendly interface in MATLAB to *exflib*. It enables us to execute fast multiple-precision arithmetic in MATLAB.

## 2 Multiple-Precision Arithmetic Library Exflib in MATLAB

We realize a multiple-precision arithmetic environment in MATLAB based on *exflib* [2] which is implemented in the assembly language of Intel 64 architecture

and the programming language C. MATLAB is one of a commercial software widely used in the fields of science, engineering, and informatics, and it adopts double precision arithmetic as default. The proposed environment runs in MATLAB on 64-bit Windows, MacOSX, and Linux, and it can be downloaded from the home page [2].

The proposed environment consists of two components (Fig. 1): one is definition of a multiple-precision number type and their methods as MATLAB class *exfloat*, and the other is interface between MATLAB and exflib. The formers are implemented in MATLAB m-files stored in `@exfloat` folder in the distributed file. The latter are provided in `exflib` folder, and are implemented by *MATLAB Executable* (MEX) [3, 4] which is a mechanism to call C/FORTRAN codes in MATLAB.

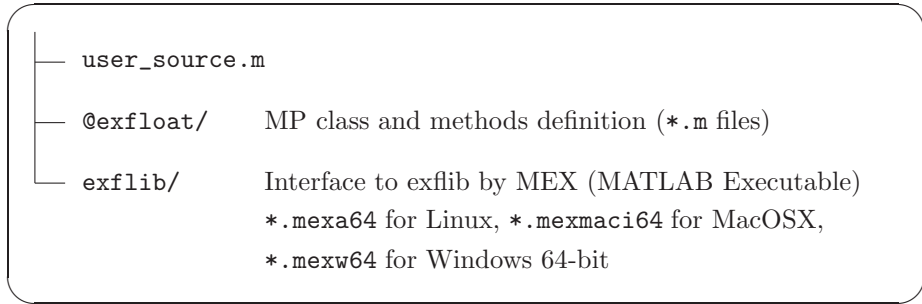


Figure 1: Structures of Proposed Environment.

Each user m-file should specify the MEX directory as Fig. 2 with the `addpath` function at the first line, and the user m-file is recommended to be located in the same directory as `@exfloat` and `exflib` (Fig. 1).

```

addpath( strcat(pwd, '/exflib') );

x = exfloat( 1 );
for n=1:100
    x = x * n;
    fprintf('fact %d = %s\n', n, num2str(x, '%f') );
end
  
```

Figure 2: Example of Factorial Code in Proposed Environment.

User can specify required precision in the file `@exfloat/exfloat.m` shown in Fig. 3. According to the precision, the size of `exfloat` is determined and each multiple-precision number is stored in a 64-bit unsigned array shown in Fig. 4, which represents a value

$$(-1)^s \times 2^{e_b - \text{BIAS}} \times \left( 1 + \sum_{k=1}^n \frac{f_k}{2^{64k}} \right)$$

where  $e_b$  and  $f_k$  are 63-bit and 64-bit unsigned integers respectively, and  $\text{BIAS} = 2^{62} - 1$ . The computational precision is determined by  $n$  as  $(\log_{10} 2)(1 + 64n) \approx$

```

classdef exfloat

    properties (Constant, Access=private)

        precision10 = 100; % required precision in decimal digits
        ...
    end
    ...
end

```

Figure 3: Precision Specification in @exfloat/exfloat.m.

19.27n digits. The auxiliary methods shown in Fig. 5 are useful to get precisions

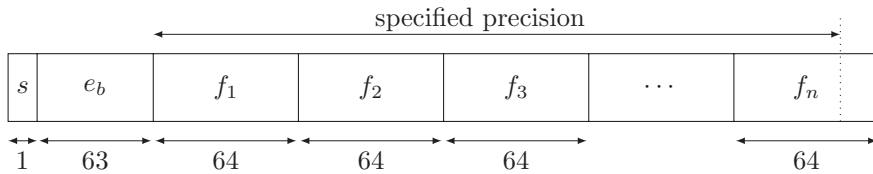


Figure 4: Data Structure of Exfloat Type.

```

% specified precision (decimal digits)
exfloat.get_req_precision()

% internal precision (decimal digits) ≈ 19.27n
exfloat.get_precision()

% memory size (bytes) = 8(n+1)
exfloat.get_exfloat_byte()

% size of fraction parts = n
exfloat.get_exfloat_precision64()

```

Figure 5: Methods to Get Precisions and Size of Proposed Exfloat Type.

and the size information used in execution. Table 1 shows examples of the user specified precision, precision in computation, and the size of each exfloat number obtained by methods in Fig. 5. From the table, if you require and specify 100 decimal digits in @exfloat/exfloat.m as Fig. 3, then approximately 115.60 digits are used in computation, and each exfloat type number is the size of 56 bytes.

Table 1: Specified and Computation Precisions in Decimal Digits.

Specified Digits	Computation Digits	$n$	Size (Bytes)
50	77.06	4	40
100	115.60	6	56
200	211.93	11	96
500	520.18	27	224
1000	1021.09	53	432

## 2.1 Initialization, Output, and Arithmetic of Exfloat in MATLAB

Fig. 6 shows the methods to initialize variables in multiple-precision accuracy. Each exfloat number should be declared or initialized by `exfloat()` at the first appearance. Fig. 7 and Fig. 8 show output methods of the exfloat type. Fig. 9 show initialization of exfloat numbers via a text file.

```

a = exfloat();           % type declaration
x = exfloat( 1 );       % by literal integer
x = exfloat( i );       % by integer variable 'i'
y = x;

x = exfloat( '0.1' );   % by string
x = exfloat( '1/10' );  % by string with expression
x = exfloat( '#PI/2+#E*2' );

x = 1;                  % Invalid : INTEGER
x = 0.1;                % Invalid : DOUBLE
x = exfloat( 0.1 );     % Invalid : DOUBLE
x = '#PI/2';           % Invalid : STRING

```

Figure 6: Initialization and Substitution of Exfloat Numbers.

At present, operations and functions in Table 2 are implemented. Arithmetic and comparisons between exfloat variables or integers can be used similarly as built-in type numbers. But those with built-in real numbers are prohibited.

```

>> cd C:\Users\...\exflib-MATLAB-distribute % Windows
>> cd /home/...\exflib-MATLAB-distribute % Linux or MacOSX
>> addpath( strcat(pwd, '/exflib') );
>> x = exfloat( '#PI' );
>> x % 20 digits as default
3.14159265358979323846
>> double( x ) % convert exfloat to double
3.1416
>> num2str( x ) % convert exfloat to string

ans =

    '3.1416e+0'

>> num2str( x ); % no output if followed by semicolon
>> disp( num2str(x) ) % remove 'ans =' line
3.1416e+0
>> disp( num2str(x) );
3.1416e+0

```

Figure 7: Output of Exfloat Type Variables.

```

>> disp( num2str(x, '%f') ); % fixed-point fmt
3.1416 % 4 digits as default

>> disp( num2str(x, '%.25f') ); % fixed-point fmt with 25 digits
3.1415926535897932384626434

>> disp( num2str(x, '%.25e') ); % exponential fmt with 25 digits
3.1415926535897932384626434e+0

>> disp( num2str(x, '%.25g') ); % general fmt with 25 digits
3.1415926535897932384626434

>> fprintf('Result : %s\n', num2str(x, '%.30e') );
Result : 3.141592653589793238462643383280e+0

>> fprintf('%f %e %g\n', x, x, x); % exfloat is automatically
3.141593 3.141593e+0 3.14159 % converted to double

```

Figure 8: Output of Exfloat Type Variables with Format Specification.

```

addpath( strcat(pwd, '/exflib') );

% result.txt is TSV format
% It contains 3x2 array with delimiter of white space ' '
% 1.1 2.2
% 3.3e0 4.4e1
% 5.5 6.6

lines = splitlines( string( fileread( 'result.txt' ) ) );

for i=1:3
    tsvs = strsplit( lines(i) );
    for j=1:2
        a(i,j) = exfloat( char( strsplit( tsvs(j) ) ) );
    end
end

```

Figure 9: Initialize Exfloat via Text File.

Table 2: Implemented Operation in Proposed Environment.

Arithmetic (unary)	+(plus) -(minus) *(mtimes) /(mrdivide) +(uplus) -(uminus)
Array Operations	\(mldivide) '(transpose) sum dot prod
Entry-wise Operations	.*(times) .\(ldivide) ./(rdivide) .^(power) max min inv
Built-in Functions	abs sqrt sin cos tan asin acos atan atan2 sinh cosh tanh exp ^(mpower) log log10
Comparisons	== ~= < <= > >=
Others	double char num2str display

mpower cannot be applicable to a matrix.

**Example** (Tikhonov Regularization). Fig. 10 shows an example to solve the linear equation  $Hx = B$  and the Tikhonov regularization  $(\alpha I + H^T H)y = H^T B$ , where  $H$  is the Hilbert matrix and  $B = (1, 1, \dots, 1)$ .

The  $(i, j)$ -th entry of the Hilbert matrix is  $h_{ij} = \frac{1}{i+j-1}$  for  $i, j \geq 1$ . But the statement

$$H(i,j) = 1 / ( i+j-1 );$$

or

$$H(i,j) = \text{exfloat}( 1 / ( i+j-1 ) );$$

is not suitable to initialize  $H(i,j)$  as the `exfloat` type, since the expression `1/(i+j-1)` is treated as double precision arithmetic as default in MATLAB, and the substituted entry  $H(i,j)$  is also interpreted as the same type. To prevent it, the explicit type specification `exfloat( 1 )` is used in the example.

```

addpath( strcat(pwd, '/exflib') );

N = 100;

for i=1:N
    for j=1:N
        H(i,j) = exfloat( 1 ) / (i+j-1);
    end
end

B(1:N) = exfloat( 1 );    % row-vector

% solve Hx = B
x = H \ B';

% Tikhonov regularization
a = exfloat( '1e-30' ); % regularization parameter
y = ( a * exflib_eye(N) + H'*H ) \ ( H'*B' );

```

Figure 10: Tikhonov Regularization w.r.t. 2-norm for the Hilbert Matrix.



## 2.2 Fast Computation by Suppressing Calling Overhead of MEX

The proposed environment is based on exflib, and operations in MATLAB calls those in exflib implemented in the assembly language and the programming language C. Fig. 11 shows a calling procedure. Addition (+) with exfloat type scalar operands in MATLAB m-file is bound to the method `@exfloat/plus.m` which is also written in MATLAB m-code. `@exfloat/plus.m` calls the function `exflib_float_add()` provided by `exflib/exflib_float_add.mexa64` (64-bit Linux), `exflib/exflib_float_add.mexmaci64` (MacOSX), or `exflib/exflib_float_add.mexw64` (64-bit Windows). These MEX files are generated by compiling `exflib/exflib_float_add.c` with MATLAB MEX compiler. The file `exflib/exflib_float_add.c` is written in the programming language C, and calls `exflib_float_add.o` written in the assembly language. Therefore executing addition (+) in MATLAB comes with calling overhead.

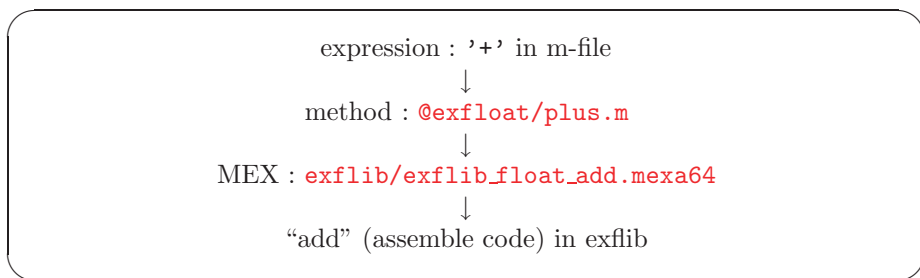


Figure 11: Calling Procedure of Arithmetic in Exflib from MATLAB M-file.

To estimate calling overhead in MATLAB, we calculate the inner product with several implementations. The inner product calculated by the program in Fig. 12 requires at least  $2N$  times MEX calling. Current implementation also provides `dot` method which calls `exflib_mex_dot.mex*`, and it requires one time MEX calling (Fig. 13). The inner product can be also calculated by `sum(a.*b)` and `a*b'`, and both require at least two times MEX calling. Results in Table 3 show that `dot` is significantly fastest among these expressions, and it can be concluded that crucial algorithms should be implemented in MEX for the sake of amortizing calling overheads.

Table 3: Computational Time with 100 Decimal Digits by Various Implementation of Inner Product to Compare Calling Overhead.

unit : sec.					
$N$	entry-wise	<code>dot(a,b)</code>	ratio	<code>sum(a.*b)</code>	<code>a*b'</code>
10	0.0020	0.0010	2.1	0.0040	0.0012
100	0.015	0.0017	8.9	0.0067	0.0028
1000	0.15	0.012	13	0.060	0.016
10000	1.1	0.097	11	0.43	0.13

```

for i=1:N
    s = s + a(i) * b(i);
end

```

Figure 12: Inner Product Implemented by Entry-wise Arithmetic.

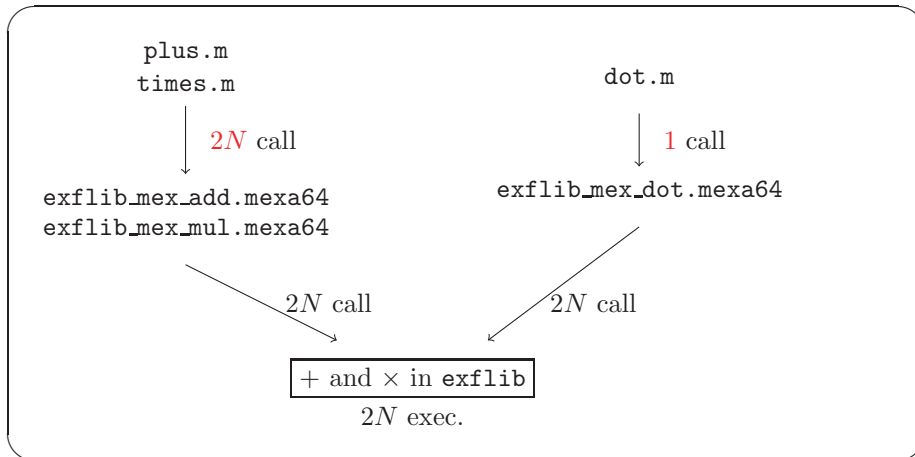


Figure 13: MEX Calling Procedures in Inner Product.

## 2.3 Performance Measurements

In MATLAB, *Variable Precision Arithmetic* (VPA) is provided in “Symbolic Math Toolbox” for multiple-precision arithmetic as an optional feature. Table 4 shows computational times in solving a system of linear equations  $Ax = b$  with a square matrix  $A$ <sup>1</sup> in MATLAB R2017b (Version 9.1.0.441655) on Linux with Xeon E5-2695 v4 (2.1GHz). The program shown in Fig. 14 was executed to measure computational time.

The proposed environment is over 15 and 4 times faster than VPA in 100 and 500 decimal digits computation respectively.

The operation `\` (`mldivide`) calls `exflib/exflib_mex_gaussian_elimination.mex*`, which uses multiple-precision addition, multiplication, and division in `exflib` implemented in the assembly language, and they also cause calling overheads. We also measure the computational times to solve the same equation with `exflib` in the programming language C++, and show them in the right-most column in Table 4. From the results, overhead in MATLAB is crucial in computational time.

## 2.4 Unsupported Features

The following features are frequently used in numerical computations, but they are not supported in the proposed environment at present.

<sup>1</sup>In MATLAB, `mldivide` (`\`) is applicable to find the least square solution to  $Ax = b$  with a rectangle matrix  $A$ .

Table 4: Computational Time in Solving Linear Equation  $Ax = b$ .

unit : sec.					
digits	size	VPA	MATLAB proposed	ratio	C++ exflib
100	100	1.9	0.12	16	0.0066
	200	13	0.73	17	0.056
	400	101	5.1	20	2.0
	800	838	37	22	16
	1000	1647	71	23	31
500	100	2.5	0.53	4.6	0.018
	200	17	3.9	4.4	1.4
	400	129	30	4.3	11
	800	1032	237	4.4	89
	1000	2008	462	4.3	176

```

size = 100;

addpath( strcat(pwd, '/exflib') ); % exflib folder
A = exflib_hilb(size); % Hilbert matrix in exflib
b = exflib_ones(size,1); % RHS in exflib, column-vector
tic; x = A\b; toc;

clearvars A, b;

digits(100); % specifying VPA precision
A = vpa( hilb(size) ); % Hilbert matrix in VPA
b = vpa( ones(size,1) ); % RHS in VPA
tic; x = A\b; toc;

```

Figure 14: Program Used in Computational Time Measurement.

- complex numbers and their arithmetic
- rounding control, interval arithmetic
- precision specification in user's M-files
- dynamic change of computation precision
- special functions
- Matrix Operations : mpower, norm
- BLAS interface

### 3 Application to Accurate Computation of Fractional Order Derivatives

We apply the proposed multiple-precision arithmetic to numerical computation of the fractional order derivative in Caputo's sense. It is also shown that multiple-precision arithmetic is effective in quantitative evaluations of reliability.

For  $f \in C^1(\mathbb{R}_{\geq 0})$  with finite  $f'(0)$  and  $0 < \alpha < 1$ , the  $\alpha$ -th order derivative of  $f$  in Caputo's sense [5, 6] is given by

$${}_c D_0^\alpha [f](x) = f^{(\alpha)}(x) = \frac{1}{\Gamma(1-\alpha)} \int_0^x \frac{f'(y)}{(x-y)^\alpha} dy, \quad x > 0, \quad (1)$$

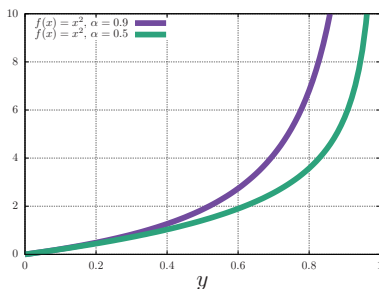
where  $\Gamma(s)$  is the gamma function. Since the integrand has a singularity at  $x$  in general (Fig 15(a)), we leverage the double exponential variable change [7] as

$$\phi(t) = \frac{x}{2} \left( \tanh\left(\frac{\pi}{2} \sinh t\right) + 1 \right).$$

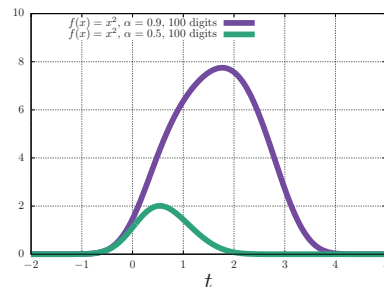
It yields that

$$f^{(\alpha)}(x) = \frac{1}{\Gamma(1-\alpha)} \int_{-\infty}^{\infty} F_{x,\alpha}(\phi(t)) \phi'(t) dt, \quad (2)$$

where  $F_{x,\alpha}[f](y) = F_{x,\alpha}(y) = \frac{f'(y)}{(x-y)^\alpha}$ . Since  $\phi'$  decays rapidly as  $|t| \rightarrow \infty$ , the integrand  $F_{x,\alpha}(\phi(t)) \phi'(t)$  also converges to zero at  $|t| \rightarrow \infty$  (Fig 15(b)).



(a)  $F_{1,\alpha}(y) = \frac{2y}{(1-y)^\alpha}$ .



(b)  $F_{1,\alpha}(\phi(t)) \phi'(t)$ .

Figure 15: Integrand  $F_{1,\alpha}[x^2]$  with  $\alpha = 0.5$ , and  $0.9$ , Calculated with 100 Digits.

### 3.1 Reliable Computation of Fractional Order Derivatives with Multiple-Precision Arithmetic

Fig. 15 are calculated with 100 decimal digits by exflib. On the other hand, results in the double precision are inaccurate shown in Fig. 16.

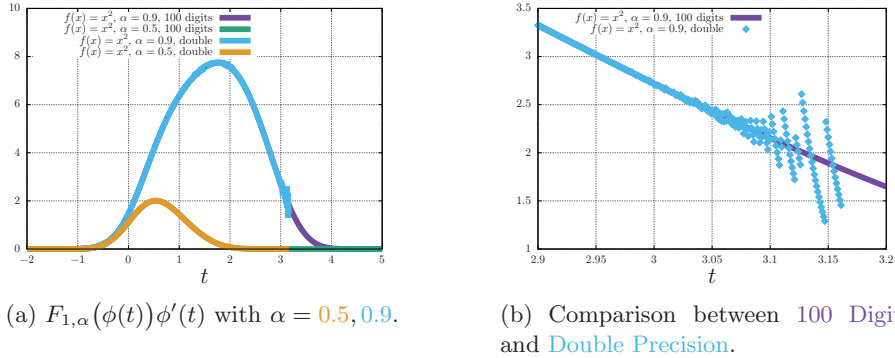


Figure 16: Integrand  $F_{1,\alpha}[x^2](\phi(t))\phi'(t)$ .

In conventional implementation of numerical integration, we calculate  $2\phi(t)$ ,  $1/(1-\phi(t))^\alpha$  and  $\phi'(t)$  separately, and multiply them to evaluate the integrand<sup>2</sup>. Particularly, since  $\phi(t)$  is close to one for large  $t$ , it causes catastrophic cancellation in  $1-\phi(t)$ . For instance, if  $t = 3.16$  then  $1-\phi(t)$  is approximately  $2.2 \times 10^{-16}$  in double precision arithmetic, which equals the unit in the last place, while that is  $1.8 \times 10^{-16}$  in 100 decimal digit (Table 5). Moreover, the double precision arithmetic returns

$$\frac{1}{(1-\phi(t))^{0.9}} = +\infty, \quad t \geq 3.17.$$

This shows that insufficiency of the double precision arithmetic, and efficiency of multiple-precision arithmetic for reliable computation of the fractional order derivative in Caputo's sense by (1).

Table 5: Numerical Results of Components in Integrand in (2) for  $\alpha = 0.9$ .

$t = 3.16$	$1 - \phi(t)$	$(1 - \phi(t))^{-0.9}$	$\phi'(t)$	integrand
100 digits	$1.8 \times 10^{-16}$	$2.8 \times 10^{14}$	$6.6 \times 10^{-15}$	1.8
double	$2.2 \times 10^{-16}$	$2.3 \times 10^{14}$	$6.6 \times 10^{-15}$	1.5

<sup>2</sup>We usually ignore the value of  $1/(1-\phi(t))^\alpha$  if  $\phi'(t)$  is small enough in the computation and evaluate the product (integrand) as zero based on a priori estimate. In this study we do not take this strategy and use the direct product

### 3.2 Discretization Parameters

In numerical computation of (2), we introduce discretization parameters  $\Delta t > 0$  and  $t_k = k\Delta t$ , and discretize it by “the trapezoidal rule” as

$$f^{(\alpha)}(x) \approx \frac{1}{\Gamma(1-\alpha)} \sum_{k \in \mathbb{Z}} F_{x,\alpha}(\phi(t_k)) \phi'(t_k) \Delta t,$$

which is truncated to a finite sum with truncation parameters  $K_0$  and  $K_1 \in \mathbb{Z}$  as

$$\approx \frac{1}{\Gamma(1-\alpha)} \sum_{K_0 \leq k \leq K_1} F_{x,\alpha}(\phi(t_k)) \phi'(t_k) \Delta t. \quad (3)$$

Tables 6 and 7 show discretization parameters and numerical results of (3) for  ${}_c D_0^\alpha [x^2] \big|_{x=1}$  for  $\alpha = 0.5$  and  $0.9$ , where  $L = K_0 \Delta t$ ,  $U = K_1 \Delta t$  and  $K = K_1 - K_0$ . The exact value

$${}_c D_0^\alpha [x^2] \big|_{x=1} = \frac{2}{\Gamma(3-\alpha)}$$

is also shown in the bottom line. The gamma function is calculated in the proposed environment as described in the next section.

From tables, the double precision arithmetic is not sufficient for accurate and reliable computation, particularly for  $\alpha = 0.9$ . And we need a larger interval  $(L, U)$  as  $\alpha$  is closer to one.

### 3.3 Examples of the Caputo Derivative of Fundamental Functions

We show some numerical examples of the Caputo derivative of fundamental functions.

First we discuss efficiency of multiple-precision arithmetic again. Fig. 17 shows fractional order derivatives for  $f(x) = x^2$  with orders  $\alpha = 0.2, 0.4, 0.6, 0.8$  and  $0.9$ . The truncation parameters are  $(L, U) = (-3, 3.16)$  in double precision and  $(L, U) = (-3, 5)$  in 100 decimal digits respectively, and  $K$  is adaptively determined with the tolerance  $10^{-5}$ . Results of  $\alpha = 0.9$  in Fig. 17(a) are unnaturally close to those of  $\alpha = 0.8$  due to lack of precision as stated so far. On the other hand, we can find reasonable results for all  $\alpha$  with 100 decimal digits shown in Fig. 17(b).

Table 6: Discretization Parameters in Numerical Integration (3) for  $\alpha = 0.5$ .

(a) Varying  $U$  and  $K$  for Fixed  $L$ .

$L$	$U$	$K$	double precision	100 digits
-5.00	3.16	8	1.506521145717490	1.50652118787726
		16	1.504513825968471	1.504513847045489
		32	1.504505544986518	1.504505555531676
-5.00	3.17	8	$+\infty$	1.507981691926983
		16	$+\infty$	1.504515197229551
		32	$+\infty$	1.504505555657249
exact value			1.50450555612735...	

(b) Varying  $L$  and  $U$ .

$L$	$U$	$K$	100 digits
-1.5	4.0	65536	1.50450468520610
-2.0	4.0	65536	1.50450555605588
-2.5	4.0	32	1.50450555612735
-2.5	3.0	65536	1.50450522557433
-2.5	3.5	65536	1.50450555611566
-2.5	4.0	32	1.50450555612735
exact value			1.50450555612735...

Table 7: Discretization Parameters in Numerical Integration (3) for  $\alpha = 0.9$ .

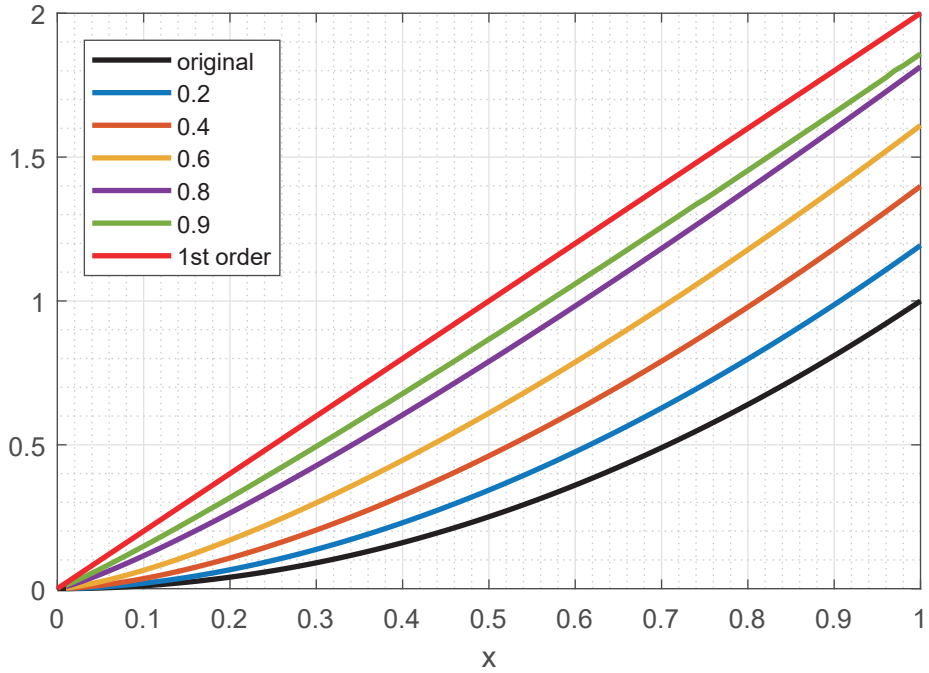
(a) Varying  $U$  and  $K$  for Fixed  $L$ .

$L$	$U$	$K$	double precision	100 digits
-5.00	3.16	8	1.87072828925	1.90636895125
		16	1.87900443987	1.89682476417
		32	1.87188368373	1.88079405669
-5.00	3.17	8	$+\infty$	1.90645242453
		16	$+\infty$	1.89759689138
		32	$+\infty$	1.88210055004
-5.00	5.00	8	$+\infty$	<b>1.90117136452</b>
		16	$+\infty$	<b>1.91113179851</b>
		32	$+\infty$	<b>1.91115819291</b>
exact value			1.911158192930505...	

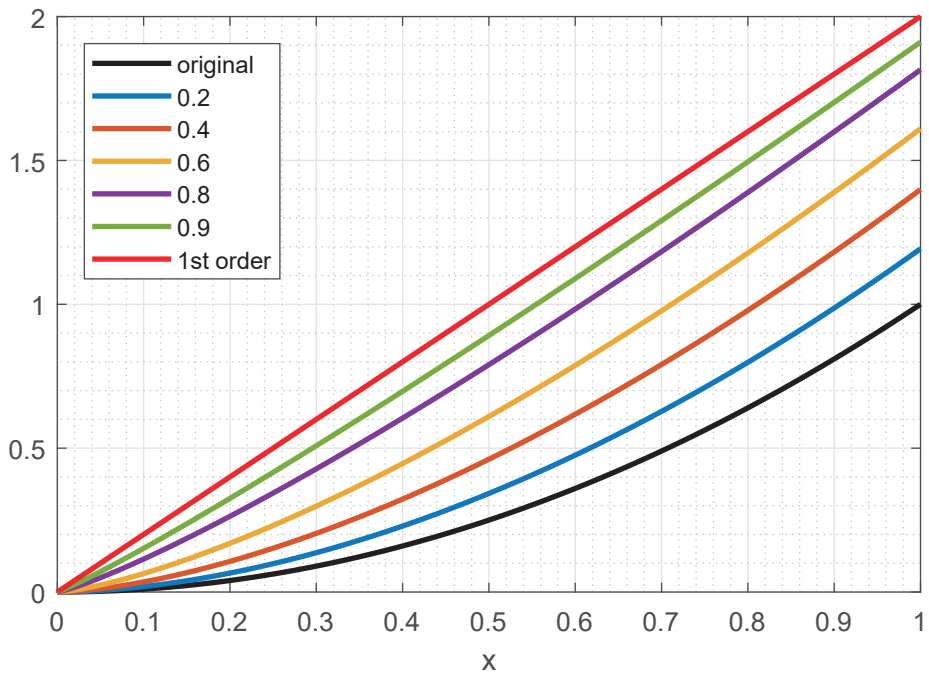
(b) Varying  $L$  and  $U$ .

$L$	$U$	$K$	100 digits
-1.5	5.0	32	<b>1.911158170719432</b>
-1.5	5.0	64	<b>1.911158199338609</b>
-2.0	5.0	32	<b>1.911158192926879</b>
-2.0	5.0	64	<b>1.911158192895752</b>
-2.5	5.0	32	<b>1.911158192928194</b>
-2.5	5.0	64	<b>1.911158192902578</b>
-3.0	4.0	32	<b>1.911033316749863</b>
-3.0	4.5	32	<b>1.911158038914574</b>
-3.0	5.0	32	<b>1.911158192928919</b>
exact value			1.911158192930505...





(a) Results with Double Precision, Results of  $\alpha = 0.9$  is Close to Those of  $\alpha = 0.8$ .



(b) Results with 100 Decimal Digits.

Figure 17:  ${}_c D_0^\alpha [x^2]$ .

The remain of this section is devoted to show profiles of fractional order derivatives of fundamental functions and their properties. In figures,  $f$  and  $f'$  are drawn as the black curve and the red curve respectively. Other colored curves are fractional order derivatives  $f^{(\alpha)}$ . From results,  $\{f^{(\alpha)}\}$  gradually change from  $f$  to  $f'$  as  $\alpha$  changes from zero to one.

- Fig. 18 :  $f^{(\alpha)}$  for  $f(+0) = f'(+0) = 0$ .
- Fig. 19 :  $f^{(\alpha)}$  for  $f(+0) = 0$ ,  $f'(+0) \neq 0$ . In Fig. 19(a), we note that  $f'(+0)$  does not exist and

$${}_cD_0^{1/2}[\sqrt{x}](x) \equiv \frac{\sqrt{\pi}}{2} \approx 0.886, \quad x \neq 0.$$

- Fig. 20 :  $f$  and  $f'$  are periodic functions, but  $f^{(\alpha)}$  does not have the same period. In fact we have  $f^{(\alpha)}(1) \neq f^{(\alpha)}(+0)$  and

$$\begin{aligned} \left(\frac{d}{dx}\right)^{1/2} \sin(\omega x) &= \sqrt{\omega} \operatorname{Im} E(\omega x), \\ \left(\frac{d}{dx}\right)^{1/2} \cos(\omega x) &= \sqrt{\omega} \operatorname{Re} E(\omega x) \end{aligned}$$

where

$$E(z) = e^{(z+\frac{\pi}{4})i} \operatorname{erf}\left(\sqrt{z} e^{\frac{\pi}{4}i}\right)$$

and  $\operatorname{erf} z$  is the complex error function defined by

$$\operatorname{erf} z = \frac{2}{\sqrt{\pi}} \sum_{n=0}^{\infty} \frac{(-1)^n z^{2n+1}}{n! (2n+1)}.$$

On the other hand, if  $n$  is an integer, we have

$$\left(\frac{d}{dx}\right)^n \sin(\omega x) = \omega^n \sin\left(\omega x + \frac{n\pi}{2}\right) = \omega^n \operatorname{Im} e^{(\omega x + \frac{n\pi}{2})i}, \quad (4a)$$

$$\left(\frac{d}{dx}\right)^n \cos(\omega x) = \omega^n \cos\left(\omega x + \frac{n\pi}{2}\right) = \omega^n \operatorname{Re} e^{(\omega x + \frac{n\pi}{2})i}, \quad (4b)$$

which are same as the Riemann-Liouville derivative with the lower terminal at  $-\infty$  [8], and have the period  $2\pi/\omega$  in common. It is clear that those in Caputo's sense do not coincide with (4).

In order to investigate their periodic behaviours more precisely, we compute  ${}_cD_0^{1/2}[\sin 2\pi x]$  by (3) and compare the results with

$$s(x) = \sqrt{2\pi} \sin\left(2\pi x + \frac{\pi}{4}\right).$$

Table 8 shows differences  $s - {}_cD_0^{1/2}[\sin 2\pi x]$  at integers, which converge to zero numerically. In Fig. 21, the horizontal line is  $x \pmod{1}$ , and the graphs of  ${}_cD_0^{1/2}[\sin 2\pi x]$  on  $[0, 1]$ ,  $[1, 2]$ ,  $[2, 3]$  and the function  $s$  are shown. Those on  $[1, 2]$  and  $[2, 3]$  are almost same as  $s(x)$ , and these numerical results strongly imply that  ${}_cD_0^\alpha[\sin 2\pi x]$  asymptotically converge to  $s$  which has the period one.

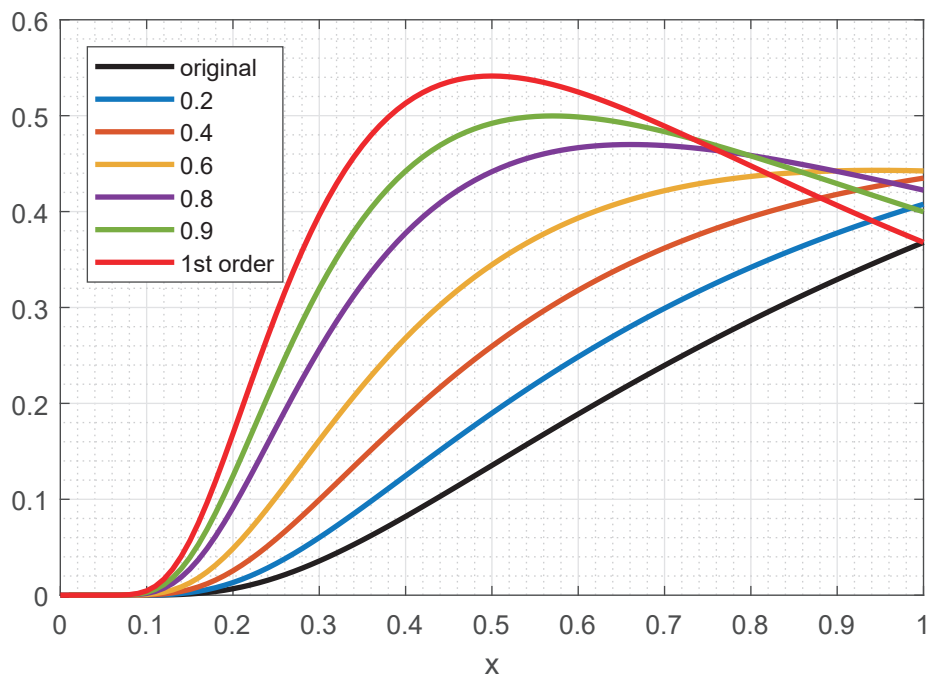
- Fig. 22 : The fractional order derivatives of

$$f(x) = \begin{cases} 0, & x < 0.25; \\ -\frac{2}{(b-a)^3}(x-a)^2 \left(x - \frac{3b-a}{2}\right), & a < x < b; \\ 1, & x > 0.5, \end{cases} \quad (5)$$

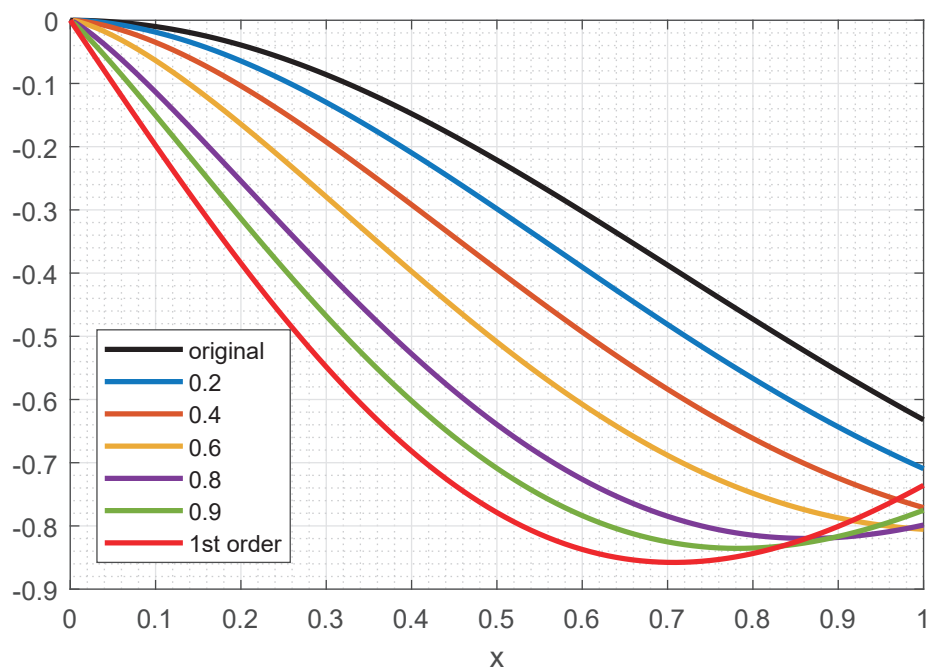
and

$$f(x) = \begin{cases} (x-a)^2(x-b)^2, & a < x < b; \\ 0, & \text{otherwise} \end{cases} \quad (6)$$

where  $a = 0.25$  and  $b = 0.5$  are shown in Figures (a) and (b) respectively. In both examples,  $f(x)$  does not vary on  $x \in I = (0, 0.25) \cup (0.5, 1)$  thus  $f'(x) \equiv 0$  on  $I$ . But  $f^{(\alpha)}$  does not vanish on  $I$ . This is called *hysteresis* or *memory effect* of the operator  ${}_cD_0^\alpha$ .

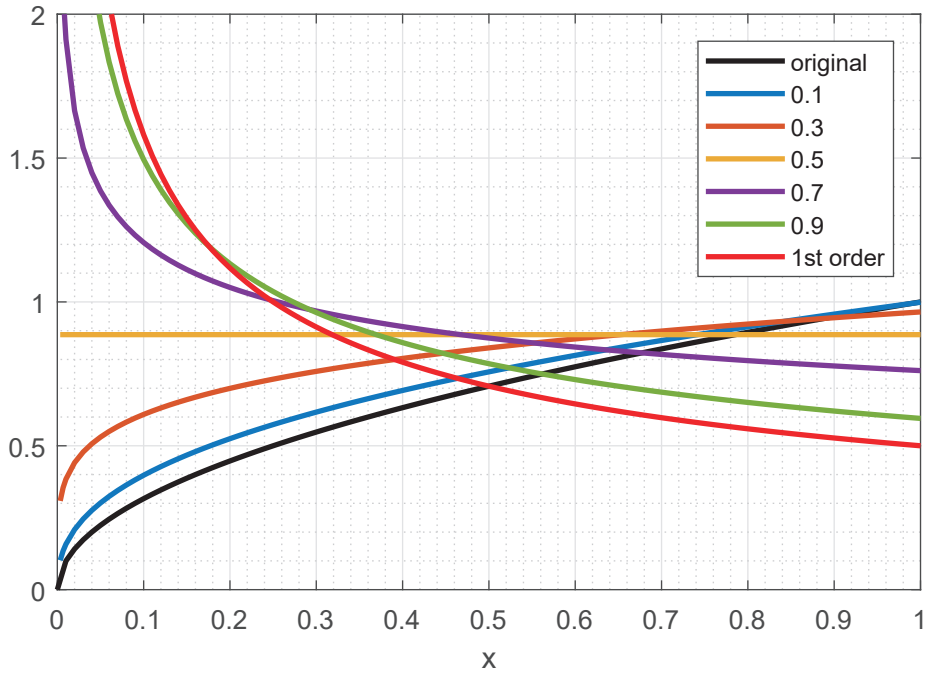


(a)  ${}_c D_0^\alpha [e^{-1/x}]$

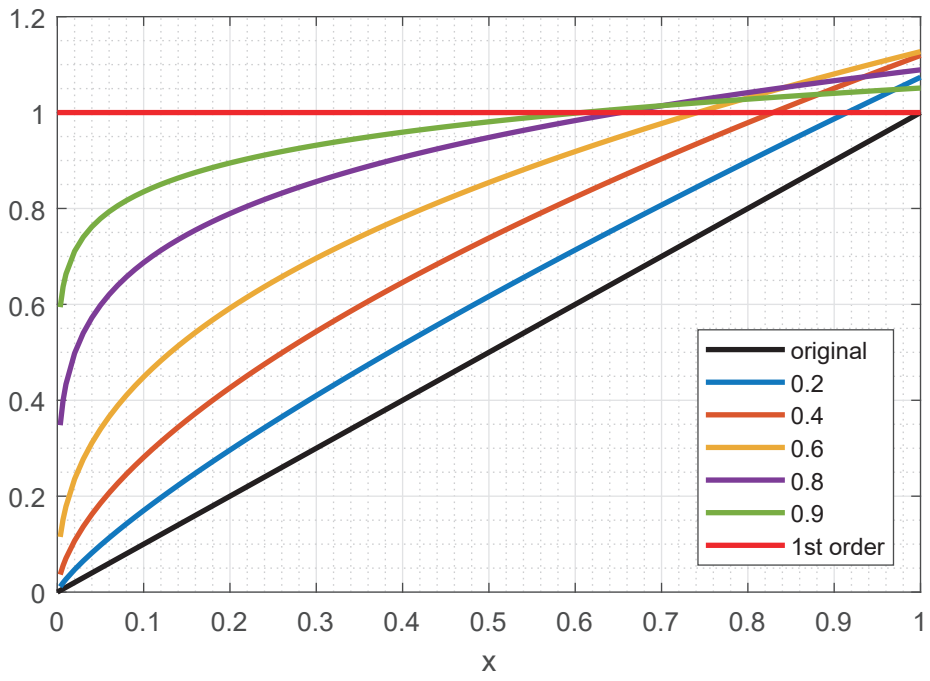


(b)  ${}_c D_0^\alpha [e^{-x^2} - 1]$

Figure 18:  $f^{(\alpha)}$  with  $f(+0) = f'(+0) = 0$ .

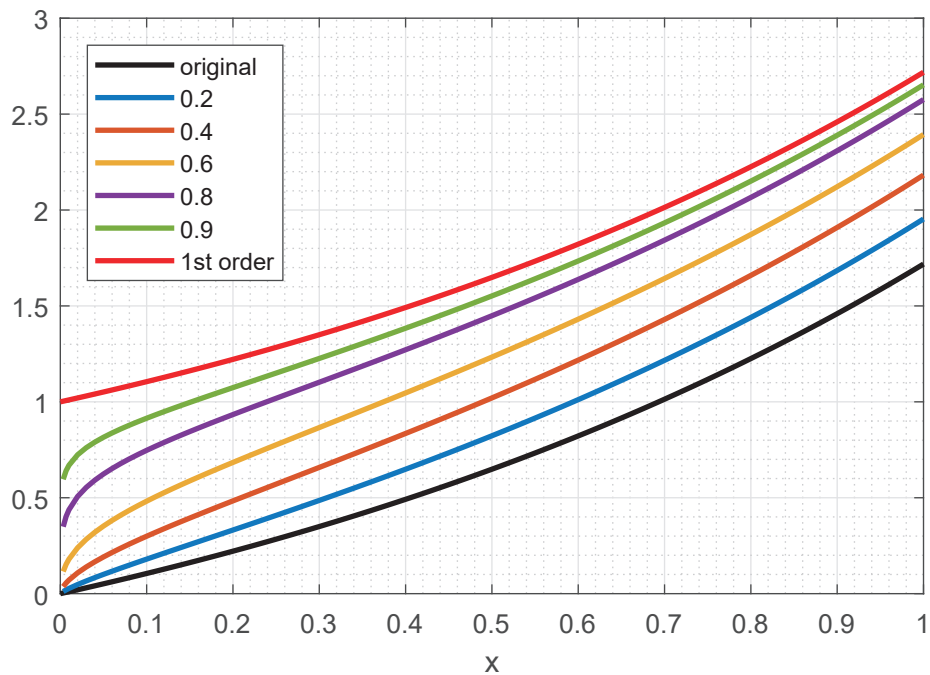


(a)  ${}_cD_0^\alpha[\sqrt{x}]$ .

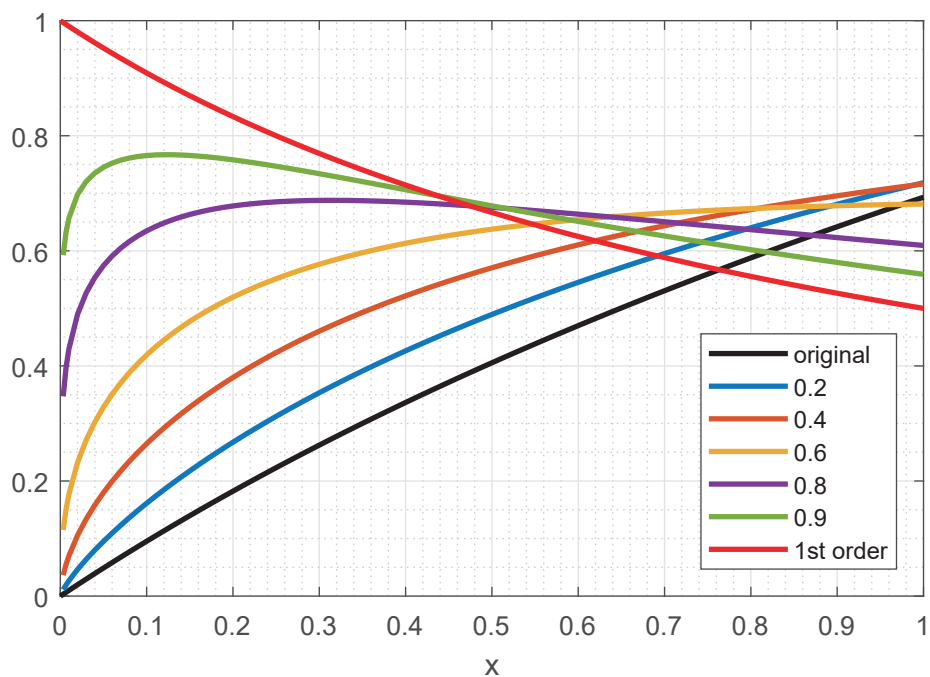


(b)  ${}_cD_0^\alpha[x]$ .

Figure 19:  $f^{(\alpha)}$  with  $f(+0) = 0$  and  $f'(+0) \neq 0$ .

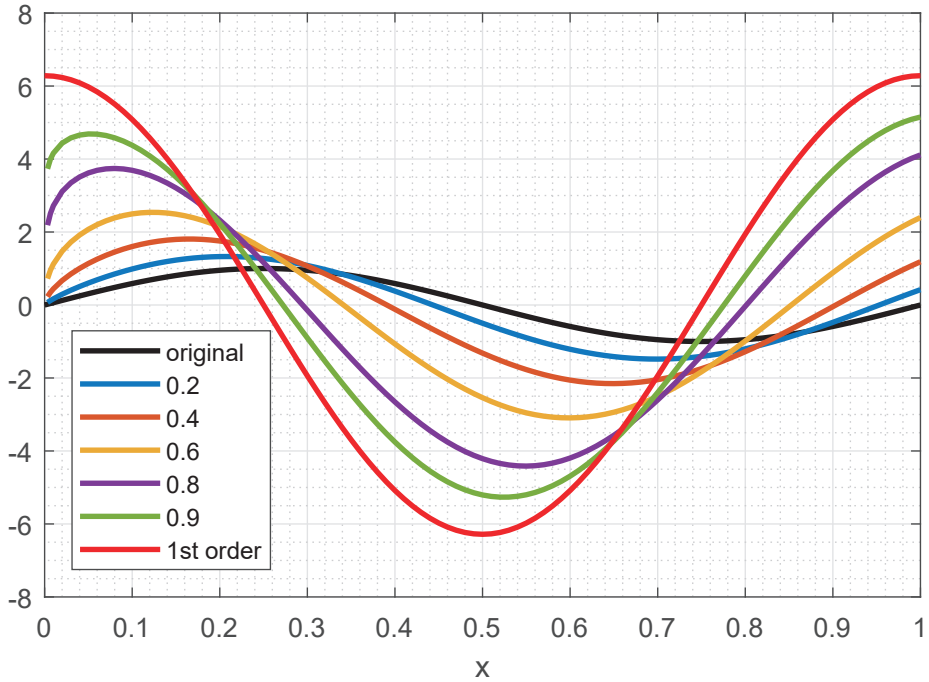


(c)  ${}_c D_0^\alpha [\exp(x) - 1]$ .

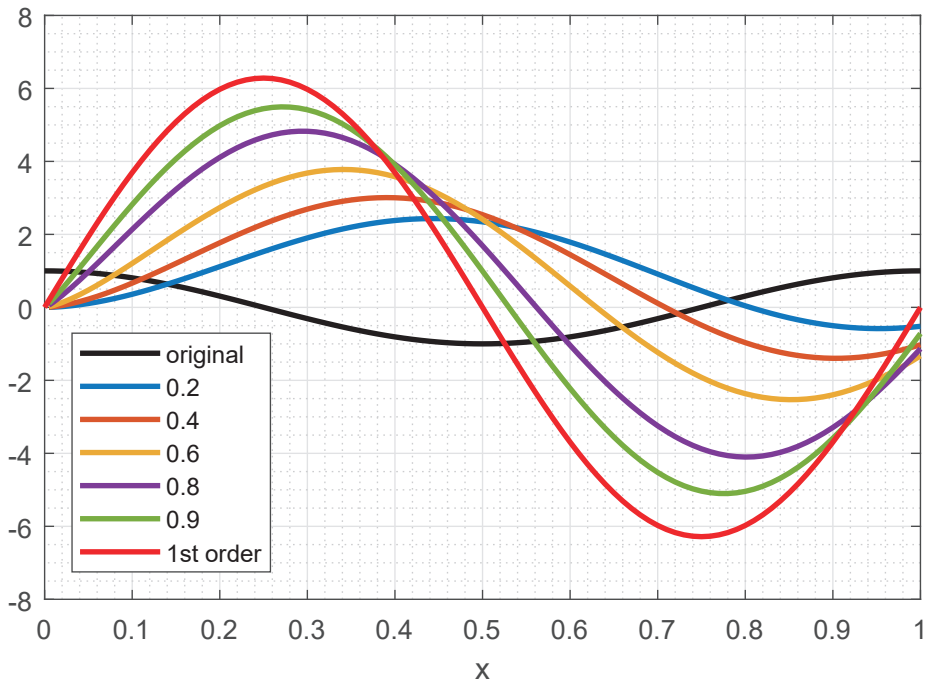


(d)  ${}_c D_0^\alpha [\log(1+x)]$ .

Figure 19: (Continued)  $f^{(\alpha)}$  with  $f(+0) = 0$  and  $f'(+0) \neq 0$ .



(a)  ${}_c D_0^\alpha [\sin 2\pi x]$ .



(b)  ${}_c D_0^\alpha [\cos 2\pi x]$ .

Figure 20: Periodic Functions and Their Fractional Derivatives  $f^{(\alpha)}$ .

Table 8: Periodicity of  ${}_C D_0^{1/2}[\sin 2\pi x]$ .

$x$	${}_C D_0^{1/2}[\sin 2\pi x]$	$\sqrt{2\pi} \sin(2\pi x + \pi/4) - {}_C D_0^{1/2}[\sin 2\pi x](x)$
0	0.00000	1.77245
1	1.73081	0.04164
2	1.75693	0.01553
3	1.76390	0.00855
4	1.76687	0.00558
5	1.76845	0.00400
6	1.76941	0.00305
7	1.77003	0.00242
8	1.77047	0.00198
9	1.77079	0.00166
10	1.77104	0.00142

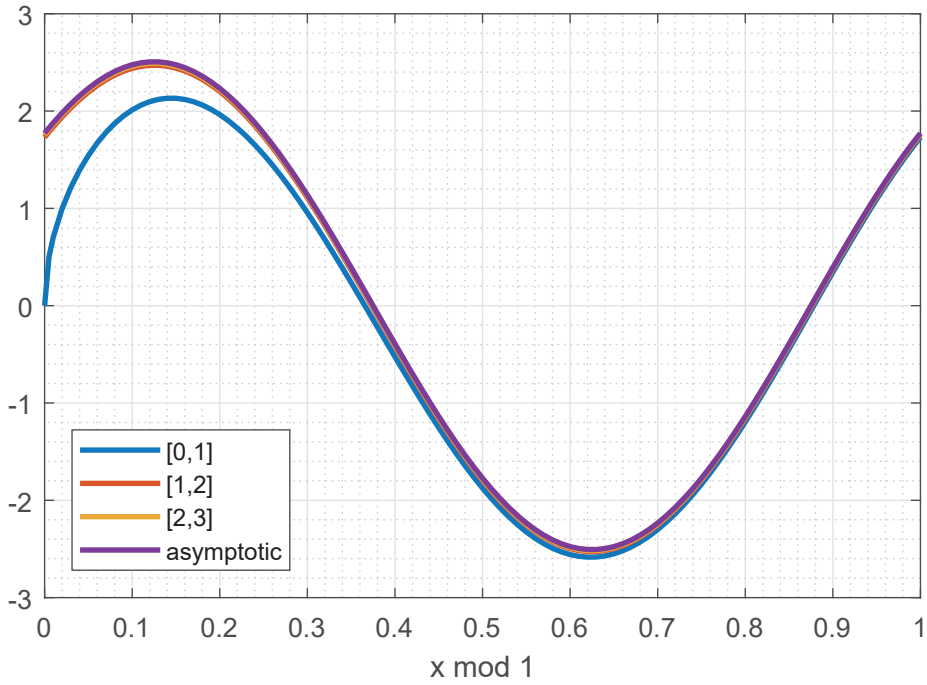
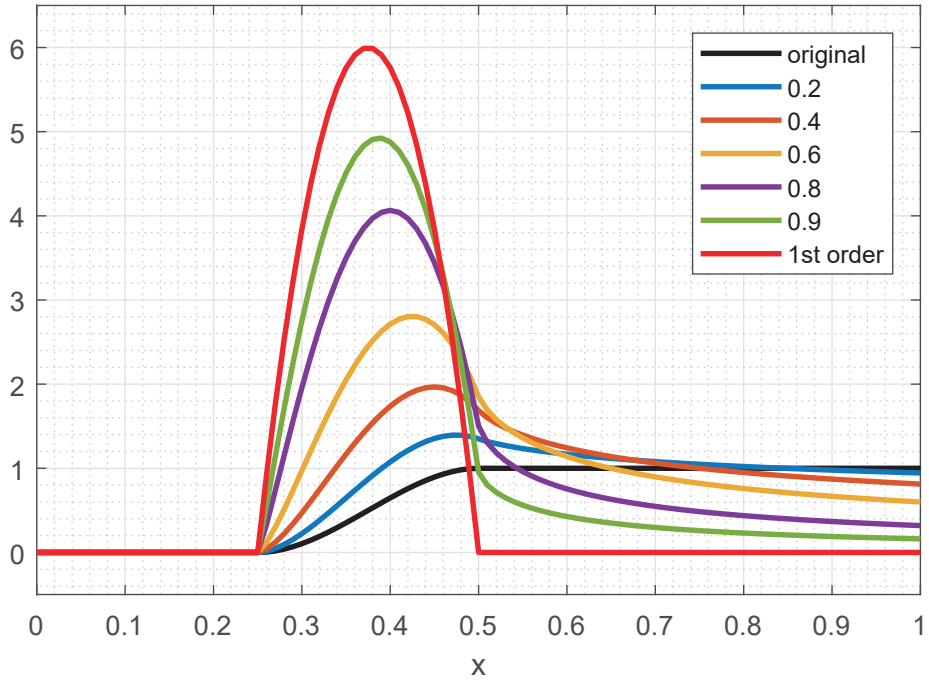
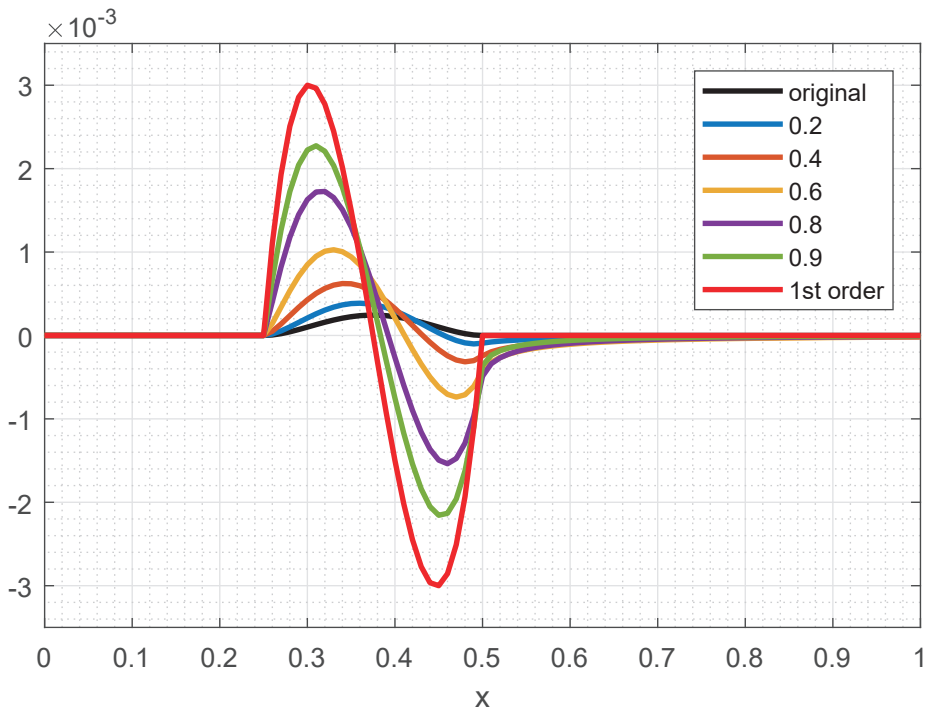


Figure 21: Profiles of  ${}_C D_0^{1/2}[\sin 2\pi x]$  and  $\sqrt{2\pi} \sin\left(2\pi x + \frac{\pi}{4}\right)$ .





(a) Cubic Function (5).



(b) Biquadratic Function (6).

Figure 22: Hysteresis Involved in the Fractional Order Derivatives.

## 4 Multiple-Precision Arithmetic of the Gamma Function

Finally we show accurate numerical computation of the gamma function which appears in the fractional order derivative (1). As stated in the last section, we concentrate on 100 decimal digit computation.

The gamma function is defined by

$$\Gamma(s) = \int_0^{\infty} e^{-x} x^{s-1} dx, \quad s > 0,$$

which satisfies  $\Gamma(s+1) = s\Gamma(s)$  and particularly  $\Gamma(n+1) = n!$  for  $n \in \mathbb{Z}_{\geq 0}$ . The double exponential transformations

$$\phi_1(t) = \exp(t - \exp(-t))$$

and

$$\phi_2(t) = \exp\left(\frac{\pi}{2} \sinh(t)\right)$$

yield

$$\Gamma(s) = \int_{-\infty}^{\infty} e^{-\phi_i(t)} \phi_i(t)^{s-1} \phi_i'(t) dt,$$

which is approximated similarly as (3) by

$$\approx \sum_{K_0 \leq k \leq K_1} e^{-\phi_i(t_k)} \phi_i(t_k)^{s-1} \phi_i'(t_k) \Delta t. \quad (7)$$

Table 9 shows the least  $K$  and the interval  $(L, U)$  which are required to find  $\Gamma(s)$  for each  $s$  of the relative error less than  $10^{-100}$  obtained by numerical experiments with 150 digits. From the results, computational costs of the transform  $\phi_1$  is smaller than those of  $\phi_2$ . We also note that since  $1 < \Gamma(s) < 2$  for  $2 < s < 3$ , an adaptive error estimate is simple from the stand point of floating-point arithmetic in this interval. Thus we propose the use of  $\phi_1(t)$  with parameters  $(L, U) = (-4.7, 5.5)$  and adaptively defined  $K$  to find  $\Gamma(s)$  for  $2 < s < 3$  by numerical integration (7) with 100 decimal digits precision. For other  $s$ , we reduce the argument to the interval  $2 < s < 3$  by the recursive use of

$$\Gamma(s) = \begin{cases} \frac{\Gamma(s+1)}{s}, & 0 < s < 2; \\ (s-1)\Gamma(s-1), & s > 3. \end{cases}$$

Additionally we can find  $\Gamma(s)$  for  $s < 0$  by reducing the argument to  $s > 0$  by

$$\Gamma(s) = \frac{\pi}{\Gamma(1-s) \sin(\pi s)}.$$

Table 9: Required Discretization Parameters to Find  $\Gamma(s)$  of the relative error less than  $10^{-100}$  by Numerical Integration (7).

$s$	$\phi_1(t)$			$\phi_2(t)$		
	$L$	$U$	$K$	$L$	$U$	$K$
0.1	-7.7	5.5	307	-8.0	2.0	1224
0.5	-6.1	5.5	271	-6.4	2.0	1041
1.0	-5.4	5.5	260	-5.7	2.0	964
1.5	-5.0	5.5	254	-5.3	2.0	922
2.0	-4.7	5.5	245	-5.0	2.0	912
2.5	-4.5	5.5	246	-4.8	2.1	892
3.0	-4.4	5.5	243	-4.6	2.0	878
3.5	-4.1	5.6	241	-4.4	2.0	846
4.0	-4.0	5.6	241	-4.3	2.0	855
4.5	-3.9	5.6	240	-4.2	2.1	845
5.0	-3.7	5.6	237	-4.1	2.0	842

## Acknowledgments

The author wish to thank Professor Chien-Hong Cho (National Chung Cheng University) for his valuable comments to development of exflib in MATLAB. This work is supported by JSPS KAKENHI Grant Numbers 26400198, 16H02155, and 16K13774. It is partially based on the discussions at 2017 IMI Joint Use Research Program Workshop (II) “Practical inverse problems based on interdisciplinary and industry-academia collaboration”.

# A Sample Codes with Proposed Muultiple-Precision Arithmetic

## A.1 Computation of the Caputo Derivative

```
%-----  
% CaputoDrvPlot.m : Compute and Plot Caputo Derivative  
% Copyright (C) 2017, FUJIWARA, Hiroshi  
%-----  
clear classes  
addpath( strcat( pwd, '/exflib' ) );  
  
BEG = exfloat( '0' ); % Find Caputo Drv on BEG < x <= END  
END = exfloat( '1' ); % ( 0 <= BEG < END)  
STEPS = 100;  
  
dx = (END-BEG)/STEPS;  
  
SS = 2; % sub-division of (BEG,BEG+dx)  
for i=1:SS % particularly BEG == 0  
    x(i) = BEG + (i-1)*dx/SS;  
end  
for i=SS+1:SS+STEPS  
    x(i) = BEG + (i-SS)*dx;  
end  
  
x(1) = []; % Skip to compute derivative at x=BEG (for BEG == 0)  
  
tic; y2 = CaputoDrv( @df, exfloat( '0.2' ), x ); toc;  
tic; y4 = CaputoDrv( @df, exfloat( '0.4' ), x ); toc;  
tic; y6 = CaputoDrv( @df, exfloat( '0.6' ), x ); toc;  
tic; y8 = CaputoDrv( @df, exfloat( '0.8' ), x ); toc;  
tic; y9 = CaputoDrv( @df, exfloat( '0.9' ), x ); toc;  
  
for i=1:STEPS+1  
    x0(i) = BEG + (i-1)*dx;  
end  
y0 = f(x0);  
y_classical = df(x0);
```

Figure 23: Computation of Caputo Derivative : CaputoDrvPlot.m

```

% plot
plot( x0,y0,'k' , x,y2, x,y4, x,y6, x,y8, x,y9, ...
      x0,y_classical, 'r', 'LineWidth',2 )
legend( 'original', '0.2', '0.4', '0.6', '0.8', '0.9', ...
        '1st order', 'location', 'southwest' )
xlabel( 'x' );
grid on
grid minor
pbaspect([3 2 2])
saveas(gcf, 'CaputoDrv', 'eps'); % EPS file (for TeX)
saveas(gcf, 'CaputoDrv', 'png'); % PNG file
%-----
function y = f( x )
    PI = exfloat( '#PI' );
    y = sin(2*PI*x);
    % y = x.*x; % y is product as array
end

function y = df( x )
    PI = exfloat( '#PI' );
    y = 2*PI*cos( 2*PI*x ); % (d/dx)sin(2*pi*x)
    % y = 2*x;
end
%-----
function y = CaputoDrv( df, order, x )

    % Followings parameters are optimized to 100 digits
    L = exfloat( '-3' );
    U = exfloat( '5' );
    N_MAX = 2048;
    TOLERANCE = exfloat( '1e-5' );

    persistent PhiArray DPhiArray

    if isempty(PhiArray)
        [PhiArray, DPhiArray] = de_initialize(L, U, N_MAX);
    end

    g = gamma( 1-order );

    N = length(x);
    y(1:N) = exfloat(0);
    for i=1:N
        y(i) = CaputoDrvCached( df, order, x(i), g, ...
                                L, U, N_MAX, ...
                                PhiArray, DPhiArray, TOLERANCE );
    end
end
%-----

```

Figure 23: (continued) Computation of Caputo Derivative : CaputoDrvPlot.m

```

% 0 < alpha < 1
function y = CaputoDrvCached ( df, order, x, g, ...
                             L, U, N_MAX, ...
                             PhiArray, DPhiArray, TOLERANCE )

    if t == 0
        y = 0;
        return;
    end

    y = adaptive_de ( @(s)df(s)/power(x-s,order), ...
                     exfloat(0), x, L, U, N_MAX, ...
                     PhiArray, DPhiArray, TOLERANCE ) / g;
end

%-----
function [PhiArray, DPhiArray] = de_initialize(L, U, N_MAX)

    PhiArray(1:1+N_MAX) = exfloat(0);
    DPhiArray(1:1+N_MAX) = exfloat(0);

    pih = exfloat( '#PI/2' );

    function x = phi ( t )
        x = tanh( pih * sinh(t) );
    end

    function x = dphi ( t )
        cs = cosh( pih * sinh(t) );
        x = pih * cosh(t) / (cs*cs);
    end

    dx = (U - L) / N_MAX;

    for i=1:N_MAX+1
        x = (i-1)*dx + L;
        PhiArray(i) = phi(x);
        DPhiArray(i) = dphi(x);
    end

end

%-----

```

Figure 23: (continued) Computation of Caputo Derivative : CaputoDrvPlot.m

```

function s = adaptive_de ( f, a, b, L, U, N_MAX, ...
                          PhiArray, DPhiArray, TOLERANCE )

    pih = exfloat( '#PI/2' );

    function y = linear (x,low,up)
        y = (up-low)/2*(x+1)+low;
    end

    h = U - L;
    N = 1;
    step = N_MAX;
    N_MIN = 16;

    s = f( linear(PhiArray(1),a,b) ) * DPhiArray(1) ...
        + f( linear(PhiArray(N_MAX+1),a,b) ) * DPhiArray(N_MAX+1);
    s = s * h;

    while 1

        t = s;
        h = h / 2;
        if step <= 1
            error( 'too small step' )
        end

        step = step / 2;

        sum = exfloat(0);
        for k=1:N
            sum = sum ...
                + f( linear(PhiArray(step*(2*k-1)+1),a,b) ) ...
                * DPhiArray(step*(2*k-1)+1);
        end
        sum = sum * h;

        s = t/2 + sum;
    end

```

Figure 23: (continued) Computation of Caputo Derivative : CaputoDrvPlot.m

```

        if abs( (s-t)/s ) < TOLERANCE && N >= N_MIN
            break;
        end
        if N > N_MAX
            break;
        end

        N = N * 2;

    end % while

    s = s * (b-a)/2;

end
%-----
% End of file
%-----

```

Figure 23: (continued) Computation of Caputo Derivative : CaputoDrvPlot.m

## A.2 Gamma Function

The function `gamma()` in MATLAB compute the gamma function. Most FORTRAN compilers also support `GAMMA()`, and C++11 has it as `tgamma()`<sup>3</sup>.

```

%-----
% gamma.m : Gamma Function, NOTE : MATLAB supports gamma()
% Copyright (C) 2017, FUJIWARA, Hiroshi
%-----
function g = gamma( s )

    g(1:length(s)) = exfloat(0);

    for i=1:length(s)
        g(i) = gamma_scalar( s(i) );
    end
end

```

Figure 23: Gamma Function : gamma.m

<sup>3</sup>In C++, `gamma()` or `lgamma()` are used to compute the natural logarithm of the gamma function:  $\log|\gamma(x)|$ . The name `tgamma()` represents “true gamma” (Linux Programmer’s Manual, TGAMMA(3))



```

function g = gamma_scalar ( s )

%-----
% s \in 0,-1,-2, ... => gamma(s) is undefined
% s < 0, gamma(s) = pi/( gamma(1-s) * sin(pi*s) );
%-----
if s < 0
    PI = exfloat( '#PI' );
    g = PI / ( gamma_scalar(1-s) * sin(PI*s) );
    return;
end

%-----
% Reducing argument into 2 < s < 3
% using gamma(s+1) = s*gamma(s)
%-----
if s == 2
    g = exfloat( 1 );
    return;
elseif s < 2
    g = gamma_scalar(s+1) / s;
    return;
elseif s == 3
    g = exfloat( 2 );
    return;
elseif s > 3
    g = (s-1) * gamma_scalar(s-1);
    return;
end

%-----
% 1 <= gamma(s) < 2, when 2 <= s < 3.
% 2 < s < 3, find gamma(s) by improper integral
% Followings parameters are optimized to 100 digits
U = exfloat( '5.5' );
L = exfloat( '-4.7' );
N_MAX = 1024;
TOL = exfloat( '1e-100' );
%-----

g = de_adaptive( @(x)integrand_gamma(x,s), ...
                @phi_gamma, @dphi_gamma, ...
                U, L, N_MAX, TOL );
end
%-----

```

Figure 23: (continued) Gamma Function : gamma.m

```

function s = de_adaptive ( integrand, phi, dphi, ...
                        U, L, N_MAX, TOLERANCE )

    N_MIN = 16;
    h = U - L;

    s = integrand( phi(L) ) * dphi(L) ...
        + integrand( phi(U) ) * dphi(U);
    s = s * h;
    N = 1;

    while 1
        t = s;
        h = h / 2;

        sum = exfloat( 0 );

        for k=1:N
            x = h*(2*k-1) + L;
            sum = sum + integrand( phi(x) ) * dphi(x);
        end
        sum = sum * h;

        s = t/2 + sum;

        if abs(s-t)/s < TOLERANCE && N >= N_MIN
            break;
        end
        if N > N_MAX
            s = -1;
            return;
        end
        if abs(s - t)/s < TOLERANCE
            break;
        end
        N = N * 2;

    end % while

end
%-----

```

Figure 23: (continued) Gamma Function : gamma.m

```

function p = phi_gamma ( t )
    p = exp( t - exp(-t) );
end

function p = dphi_gamma ( t )
    p = exp( t - exp(-t) ) * ( 1 + exp(-t) );
end

function y = integrand_gamma ( x, nu )
    y = power(x, nu-1) * exp(-x);
end
%-----
% End of file
%-----

```

Figure 23: (continued) Gamma Function : `gamma.m`

### A.3 A Cauchy Problem of the Laplace Equation in 2D

Let  $\Omega = (0,1)^2 \subset \mathbb{R}^2$  and we consider a Cauchy Problem of the Laplace Equation:

$$\Delta u(x, y) = 0, \quad (x, y) \in \Omega, \quad (8a)$$

$$u(x, 0) = x^2, \quad x \in \mathbb{R}, \quad (8b)$$

$$\frac{\partial u}{\partial y}(x, 0) = 0, \quad x \in \mathbb{R}, \quad (8c)$$

which is known as one of typical ill-posed problems. Fig. 23 is a finite difference scheme to solve the problem, and Fig. 24(a) and (b) are numerical results by the standard double precision arithmetic and multiple-precision arithmetic respectively. Numerical results of double precision oscillates and does not approximate the exact solution around  $y = 0.2$  due to accumulation of rounding errors, while those of 100 digits approximate it in  $y < 0.5$  (Fig. 24(b)).

In the example code, the computational precision is determined by uncommenting either of the following lines. The first line indicates the multiple-precision arithmetic, and the second line indicates the double precision arithmetic.

```

one = exfloat(1);
one = 1;

```

The result shows the efficiency of multiple-precision arithmetic in numerical computation of ill-posed problems.

```

%-----
% Cauchy Problem of the Laplace Equation in 2D Rectangle
% FDM Computation with 3D plot
%
% Copyright (C) 2017, FUJIWARA,Hiroshi
%-----
clear classes
addpath( strcat( pwd, '/exflib' ) );

Nx = 80; % division number of the interval 0 <= x <= 1.
Ny = 160; % division number of the interval 0 <= y <= 1.

I = 6*Nx; % Computation Domain
J = Ny/2; % 100 digits

%-----
% Select Computational Precision
% MULTIPLE-PRECISION or DOUBLE
%-----
%one = 1; % double precision arithmetic
one = exfloat(1); % multiple-precision arithmetic

%-----
% Setup Lattice
%-----
dx = one / Nx;
dy = one / Ny;

for i=1:I+1
    x( i ) = dx * (i-I/2-1);
end
for j=1:J+1
    y( j ) = dy * (j-1);
end

%-----
% Initial Value
%-----
f = x.*x;
g = 0.*x;
%-----
u(1:I+1, 1) = f;
u(1:I+1, 2) = f + dy*g(1:I+1);

```

Figure 23: Program to Solve Cauchy Problem of the Laplace Equation in 2D (8)

```

%-----
% Finite Difference Scheme
%-----
lambda = dy*dy/(dx*dx);

for j=2:J
    % Boundary Condition
    u(1,j+1) = 0;

    % FDM
    u(2:I,j+1) = 2*u(2:I,j) - u(2:I,j-1)...
        - lambda.*( u(3:I+1,j) - 2*u(2:I,j) + u(1:I-1,j) );

    % Boundary Condition
    u(I+1,j+1) = 0;

end

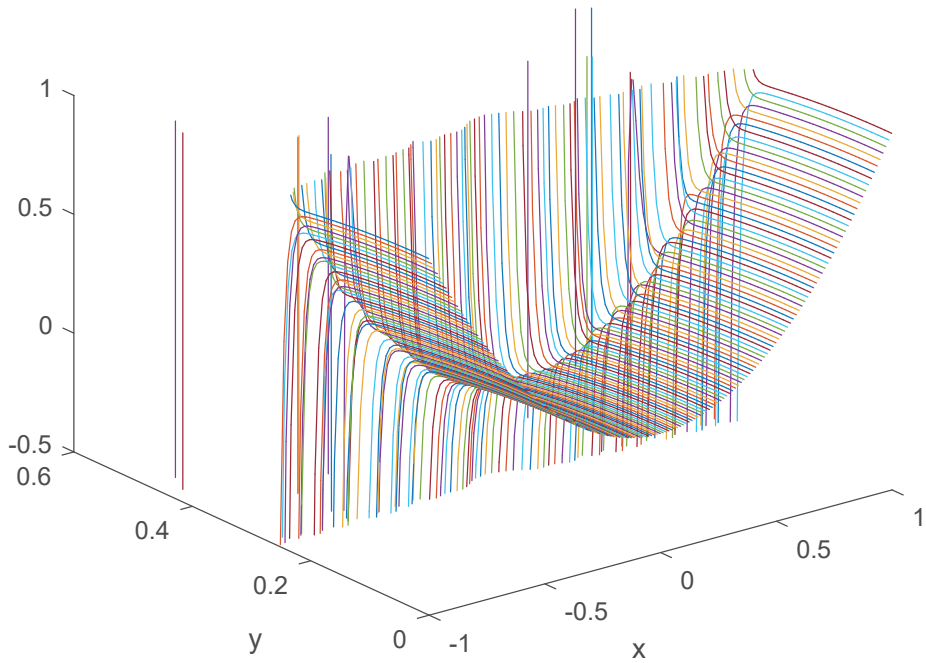
%-----
% Output
%-----
[xx,yy] = meshgrid( -1:double(dx):1, 0:double(dy):double(J*dy) );
uu = double ( u(2*Nx+1:4*Nx+1, 1:J+1) );
plot3 (xx, yy, uu);

xlabel( 'x' );
ylabel( 'y' );
zlim( [-0.5 1] );

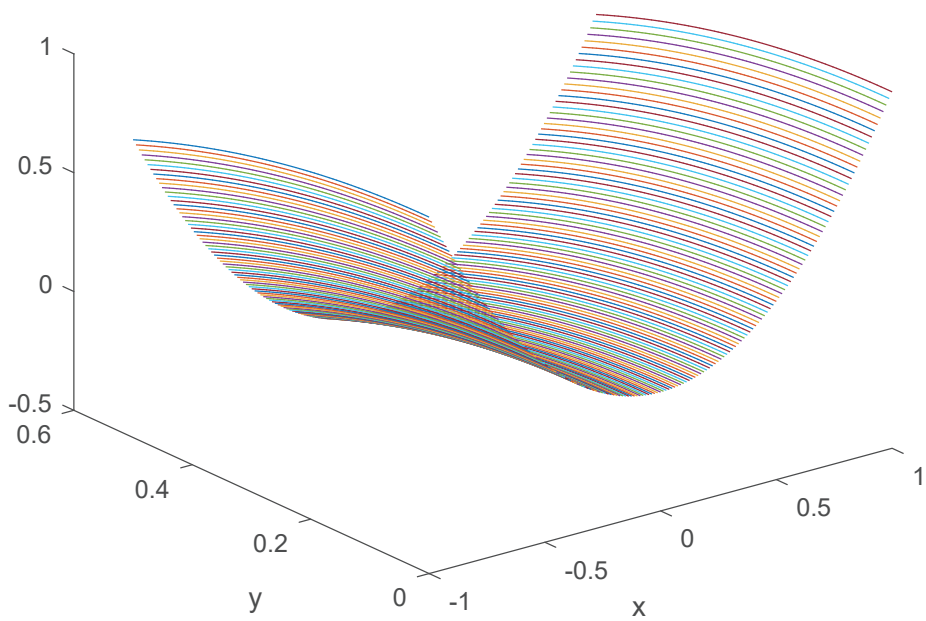
saveas(gcf, 'CauchyPbLaplace2D', 'eps'); % EPS file (for TeX)
saveas(gcf, 'CauchyPbLaplace2D', 'png'); % PNG file
%-----
% End of file
%-----

```

Figure 23: (continued) Program to Solve Cauchy Problem of the Laplace Equation in 2D (8)



(a) Numerical Results by Double Precision Arithmetic



(b) Numerical Results by 100 Decimal Digits.

Figure 24: Numerical Results for a Cauchy Problem of the Laplace Equation (8) using Program Fig. 23.

## References

- [1] IEEE Standard for Binary Floating-Point Arithmetic, IEEE Std 754-1985 (1985).
- [2] Exflib Home Page, <http://www-an.acs.i.kyoto-u.ac.jp/~fujiwara/exflib>
- [3] Introducing MEX Files, [https://ch.mathworks.com/help/matlab/matlab\\_external/introducing-mex-files.html](https://ch.mathworks.com/help/matlab/matlab_external/introducing-mex-files.html)
- [4] P. Getreuer, Writing MATLAB C/MEX Code <https://ch.mathworks.com/matlabcentral/fileexchange/27151-writing-matlab-c-mex-code> (2010).
- [5] M. Caputo, Linear Models of dissipation whose  $A$  is almost frequency independent: Part II., *Geophys. J. R. Astr. Soc.* **13** (1967) pp. 529–539.
- [6] M. Caputo, *Elasticità e Dissipazione*, Zanichelli, Bologna (in Italian) (1969).
- [7] H. Takahashi and M. Mori, Double Exponential Formulas for Numerical Integration, *Publ. Res. Inst. Math. Sci.* **9** (1974) pp. 721–741.
- [8] I. Podlubny, *Fractional Differential Equations*, Academic Press (1998).

# Identification of moving wave sources from boundary measurements

Takashi Ohe

Department of Applied Mathematics, Faculty of Science, Okayama University of Science  
e-mail: ohe@xmath.ous.ac.jp

## Abstract

Identification of wave sources is an important inverse problem because it has a lot of applications in various fields. In inverse source problems, choice of source model is a key point for theoretical and numerical discussions. Point source model and dipole source model are simple but useful models that are widely discussed in many papers [6, 8, 9, 15]. Here, we concentrate our attention to an algebraic restriction method for these models.

In the previous workshop in 2015, we consider the case where several unknown dipoles moves slowly in some region, and discuss a identification procedure the parameters of dipole [19]. Here, the word 'slowly' means that moving speed of dipoles are sufficiently small (smaller than 10% of the wave propagation speed). In this report, we remove this restriction to which the moving speed of dipoles are only smaller (not sufficiently small) than the wave propagation speed, and propose a new procedure to reconstruct moving point and dipole sources.

## 1 Introduction

Identification problem of waves sources frequently arises in many science and engineering fields e.g. identification of seismic sources, passive sonar [2, 21]. Assuming that the media is isotropic, such kind of problem can be mathematically formulated as an inverse source problem for wave equation[4, 12]. In inverse source problems, the choice of source model is a key point in theoretical studies on uniqueness or stability, and numerical studies on reconstruction methods. Point source model and dipole source model are simple but useful models, and are widely discussed in many papers[5, 9, 13, 16, 17, 20]. In the report, we discuss a real-time algebraic reconstruction method of these models.

In the previous workshop in 2015, we propose a identification procedure the unknown parameters of dipole source models assuming that dipoles move slowly[19]. Here, the word 'slowly' means that moving velocities of points or dipole sources are sufficiently small (smaller than 10%) comparing to the wave propagation speed, and then we can neglect the effect of the moving speed of sources. In this report, we discuss a method to remove the restriction of our previous result, and propose a new procedure to identify moving point and dipole sources accounting the effect of the velocities of these kind of sources.



## 2 Mathematical formulation

Let  $u$  be a scalar wave field described as a solution of the initial-value boundary-value problem for three dimensional scalar wave equation:

$$\left\{ \begin{array}{ll} \frac{1}{c^2} \partial_t^2 u(t, \mathbf{r}) - \Delta u(t, \mathbf{r}) = F(t, \mathbf{r}), & \text{in } (0, T) \times \Omega, \\ u(0, \mathbf{r}) = 0, & \text{in } \Omega, \\ \partial_t u(0, \mathbf{r}) = 0, & \text{in } \Omega, \\ u(t, \mathbf{r}) = 0, & \text{on } (0, T) \times \Gamma, \end{array} \right. \quad (1)$$

where  $\Omega \subset \mathbb{R}^3$  is a simply connected bounded domain with  $C^\infty$ -class boundary  $\Gamma = \partial\Omega$ ,  $c > 0$  is the wave propagation speed,  $T > 2 \cdot \text{diam } \Omega > 0$  is a constant, and  $F(t, \mathbf{r})$  describes the wave source. Suppose that  $F(t, \mathbf{r})$  is unknown, and consider the problem to reconstruct it from observation  $\phi$  of the normal derivative of  $u$  on  $\Gamma$ :

$$\phi(t, \mathbf{r}) = \partial_\nu u(t, \mathbf{r}), \text{ on } (0, T) \times \Gamma.$$

This problem is called *inverse source problem* for scalar wave equation, and many researchers discussed this problem from theoretical and numerical points of view, e.g. [5, 9, 18].

In inverse source problems, the choice of source model is a key point for theoretical and numerical discussions. In this report, we assume that the source term is described by multiple moving point sources

$$F(t, \mathbf{r}) = \sum_{k=1}^K q_k(t) \delta(\mathbf{r} - \mathbf{p}_k(t)), \quad (2)$$

or moving dipole sources

$$F(t, \mathbf{r}) = - \sum_{k=1}^K \mathbf{m}_k(t) \cdot \nabla \delta(\mathbf{r} - \mathbf{p}_k(t)). \quad (3)$$

In (2),  $K$  denotes the number of point sources,  $\mathbf{p}_k(t) \in D$  and  $q_k(t) \in \mathbb{R}$  the location and magnitude of  $k$ -th point source at  $t$ , where  $D$  is a compact subset in  $\Omega$ . Note that we do not need to specify the domain  $D$ . The symbol  $\delta$  describes the Dirac's delta distribution. And in (3),  $K$  denotes the number of dipole sources,  $\mathbf{p}_k(t) \in D$  and  $\mathbf{m}_k(t) \in \mathbb{R}^3$  the location and dipole moment of  $k$ -th dipole source at  $t$ . Hence, we consider the solution  $u$  of (1) in a weak sense, i.e.  $u \in C^1([0, T]; L^2(\Omega))$  that satisfies

$$\begin{aligned} & \frac{1}{c^2} \int_{\Omega} \partial_t u(T, \mathbf{r}) v(T, \mathbf{r}) dV(\mathbf{r}) - \frac{1}{c^2} \int_{\Omega} u(T, \mathbf{r}) \partial_t v(T, \mathbf{r}) dV(\mathbf{r}) \\ & - \int_0^T \int_{\Gamma} \partial_\nu u(t, \mathbf{r}) v(t, \mathbf{r}) dS(\mathbf{r}) dt \\ & + \int_0^T \int_{\Omega} u(t, \mathbf{r}) \left( \frac{1}{c^2} \partial_t^2 v(t, \mathbf{r}) - \Delta v(t, \mathbf{r}) \right) dV(\mathbf{r}) dt \\ & = \mathcal{F}(v), \end{aligned} \quad (4)$$

for any  $v \in C^\infty([0, T] \times \bar{\Omega})$ . In (4), the right hand side term  $\mathcal{F}(v)$  is expressed by

$$\mathcal{F}(v) = \langle F, v \rangle = \begin{cases} \sum_{k=1}^K \int_0^T q_k(t) v(t, \mathbf{p}_k(t)) dt, & \text{for point source model,} \\ \sum_{k=1}^K \int_0^T \mathbf{m}_k(t) \cdot \nabla v(t, \mathbf{p}_k(t)) dt, & \text{for dipole source model.} \end{cases}$$

With the aid of [14], we obtain the following regularity result for the case that the point and dipole sources move smoothly in time and space and magnitudes or moments change smoothly in time:

**PROPOSITION 1.** *Let  $\ell$  be a non-negative integer. For moving point sources (2), assume that  $\mathbf{p}_k \in C^{\ell+2}([0, T]; D)$ ,  $q_k \in C^{\ell+1}([0, T]; \mathbb{R})$ ,  $|\mathbf{d}_t \mathbf{p}_k(t)| < c$  and  $q_k(0) = \mathbf{d}_t q_k(0) = \mathbf{d}_t^2 q_k(0) = \dots = \mathbf{d}_t^{(\ell+1)} q_k(0) = 0$ , where  $\mathbf{d}_t$  denotes the derivative with respect to  $t$ . Then, the solution  $u$  of (1) satisfies  $u \in C([0, T]; L^2(\Omega))$ ,  $\partial_t u \in C([0, T]; L^2(\Omega))$ . Specifically, the restriction  $u$  on  $[0, T] \times (\Omega \setminus D)$  satisfies*

$$u|_{[0, T] \times (\Omega \setminus D)} \in C([0, T]; H^{\ell+1}(\Omega \setminus D)), \quad (5)$$

$$\nabla u|_{[0, T] \times (\Omega \setminus D)} \in C([0, T]; H^\ell(\Omega \setminus D)), \quad (6)$$

$$\nabla \partial_t^m u|_{[0, T] \times (\Omega \setminus D)} \in C([0, T]; H^{\ell-m}(\Omega \setminus D)), \quad 0 \leq m \leq \ell, \quad (7)$$

and the normal derivative  $\partial_\nu u$  on  $\Gamma$  satisfies

$$\partial_\nu u \in H^\ell([0, T] \times \Gamma). \quad (8)$$

For moving dipole sources (3), assume that  $\mathbf{p}_k \in C^{\ell+2}([0, T]; D)$ ,  $\mathbf{m}_k \in C^{\ell+2}([0, T]; \mathbb{R}^3)$ ,  $|\mathbf{d}_t \mathbf{p}_k(t)| < c$ , and  $\mathbf{m}_k(0) = \mathbf{d}_t \mathbf{m}_k(0) = \mathbf{d}_t^2 \mathbf{m}_k(0) = \dots = \mathbf{d}_t^{(\ell+2)} \mathbf{m}_k(0) = \mathbf{0}$ . Then, the solution  $u$  satisfies  $u \in C([0, T]; H^{-1}(\Omega))$ ,  $\partial_t u \in C([0, T]; H^{-1}(\Omega))$ . Specifically, the restriction  $u$  on  $[0, T] \times (\Omega \setminus D)$  and the normal derivative  $\partial_\nu u$  satisfy the same regularities (5)-(8) as the results for moving point sources.

## 3 Reconstruction method

### 3.1 Reciprocity gap functional

In our reconstruction method, the key technique is the reciprocity gap functional that is defined on the subspace of test functions  $v$  in (4). This technique is widely applied to various inverse problems [1, 3, 7, 8, 11]. First, we show a definition of the reciprocity gap functional for scalar wave equations.

Let  $\mathcal{W} \subset C^\infty([0, T] \times \bar{\Omega}; \mathbb{C})$  be a class of complex-valued functions  $v$  that satisfy the homogeneous wave equation and the zero final state condition:

$$\begin{cases} \frac{1}{c^2} \partial_t^2 v - \Delta v = 0, & \text{in } (0, T) \times \Omega, \\ v(T, \mathbf{r}) = 0, & \text{in } \Omega, \\ \partial_t v(T, \mathbf{r}) = 0, & \text{in } \Omega. \end{cases} \quad (9)$$

We define the reciprocity gap functional  $\mathcal{R}_\phi$  on  $\mathcal{W}$  for given observation data  $\phi \in L^2((0, T) \times \Gamma)$  by

$$\mathcal{R}_\phi(v) \equiv - \int_0^T \int_\Gamma \phi(t, \mathbf{r}) v(t, \mathbf{r}) dt dS(\mathbf{r}), \quad v \in \mathcal{W}. \quad (10)$$

Since  $u$  satisfies the weak form (4) and  $\phi = \partial_\nu u$ , we establish

$$\mathcal{R}_\phi(v) = \mathcal{F}(v), \quad \text{for any } v \in \mathcal{W}. \quad (11)$$

The equation (11) shows relation between the reciprocity gap functional  $\mathcal{R}_\phi(v)$  and the source term  $F$ , and suggests that we can pick up some information on the unknown parameters of the source term using  $\mathcal{R}_\phi(v)$ .

### 3.2 Reconstruction of moving point sources

In this subsection, we assume that  $\mathbf{p}_k \in C^6([0, T]; D)$ ,  $q_k \in C^5([0, T]; \mathbb{R})$  and  $q_k(0) = d_t q_k(0) = d_t^2 q_k(0) = \dots = d_t^5 q_k(0) = 0$ . Then, from proposition 1, we have observation data  $\phi \in H^4((0, T) \times \Gamma)$ . For the reconstruction of moving point sources, we choose the following five sequences of functions in  $\mathcal{W}$  :

$$f_{n,\varepsilon}(t, \mathbf{r}; \tau) = (x + iy)^n \eta_\varepsilon \left( t - \left( \tau - \frac{z}{c} \right) \right), \quad n = 0, 1, 2, \dots, \quad (12)$$

$$g_{n,\varepsilon}(t, \mathbf{r}; \tau) = -\partial_t f_{n,\varepsilon}(t, \mathbf{r}; \tau), \quad n = 0, 1, 2, \dots, \quad (13)$$

$$h_{n,\varepsilon}(t, \mathbf{r}; \tau) = z(\partial_x - i\partial_y) f_{n,\varepsilon}(t, \mathbf{r}; \tau) - (x - iy)\partial_z f_{n,\varepsilon}(t, \mathbf{r}; \tau), \quad n = 1, 2, \dots, \quad (14)$$

$$i_{n,\varepsilon}(t, \mathbf{r}; \tau) = \partial_t^2 f_{n,\varepsilon}(t, \mathbf{r}; \tau), \quad n = 0, 1, 2, \dots, \quad (15)$$

$$j_{n,\varepsilon}(t, \mathbf{r}; \tau) = -\partial_t h_{n,\varepsilon}(t, \mathbf{r}; \tau), \quad n = 1, 2, \dots, \quad (16)$$

where  $\tau \in [\sup_{\mathbf{r} \in \Omega} z/c + \varepsilon, T + \inf_{\mathbf{r} \in \Omega} z/c - \varepsilon]$ ,  $0 < \varepsilon \ll 1$ , and  $\eta_\varepsilon \in C^\infty(\mathbb{R}; \mathbb{R})$  denotes the standard mollifier function (see Appendix C in [10]). We note that sequences  $\{f_{n,\varepsilon}\}$ ,  $\{g_{n,\varepsilon}\}$  and  $\{h_{n,\varepsilon}\}$  have already utilized for the reconstruction of fixed point sources [18]. We add sequences  $\{i_{n,\varepsilon}\}$  and  $\{j_{n,\varepsilon}\}$  to treat the effect of moving velocities of sources.

Due to the assumption for  $\mathbf{p}_k(t)$  and  $q_k(t)$ , the observation data  $\phi$  is in  $H^4((0, T) \times \Gamma) \subset C^2([0, T] \times \Gamma)$ . Then, reciprocity gap functionals  $\mathcal{R}_\phi(f_{n,\varepsilon})$ ,  $\mathcal{R}_\phi(g_{n,\varepsilon})$ ,  $\dots$ ,  $\mathcal{R}_\phi(j_{n,\varepsilon})$  converge as  $\varepsilon \rightarrow +0$ , and we have

$$\begin{aligned} \mathcal{R}_\phi(f_n)(\tau) &\equiv \lim_{\varepsilon \rightarrow +0} \mathcal{R}(f_{n,\varepsilon}(\cdot, \cdot; \tau)) \\ &= - \lim_{\varepsilon \rightarrow +0} \int_0^T \int_\Gamma \phi(t, \mathbf{r}) f_{n,\varepsilon}(t, \mathbf{r}; \tau) dS(\mathbf{r}) dt \\ &= - \int_\Gamma (x + iy)^n \phi \left( \tau - \frac{z}{c}, \mathbf{r} \right) dS(\mathbf{r}), \\ \mathcal{R}_\phi(g_n)(\tau) &\equiv \lim_{\varepsilon \rightarrow +0} \mathcal{R}(g_{n,\varepsilon}(\cdot, \cdot; \tau)) \\ &= - \int_\Gamma (x + iy)^n \partial_t \phi \left( \tau - \frac{z}{c}, \mathbf{r} \right) dS(\mathbf{r}), \\ \mathcal{R}_\phi(h_n)(\tau) &\equiv \lim_{\varepsilon \rightarrow +0} \mathcal{R}(h_{n,\varepsilon}(\cdot, \cdot; \tau)) \\ &= - \int_\Gamma 2nz(x + iy)^{n-1} \phi \left( \tau - \frac{z}{c}, \mathbf{r} \right) dS(\mathbf{r}) \\ &\quad - \frac{1}{c} \int_\Gamma (x - iy)(x + iy)^n \partial_t \phi \left( \tau - \frac{z}{c}, \mathbf{r} \right) dS(\mathbf{r}), \\ \mathcal{R}_\phi(i_n)(\tau) &\equiv \lim_{\varepsilon \rightarrow +0} \mathcal{R}(i_{n,\varepsilon}(\cdot, \cdot; \tau)) \\ &= - \int_\Gamma (x + iy)^n \partial_t^2 \phi \left( \tau - \frac{z}{c}, \mathbf{r} \right) dS(\mathbf{r}), \\ \mathcal{R}_\phi(j_n)(\tau) &\equiv \lim_{\varepsilon \rightarrow +0} \mathcal{R}(j_{n,\varepsilon}(\cdot, \cdot; \tau)) \\ &= - \int_\Gamma 2nz(x + iy)^{n-1} \partial_t \phi \left( \tau - \frac{z}{c}, \mathbf{r} \right) dS(\mathbf{r}) \\ &\quad - \frac{1}{c} \int_\Gamma (x - iy)(x + iy)^n \partial_t^2 \phi \left( \tau - \frac{z}{c}, \mathbf{r} \right) dS(\mathbf{r}). \end{aligned}$$

Also  $\mathcal{F}(f_{n,\varepsilon})$ ,  $\mathcal{F}(g_{n,\varepsilon})$ ,  $\dots$ ,  $\mathcal{F}(i_{n,\varepsilon})$  converge as  $\varepsilon \rightarrow +0$ , and we establish the following explicit

expressions with respect to the parameters of moving point sources:

$$\begin{aligned}
\mathcal{F}(f_n)(\tau) &= \lim_{\varepsilon \rightarrow +0} \mathcal{F}(f_{n,\varepsilon}(\cdot, \cdot; \tau)) \\
&= \lim_{\varepsilon \rightarrow +0} \sum_{k=1}^K \int_0^T q_k(t) f_{n,\varepsilon}(t, \mathbf{p}_k(t); \tau) \\
&= \sum_{k=1}^K q_k(t_k(\tau)) \xi_k(t_k(\tau)) (p_{k,xy}(t_k(\tau)))^n,
\end{aligned} \tag{17}$$

$$\begin{aligned}
\mathcal{F}(g_n)(\tau) &= \lim_{\varepsilon \rightarrow +0} \mathcal{F}(g_{n,\varepsilon}(\cdot, \cdot; \tau)) \\
&= \sum_{k=1}^K d_\tau(q_k \xi_k) \cdot (p_{k,xy})^n + n \sum_{k=1}^K q_k \xi_k \cdot d_\tau(p_{k,xy}) \cdot (p_{k,xy})^{n-1},
\end{aligned} \tag{18}$$

$$\begin{aligned}
\mathcal{F}(h_n)(\tau) &= \lim_{\varepsilon \rightarrow +0} \mathcal{F}(h_{n,\varepsilon}(\cdot, \cdot; \tau)) \\
&= 2n \sum_{k=1}^K q_k \xi_k \cdot p_{k,z} \cdot (p_{k,xy})^{n-1} \\
&\quad + \frac{1}{c} \sum_{k=1}^K \{d_\tau(q_k \xi_k) \cdot \overline{p_{k,xy}} + q_k \xi_k \cdot d_\tau(\overline{p_{k,xy}})\} (p_{k,xy})^n \\
&\quad + \frac{n}{c} \sum_{k=1}^K q_k \xi_k \cdot d_\tau(p_{k,xy}) \cdot \overline{p_{k,xy}} \cdot (p_{k,xy})^{n-1},
\end{aligned} \tag{19}$$

$$\begin{aligned}
\mathcal{F}(i_n)(\tau) &= \lim_{\varepsilon \rightarrow +0} \mathcal{F}(i_{n,\varepsilon}(\cdot, \cdot; \tau)) \\
&= \sum_{k=1}^K d_\tau^2(q_k \xi_k) p_{k,xy}^n + n \sum_{k=1}^K \{2d_\tau(q_k \xi_k) \cdot d_\tau(p_{k,xy}) + q_k \xi_k \cdot d_\tau^2(p_{k,xy})\} (p_{k,xy})^{n-1} \\
&\quad + n(n-1) \sum_{k=1}^K q_k \xi_k \cdot (d_\tau(p_{k,xy}))^2 \cdot (p_{k,xy})^{n-2},
\end{aligned} \tag{20}$$

$$\begin{aligned}
\mathcal{F}(j_n)(\tau) &= \lim_{\varepsilon \rightarrow +0} \mathcal{F}(j_{n,\varepsilon}(\cdot, \cdot; \tau)) \\
&= 2n \sum_{k=1}^K q_k \xi_k \cdot d_\tau(p_{k,z}) \cdot (p_{k,xy})^{n-1} + \hat{R}_{j_n},
\end{aligned} \tag{21}$$

where

- The symbol  $d_\tau$  denotes the derivative with respect to  $\tau$ , e.g.  $d_\tau(p_{k,xy}) = d_t p_{k,xy}(t_k(\tau)) \cdot \xi_k(\tau)$ ,
- $p_{k,xy}(t_k(\tau)) = p_{k,x}(t_k(\tau)) + i p_{k,y}(t_k(\tau))$ ,
- $t_k(\tau)$  is the unique solution  $t$  of the equation

$$t - \tau + \frac{p_{k,z}(t)}{c} = 0, \tag{22}$$

for each  $k$  and  $\tau$ ,

- $\xi_k(\tau)$  is the derivative of  $t_k$  with respect to  $\tau$ , and it is expressed as

$$\xi_k(\tau) = \frac{dt_k}{d\tau}(\tau) = 1 - \frac{d_t p_{k,z}(t_k(\tau))}{c}, \tag{23}$$

- $\hat{R}_{j_n}$  is a polynomial defined by

$$\begin{aligned}
\hat{R}_{j_n} = & 2n \sum_{k=1}^K \{d_\tau(q_k \xi_k) \cdot p_{k,xy} + (n-1)q_k \xi_k \cdot d_\tau(p_{k,xy})\} \cdot p_{k,z} \cdot (p_{k,xy})^{n-2} \\
& + \frac{1}{c} \sum_{k=1}^K d_\tau^2(q_k \xi_k) \cdot \overline{p_{k,xy}} \cdot (p_{k,xy})^n \\
& + \frac{1}{c} \sum_{k=1}^K \{2d_\tau(q_k \xi_k) \cdot d_\tau(\overline{p_{k,xy}}) + q_k \xi_k \cdot d_\tau^2(\overline{p_{k,xy}})\} \cdot (p_{k,xy})^n \\
& + \frac{n}{c} \sum_{k=1}^K \{2d_\tau(q_k \xi_k) \cdot d_\tau(p_{k,xy}) + q_k \xi_k \cdot d_\tau^2(p_{k,xy})\} \cdot \overline{p_{k,xy}} \cdot (p_{k,xy})^{n-1} \\
& + \frac{n}{c} \sum_{k=1}^K 2q_k \xi_k \cdot d_\tau(p_{k,xy}) \cdot d_\tau(\overline{p_{k,xy}}) \cdot (p_{k,xy})^{n-1} \\
& + \frac{n(n-1)}{c} \sum_{k=1}^K q_k \xi_k \cdot (d_\tau(p_{k,xy}))^2 \cdot \overline{p_{k,xy}} \cdot (p_{k,xy})^{n-2}.
\end{aligned}$$

Here, except for (17), we omit the argument  $(t_k(\tau))$  on  $q_k$ ,  $p_{k,xy}$ ,  $p_{k,z}$  and their derivatives, and the argument  $(\tau)$  on  $\xi_k$  to simplify the expression.

Using expressions (17) - (21), we obtain the following reconstruction theorem for moving point sources:

**THEOREM 3.1.** *For each  $\tau$ , let  $K(\tau)$  be the number of point sources such that  $q_k(t_k(\tau)) \neq 0$ . Assume that  $K(\tau) \leq K_M$  for some  $K_M > 0$ , and  $p_{j,xy}(t_j(\tau)) \neq p_{k,xy}(t_k(\tau))$  if  $j \neq k$ . Then, we can determine  $K(\tau)$  from the reciprocity gap functionals  $\mathcal{R}_\phi(f_n)(\tau)$ ,  $n = 0, 1, 2, \dots, 2K_M + 1$ . Also we can uniquely determine  $\mathbf{p}_k(t_k(\tau))$  and  $q_k(t_k(\tau))$ ,  $k = 1, 2, \dots, K(\tau)$  from the reciprocity gap functionals*

- $\mathcal{R}_\phi(f_n)(\tau)$ ,  $n = 0, 1, 2, \dots, 2K(\tau)$ ,
- $\mathcal{R}_\phi(g_n)(\tau)$ ,  $n = 0, 1, 2, \dots, 2K(\tau) - 1$ ,
- $\mathcal{R}_\phi(h_n)(\tau)$ ,  $n = 1, 2, 3, \dots, K(\tau)$ ,
- $\mathcal{R}_\phi(i_n)(\tau)$ ,  $n = 1, 2, 3, \dots, 2K(\tau)$ ,
- $\mathcal{R}_\phi(j_n)(\tau)$ ,  $n = 1, 2, 3, \dots, K(\tau)$ .

### Sketch of proof

We can prove the theorem by the following five steps. These steps also provide a reconstruction procedure of moving point sources.

**Step 1.** Identify  $K(\tau)$  from  $\mathcal{R}_\phi(f_n)(\tau)$ ,  $n = 0, 1, 2, \dots, 2K(\tau) + 1$ .

**Step 2.** Reconstruct  $p_{k,xy}(t_k(\tau))$ ,  $k = 1, 2, \dots, K(\tau)$ , and identify perturbed magnitudes  $q_k(t_k(\tau))\xi_k(\tau)$  from  $\mathcal{R}_\phi(f_n)(\tau)$ ,  $n = 0, 1, 2, \dots, 2K(\tau)$ .

**Step 3.** Reconstruct  $p_{k,z}(t_k(\tau))$ ,  $k = 1, 2, \dots, K(\tau)$  from  $\mathcal{R}_\phi(g_n)(\tau)$ ,  $n = 0, 1, 2, \dots, 2K(\tau) - 1$  and  $\mathcal{R}_\phi(h_n)(\tau)$ ,  $n = 1, 2, 3, \dots, K(\tau)$ .

**Step 4.** Identify  $d_\tau(p_{k,z}(t_k(\tau)))$ ,  $k = 1, 2, \dots, K(\tau)$  from  $\mathcal{R}_\phi(i_n)(\tau)$ ,  $n = 1, 2, 3, \dots, 2K(\tau)$  and  $\mathcal{R}_\phi(j_n)(\tau)$ ,  $n = 1, 2, 3, \dots, K(\tau)$ .

**Step 5.** Compute  $\xi_k(\tau)$  using  $d_\tau(p_{k,z}(t_k(\tau)))$  for each  $k = 1, 2, \dots, K(\tau)$ , and reconstruct magnitudes  $q_k(t_k(\tau))$ .

**Step 1.** Define  $L \times L$  Hankel matrix

$$H_{L,\mu}(\tau) = \begin{pmatrix} \mathcal{R}_\phi(f_\mu)(\tau) & \mathcal{R}_\phi(f_{\mu+1})(\tau) & \cdots & \mathcal{R}_\phi(f_{\mu+L})(\tau) \\ \mathcal{R}_\phi(f_{\mu+1})(\tau) & \mathcal{R}_\phi(f_{\mu+2})(\tau) & \cdots & \mathcal{R}_\phi(f_{\mu+L-1})(\tau) \\ \vdots & \vdots & \ddots & \vdots \\ \mathcal{R}_\phi(f_{\mu+L-1})(\tau) & \mathcal{R}_\phi(f_{\mu+L})(\tau) & \cdots & \mathcal{R}_\phi(f_{\mu+2L-1})(\tau) \end{pmatrix}.$$

Then, from (17) and using corollary 3 in [17], we can determine  $K(\tau)$  by

$$K(\tau) = \max \{L \mid \det H_{L,0}(\tau) \neq 0\}. \quad (24)$$

**Step 2.** From the definition of  $H_{L,\mu}(\tau)$  and using Theorem 2 in [8], we can reconstruct  $p_{k,xy}(t_k(\tau))$ ,  $k = 1, 2, \dots, K(\tau)$  as eigenvalues of  $(H_{K(\tau),0}(\tau))^{-1}H_{K(\tau),1}(\tau)$ . Then, we can reconstruct the perturbed magnitudes  $q_k(t_k(\tau))\xi_k(\tau)$ ,  $k = 1, 2, \dots, K(\tau)$  as a unique solution of

$$\sum_{k=1}^K q_k(t_k(\tau))\xi_k(t_k(\tau)) \cdot (p_{k,xy}(t_k(\tau)))^n = \mathcal{R}_\phi(f_n)(\tau), \quad n = 0, 1, 2, \dots, K(\tau) - 1.$$

**Step 3.** Considering the equation (18) for  $n = 0, 1, 2, \dots, 2K(\tau) - 1$ , we can uniquely solve  $(q_k\xi_k) \cdot d_\tau(p_{k,xy})$  and  $d_\tau(q_k\xi_k)$  for  $k = 1, 2, \dots, K(\tau)$  from  $\mathcal{R}_\phi(g_n)$ ,  $n = 0, 1, 2, \dots, 2K(\tau) - 1$ . Let

$$\begin{aligned} \hat{R}_{h_n} &= \frac{1}{c} \sum_{k=1}^K \{d_\tau(q_k\xi_k) \cdot \overline{p_{k,xy}} + q_k\xi_k(\tau) \cdot d_\tau(\overline{p_{k,xy}})\} (p_{k,xy})^n \\ &\quad + \frac{n}{c} \sum_{k=1}^K q_k\xi_k \cdot d_\tau(p_{k,xy}) \cdot \overline{p_{k,xy}} \cdot (p_{k,xy})^{n-1}. \end{aligned}$$

Then we can compute  $\hat{R}_{h_n}$ , and identify  $q_k\xi_k \cdot p_{k,z}$ ,  $k = 1, 2, \dots, K(\tau)$  as a solution of the following system of linear equation:

$$(q_k\xi_k \cdot p_{k,z}) \cdot (p_{k,xy})^{n-1} = \frac{1}{2n} \left( \mathcal{R}(h_n)(\tau) - \hat{R}_{h_n} \right), \quad n = 1, 2, \dots, K(\tau). \quad (25)$$

Dividing each solution  $q_k\xi_k \cdot p_{k,z}$  of (25) by  $q_k\xi_k$ , we reconstruct  $p_{k,z}$ ,  $k = 1, 2, \dots, K(\tau)$ .

**Step 4.** Similar to Step 3, we can solve  $d_\tau^2(q_k\xi_k)$  and  $2d_\tau(q_k\xi_k) \cdot d_\tau(p_{k,xy}) + q_k\xi_k \cdot d_\tau^2(p_{k,xy})$  using the equation (20) for  $\mathcal{R}_\phi(i_n)(\tau)$ . Then, we can estimate  $q_k\xi_k \cdot d_\tau(p_{k,z})$  as a solution of the system of linear equation:

$$(q_k\xi_k \cdot d_\tau(p_{k,z})) \cdot (p_{k,xy})^{n-1} = \frac{1}{2n} \left( \mathcal{R}_\phi(j_n)(\tau) - \hat{R}_{j_n} \right), \quad n = 1, 2, \dots, K(\tau),$$

and obtain  $d_\tau(p_{k,z}(t_k(\tau)))$ ,  $k = 1, 2, \dots, K(\tau)$ .

**Step 5.** Since we have identified  $d_\tau(p_{k,z})$ , we can compute  $\xi_k(\tau)$  from (23), and reconstruct magnitude  $q_k(t_k(\tau))$  of each point source from its perturbed values  $q_k(t_k(\tau))\xi_k(\tau)$ .  $\square$

### 3.3 Reconstruction of moving dipole sources

Next, we consider the reconstruction of moving dipole sources. Here, we assume that  $\mathbf{p}_k \in C^6([0, T]; D)$ ,  $\mathbf{m}_k \in C^6([0, T]; \mathbb{R}^3)$  and  $\mathbf{m}_k(0) = \mathbf{d}_t \mathbf{m}_k(0) = \mathbf{d}_t^2 \mathbf{m}_k(0) = \cdots = \mathbf{d}_t^6 \mathbf{m}_k(0) = \mathbf{0}$ , then the observation data is in  $H^4([0, T] \times \Gamma) \subset C^2([0, T] \times \Gamma)$ . In addition, we assume that  $m_{z,k}(t) \equiv 0$  for all  $k$ . For the reconstruction of moving dipole sources, we use the same five sequences of functions  $\{f_{n,\varepsilon}\}, \{g_{n,\varepsilon}\}, \cdots, \{j_{n,\varepsilon}\}$  as for the reconstruction of moving point sources. The explicit expression of  $\mathcal{F}(f_n), \mathcal{F}(g_n), \cdots, \mathcal{F}(i_n)$  for moving dipole sources are given as follows:

$$\mathcal{F}(f_n)(\tau) = n \sum_{k=1}^K m_{k,xy} \xi_k \cdot (p_{k,xy})^{n-1}, \quad n = 1, 2, \cdots, \quad (26)$$

$$\begin{aligned} \mathcal{F}(g_n)(\tau) = & n \sum_{k=1}^K \mathbf{d}_\tau(m_{k,xy} \xi_k) \cdot (p_{k,xy})^{n-1} \\ & + n(n-1) \sum_{k=1}^K m_{k,xy} \xi_k \cdot \mathbf{d}_\tau(p_{k,xy}) \cdot (p_{k,xy})^{n-2}, \quad n = 1, 2, \cdots, \end{aligned} \quad (27)$$

$$\begin{aligned} \mathcal{F}(h_n)(\tau) = & 2n(n-1) \sum_{k=1}^K m_{k,xy} \xi_k \cdot p_{k,z} \cdot (p_{k,xy})^{n-2} \\ & + \frac{1}{c} \sum_{k=1}^K \mathbf{d}_\tau(\overline{m_{k,xy}} \xi_k) \cdot (p_{k,xy})^n \\ & + \frac{n}{c} \sum_{k=1}^K \{ \mathbf{d}_\tau(m_{k,xy} \xi_k) \cdot \overline{p_{k,xy}} + \overline{m_{k,xy}} \xi_k \cdot \mathbf{d}_\tau(p_{k,xy}) + m_{k,xy} \xi_k \cdot \mathbf{d}_\tau(\overline{p_{k,xy}}) \} (p_{k,xy})^{n-1} \\ & + \frac{n(n-1)}{c} \sum_{k=1}^K m_{k,xy} \xi_k \cdot \mathbf{d}_\tau(p_{k,xy}) \cdot \overline{p_{k,xy}} \cdot (p_{k,xy})^{n-2}, \quad n = 2, 3, \cdots, \end{aligned} \quad (28)$$

$$\begin{aligned} \mathcal{F}(i_n)(\tau) = & n \sum_{k=1}^K \mathbf{d}_\tau^2(m_{k,xy} \xi_k) \cdot (p_{k,xy})^{n-1} \\ & + n(n-1) \sum_{k=1}^K \{ 2\mathbf{d}_\tau(m_{k,xy} \xi_k) \cdot \mathbf{d}_\tau(p_{k,xy}) + m_{k,xy} \xi_k \cdot \mathbf{d}_\tau^2(p_{k,xy}) \} (p_{k,xy})^{n-2} \\ & + n(n-1)(n-2) \sum_{k=1}^K m_{k,xy} \xi_k \cdot (\mathbf{d}_\tau(p_{k,xy}))^2 \cdot (p_{k,xy})^{n-3}, \quad n = 1, 2, \cdots, \end{aligned} \quad (29)$$

$$\mathcal{F}(j_n)(\tau) = 2n(n-1) \sum_{k=1}^K m_{k,xy} \xi_k \cdot \mathbf{d}_\tau(p_{k,z}) \cdot (p_{k,xy})^{n-2} + \hat{R}_{j_n}, \quad n = 2, 3, \cdots, \quad (30)$$

where

- $m_{k,xy} \equiv m_{k,x}(t_k(\tau)) + im_{k,y}(t_k(\tau))$ ,

- $\hat{R}_{j_n}$  is expressed by

$$\begin{aligned}
\hat{R}_{j_n} = & 2n(n-1) \sum_{k=1}^K \{d_\tau(m_{k,xy}\xi_k) \cdot p_{k,xy} + (n-2)m_{k,xy}\xi_k \cdot d_\tau(p_{k,xy})\} \cdot p_{k,z} \cdot (p_{k,xy})^{n-3} \\
& + \frac{1}{c} \sum_{k=1}^K d_\tau^2(\overline{m_{k,xy}\xi_k}) \cdot (p_{k,xy})^n + \frac{n}{c} \sum_{k=1}^K d_\tau^2(m_{k,xy}\xi_k) \cdot \overline{p_{k,xy}} \cdot (p_{k,xy})^{n-1} \\
& + \frac{n}{c} \sum_{k=1}^K \{2d_\tau(\overline{m_{k,xy}\xi_k}) \cdot d_\tau(p_{k,xy}) + \overline{m_{k,xy}\xi_k} \cdot d_\tau^2(p_{k,xy})\} \cdot (p_{k,xy})^{n-1} \\
& + \frac{n}{c} \sum_{k=1}^K \{2d_\tau(m_{k,xy}\xi_k) \cdot d_\tau(\overline{p_{k,xy}}) + m_{k,xy}\xi_k \cdot d_\tau^2(\overline{p_{k,xy}})\} \cdot (p_{k,xy})^{n-1} \\
& + \frac{n(n-1)}{c} \sum_{k=1}^K \overline{m_{k,xy}\xi} \cdot (d_\tau(p_{k,xy}))^2 \cdot (p_{k,xy})^{n-2} \\
& + \frac{n(n-1)}{c} \sum_{k=1}^K \{2d_\tau(m_{k,xy}\xi_k) \cdot d_\tau(p_{k,xy}) + m_{k,xy}\xi_k \cdot d_\tau^2(p_{k,xy})\} \cdot \overline{p_{k,xy}} \cdot (p_{k,xy})^{n-2} \\
& + \frac{n(n-1)}{c} \sum_{k=1}^K 2m_{k,xy}\xi_k \cdot d_\tau(\overline{p_{k,xy}}) \cdot d_\tau(p_{k,xy}) \cdot (p_{k,xy})^{n-2} \\
& + \frac{n(n-1)(n-2)}{c} \sum_{k=1}^K m_{k,xy}\xi_k \cdot \overline{p_{k,xy}} \cdot (d_\tau(p_{k,xy}))^2 \cdot (p_{k,xy})^{n-3}.
\end{aligned}$$

As we have already shown for moving point sources, we can establish the following reconstruction theorem for moving dipole sources:

**THEOREM 3.2.** *For each  $\tau$ , let  $K(\tau)$  be the number of dipole sources such that  $\mathbf{m}_k(t_k(\tau)) \neq \mathbf{0}$ . Assume that  $K(\tau) \leq K_M$  for some  $K_M > 0$ , and  $p_{j,xy}(t_j(\tau)) \neq p_{k,xy}(t_k(\tau))$  if  $j \neq k$ . Then, we can determine  $K(\tau)$  from the reciprocity gap functionals  $\mathcal{R}_\phi(f_n)(\tau)$ ,  $n = 1, 2, \dots, 2K_M + 2$ . Also we can uniquely reconstruct  $\mathbf{p}_k(t_k(\tau))$  and  $\mathbf{m}_k(t_k(\tau))$  for  $k = 1, 2, \dots, K(\tau)$  from*

- $\mathcal{R}(f_n)(\tau)$ ,  $n = 1, 2, \dots, 2K(\tau) + 1$ ,
- $\mathcal{R}(g_n)(\tau)$ ,  $n = 1, 2, \dots, 2K(\tau)$ ,
- $\mathcal{R}(h_n)(\tau)$ ,  $n = 2, \dots, K(\tau) + 1$ ,
- $\mathcal{R}(i_n)(\tau)$ ,  $n = 1, 2, \dots, 2K(\tau)$ ,
- $\mathcal{R}(j_n)(\tau)$ ,  $n = 2, \dots, K(\tau) + 1$ .

We can prove Theorem 3.2 using similar steps in Theorem 3.1, but we omit it here.

## 4 Numerical Experiments

We give some numerical experiments for the reconstruction method proposed in the previous section. We consider the case that two point sources move in the domain  $\Omega = \{\mathbf{r} \mid |\mathbf{r}| = 1\}$ , and the wave propagation speed  $c = 1$ . Each point source moves as following, and the orbit of each point source is shown in Figure 1.

**Point source 1:** Moves on a circle vertical with respect to  $xy$ -plane.



**Point source 2:** Moves on a circle horizontal with respect to  $xy$ -plane.

In our experiments, moving speed of both point sources are constant, i.e.  $\frac{|p'_k(t)|}{c} = 35\%$ ,  $k = 1, 2$ . Magnitude of each point source changes in time as shown in Figure 2. To give the observation data, we solve (1) by boundary integral equation method, and give observation data on 384 points on  $\Gamma$  with time step  $\Delta t = 0.1$ . To simulate practical observation condition, we add 0.0%, 1.0%, and 5.0% random noise to observation data.

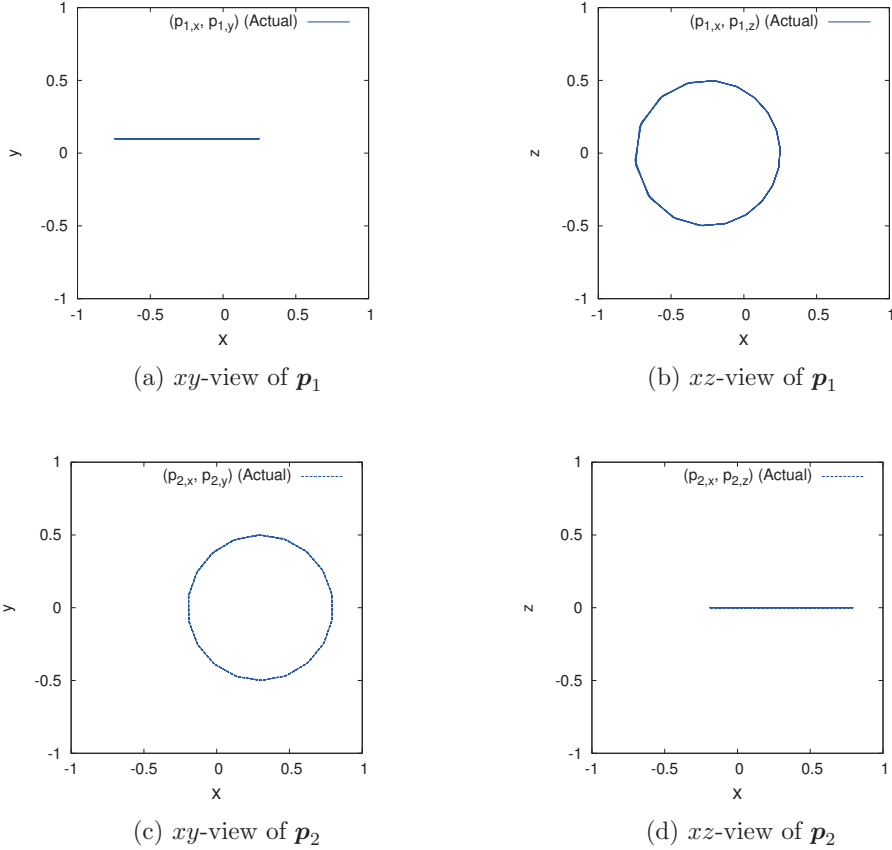


Figure 1: The orbit of each point source.

Figures 3 and 4 show the reconstruction result for noise-free case. Figure 3 gives the reconstructed orbits of point sources, and Figure 4 displays the time-profiles of location and magnitude of each reconstructed point source. From these reconstruction results, we may consider that our method gives good estimates for both locations and magnitudes under noise free observation condition.

Next, we show reconstruction results for noisy observation cases. Figures 5 and 7 show the reconstruction results of orbits, and Figures 6 and 8 display the time-profiles of estimated locations, and magnitudes for observations with 1.0%, and 5.0% noise cases, respectively. From these reconstruction results, we consider that our method gives reliable estimates for both locations and magnitudes in the case where noise is 1%, but observation noise becomes 5%, the estimates become unreliable, especially, for magnitudes of point sources.

To avoid the bad effect of noise, we apply 5 points Gaussian filter with respect to  $t$  to

observation data  $\phi$ . Figure 9 shows the reconstruction results of orbits of point sources, and Figure 10 displays the time-profiles of estimated locations, and magnitudes of point sources. From these results, we can see that the filtering process is effective to remove noise effect on the reconstruction results.

## 5 Conclusions

In this report, we discuss a reconstruction of moving point and dipole sources in three dimensional scalar wave equation. We propose a real-time algebraic procedure for unknown parameters of moving point and dipole sources. We examine proposed method by some numerical experiments. Numerical results shows that our method gives good estimates of parameters of moving point sources in the case where the noise is smaller than 1%. However reconstruction results become unreliable if the observation noise is larger than 5%, and we need filtering process to observation data to obtain better reconstruction results.

### Acknowledgments

The author thanks to the discussions at 2017 IMI Joint Use Research Program Workshop (II) "Practical inverse problems based on interdisciplinary and industry-academia collaboration". This work was supported in part by A3 Foresight Program "Modeling and Computation of Applied Inverse Problems" and Grant-in-Aid for Scientific Research (S) 15H05740 of Japan Society for the Promotion of Science.

## References

- [1] Athanasiadis, C.E. et al., An application of the reciprocity gap functional to inverse mixed impedance problems in elasticity, *Inverse Problems*, **26**(2010), 085011 (19pp).
- [2] Ando, S., Nara, T. and Levy, T., Partial differential equation-based localization of a monopole source from a circular array, *J. Acoust. Soc. Am.*, **134**(2013), No.4, 2799–2813.
- [3] Andrieux, S. and Ben Abda, A., Identification of planar cracks by complete overdetermined data: inversion formulae, *Inverse Problems*, **12**(1996), No.5, 553–563.
- [4] Anikonov, Y.E., Bubnov, B.A. and Erokhin, G.N., *Inverse and Ill-Posed Source Problems*(Utrecht: VSP) (1997).
- [5] Bruckner, G. and Yamamoto, M., Determination of point wave sources by pointwise observations: stability and reconstruction, *Inverse Problems*, **16**(2000) 723–48.
- [6] Chung, Y-S. and Chung, S-Y., Identification of the combination of monopolar and dipolar sources for elliptic equations, *Inverse Problems*, **25**(2009), 085006 (16pp).
- [7] Colton, D. and Haddar, H., An application of the reciprocity gap functional to inverse scattering theory, *Inverse Problems*, **21**(2005), 383–398.
- [8] El Badia, A. and Ha-Duong, T., An inverse source problem in potential analysis, *Inverse Problems*, **16**(2000), 651–663.
- [9] El Badia, A. and Ha-Duong, T., Determination of point wave sources by boundary measurements, *Inverse Problems*, **17**(2001) 1127–1139.
- [10] Evans, L.C., *Partial Differential Equations (2nd ed)*, Graduate Studies in Mathematics **19** (Rhode Island: American Mathematical Society)(2010)

- [11] Haddar, H. and Mdimagh, R., Identification of small inclusions from multistatic data using the reciprocity gap concept, *Inverse Problems*, **28**(2012) 045011 (19pp).
- [12] Isakov, V., *Inverse Problems for Partial Differential Equations* (New York: Springer-Verlag) (1998).
- [13] Komornik, V. and Yamamoto, M., Estimation of point sources and applications to inverse problems, *Inverse Problems*, **21**(2005) 2051–70.
- [14] Lasićka, I., Lions, J-L., and Triggiani, R., Non homogeneous boundary value problems for second order hyperbolic operators, *J. Math. pures et apple.*, **65**(1986) 149–192
- [15] Ling, L. and Takeuchi, T., Point source identification problems for heat equations, *Commun. Comput. Phys*, **5**(2009), No. 5, 897–913.
- [16] Nakaguchi, E., Inui, H. and Ohnaka, K., An algebraic reconstruction of a moving point source for a scalar wave equation, *Inverse Problems*, **28**(2012), 065018 (21pp).
- [17] Nara, T. and Ando, S., A projective method for an inverse source problem of the Poisson equation, *Inverse Problems*, **19**(2003), 355–369.
- [18] Ohe, T., Inui, H. and Ohnaka, K., Real-time reconstruction of time-varying point sources in a three-dimensional scalar wave equation, *Inverse Problems*, **27**(2011), 115011 (19pp).
- [19] Ohe, T., Reconstruction of slowly-moving dipole wave sources from boundary observations, *Mathematical Backgrounds and Future Progress of Practical Inverse Problems* (eds. Takiguchi, T. and Fujiwara H.), Mathematics for Industry Research, **5**(2016), 27–53.
- [20] Rashedi, K. and Sini M., Stable recovery of the time-dependent source term from one measurement for the wave equation, *Inverse Problems*, **31**(2015), 105011 (17pp).
- [21] Wang, J.H. and Lee, P.L., Determination of the acoustic position vector of a moving sound source with constant acceleration motion, *Eng. Anal. Bound. Elem.*, **33**(2009), 1141–1144

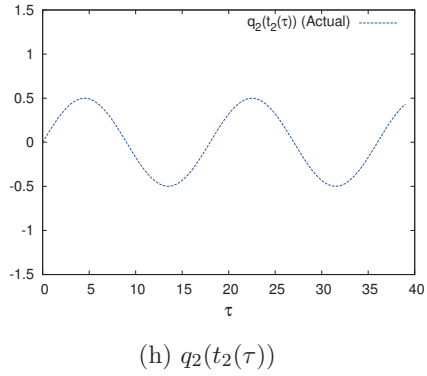
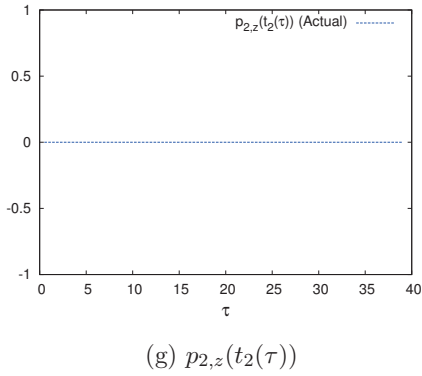
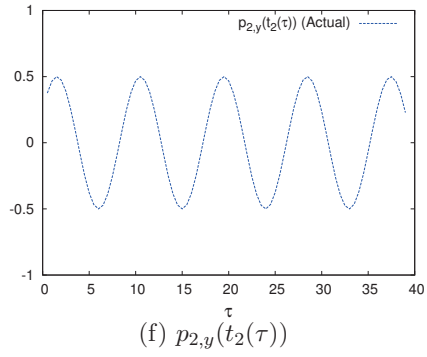
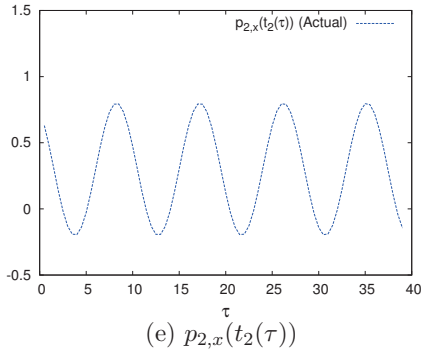
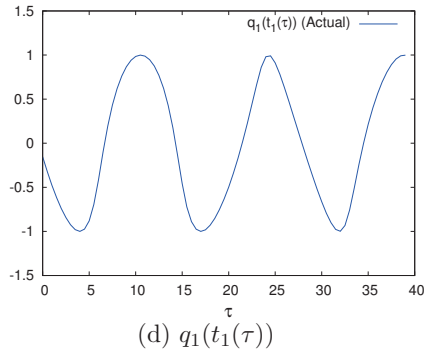
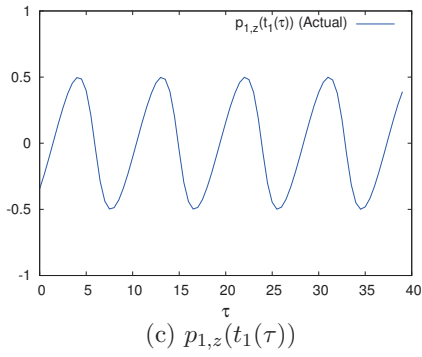
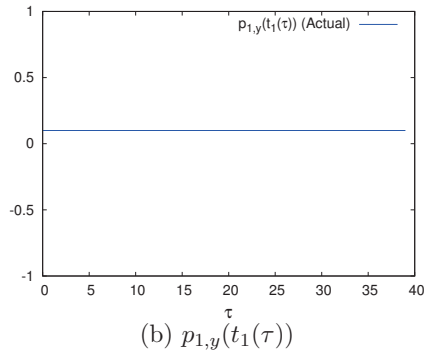
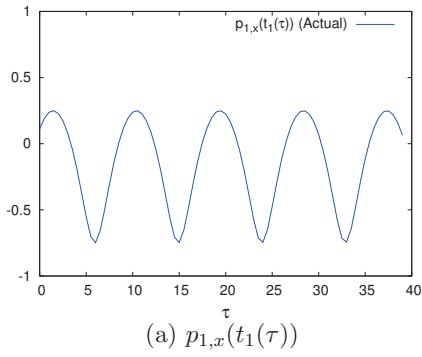
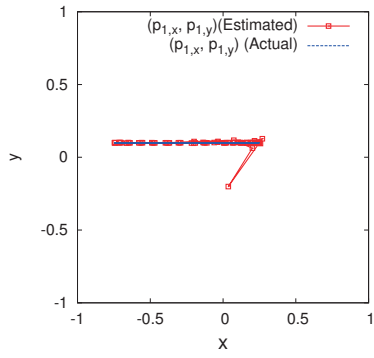
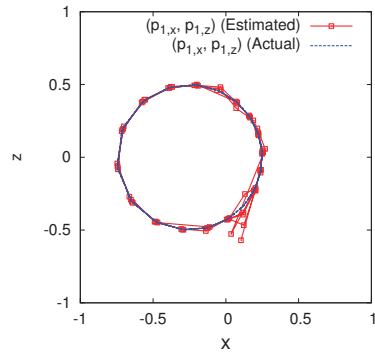


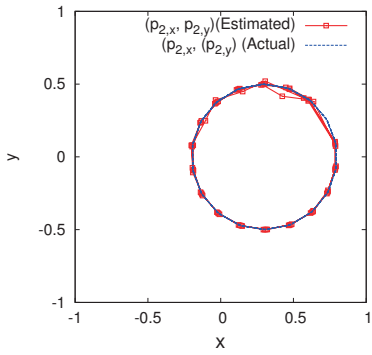
Figure 2: Time-profiles of locations and magnitudes of point sources.



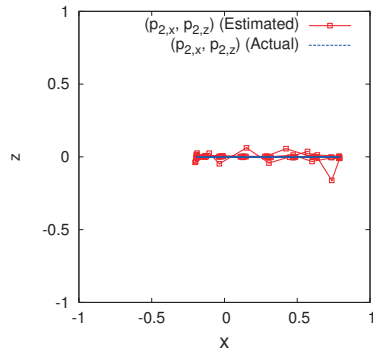
(a)  $xy$ -view of  $p_1$



(b)  $xz$ -view of  $p_1$



(c)  $xy$ -view of  $p_2$



(d)  $xz$ -view of  $p_2$

Figure 3: Reconstructed orbits of point sources for noise free case.

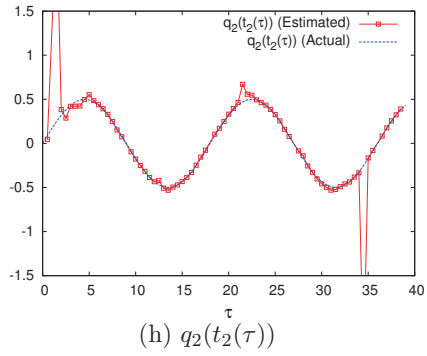
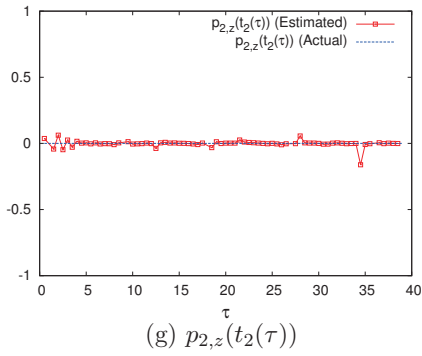
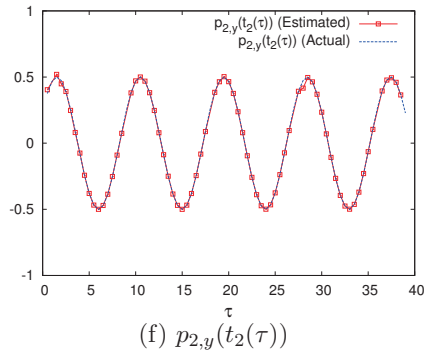
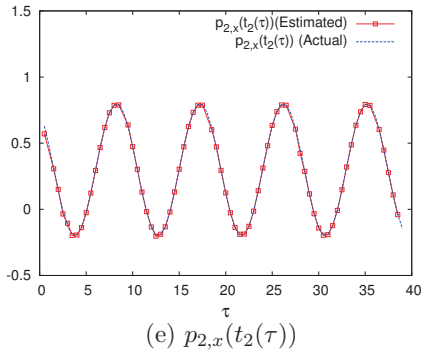
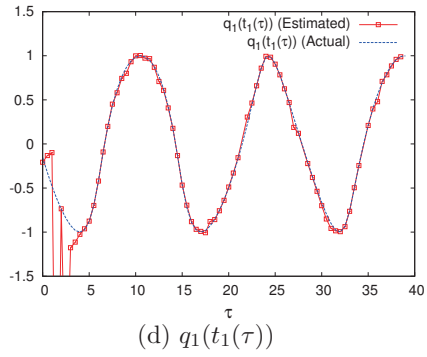
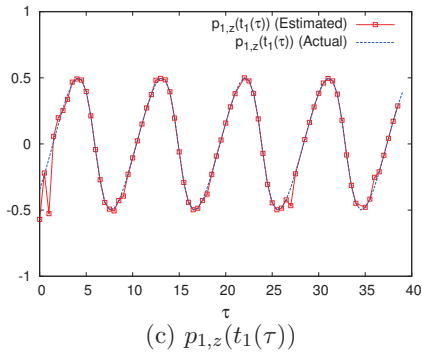
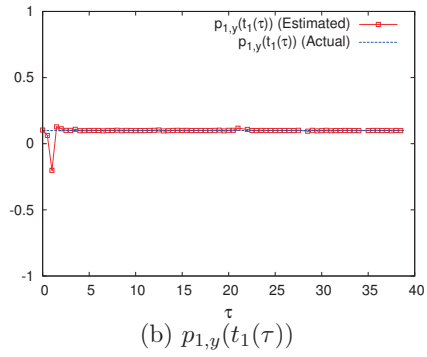
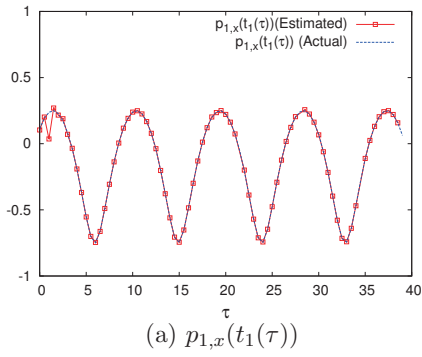


Figure 4: Time-profiles of estimated locations and magnitudes of point sources for noise free case.

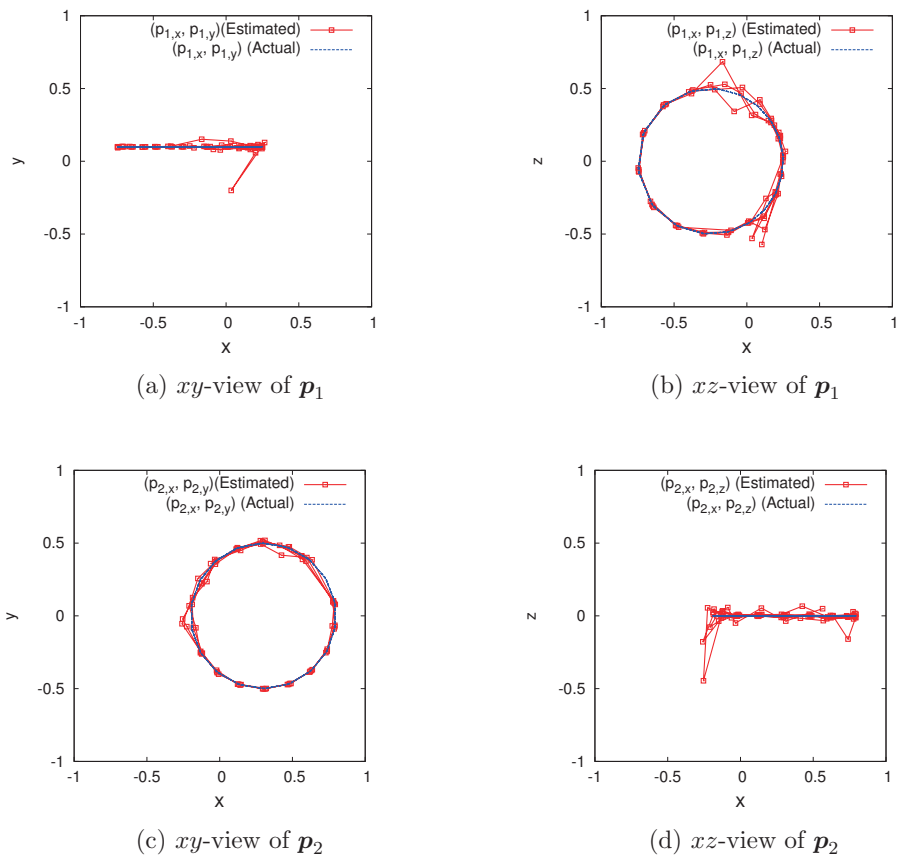
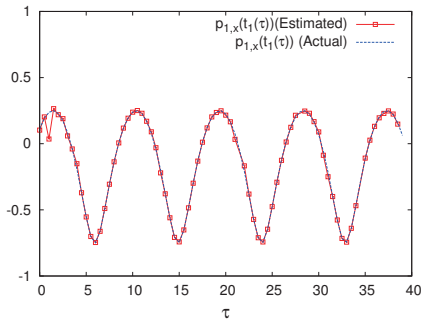
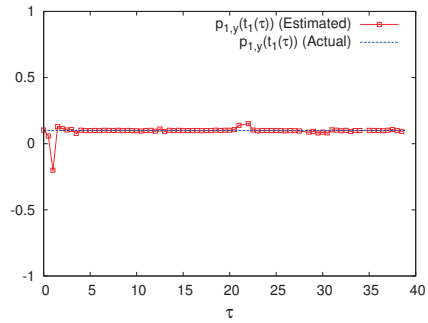


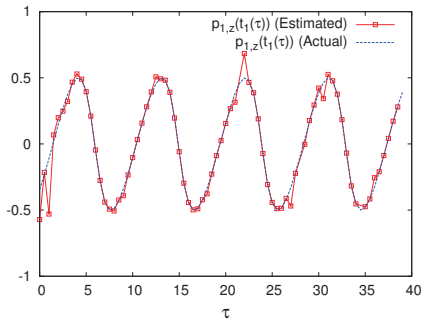
Figure 5: Estimated orbits of point sources for 1% noisy observation case.



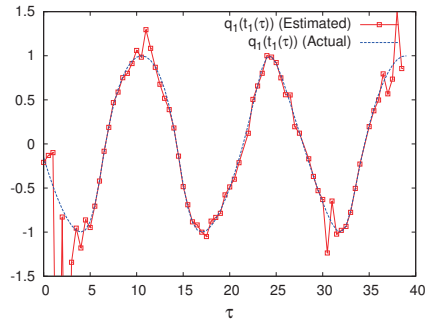
(a)  $p_{1,x}(t_1(\tau))$



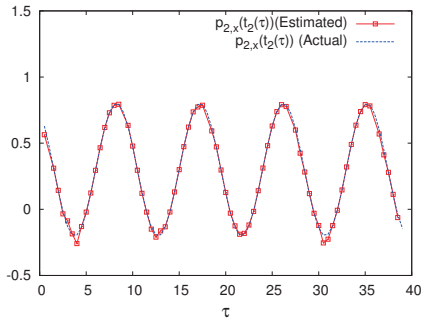
(b)  $p_{1,y}(t_1(\tau))$



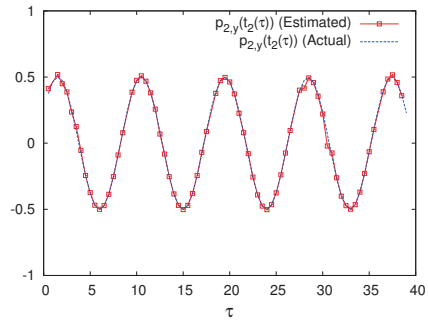
(c)  $p_{1,z}(t_1(\tau))$



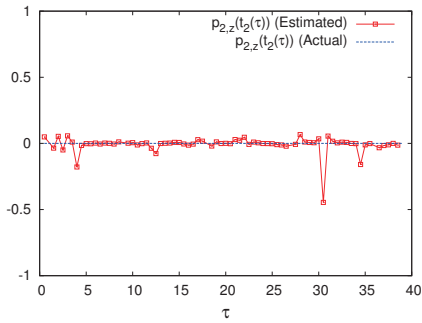
(d)  $q_1(t_1(\tau))$



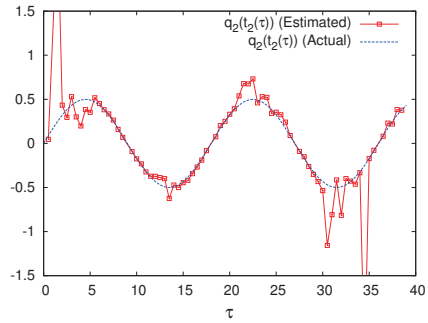
(e)  $p_{2,x}(t_2(\tau))$



(f)  $p_{2,y}(t_2(\tau))$



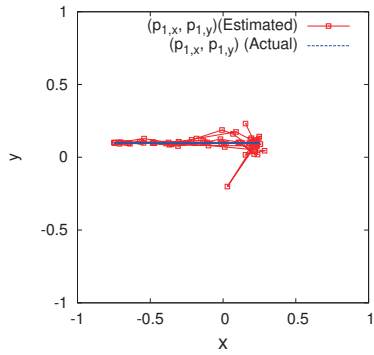
(g)  $p_{2,z}(t_2(\tau))$



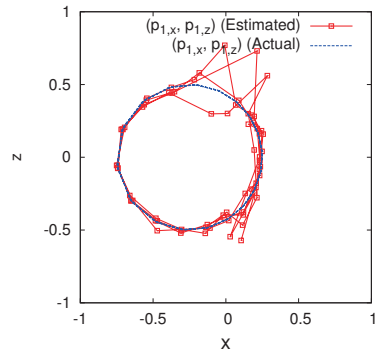
(h)  $q_2(t_2(\tau))$

Figure 6: Time-profiles of estimated locations and magnitudes of point sources for 1% noisy observation case.

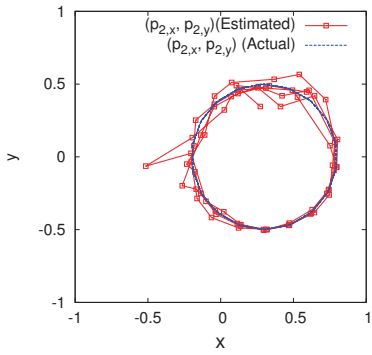




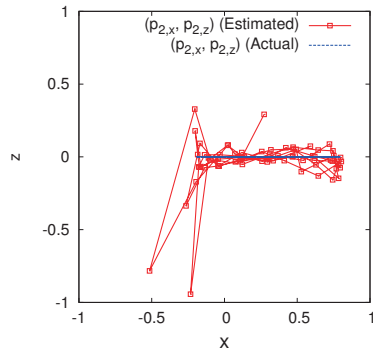
(a)  $xy$ -view of  $p_1$



(b)  $xz$ -view of  $p_1$



(c)  $xy$ -view of  $p_2$



(d)  $xz$ -view of  $p_2$

Figure 7: Estimated orbits of point sources for 5% noisy observation case.

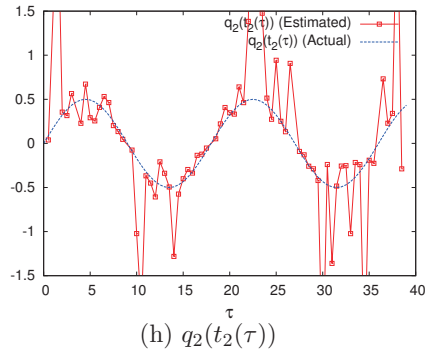
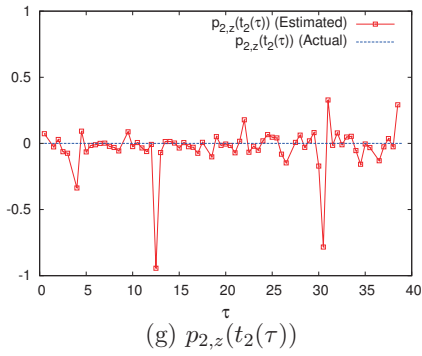
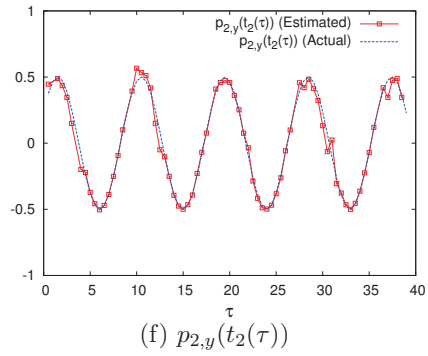
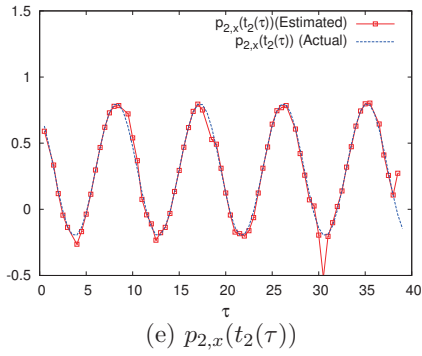
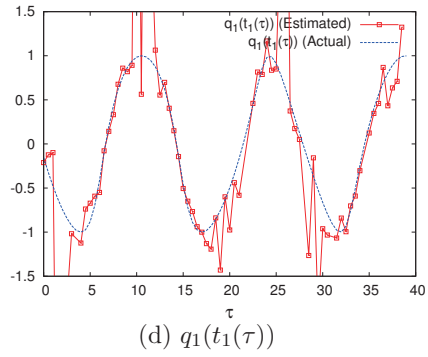
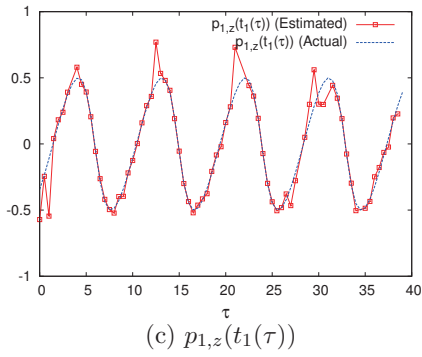
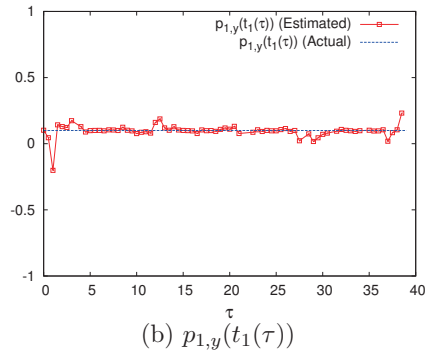
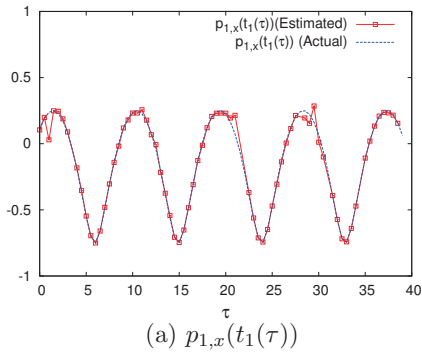


Figure 8: Time-profiles of estimated locations and magnitudes of point sources for 5% noisy observation case.

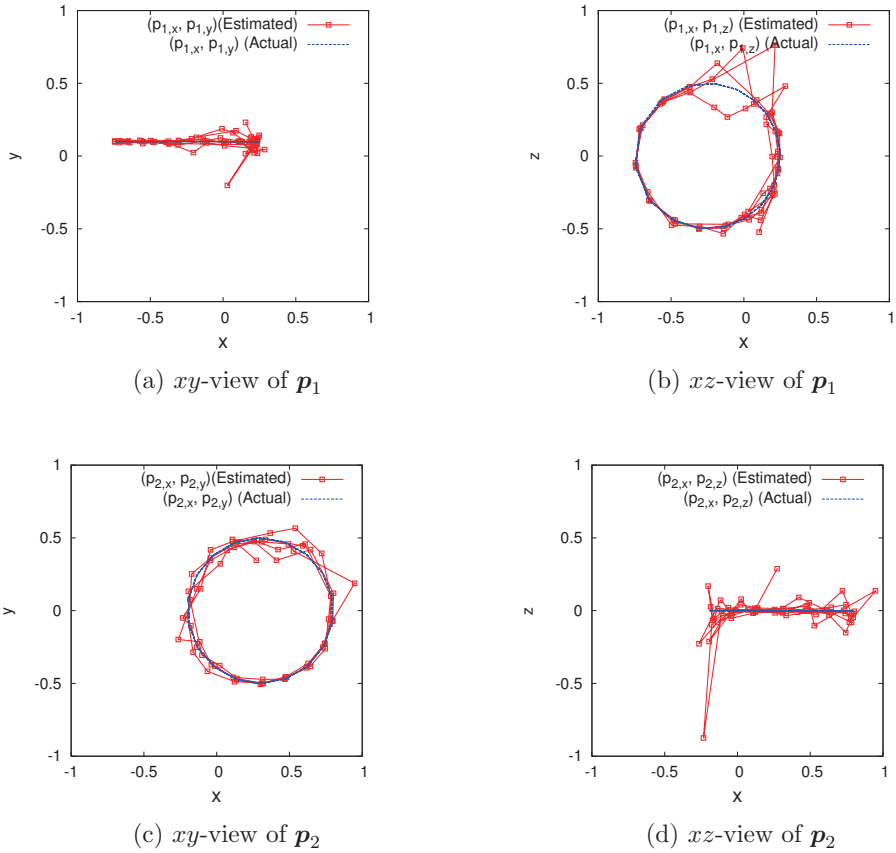
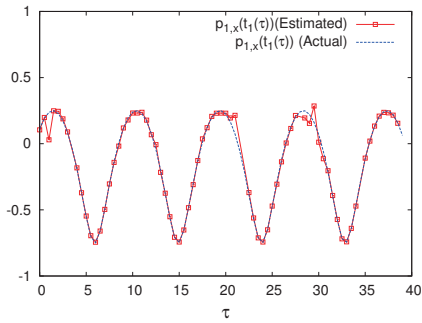
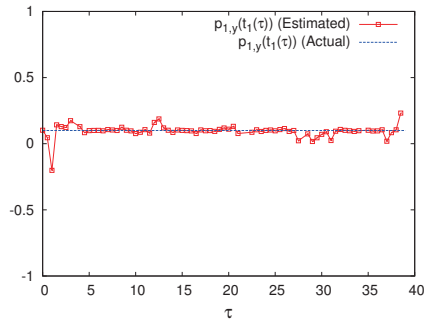


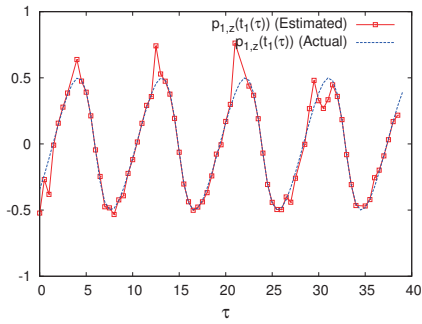
Figure 9: Estimated orbits of point sources for 5% noisy observation case with filtering process to observation data.



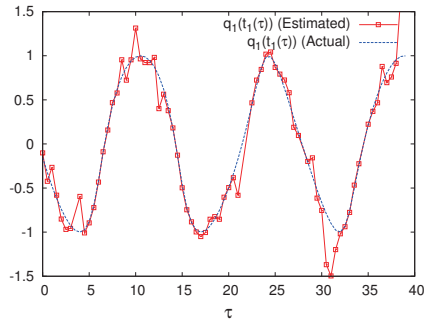
(a)  $p_{1,x}(t_1(\tau))$



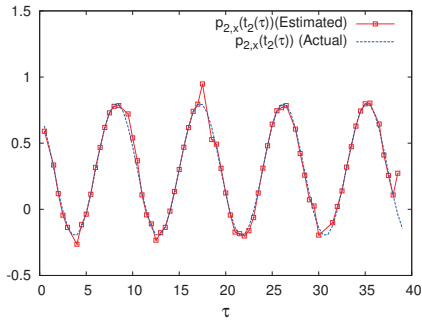
(b)  $p_{1,y}(t_1(\tau))$



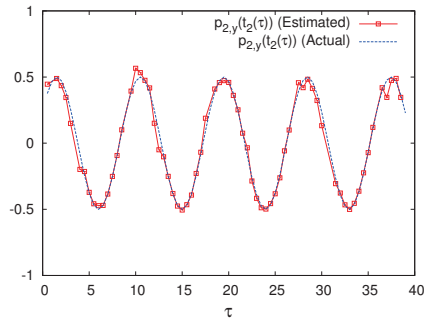
(c)  $p_{1,z}(t_1(\tau))$



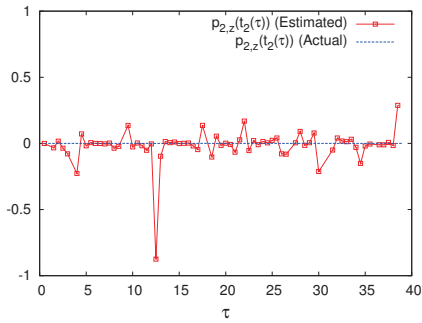
(d)  $q_1(t_1(\tau))$



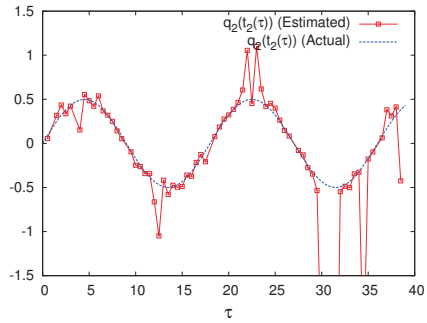
(e)  $p_{2,x}(t_2(\tau))$



(f)  $p_{2,y}(t_2(\tau))$



(g)  $p_{2,z}(t_2(\tau))$



(h)  $q_2(t_2(\tau))$

Figure 10: Time-profiles of estimated locations and magnitudes of point sources for 5% noisy observation case with filtering process to observation data.

# Identification of moving wave sources from boundary measurements

Takashi OHE

Okayama University of Science, JAPAN

IMI conference on  
Practical inverse problems based on interdisciplinary and  
industry-academia collaboration  
October 26th, 2017

1 / 92

## Table of contents

- 1 Problem formulation
- 2 Known results
- 3 Regularity results for observation data
- 4 Key idea of the identification scheme : Reciprocity gap functional
- 5 Reconstruction of moving point sources
- 6 Reconstruction scheme for moving dipole sources
- 7 Numerical experiments
- 8 Conclusions

2 / 92

# Estimation of wave source

- **Applications**

- Estimation of seismic source
- Estimation of acoustic source (passive sonar)
- Estimation of action of brain (electromagnetic source)
- ...

- **Mathematical formulation**

- inverse source problem for wave equation

3 / 92

## 1 Problem formulation

4 / 92

## Inverse source problem for scalar wave equations

- $\Omega$  : bounded domain in  $\mathbb{R}^3$ , simply connected.
- $\Gamma = \partial\Omega$  : the boundary of  $\Omega$  ( $C^\infty$ -class)
- $F(t, \mathbf{r})$  : the source term (unknown)
- $u(t, \mathbf{r})$  : The solution of initial-value-boundary-value problem

$$(E) \begin{cases} \frac{1}{c^2} \partial_t^2 u(t, \mathbf{r}) - \Delta u(t, \mathbf{r}) = F(t, \mathbf{r}), & (t, \mathbf{r}) \in (0, T) \times \Omega, \\ u(t, \mathbf{r}) = 0, & (t, \mathbf{r}) \in (0, T) \times \Gamma, \\ u(0, \mathbf{r}) = 0, & \mathbf{r} \in \Omega, \\ \partial_t u(0, \mathbf{r}) = 0, & \mathbf{r} \in \Omega, \end{cases}$$

( $c > 0, T > 0$ : given constants)

5 / 92

## Model of unknown source 1: point sources model

$$F(t, \mathbf{r}) = \sum_{k=1}^K q_k(t) \delta(\mathbf{r} - \mathbf{p}_k(t))$$

- $K$  : number of sources (unknown)
- $\mathbf{p}_k(t) \in C^6([0, T]; D)$  : location of  $k$ -th source (unknown)  
 $|\dot{\mathbf{p}}_k(t)| < c$  ( $D \subset \Omega$ : compact)
- $q_k(t) \in C^5([0, T]; \mathbb{R})$  : magnitude of  $k$ -th source (unknown)  
 $q_k(0) = \dot{q}_k(0) = \dots = q_k^{(5)}(0) = 0$

(Continuity conditions for  $\mathbf{p}_k$  and  $q_k$  are given for sufficient regularity on observation data)

6 / 92

# Model of unknown source 2: dipole sources model

$$F(t, \mathbf{r}) = - \sum_{k=1}^K \mathbf{m}_k(t) \cdot \nabla \delta(\mathbf{r} - \mathbf{p}_k(t))$$

- $K$  : number of sources (**unknown**)
- $\mathbf{p}_k(t) \in C^6([0, T]; D)$  : location of  $k$ -th source (**unknown**)  
 $|\dot{\mathbf{p}}_k(t)| < c$  ( $D \subset \Omega$ : compact)
- $\mathbf{m}_k(t) \in C^6([0, T]; \mathbb{R}^3)$  : moment of  $k$ -th source (**unknown**)  
 $\mathbf{m}_k(0) = \dot{\mathbf{m}}_k(0) = \dots = \mathbf{m}_k^{(6)}(0) = \mathbf{0}$

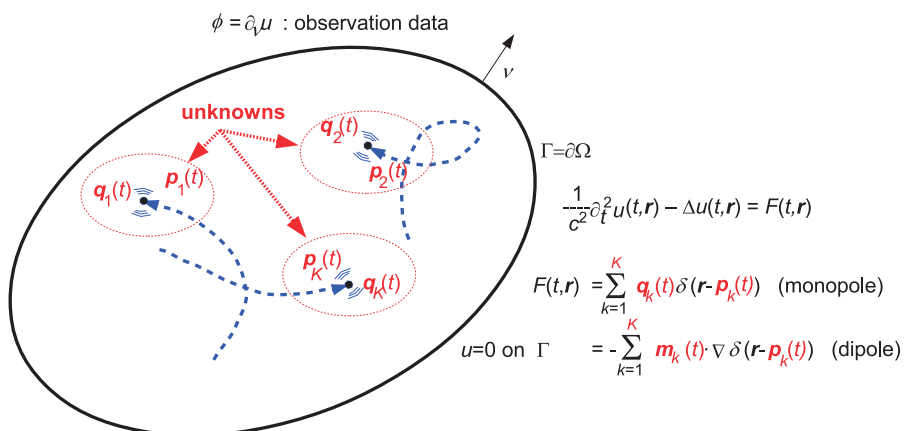
(Continuity Conditions for  $\mathbf{p}_k$  and  $\mathbf{m}_k$  are given for sufficient regularity on observation data)

7 / 92

## Problem

Given information  $\phi$  : the normal derivative  $\partial_\nu u$  on  $(0, T) \times \Gamma$ .

Reconstruct  $K$ ,  $\mathbf{p}_k(t)$ , and  $q_k(t)$  (for point sources)  
 or  $\mathbf{m}_k(t)$  (for dipole sources)



8 / 92



In both cases, we consider the solution  $u$  in a weak sense, i.e.  $u \in C^1([0, T]; L^2(\Omega))$  satisfies that  $\partial_\nu u \in C([0, T]; L^2(\Gamma))$  and

$$\begin{aligned} & \frac{1}{c^2} \int_{\Omega} \partial_t u(T, \mathbf{r}) v(T, \mathbf{r}) dV(\mathbf{r}) - \frac{1}{c^2} \int_{\Omega} u(T, \mathbf{r}) \partial_t v(T, \mathbf{r}) dV(\mathbf{r}) \\ & - \int_0^T \int_{\Gamma} \partial_\nu u(t, \mathbf{r}) v(t, \mathbf{r}) dS(\mathbf{r}) dt \\ & + \int_0^T \int_{\Omega} u(t, \mathbf{r}) \left( \frac{1}{c^2} \partial_t^2 v(t, \mathbf{r}) - \Delta v(t, \mathbf{r}) \right) dV(\mathbf{r}) dt \\ = & \mathcal{F}(v) \quad \text{for any } v \in C^\infty([0, T] \times \bar{\Omega}) \end{aligned}$$

where

$$\mathcal{F}(v) = \begin{cases} \sum_{k=1}^K \int_0^T q_k(t) v(t, \mathbf{p}_k(t)) dt & \text{point sources} \\ \sum_{k=1}^K \int_0^T \mathbf{m}_k(t) \cdot \nabla v(t, \mathbf{p}_k(t)) dt & \text{dipole sources} \end{cases}$$

## 2 Known results

## Known results for ISP for wave equations (Theoretical, summary)

- El Badia & Ha Duong (2001) ... uniqueness of fixed point sources, algebraic approach.
- Komornik & Yamamoto (2005) ... uniqueness and stability of fixed point sources with same magnitudes, analytic approach.
- As long as I know, no result is presented for uniqueness of the solution for **moving** point sources (and dipoles). (Also for stability)

11 / 92

## Known results for ISP for wave equations (Numerical, summary)

- Ohnaka (1991) ... one or two fixed point sources, 2 dimensional space, optimization method.
- El Badia & Ha Duong (2001) ... **multiple fixed point** sources, algebraic method.
- Ohe, Inui & Ohnaka (2011) ... **multiple fixed point** sources, **real-time** algebraic method.
- Nakaguchi, Inui & Ohnaka (2011) ... moving **single** point source, algebraic method.
- Ando, Nara & Levy(2013) ... **fixed, single** point source, algebraic method.

12 / 92

## Problems in known results

- In El Badia-Ha Duong (2001), they applied the Fourier in the time domain. Therefore, they can not estimate unknown sources instantaneously.
- Using the method in Ohe-Inui-Ohnaka (2011), one can estimate parameters of point sources in a small delay if the locations of point sources are fixed. However, if point sources move fast, estimation results are perturbed by moving speeds of point sources.

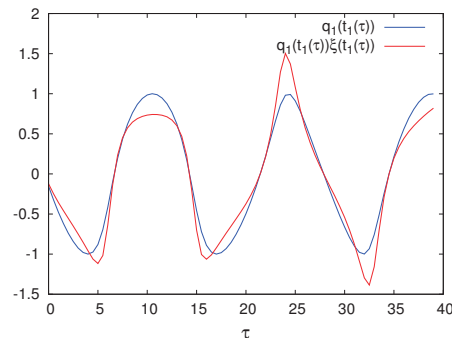


Fig. An example of effect of the moving-speed of sources ( $|\dot{p}_{k,z}/c| = 35\%$ ).

13 / 92

## Target

- In the previous conference in 2015, we extend Ohe-Inui-Ohnaka(IP, 2011) to **slowly-moving** ( $|\dot{p}_k(t)|/c \ll 1$ ) multiple moving point sources.
- Our target: Extend Ohe-Inui-Ohnaka(IP, 2011) to **multiple moving (not slowly!) point and/or dipole** sources.

14 / 92

### 3 Regularity results for observation data

15 / 92

## Regularity results for observation data $\phi = \partial_\nu u$

### Proposition 1 (for point sources)

Let  $\ell$  be a non-negative integer. For moving point sources model, assume that  $\mathbf{p}_k \in C^{\ell+2}([0, T]; D)$ ,  $q_k \in C^{\ell+1}([0, T]; \mathbb{R})$ . Also assume that  $|\dot{\mathbf{p}}_k(t)| < c$  and  $q^{(m)}(0) = 0$  for  $m = 0, 1, 2, \dots, \ell + 1$ . Then, the solution  $u$  of (E) satisfies  $u \in ([0, T]; L^2(\Omega))$ . More specifically, the restriction of  $u$  on  $\Omega \setminus D$  satisfies

$$\begin{aligned} u|_{[0, T] \times \Omega \setminus D} &\in C([0, T]; H^{\ell+1}(\Omega \setminus D)) \\ \nabla u|_{[0, T] \times \Omega \setminus D} &\in C([0, T]; H^\ell(\Omega \setminus D)) \\ \nabla \partial_t^m u|_{[0, T] \times \Omega \setminus D} &\in C([0, T]; H^{\ell-m}(\Omega \setminus D)), \quad 0 \leq m \leq \ell \end{aligned}$$

and the normal derivative on  $\Gamma$  satisfies

$$\partial_\nu u \in H^\ell(\Sigma). \quad (\Sigma = (0, T) \times \Gamma)$$

16 / 92

## Regularity results for observation data $\phi = \partial_\nu u$

### Proposition 2 (for dipole sources)

Let  $\ell$  be a non-negative integer. For moving dipole sources model, assume that  $\mathbf{p}_k \in C^{\ell+2}([0, T]; D)$ ,  $\mathbf{m}_k \in C^{\ell+2}([0, T]; \mathbb{R})$ . Also assume that  $|\dot{\mathbf{p}}_k(t)| < c$  and  $q^{(m)}(0) = 0$  for  $m = 0, 1, 2, \dots, \ell + 2$ . Then, the solution  $u$  of (E) satisfies  $u \in ([0, T]; H^{-1}(\Omega))$ . More specifically, the restriction of  $u$  on  $\Omega \setminus D$  satisfies

$$\begin{aligned} u|_{[0, T] \times \Omega \setminus D} &\in C([0, T]; H^{\ell+1}(\Omega \setminus D)) \\ \nabla u|_{[0, T] \times \Omega \setminus D} &\in C([0, T]; H^\ell(\Omega \setminus D)) \\ \nabla \partial_t^m u|_{[0, T] \times \Omega \setminus D} &\in C([0, T]; H^{\ell-m}(\Omega \setminus D)), \quad 0 \leq m \leq \ell \end{aligned}$$

and the normal derivative on  $\Gamma$  satisfies

$$\partial_\nu u \in H^\ell(\Sigma).$$

17 / 92

## Proof of Proposition 1

- Divide  $u$  into  $u = u_p + u_h$ , where  $u_p$  and  $u_h$  are the solutions of

$$(N) \left\{ \begin{aligned} \frac{1}{c^2} \partial_t^2 u_p(t, \mathbf{r}) - \Delta u_p(t, \mathbf{r}) &= \sum_{k=1}^K q_k(t) \delta(\mathbf{r} - \mathbf{p}_k(t)), & (t, \mathbf{r}) \in (0, T) \times \mathbb{R}^3, \\ u_p(0, \mathbf{r}) &= 0, & \mathbf{r} \in \mathbb{R}^3, \\ \partial_t u_p(0, \mathbf{r}) &= 0, & \mathbf{r} \in \mathbb{R}^3, \end{aligned} \right.$$

$$(H) \left\{ \begin{aligned} \frac{1}{c^2} \partial_t^2 u_h(t, \mathbf{r}) - \Delta u_h(t, \mathbf{r}) &= 0, & (t, \mathbf{r}) \in (0, T) \times \Omega, \\ u_h(t, \mathbf{r}) &= -u_p(t, \mathbf{r}), & (t, \mathbf{r}) \in (0, T) \times \Gamma \\ u_h(0, \mathbf{r}) &= 0, & \mathbf{r} \in \Omega, \\ \partial_t u_h(0, \mathbf{r}) &= 0, & \mathbf{r} \in \Omega, \end{aligned} \right.$$

18 / 92

- The solution  $u_p$  of (N) is expressed by

$$u_p(t, \mathbf{r}) = \sum_{k=1}^K \frac{1}{4\pi} \cdot \frac{q_k(s_k(t, \mathbf{r}))}{|\mathbf{r} - \mathbf{p}_k(s_k(t, \mathbf{r}))| \cdot h_k(s_k(t, \mathbf{r}), \mathbf{r})},$$

where

- $s_k(t, \mathbf{r})$ : a solution  $s$  of the equation

$$t = s + \frac{|\mathbf{r} - \mathbf{p}_k(s)|}{c},$$

- $h_k(s, \mathbf{r}) = 1 - \frac{\dot{\mathbf{p}}_k(s) \cdot (\mathbf{r} - \mathbf{p}_k(s))}{c |\mathbf{r} - \mathbf{p}_k(s)|}$ .
- $s_k \in C^{l+2}(\Omega \setminus \{(t, \mathbf{p}_k(t)), t \in [0, T]\})$
- $h_k \in C^{l+1}(\Omega \setminus \{(t, \mathbf{p}_k(t)), t \in [0, T]\})$

- Then

- $u_p|_{[0, T] \times \Omega} \in C([0, T]; L^2(\Omega))$
- $u_p|_{[0, T] \times (\Omega \setminus D)} \in C^{\ell+1}([0, T] \times (\Omega \setminus D))$
- $\nabla u_p|_{[0, T] \times (\Omega \setminus D)} \in C^\ell([0, T] \times (\Omega \setminus D))$

19 / 92

- Moreover

- $u_p|_{[0, T] \times \Gamma} \in C^{\ell+1}([0, T] \times \Gamma) \subset H^{\ell+1}((0, T) \times \Gamma)$
- $\boldsymbol{\nu} \cdot \nabla u_p|_{[0, T] \times \Gamma} \in C^\ell([0, T] \times \Gamma) \subset H^\ell((0, T) \times \Gamma)$

- By Lasiacka-Lions-Triggani(1986), The solution  $u_h$  of (H) satisfies

- $u_h \in C([0, T]; H^{\ell+1}(\Omega)),$
- $\partial_t^m u_h \in C([0, T]; H^{\ell-m+1}(\Omega))$
- $\partial_\nu u_h \in H^\ell(\Sigma).$

- Hence, for  $u = u_p + u_h$ , we have

- $u|_{[0, T] \times \Omega \setminus D} \in C([0, T]; H^{\ell+1}(\Omega \setminus D))$
- $\nabla u|_{[0, T] \times \Omega \setminus D} \in C([0, T]; H^\ell(\Omega \setminus D))$
- $\nabla \partial_t^m u|_{[0, T] \times \Omega \setminus D} \in C([0, T]; H^{\ell-m}(\Omega \setminus D)), \quad 0 \leq m \leq \ell$
- $\partial_\nu u \in H^\ell(\Sigma).$

20 / 92

## Proof of Proposition 2 (Outline)

- Using the same decomposition as proposition 1, we obtain

$$u_p(t, \mathbf{r}) = \sum_{k=1}^K \frac{1}{4\pi} \cdot \frac{\mathbf{m}_k(s_k(t, \mathbf{r})) \cdot (\mathbf{r} - \mathbf{p}_k(s_k(t, \mathbf{r})))}{|\mathbf{r} - \mathbf{p}_k(s_k(t, \mathbf{r}))|^3 \cdot h_k(s_k(t, \mathbf{r}), \mathbf{r})} + \sum_{k=1}^K \frac{1}{4\pi c} \cdot \frac{d}{dt} \left( \frac{\mathbf{m}_k(s_k(t, \mathbf{r})) \cdot (\mathbf{r} - \mathbf{p}_k(s_k(t, \mathbf{r})))}{|\mathbf{r} - \mathbf{p}_k(s_k(t, \mathbf{r}))|^2 \cdot (h_k(s_k(t, \mathbf{r}), \mathbf{r}))^2} \right)$$

- Then

- $u_p|_{[0, T] \times \Omega} \in C([0, T]; H^{-1}(\Omega))$
- $u_p|_{[0, T] \times (\Omega \setminus D)} \in C^{\ell+1}([0, T] \times (\Omega \setminus D))$
- $\nabla u_p|_{[0, T] \times (\Omega \setminus D)} \in C^{\ell}([0, T] \times (\Omega \setminus D))$

- And hence, we obtain the same regularity results for  $u$  outside of the domain  $D$ .

21 / 92

- 4 Key idea of the identification scheme : Reciprocity gap functional

22 / 92

## Definition of reciprocity gap

- **Weak form of the wave equation:**  $u \in C^1([0, T]; L^2(\Omega))$  satisfies that  $\partial_\nu u \in C([0, T]; L^2(\Gamma))$  and

$$\begin{aligned} & \frac{1}{c^2} \int_{\Omega} \partial_t u(T, \mathbf{r}) v(T, \mathbf{r}) dV(\mathbf{r}) - \frac{1}{c^2} \int_{\Omega} u(T, \mathbf{r}) \partial_t v(T, \mathbf{r}) dV(\mathbf{r}) \\ & - \int_0^T \int_{\Gamma} \partial_\nu u(t, \mathbf{r}) v(t, \mathbf{r}) dS(\mathbf{r}) dt \\ & + \int_0^T \int_{\Omega} u(t, \mathbf{r}) \left( \frac{1}{c^2} \partial_t^2 v(t, \mathbf{r}) - \Delta v(t, \mathbf{r}) \right) dV(\mathbf{r}) dt \\ = & \mathcal{F}(v) \quad \text{for any } v \in C^\infty([0, T] \times \bar{\Omega}) \end{aligned}$$

23 / 92

- $\mathcal{W} \subset C^\infty([0, T] \times \bar{\Omega})$  : a set of complex-valued solutions of adjoint problem: **Homogeneous scalar wave equation**

$$\frac{1}{c^2} \partial_t^2 v(t, \mathbf{r}) - \Delta v(t, \mathbf{r}) = 0, \quad (t, \mathbf{r}) \in \Omega \times (0, T)$$

with final state condition

$$v(T, \mathbf{r}) = \partial_t v(T, \mathbf{r}) = 0, \quad \mathbf{r} \in \Omega$$

- $\mathcal{R}_\phi(\cdot)$  : The reciprocity gap functional on  $\mathcal{W}$

$$\mathcal{R}_\phi(v) = - \int_0^T \int_{\Gamma} \phi(t, \mathbf{r}) v(t, \mathbf{r}) dS(\mathbf{r}) dt$$

24 / 92



Since  $v \in \mathcal{W}$

$$\begin{aligned}
 \mathcal{R}_\phi(v) &= - \int_0^T \int_\Gamma \partial_\nu u(t, \mathbf{r}) v(t, \mathbf{r}) dS(\mathbf{r}) dt \\
 &= - \frac{1}{c^2} \int_\Omega \partial_t u(T, \mathbf{r}) v(T, \mathbf{r}) dV(\mathbf{r}) + \frac{1}{c^2} \int_\Omega u(T, \mathbf{r}) \partial_t v(T, \mathbf{r}) dV(\mathbf{r}) \\
 &\quad - \int_0^T \int_\Omega u(t, \mathbf{r}) \left( \frac{1}{c^2} \partial_t^2 v(t, \mathbf{r}) - \Delta v(t, \mathbf{r}) \right) dV(\mathbf{r}) dt \\
 &\quad + \mathcal{F}(v) \\
 &= \mathcal{F}(v)
 \end{aligned}$$

25 / 92

## Reciprocity gap functional for point sources and dipole sources

- For point sources model

$$\mathcal{R}_\phi(v) = \mathcal{F}(v) = \sum_{k=1}^K \int_0^T \mathbf{q}_k(t) \cdot v(t, \mathbf{p}_k(t)) dt$$

- For dipole sources model

$$\mathcal{R}_\phi(v) = \mathcal{F}(v) = \sum_{k=1}^K \int_0^T \mathbf{m}_k(t) \cdot \nabla v(t, \mathbf{p}_k(t)) dt$$

- In both cases, we can pick up some information on the parameters of sources choosing **suitable functions**  $v$  in  $\mathcal{W}$ .

26 / 92

## 5 Reconstruction of moving point sources

27 / 92

### Choice of $v(t, \mathbf{r})$ in $\mathcal{W}$ for moving point sources

$$\begin{aligned}
 f_{n,\varepsilon}(t, \mathbf{r}; \tau) &= (x + iy)^n \rho_\varepsilon \left( t - \left( \tau - \frac{z}{c} \right) \right), \quad n = 0, 1, 2, \dots, \\
 g_{n,\varepsilon}(t, \mathbf{r}; \tau) &= -\partial_t f_{n,\varepsilon}(t, \mathbf{r}; \tau), \quad n = 0, 1, 2, \dots, \\
 h_{n,\varepsilon}(t, \mathbf{r}; \tau) &= z(\partial_x - i\partial_y) f_{n,\varepsilon}(t, \mathbf{r}; \tau) - (x - iy)\partial_z f_{n,\varepsilon}(t, \mathbf{r}; \tau), \\
 &\quad n = 1, 2, 3, \dots, \\
 i_{n,\varepsilon}(t, \mathbf{r}; \tau) &= \partial_t^2 f_{n,\varepsilon}(t, \mathbf{r}; \tau), \quad n = 0, 1, 2, \dots, \\
 j_{n,\varepsilon}(t, \mathbf{r}; \tau) &= -\partial_t h_{n,\varepsilon}(t, \mathbf{r}; \tau), \quad n = 1, 2, 3, \dots,
 \end{aligned}$$

- $\rho_\varepsilon \in C^\infty(\mathbb{R})$ : a standard mollifier function.
- $\tau \in [0, T + \inf_\Omega z/c - \varepsilon]$ ,  $0 < \varepsilon \ll 1$ .

28 / 92

From our assumption,  $\phi \in H^4(\Gamma \times [0, T]) \subset C^2(\Gamma \times [0, T])$ , then, although  $f_{n,\varepsilon}$  does not converges in  $C^\infty([0, T] \times \bar{\Omega})$ ,  $\lim_{\varepsilon \rightarrow 0} \mathcal{R}(f_{n,\varepsilon}(\cdot, \cdot; \tau))$  exists, and we have

$$\begin{aligned} \mathcal{R}_\phi(f_n)(\tau) &\equiv \lim_{\varepsilon \rightarrow 0} \mathcal{R}_\phi(f_{n,\varepsilon}(\cdot, \cdot; \tau)) \\ &= - \lim_{\varepsilon \rightarrow 0} \int_0^T \int_\Gamma (x + iy)^n \rho_\varepsilon \left( t - \left( \tau - \frac{z}{c} \right) \right) \phi(t, \mathbf{r}) dS(\mathbf{r}) dt \\ &= - \lim_{\varepsilon \rightarrow 0} \int_\Gamma (x + iy)^n \left\{ \int_0^T \rho_\varepsilon \left( t - \left( \tau - \frac{z}{c} \right) \right) \phi(t, \mathbf{r}) dt \right\} dS(\mathbf{r}) \\ &= - \int_\Gamma (x + iy)^n \phi \left( \tau - \frac{z}{c}, \mathbf{r} \right) dS(\mathbf{r}) \end{aligned}$$

29 / 92

Similarly, we have

$$\begin{aligned} \mathcal{R}_\phi(g_n)(\tau) &= - \int_\Gamma (x + iy)^n \partial_t \phi \left( \tau - \frac{z}{c}, \mathbf{r} \right) dS(\mathbf{r}) \\ \mathcal{R}_\phi(h_n)(\tau) &= - \int_\Gamma 2nz(x + iy)^{n-1} \phi \left( \tau - \frac{z}{c}, \mathbf{r} \right) dS(\mathbf{r}) \\ &\quad - \frac{1}{c} \int_\Gamma (x - iy)(x + iy)^n \partial_t \phi \left( \tau - \frac{z}{c}, \mathbf{r} \right) dS(\mathbf{r}) \end{aligned}$$

30 / 92

$$\mathcal{R}_\phi(i_n)(\tau) = \int_\Gamma (x + iy)^n \partial_t^2 \phi \left( \tau - \frac{z}{c}, \mathbf{r} \right) dS(\mathbf{r})$$

$$\begin{aligned} \mathcal{R}_\phi(j_n)(\tau) &= \int_\Gamma 2nz(x + iy)^{n-1} \partial_t \phi \left( \tau - \frac{z}{c}, \mathbf{r} \right) dS(\mathbf{r}) \\ &\quad + \frac{1}{c} \int_\Gamma (x - iy)(x + iy)^n \partial_t^2 \phi \left( \tau - \frac{z}{c}, \mathbf{r} \right) dS(\mathbf{r}) \end{aligned}$$

31 / 92

## Reconstruction theorem for moving point sources

### Theorem 1 (for point sources)

Let  $K(\tau)$  be the number of point sources such that  $q_k(t_k(\tau)) \neq 0$  for each  $\tau$ . Assume that  $p_{j,xy}(t_j(\tau)) \neq p_{k,xy}(t_k(\tau))$  if  $j \neq k$ . Then, for each  $\tau$ , we can uniquely determine  $K(\tau)$ ,  $\mathbf{p}_k(t_k(\tau))$  and  $q_k(t_k(\tau))$ ,  $k = 1, 2, \dots, K(\tau)$  from the reciprocity gap functionals

- $\mathcal{R}_\phi(f_n)(\tau)$ ,  $n = 0, 1, 2, \dots, 2K(\tau) + 1$ ,
- $\mathcal{R}_\phi(g_n)(\tau)$ ,  $n = 0, 1, 2, \dots, 2K(\tau) - 1$ ,
- $\mathcal{R}_\phi(h_n)(\tau)$ ,  $n = 1, 2, 3, \dots, K(\tau)$ ,
- $\mathcal{R}_\phi(i_n)(\tau)$ ,  $n = 1, 2, 3, \dots, 2K(\tau)$ ,
- $\mathcal{R}_\phi(j_n)(\tau)$ ,  $n = 1, 2, 3, \dots, K(\tau)$ .

32 / 92

## Reconstruction theorem for moving dipole sources

### Theorem 2 (for dipole sources)

Let  $K(\tau)$  be the number of dipole sources such that  $\mathbf{m}_k(t_k(\tau)) \neq 0$  for each  $\tau$ . Assume that  $p_{j,xy}(t_j(\tau)) \neq p_{k,xy}(t_k(\tau))$  if  $j \neq k$ , and  $m_{k,z}(t) \equiv 0$ , i.e. the dipole moments have only  $xy$ -components. Then, for each  $\tau$ , we can uniquely determine  $K(\tau)$ ,  $\mathbf{p}_k(t_k(\tau))$  and  $\mathbf{m}_k(t_k(\tau))$ ,  $k = 1, 2, \dots, K(\tau)$  from the reciprocity gap functionals

- $\mathcal{R}_\phi(f_n)(\tau)$ ,  $n = 1, 2, 3, \dots, 2K(\tau) + 2$ ,
- $\mathcal{R}_\phi(g_n)(\tau)$ ,  $n = 1, 2, 3, \dots, 2K(\tau)$ ,
- $\mathcal{R}_\phi(h_n)(\tau)$ ,  $n = 2, 3, 4, \dots, K(\tau) + 1$ ,
- $\mathcal{R}_\phi(i_n)(\tau)$ ,  $n = 1, 2, 3, \dots, 2K(\tau)$ ,
- $\mathcal{R}_\phi(j_n)(\tau)$ ,  $n = 2, 3, 4, \dots, K(\tau) + 1$ .

33 / 92

## Outline of the proof of theorem 1: summary of reconstruction procedure for moving point sources

- Step 1.** Identify the number  $K(\tau)$  of point sources from  $\mathcal{R}_\phi(f_n)(\tau)$ ,  $n = 0, 1, 2, \dots, 2K(\tau) + 1$ .
- Step 2.** Reconstruct  $x$  and  $y$  components of the locations of point sources  $\mathbf{p}_{k,xy}(t_k(\tau))$  from  $\mathcal{R}_\phi(f_n)(\tau)$ ,  $n = 0, 1, 2, \dots, 2K(\tau)$ .
- Step 3.** Identify perturbed magnitudes  $q_k(t_k(\tau))\xi_k(\tau)$  from  $\mathcal{R}_\phi(f_n)(\tau)$ ,  $n = 0, 1, 2, \dots, K(\tau) - 1$ . ( $\xi_k(\tau)$ : perturbation term)
- Step 4.** Reconstruct  $z$  component of the locations of point sources  $\mathbf{p}_{k,z}(t_k(\tau))$  from  $\mathcal{R}_\phi(g_n)(\tau)$ ,  $n = 0, 1, 2, \dots, 2K(\tau) - 1$  and  $\mathcal{R}_\phi(h_n)(\tau)$ ,  $n = 1, 2, 3, \dots, K(\tau)$ .
- Step 5.** Identify of  $z$ -component of perturbed velocity of point sources  $\dot{\mathbf{p}}_{k,z}(t_k(\tau))\xi_k(\tau)$  from  $\mathcal{R}_\phi(i_n)(\tau)$ ,  $n = 1, 2, 3, \dots, 2K(\tau)$  and  $\mathcal{R}_\phi(j_n)(\tau)$ ,  $n = 1, 2, 3, \dots, K(\tau)$ .
- Step 6.** Compute  $\xi_k(\tau)$  using perturbed velocity  $\dot{\mathbf{p}}_{k,z}(t_k(\tau))\xi_k(\tau)$ , and reconstruct the magnitudes  $q_k(t_k(\tau))$  from perturbed ones  $q_k(t_k(\tau))\xi_k(\tau)$ .

34 / 92

## Step 1. Identification of the number of point sources from $\mathcal{R}_\phi(f_n)(\tau)$

- Relation between  $\mathcal{R}_\phi(f_n)(\tau)$  and parameters of moving point sources

$$\mathcal{R}_\phi(f_n)(\tau) = \sum_{k=1}^K q_k(t_k(\tau)) \xi_k(\tau) \cdot (p_{k,xy}(t_k(\tau)))^n,$$

where

- $t_k(\tau)$ : the solution of  $\tau = t_k + \frac{p_{k,z}(t_k)}{c}$  for each  $k$  and  $\tau$
- $p_{k,xy}(t_k(\tau)) = p_{k,x}(t_k(\tau)) + ip_{k,y}(t_k(\tau))$
- $\xi_k(\tau) \equiv \frac{dt_k}{d\tau} = \left(1 + \frac{\dot{p}_{k,z}(t_k(\tau))}{c}\right)^{-1}$

35 / 92

- For each  $\tau$ , define  $L \times L$ -Hankel matrix

$$H_{L,\mu}(\tau) = \begin{pmatrix} \mathcal{R}_\phi(f_\mu) & \mathcal{R}_\phi(f_{\mu+1}) & \mathcal{R}_\phi(f_{\mu+2}) & \cdots & \mathcal{R}_\phi(f_{\mu+L-1}) \\ \mathcal{R}_\phi(f_{\mu+1}) & \mathcal{R}_\phi(f_{\mu+2}) & \mathcal{R}_\phi(f_{\mu+3}) & \cdots & \mathcal{R}_\phi(f_{\mu+L}) \\ \mathcal{R}_\phi(f_{\mu+2}) & \mathcal{R}_\phi(f_{\mu+3}) & \mathcal{R}_\phi(f_{\mu+4}) & \cdots & \mathcal{R}_\phi(f_{\mu+L+1}) \\ \vdots & \vdots & \vdots & \ddots & \vdots \\ \mathcal{R}_\phi(f_{\mu+L-1}) & \mathcal{R}_\phi(f_{\mu+L}) & \mathcal{R}_\phi(f_{\mu+L+1}) & \cdots & \mathcal{R}_\phi(f_{\mu+2L-2}) \end{pmatrix}.$$

(for simplicity, we omit the argument  $(\tau)$  for  $\mathcal{R}_\phi(f_n)$ )

Then, we can identify the number  $K(\tau)$  of point sources such that  $q_k(t_k(\tau)) \neq 0$  by

$$K(\tau) = \max\{L \mid \det H_{L,0}(\tau) \neq 0\}$$

(Ref. El Badia-Ha Duong(2000) or Nara-Ando(2003))

36 / 92

## Step 2. Reconstruction of $xy$ -components of locations from $\mathcal{R}_\phi(f_n)(\tau)$

$$\mathcal{R}_\phi(f_n)(\tau) = \sum_{k=1}^K q_k(t_k(\tau)) \xi_k(\tau) \cdot (p_{k,xy}(t_k(\tau)))^n,$$

- We can determine  $p_{k,xy}(t_k(\tau))$  using the relation

$$\begin{aligned} & \{p_{k,xy}(t_k(\tau)), k = 1, 2, \dots, K(\tau)\} \\ & = \{ \text{eigenvalues of } (H_{K(\tau),0}(\tau))^{-1} H_{K(\tau),1}(\tau) \}. \end{aligned}$$

(Ref. El Badia-Ha Duong (2000))

37 / 92

## Step 3. Reconstruction of perturbed magnitudes from $\mathcal{R}_\phi(f_n)(\tau)$

- Let us consider  $K(\tau) \times K(\tau)$ -matrix

$$V_{K(\tau)} = \begin{pmatrix} 1 & 1 & \dots & 1 \\ p_{1,xy} & p_{2,xy} & \dots & p_{K(\tau),xy} \\ p_{1,xy}^2 & p_{2,xy}^2 & \dots & p_{K(\tau),xy}^2 \\ \vdots & \vdots & \ddots & \vdots \\ p_{1,xy}^{K(\tau)-1} & p_{2,xy}^{K(\tau)-1} & \dots & p_{K(\tau),xy}^{K(\tau)-1} \end{pmatrix},$$

and let  $Q_{K(\tau)}$  and  $F_{K(\tau)}$  be  $K(\tau)$ -vectors defined by

$$Q_{K(\tau)} = \begin{pmatrix} q_1 \xi_1 \\ q_2 \xi_2 \\ \vdots \\ q_{K(\tau)} \xi_{K(\tau)} \end{pmatrix}, \quad F_{K(\tau)} = \begin{pmatrix} \mathcal{R}_\phi(f_0)(\tau) \\ \mathcal{R}_\phi(f_2)(\tau) \\ \vdots \\ \mathcal{R}_\phi(f_{K(\tau)-1})(\tau) \end{pmatrix}.$$

38 / 92

- Then, we have

$$V_{K(\tau)} Q_{K(\tau)} = F_{K(\tau)} \quad (*)$$

- Since  $V_K(\tau)$  is a **Vandermonde matrix**, assuming  $p_{j,xy}(t_j(\tau)) \neq p_{k,xy}(t_k(\tau))$  for  $j \neq k$ ,  $\det V_{K(\tau)} \neq 0$ . Therefore, (\*) is uniquely solvable.
- Hence, we can obtain **perturbed magnitudes**  $q_k(t_k(\tau))\xi_k(\tau)$ ,  $k = 1, 2, \dots, K(\tau)$

## Step 4. Reconstruction of z-component of location of moving point sources from $\mathcal{R}_\phi(g_n)(\tau)$ and $\mathcal{R}_\phi(h_n)(\tau)$

$$\begin{aligned} & \mathcal{R}_\phi(h_n)(\tau) \\ = & 2n \sum_{k=1}^K q_k \xi_k \cdot p_{k,z} \cdot p_{k,xy}^{n-1} \\ & + \frac{1}{c} \sum_{k=1}^K \{ (q_k \xi_k)' \cdot \overline{p_{k,xy}} + q_k \xi_k \cdot (\overline{p_{k,xy}})' \} p_{k,xy}^n \\ & + \frac{n}{c} \sum_{k=1}^K q_k \xi_k \cdot (p_{k,xy})' \cdot \overline{p_{k,xy}} \cdot p_{k,xy}^{n-1}, \quad n = 1, 2, 3, \dots \end{aligned}$$

(For simplicity, we omit the arguments  $(\tau)$  for  $\xi_k$ , and  $(t_k(\tau))$  for  $q_k$ ,  $p_{k,xy}$  and  $p_{k,z}$ .)

- the symbol ' means  $\frac{d}{d\tau}$ .



- If we know  $(q_k \xi_k)'$  and  $(p_{k,xy})'$ , we can identify  $q_k \xi_k \cdot p_{k,z}$  as the solution of linear equations

$$\begin{aligned}
 & \sum_{k=1}^K q_k \xi_k \cdot p_{k,z} \cdot p_{k,xy}^{n-1} \\
 = & \frac{1}{2n} \mathcal{R}(h_n)(\tau) \\
 & - \frac{1}{2nc} \sum_{k=1}^K \{ (q_k \xi_k)' \cdot \overline{p_{k,xy}} + q_k \xi_k \cdot (\overline{p_{k,xy}})' \} p_{k,xy}^n \\
 & - \frac{1}{2c} \sum_{k=1}^K q_k \xi_k \cdot (p_{k,xy})' \cdot \overline{p_{k,xy}} \cdot p_{k,xy}^{n-1}, \quad n = 1, 2, \dots, K
 \end{aligned}$$

- Then, dividing by  $q_k \xi_k$  we can reconstruct  $p_{k,z}$ .

41 / 92

## Identification of $(q_k \xi_k)'$ and $(p_{k,xy})'$ from $\mathcal{R}_\phi(g_n)(\tau)$

$$\mathcal{R}_\phi(g_n)(\tau) = \sum_{k=1}^K (q_k \xi_k)' \cdot p_{k,xy}^n + n \sum_{k=1}^K q_k \xi_k \cdot (p_{k,xy})' \cdot p_{k,xy}^{n-1},$$

- We can estimate  $(q_k \xi_k)'$  and  $q_k \xi_k \cdot (p_{k,xy})'$  from  $\mathcal{R}(g_n)(\tau)$ ,  $n = 0, 1, 2, \dots, 2K - 1$  and  $p_{k,xy}$ ,  $k = 1, 2, \dots, K$ . (see next slide)
- Since  $q_k \xi_k$  have been already estimated, we can reconstruct  $(p_{k,xy})'$ .

42 / 92

- **Coefficient matrix of the linear equation derived from the expression of  $\mathcal{R}_\phi(g_n)(\tau)$**

$$V = \begin{pmatrix} 1 & 1 & \dots & 1 & 0 & 0 & \dots & 0 \\ p_{1,xy}^1 & p_{2,xy}^1 & \dots & p_{K,xy}^1 & 1 & 1 & \dots & 1 \\ p_{1,xy}^2 & p_{2,xy}^2 & \dots & p_{K,xy}^2 & 2p_{1,xy}^2 & 2p_{2,xy}^2 & \dots & 2p_{K,xy}^2 \\ p_{1,xy}^3 & p_{2,xy}^3 & \dots & p_{K,xy}^3 & 3p_{1,xy}^3 & 3p_{2,xy}^3 & \dots & 3p_{K,xy}^3 \\ \vdots & \vdots & \ddots & \vdots & \vdots & \vdots & \ddots & \vdots \\ p_{1,xy}^{2K-1} & p_{2,xy}^{2K-1} & \dots & p_{K,xy}^{2K-1} & (2K-1)p_{1,xy}^{2K-2} & (2K-1)p_{2,xy}^{2K-2} & \dots & (2K-1)p_{K,xy}^{2K-2} \end{pmatrix}$$

- **We can establish**

$$\det V = (-1)^{K(K-1)/2} \prod_{j>k} (p_{j,xy} - p_{k,xy})^4$$

## Steps 5 and 6. Estimation of perturbation term $\xi_k(\tau)$ : What do we need to estimate?

- **Perturbation term  $\xi_k$  is defined by**

$$\xi_k(\tau) \equiv \frac{dt_k}{d\tau} = \left( 1 + \frac{\dot{p}_{k,z}(t_k(\tau))}{c} \right)^{-1}$$

- **Hence, it seems that we need to estimate  $\dot{p}_{k,z}(t_k(\tau))$ , however, we can easily derive another expression**

$$\xi_k(\tau) = 1 - \frac{(p_{k,z}(t_k(\tau)))'}{c}$$

**Therefore we estimate  $(p_{k,z}(t_k(\tau)))'$  instead of  $\dot{p}_{k,z}(t_k(\tau))$ .**

## Step 5. Estimation of $(p_{k,z})'$ from $\mathcal{R}_\phi(i_n)(\tau)$ and $\mathcal{R}_\phi(j_n)(\tau)$

$$\mathcal{R}_\phi(j_n)(\tau) = 2n \sum_{k=1}^K q_k \xi_k \cdot (p_{k,z})' \cdot p_{k,xy}^{n-1} + R_n$$

- $R_n$  : a polynomial consists of terms
  - $p_{k,xy}$ ,  $(p_{k,xy})'$  and  $(p_{k,xy})''$
  - $q_k \xi_k$ ,  $(q_k \xi_k)'$  and  $(q_k \xi_k)''$
  - and their complex conjugates.

45 / 92

$$\begin{aligned} & \mathcal{R}_\phi(i_n)(\tau) \\ = & \sum_{k=1}^K (q_k)'' \cdot p_{k,xy}^n + n \sum_{k=1}^K q_k \xi_k \cdot (p_{k,xy})'' \cdot p_{k,xy}^{n-1} \\ & + 2n \sum_{k=1}^K (q_k \xi_k)' \cdot (p_{k,xy})' \cdot p_{k,xy}^{n-1} \\ & + n(n-1) \sum_{k=1}^K q_k \xi_k \cdot ((p_{k,xy})')^2 \cdot p_{k,xy}^{n-2}, \end{aligned}$$

46 / 92

## Steps 5 and 6.

- We can estimate  $(q_k)''$  and  $q_k \xi_k \cdot (p_{k,xy})''$  uniquely from  $\mathcal{R}_\phi(i_n)(\tau)$ ,  $n = 0, 1, 2, \dots, 2K(\tau) - 1$ , since we have already estimated  $p_{k,xy}$ ,  $q_k \xi_k$ ,  $(p_{k,xy})'$  and  $(q_k \xi_k)'$ .
- Substituting these terms into  $R_n$  of the expression of  $\mathcal{R}(j_n)(\tau)$ , we can identify  $q_k \xi_k \cdot (p_{k,z})'$  from  $\mathcal{R}_\phi(j_n)$ ,  $n = 1, 2, \dots, K$ , and then, dividing by  $q_k \xi_k$  we can identify  $(p_{k,z})'$ .
- Substituting  $(p_{k,z})'$  to the equation

$$\xi_k = 1 - \frac{(p_{k,z})'}{c}$$

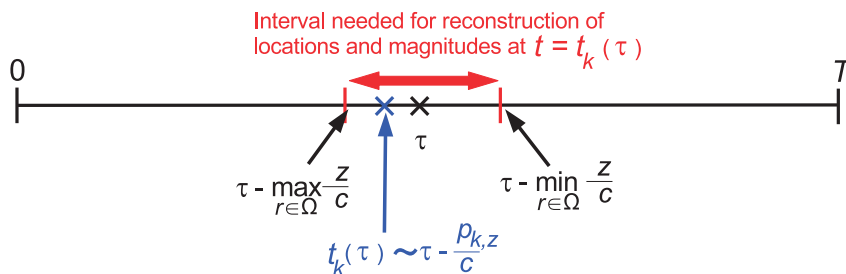
we can estimate perturbation terms  $\xi_k$  for each  $k$  and  $\tau$ , and we can correct perturbed magnitudes  $q_k \xi_k$ .

47 / 92

## Note 1

- Our procedure have a merit in the sense of 'realtimeness' comparing to the method by El Badia & Ha Duong.

$$\mathcal{R}_\phi(f_n)(\tau) = - \int_{\Gamma} (x + iy)^n \phi \left( \tau - \frac{z}{c}, \mathbf{r} \right) dS(\mathbf{r})$$



48 / 92

## Note 2

- Our method reconstructs the locations and magnitudes at  $t_k(\tau)$ . Therefore, we have to correct the 'time' variable using  $\mathbf{p}_{k,z}(t_k(\tau))$ .

49 / 92

## 6 Reconstruction scheme for moving dipole sources

50 / 92

## Reconstruction theorem for moving dipole sources

### Theorem 2 (for dipole sources)

Let  $K(\tau)$  be the number of dipole sources such that  $\mathbf{m}_k(t_k(\tau)) \neq 0$  for each  $\tau$ . Assume that  $p_{j,xy}(t_j(\tau)) \neq p_{k,xy}(t_k(\tau))$  if  $j \neq k$ , and  $m_{k,z}(t) \equiv 0$ , i.e. the dipole moments have only  $xy$ -components. Then, for each  $\tau$ , we can uniquely determine  $K(\tau)$ ,  $\mathbf{p}_k(t_k(\tau))$  and  $\mathbf{m}_k(t_k(\tau))$ ,  $k = 1, 2, \dots, K(\tau)$  from the reciprocity gap functionals

- $\mathcal{R}_\phi(f_n)(\tau)$ ,  $n = 1, 2, 3, \dots, 2K(\tau) + 2$ ,
- $\mathcal{R}_\phi(g_n)(\tau)$ ,  $n = 1, 2, 3, \dots, 2K(\tau)$ ,
- $\mathcal{R}_\phi(h_n)(\tau)$ ,  $n = 2, 3, 4, \dots, K(\tau) + 1$ ,
- $\mathcal{R}_\phi(i_n)(\tau)$ ,  $n = 1, 2, 3, \dots, 2K(\tau)$ ,
- $\mathcal{R}_\phi(j_n)(\tau)$ ,  $n = 2, 3, 4, \dots, K(\tau) + 1$ .

51 / 92

## Relation between $\mathcal{R}_\phi(f)(\tau)$ and parameters of moving dipole sources

$$\mathcal{R}_\phi(f_n)(\tau) = n \sum_{k=1}^K m_{k,xy}(t_k(\tau)) \xi_k(t_k(\tau)) \cdot p_{k,xy}(t_k(\tau))^{n-1},$$

where

- $m_{k,xy}(t_k(\tau)) \equiv m_{k,x}(t_k(\tau)) + im_{k,y}(t_k(\tau))$
- c.f. For moving point sources, we have

$$\mathcal{R}_\phi(f_n)(\tau) = \sum_{k=1}^K q_k(t_k(\tau)) \xi_k(t_k(\tau)) \cdot p_{k,xy}(t_k(\tau))^n,$$

52 / 92

## Relation between $\mathcal{R}_\phi(g_n)(\tau)$ , $\mathcal{R}_\phi(h_n)(\tau)$ and parameters of moving dipole sources

$$\mathcal{R}_\phi(g_n)(\tau) = n \sum_{k=1}^K (m_{k,xy}\xi_k)' \cdot p_{k,xy}^{n-1} + n(n-1) \sum_{k=1}^K m_{k,xy}\xi_k \cdot (p_{k,xy})' \cdot p_{k,xy}^{n-2},$$

$$\mathcal{R}_\phi(h_n)(\tau) = 2n(n-1) \sum_{k=1}^K m_{k,xy}\xi_k \cdot p_{k,z} \cdot p_{k,xy}^{n-2} + H_n$$

where  $H_n$  is a polynomial consists of the terms

- $p_{k,xy}$  and  $(p_{k,xy})'$
- $m_{k,xy}\xi_k$  and  $(m_{k,xy}\xi_k)'$
- and their complex conjugates

53 / 92

## Relation between $\mathcal{R}_\phi(i)(\tau)$ and parameters of moving dipole sources

$$\begin{aligned} & \mathcal{R}_\phi(i_n)(\tau) \\ = & n \sum_{k=1}^K (m_{k,xy}\xi_k)'' \cdot p_{k,xy}^{n-1} + n(n-1) \sum_{k=1}^K m_{k,xy}\xi_k \cdot (p_{k,xy})'' \cdot p_{k,xy}^{n-2} \\ & + 2n(n-1) \sum_{k=1}^K (m_{k,xy}\xi_k)' \cdot (p_{k,xy})' \cdot p_{k,xy}^{n-2} \\ & + n(n-1)(n-2) \sum_{k=1}^K m_{k,xy}\xi_k \cdot ((p_{k,xy})')^2 p_{k,xy}^{n-3}, \end{aligned}$$

54 / 92

## Relation between $\mathcal{R}_\phi(j_n)(\tau)$ and parameters of moving dipole sources

$$\mathcal{R}_\phi(j_n)(\tau) = 2n(n-1) \sum_{k=1}^K m_{k,xy} \xi_k \cdot (p_{k,z})' \cdot p_{k,xy}^{n-1} + J_n$$

$J_n$  : a polynomial consists of the terms

- $p_{k,xy}$ ,  $(p_{k,xy})'$  and  $(p_{k,xy})''$
- $m_{k,xy} \xi_k$ ,  $(m_{k,xy} \xi_k)'$  and  $(m_{k,xy} \xi_k)''$
- and their complex conjugates.

55 / 92

## Note

- Without assumption that  $m_{k,z}(t) \equiv 0$ , the relation between the reciprocity gap functional and parameters of dipole sources becomes more complicated. For example

$$\begin{aligned} \mathcal{R}_\phi(f_n)(\tau) = & n \sum_{k=1}^K m_{k,xy} \xi_k \cdot p_{k,xy}^{n-1} \\ & - \frac{1}{c} \sum_{k=1}^K (m_{k,xy} \xi_k)' \cdot p_{k,xy}^n - \frac{n}{c} \sum_{k=1}^K m_{k,xy} \xi_k \cdot (p_{k,xy})' \cdot p_{k,xy}^{n-1} \end{aligned}$$

56 / 92



## 7 Numerical experiments

57 / 92

## Numerical experiments

- **Domain** :  $\Omega = \{\mathbf{r} \mid |\mathbf{r}| = 1\}$
- **wave propagation speed** :  $c = 1$
- **Time interval** :  $0 < t < T = 40.0$
- **Solver for the wave equation**: boundary integral equation method.
- **The number of observation points for  $\partial_\nu u(\mathbf{r}, t)$** : 384
- **The observation time step** :  $\Delta t = 0.1$
- **The noise of observation data** : 0.0%, 5.0%, 5.0%

58 / 92

## Parameters of point sources

- Number of point sources :  $K = 2$
- Locations  $\mathbf{p}_k(t)$  of point sources
  - point source 1: moves on a **vertical** circle with respect to  $xy$ -plane
  - point source 2: moves on a **horizontal** circle with respect to  $xy$ -plane
- Moving speed:  $\frac{|\dot{\mathbf{p}}_k(t)|}{c} = 35\%$

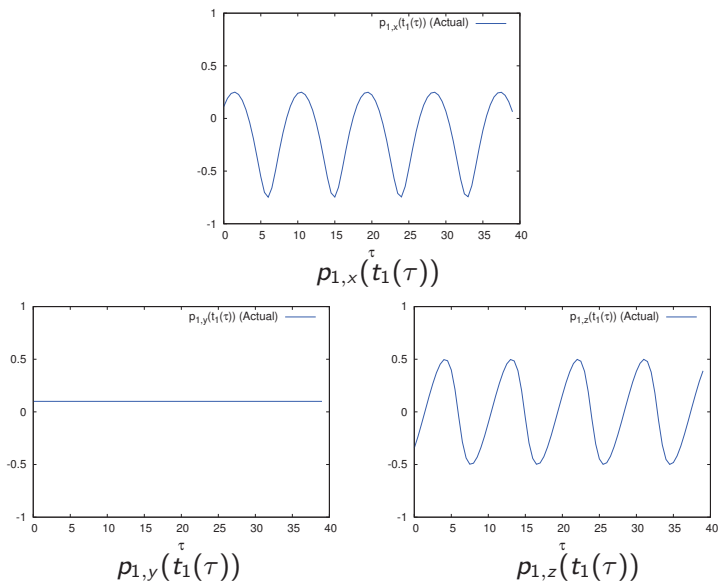
59 / 92

## Identification Process

- Time interval for identification:  $\Delta\tau = 0.5$
- Approximation of the time derivative in the computation of the reciprocity gap functionals: central differences

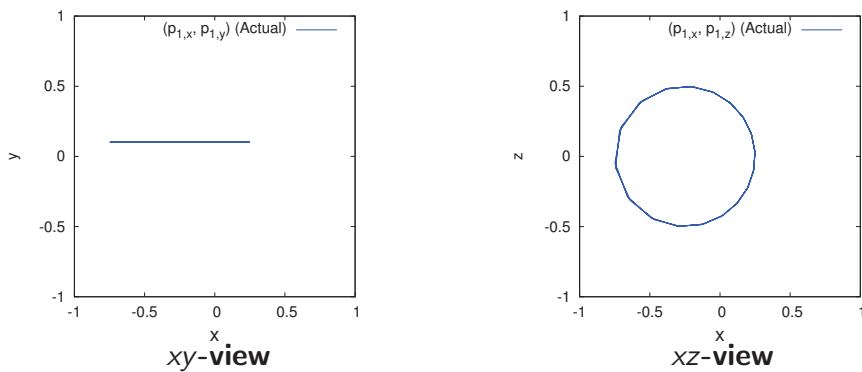
60 / 92

# Time profile of locations of source 1



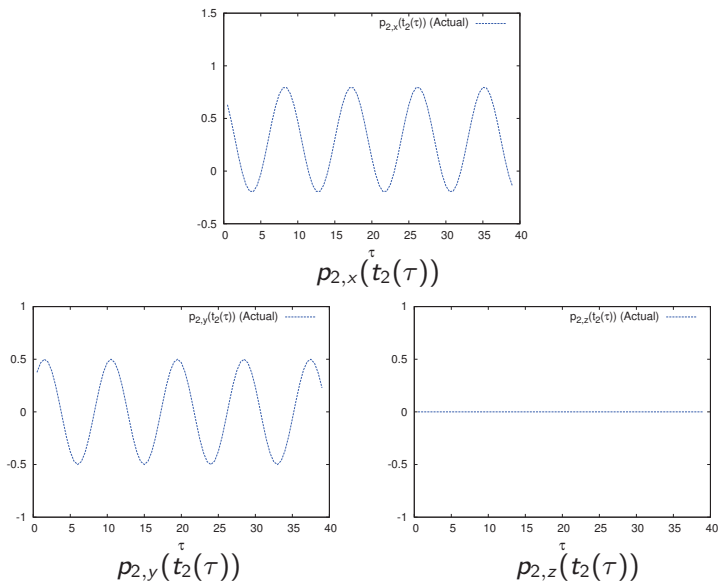
61 / 92

# The orbit of source 1: $xy$ -view and $xz$ -view



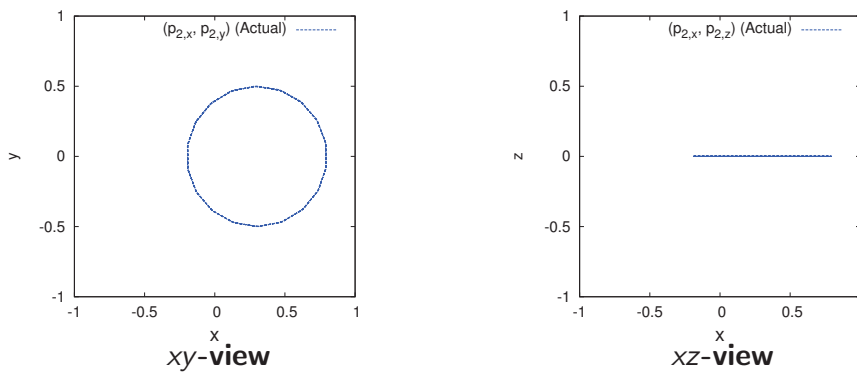
62 / 92

## Time profile of location of source 2



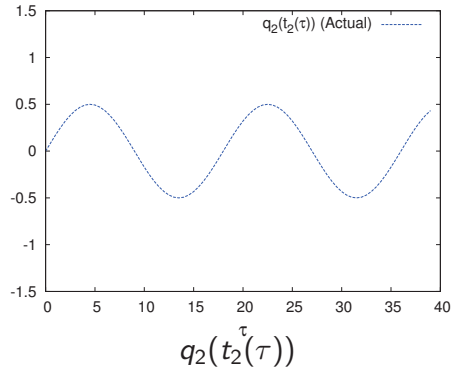
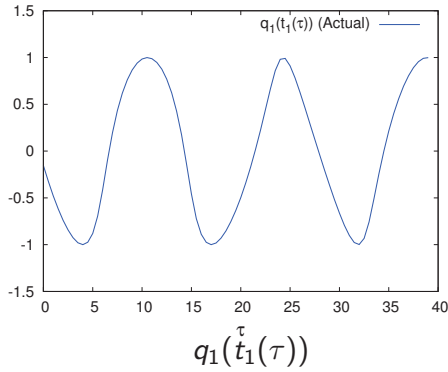
63 / 92

## The orbit of source 2: $xy$ -view and $xz$ -view



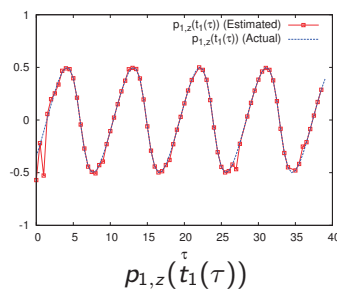
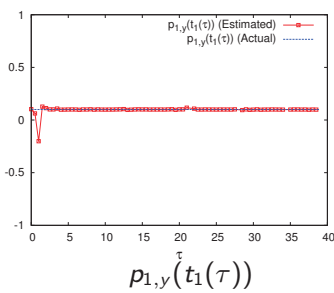
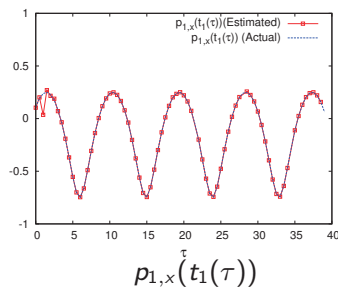
64 / 92

# Time profile of magnitudes of point sources 1 and 2



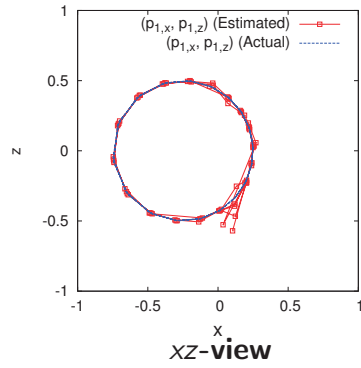
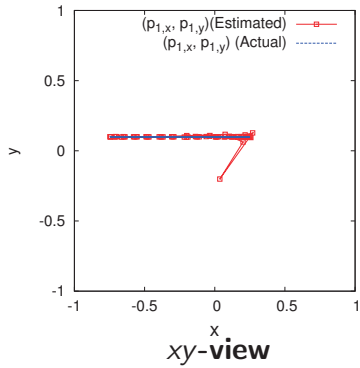
65 / 92

# Reconstruction result for noise free case: Time profile of location of source 1



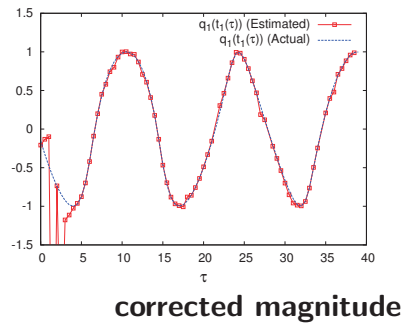
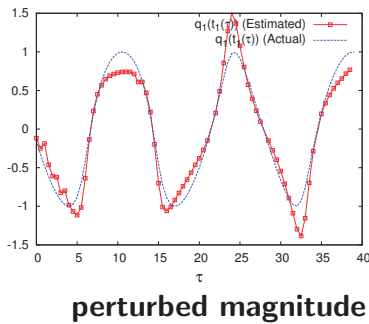
66 / 92

# Reconstruction result for noise free case: the orbit of source 1 ··· $xy$ -view and $xz$ -view



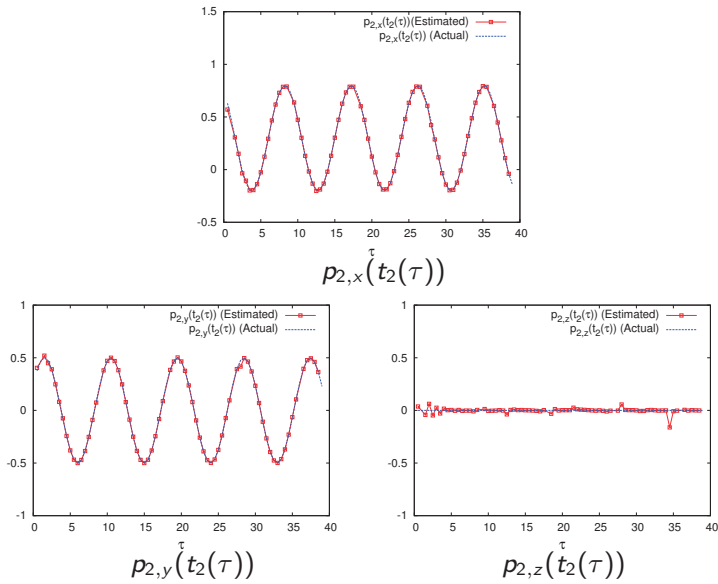
67 / 92

# Reconstruction result for noise free case: Time profile of magnitude of point sources 1



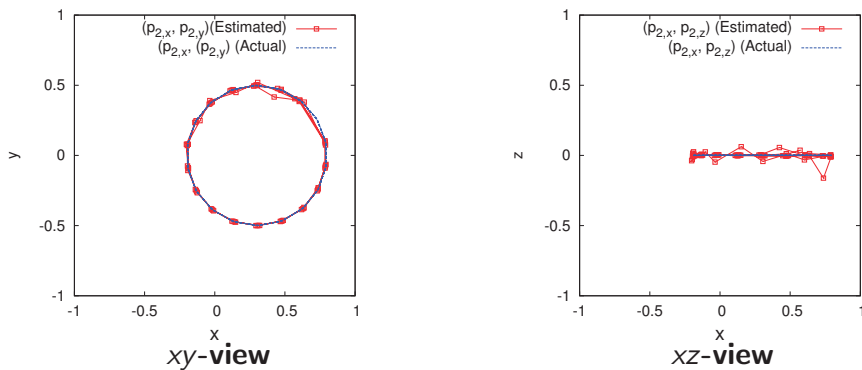
68 / 92

## Reconstruction result for noise free case: Time profile of location of source 2



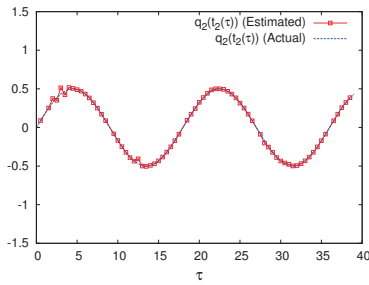
69 / 92

## Reconstruction result for noise free case: The orbit of source 2 ... $xy$ -view and $xz$ -view

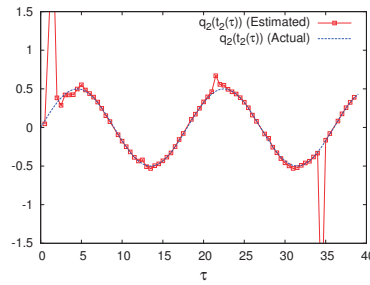


70 / 92

# Reconstruction result for noise free case: Time profile of magnitude of point sources 2

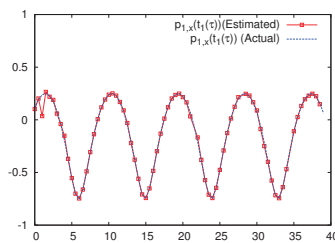


**perturbed magnitude**

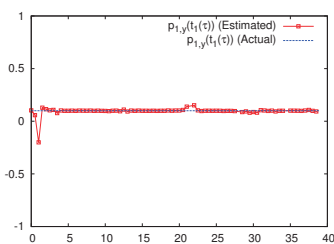


**corrected magnitude**

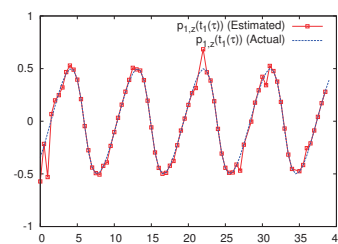
# Reconstruction result under 1% noise: Time profile of location of source 1



$p_{1,x}(t_1(\tau))$



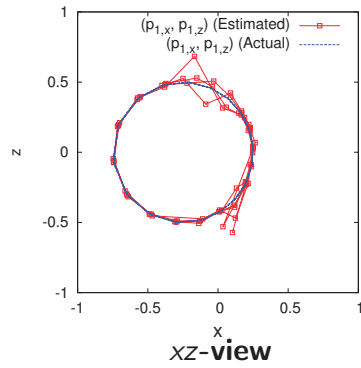
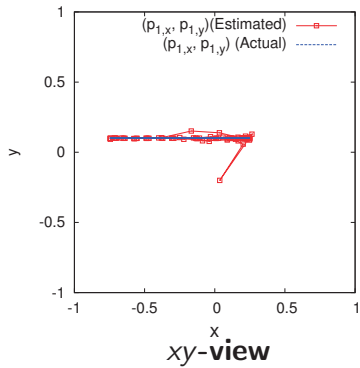
$p_{1,y}(t_1(\tau))$



$p_{1,z}(t_1(\tau))$

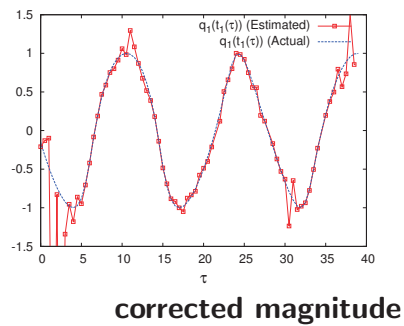
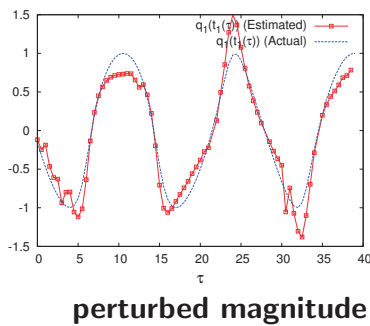


# Reconstruction result under 1% noise: The orbit of source 1 ··· $xy$ -view and $xz$ -view



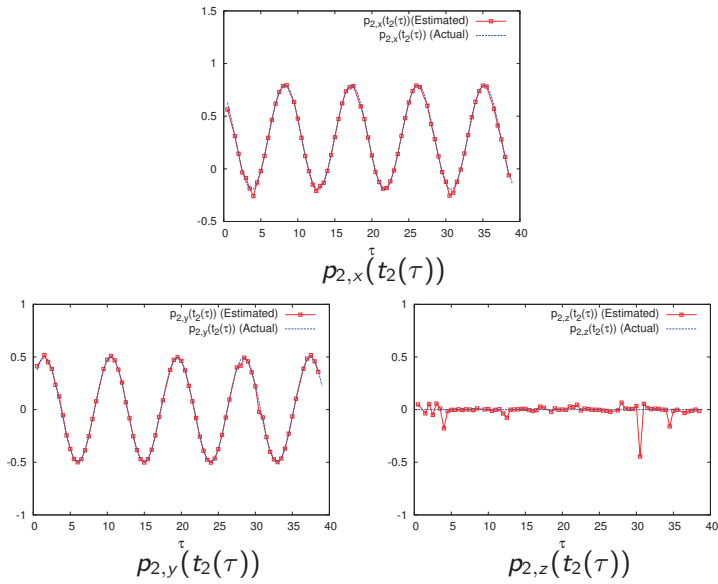
73 / 92

# Reconstruction result under 1% noise: Time profile of magnitude of point sources 1



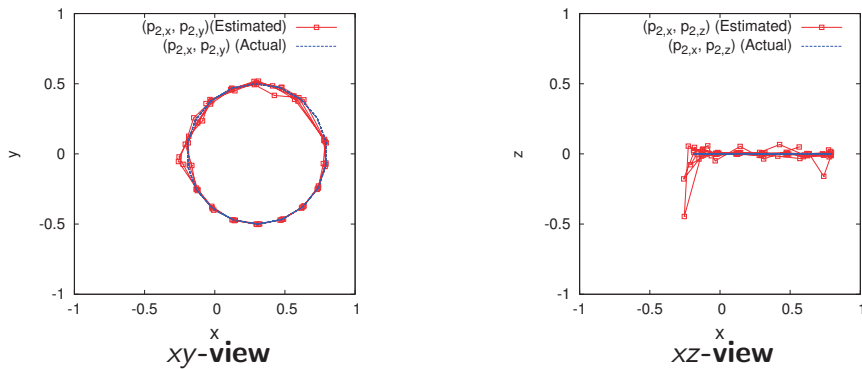
74 / 92

## Reconstruction result under 1% noise: Time profile of location of source 2



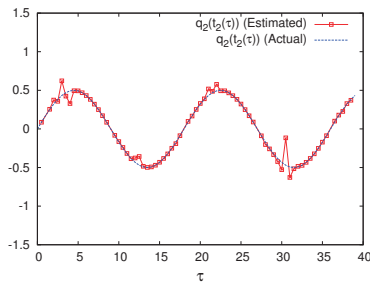
75 / 92

## Reconstruction result under 1% noise: The orbit of source 2 ··· xy-view and xz-view

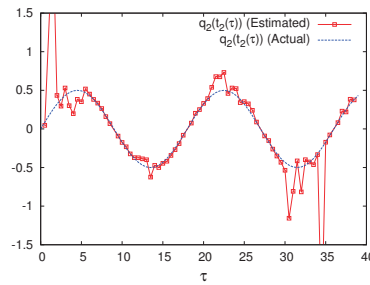


76 / 92

# Reconstruction result under 1% noise: Time profile of magnitude of point sources 2

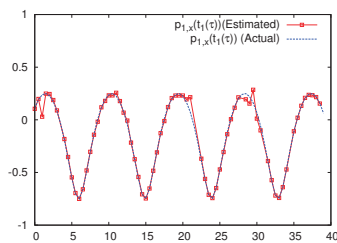


**perturbed magnitude**

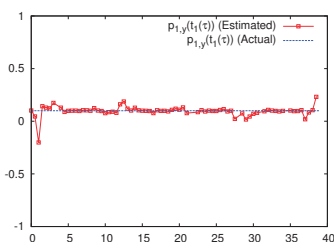


**corrected magnitude**

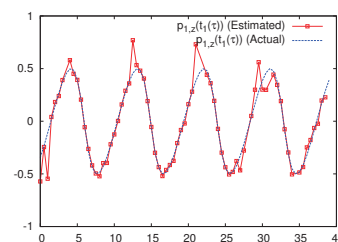
# Reconstruction result under 5% noise: Time profile of location of source 1



$p_{1,x}(t_1(\tau))$

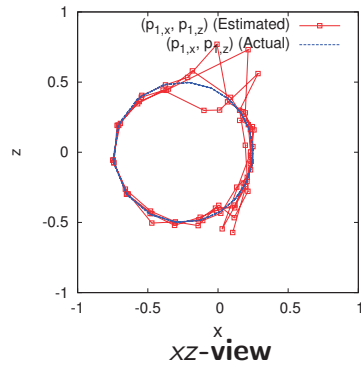
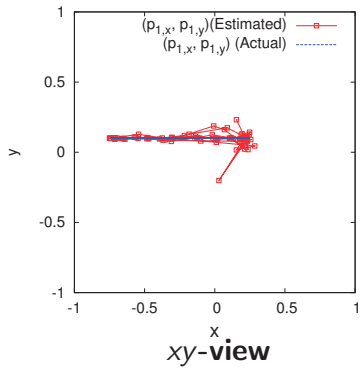


$p_{1,y}(t_1(\tau))$



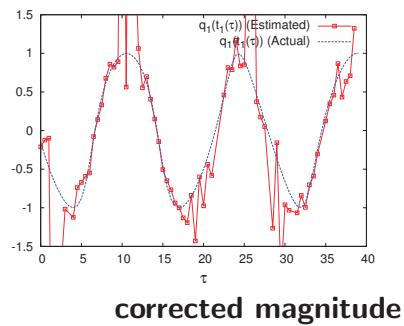
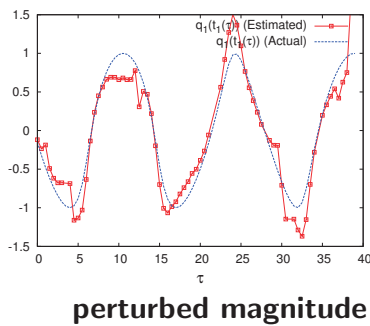
$p_{1,z}(t_1(\tau))$

# Reconstruction result under 5% noise: The orbit of source 1 ··· $xy$ -view and $xz$ -view



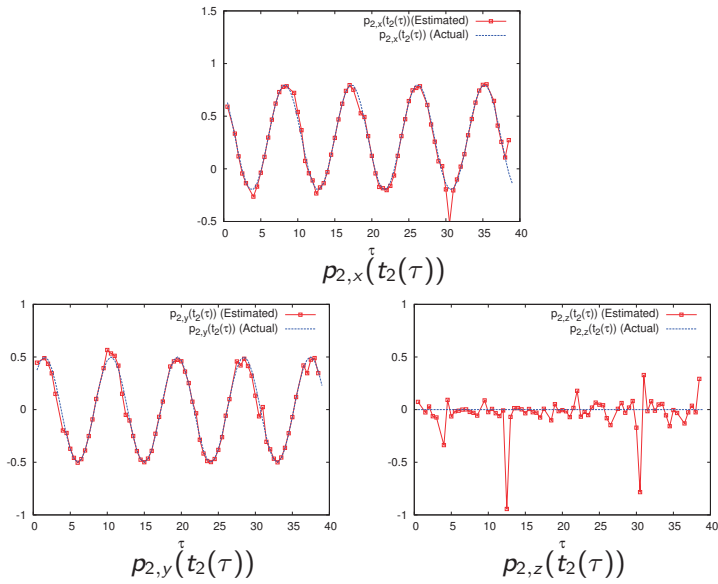
79 / 92

# Reconstruction result under 5% noise: Time profile of magnitude of point sources 1



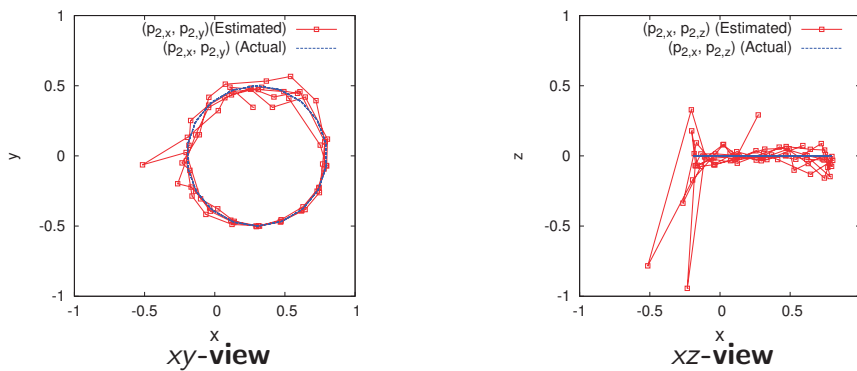
80 / 92

## Reconstruction result under 5% noise: Time profile of location of source 2



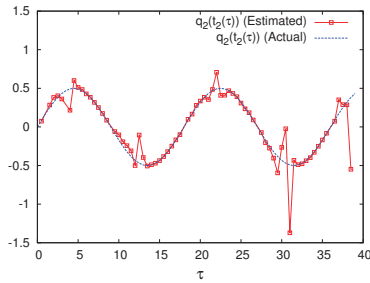
81 / 92

## Reconstruction result under 5% noise: The orbit of source 2 ··· xy-view and xz-view

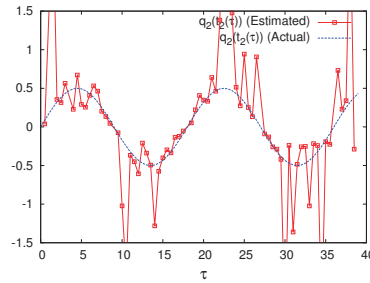


82 / 92

# Reconstruction result under 5% noise: Time profile of magnitude of point sources 2



**perturbed magnitude**



**corrected magnitude**

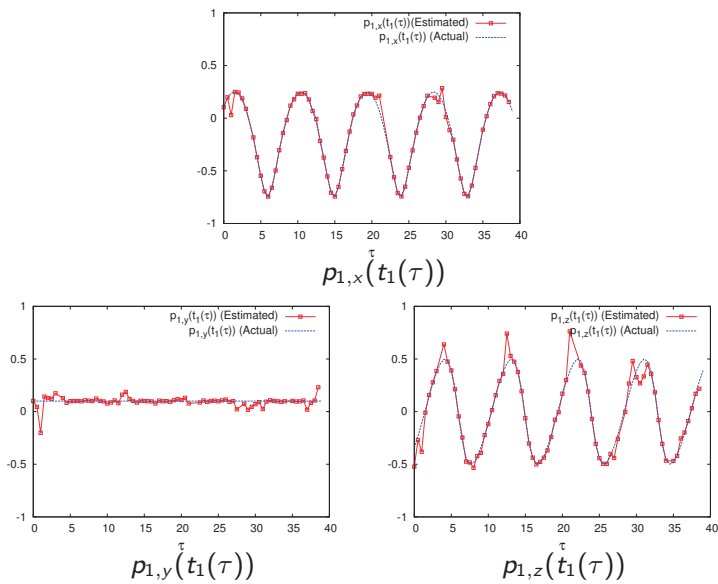
83 / 92

## To reduce the effect of noise

- The estimation results become worse as the noise becomes large. Especially, under 5% noise, the estimation results becomes very bad!
- This phenomenon is caused by the instability of the numerical differentiation.
- To avoid this instability, we apply a filtering process (5 points Gaussian filter) before numerical differentiation

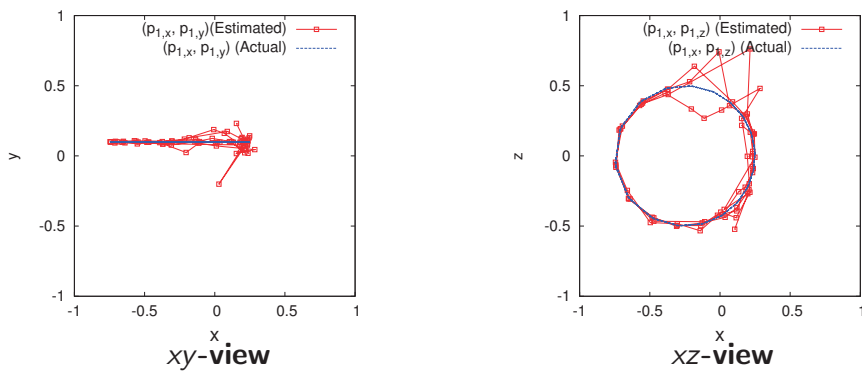
84 / 92

# Reconstruction result with Gaussian filter under 5% noise: Time profile of location of source 1



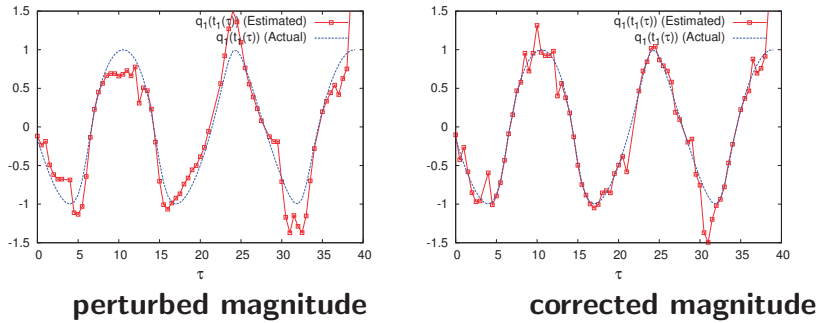
85 / 92

# Reconstruction result with Gaussian filter under 5% noise: The orbit of source 1 ··· xy-view and xz-view



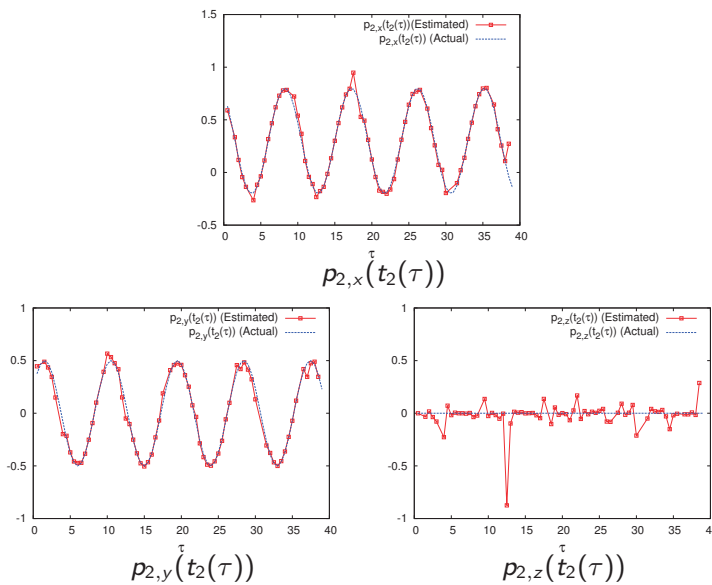
86 / 92

# Reconstruction result with Gaussian filter under 5% noise: Time profile of magnitude of point sources 1



87 / 92

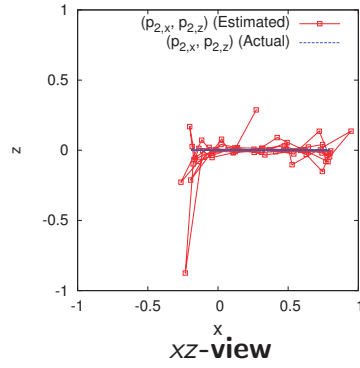
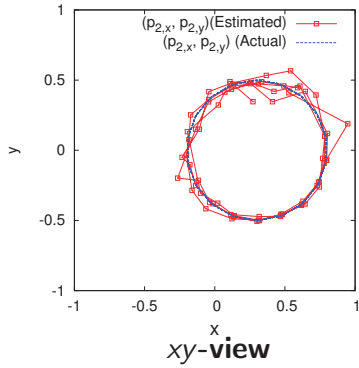
# Reconstruction result with Gaussian filter under 5% noise: Time profile of location of source 2



88 / 92

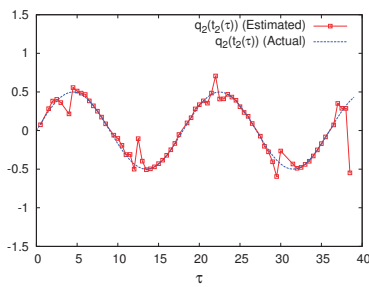


# Reconstruction result with Gaussian filter under 5% noise: The orbit of source 2 ··· $xy$ -view and $xz$ -view

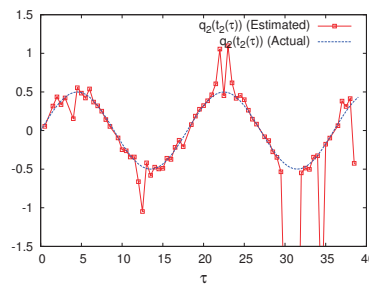


89 / 92

# Reconstruction result with Gaussian filter under 5% noise: Time profile of magnitude of point sources 2



**perturbed magnitude**



**corrected magnitude**

90 / 92

## 8 Conclusions

91 / 92

# Conclusion

- We consider a reconstruction problem of unknown moving point or dipole sources from boundary measurements. This problem is a kind of inverse source problem for the scalar wave equation.
- We give some theorems to guarantee the regularity of observation data.
- We extend the results in Ohe-Inui-Ohnaka (2011), which is for fixed point sources, for the reconstruction of several moving point or dipole sources.
- We present some numerical experiments, and the results show that our procedure gives good reconstruction of unknown sources under small noises
- We need further discussions to distinguish point and dipole sources when they are convined, and to reconstruct the  $z$ -component of dipole sources

92 / 92



# A mathematical study for mixed-mode loading crack problem in viscoelastic composite material

Cheng Hua

Department of Aeronautics and Astronautics, Fudan University, Shanghai, China

**Abstract:** When subjected to a series of long-term repeated application of loads (stress) or thermal cycling or a combination of the two cases, viscoelastic materials experience a time-dependent increase in deformation (strain). This phenomenon is known as viscoelastic creep. Viscoelastic creep is important when considering long-term structural design, given loading and temperature conditions, designers can choose viscoelastic materials that best suit component lifetimes.

Asphalt concrete is a kind of viscoelastic and composite material commonly used to ground roads and other industries. Due to effect of repeated traffic loads, viscoelastic creep phenomenon widely exists in asphalt concrete pavements. In addition, cracking is also considered as one of the major structural damage in such a special material. From the point of view of mathematical modeling, the creep-fracture mechanics parameter  $J'$  or  $C^*$  is widely accepted for a cracked viscoelastic body undergoing creep deformation, but this is valid only for mode I loading conditions<sup>[1]</sup>. While cracks in viscoelastic composite materials are mostly of mixed mode, thus the fracture criteria for mixed-mode crack under creep loadings are very important in mathematical modeling on structural design of viscoelastic composite materials. Although a lot of effort has been made, mathematical modeling for mixed-mode creep crack problem has not been well solved so far.

This study tries to propose a method to characterize mixed-mode crack undergoing creep deformation of viscoelastic composite materials using a new path-independent integral, based on *CED* (Crack Energy Density)<sup>[2]</sup> and Hoff analogy<sup>[3]</sup>. It is expected that the new path-independent integral will be applicable to predict creep crack growth in an arbitrary direction for mixed-mode creep crack problem in viscoelastic composite materials, such as asphalt concrete.

**Keywords:** viscoelastic creep; mixed-mode crack; fracture mechanics parameter; path-independent integral

## References

- [1] Ohji K, Ogura K, Kubo S (1975), *Jpn Soc Mech Engng*, **44**:183[in Japanese]; Landes JD, Begley JA (1976), "A fracture mechanics approach to creep crack growth", *ASTM STP ASTM STP*, **590**: 128–148; Elmukashfi E, Cocks A (2017). "A theoretical and computational framework for studying creep crack growth". *International Journal of Fracture* (2), 1-26.
- [2] Watanabe K (1981), "New Proposal of Crack Energy Density Concept as a Fundamental Fracture Mechanics Parameter", *Bulletin of the JSME*, **24(198)**: 2059-2066.
- [3] Hoff NJ (1954), "Approximate Analysis of Structures in The Presence of Moderately Large Creep Deformations", *Quart. Appl.Math.*, **12**: 49-55.

## Acknowledgement

This work is partially supported by 2017 IMI Joint Use Research Program Workshop (II) "Practical inverse problems based on interdisciplinary and industry-academia collaboration".

This work is partially based on the discussions at 2017 IMI Joint Use Research Program Workshop (II) "Practical inverse problems based on interdisciplinary and industry-academia collaboration".

## Basic concepts of Fracture Mechanics:

Fracture Mechanics is mechanics of solids containing displacement discontinuities (cracks) with special attention to their growth. Fracture mechanics is a theory that determines material failure by fracture criteria. Linear Elastic Fracture Mechanics (LEFM) is the basic theory of fracture that deals with sharp cracks in elastic bodies. It is applicable to any materials only as long as they are elastic except in a vanishingly small region at the crack tip (assumption of small scale yielding). Elastic-Plastic Fracture Mechanics (EPFM) is the theory of ductile fracture, usually characterized by stable crack growth (ductile metals). The fracture process is accompanied by formation of large plastic zone at the crack tip.

Fracture Mechanics has been accepted as an effective engineering methodology to evaluate the behavior of a crack tip fields and it seems to be considered as an almost established method. However, its system widely accepted at present contains some substantial problems that remain to be solved. For instance, although the energy release rate  $G$  is positioned as an important parameter in linear fracture mechanics, it cannot be extended inelastic fracture problems and, moreover, the crack parameters used in fracture mechanics such as stress intensity factor  $K$ ,  $J$ -integral and  $C^*$  parameter are defined just under special constitutive equation. As the results, the scope of the application of fracture mechanics is compelled to be limited without due cause. In this lecture, the outline of fracture mechanics is introduced first, then, what the basic issues are in the role of fracture mechanics is made clear.

### 1. Basic forms of cracks propagating:

- Crack I (opening mode): By normal stress  $\sigma$ , the cracks propagating direction is vertical to the direction of loading stress;
- Crack II (slipping mode): By shear stress  $\tau$ , the cracks propagating direction is parallel to the direction of loading stress;
- Crack III (tearing mode): By shear stress  $\tau$ , the cracks line is parallel to the direction of loading stress.

### 2. Stress field at the crack tip

for crack mode I: 
$$\begin{cases} \sigma_x = \frac{K_I}{\sqrt{2\pi r}} \cos \frac{\theta}{2} \left(1 - \sin \frac{\theta}{2} \sin \frac{3\theta}{2}\right) \\ \sigma_y = \frac{K_I}{\sqrt{2\pi r}} \cos \frac{\theta}{2} \left(1 + \sin \frac{\theta}{2} \sin \frac{3\theta}{2}\right) \\ \tau_{xy} = \frac{K_I}{\sqrt{2\pi r}} \cos \frac{\theta}{2} \sin \frac{\theta}{2} \cos \frac{3\theta}{2} \end{cases}$$

while  $K_I = \sigma\sqrt{\pi a}$  is Stress Intensity Factor (SIF).

Generally, the stresses at the crack tip can be expressed as:

$$\sigma_{ij} = K_p f(r, \theta) \quad (i, j = x, y, z) \quad (p = I, II, III)$$

Stress Intensity Factors

$$\left. \begin{aligned} K_I &= \sigma\sqrt{\pi a} \\ K_{II} &= \tau\sqrt{\pi a} \\ K_{III} &= \tau\sqrt{\pi a} \end{aligned} \right\}$$

### Discussion:

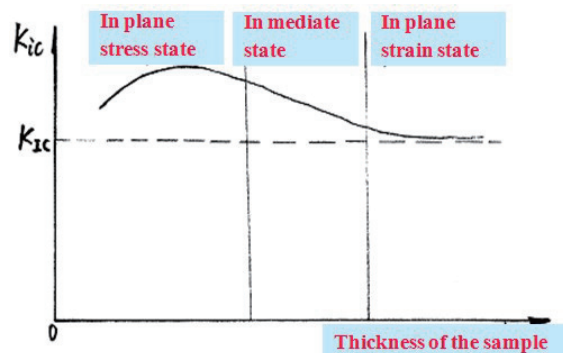
- ⊙  $K_i$  ( $i= I, II, III$ ) are independent of co-ordinate. They are parameters to describe the intensity of the stress field around the crack tips;
- ⊙  $K_i$  ( $i= I, II, III$ ) are close-related with the form, the size and the direction of the cracks;
- ⊙  $K_i$  ( $i= I, II, III$ ) are correlated with the value of the loading and the loading form;
- ⊙  $K_i$  ( $i= I, II, III$ ) are interrelated with the properties of the loaded material;
- The physical meaning of  $K_i$  ( $i= I, II, III$ ) : They are mechanical parameters which are artificially introduced to describe the intensity of the stress field around the crack tips;
- By using these factors, the problem of solving the stress fields and displacements is simplified as just seeking for  $K_i$  ( $i= I, II, III$ );
- Unit:  $K_i$  ( $i= I, II, III$ ) ——[force]×[length]<sup>-3/2</sup> =[N]×[m]<sup>-3/2</sup>

### 3. Fracture criterion

$$K_i \geq K_{iC} \quad (i = I, II, III)$$

$K_{iC}$  ——fracture tenacity/toughness, describing the resistance of crack propagating, determined by test ( plane stress crack and plane strain crack ) .

- When the thickness of the sample is small enough, the crack tip will be in a state of plane stress. When the crack line moves, its plastic area is relatively big enough to enhance  $K_{iC}$ ;
- When the thickness of the sample is big enough, the crack tip will be in a state of plane strain. When the crack line moves, its plastic area is relatively small enough to decrease  $K_{iC} \rightarrow K_{iC}$  .



$K_{iC}$  —— plane strain fracture toughness  
 $K_I = K_{iC}$  ( fracture criterion for crack I )

$K_{iC}$  is a material constant, independent of the geometry of the testing sample. The thickness of the sample should be large enough to guarantee that the crack tip is in a state of plane strain.

### 4. J-integral definition

The  $J$ -integral can be defined as a path-independent contour integral that measures the strength of the singular stresses and strains near a crack tip. Its value should be approximate constant far-field as well as near-crack field. However,  $J$ -integral constancy may be questionable after crack initiation.

Also, dominance of the  $J$ -integral becomes more debatable if the structure composition is heterogeneous. The following equation shows an expression for  $J$  in its 2-D form, where crack lies in the  $XY$  plane with  $x$ -axis parallel to the crack (the following Figure):

$$J = \int_{\Gamma} \left[ \left( W - \sigma_x \frac{\partial u}{\partial x} - \tau_{xy} \frac{\partial v}{\partial x} \right) dy + \left( \tau_{yx} \frac{\partial u}{\partial x} + \sigma_y \frac{\partial v}{\partial x} \right) dx \right]$$

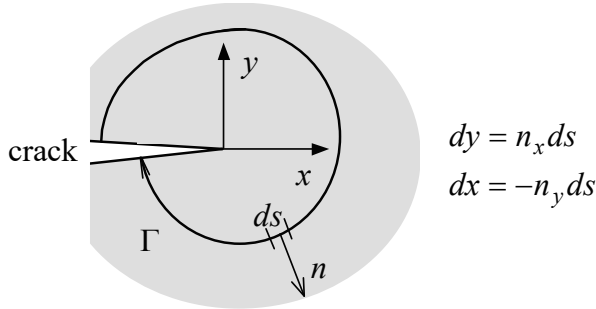


Fig. Definition of contour for  $J$ -integral evaluation

In the above equation,  $\Gamma$  means any path surrounding the crack tip,  $W$  is strain energy density,  $\sigma_{ij}$  is component stress and  $u_i$  is displacement vector.

## 5. Energy Release Rate $G$

### (5.1) Strain energy

Work done by the external force is changed to the strain energy stored in the elastic deformation. The strain energy can be released and the elastic deformation then disappears.

Strain energy density  $w$ : strain energy per unit volume.

$$w = \int_0^{\epsilon_{ij}} \sigma_{ij}^* d\epsilon_{ij}^* = \frac{1}{2} \sigma_{ij} \epsilon_{ij}, \text{ (for linear elastic body)}$$

Total strain energy  $U$  (Internal force potential): total energy stored in the volume  $V$

$$U = \int_V w dV$$

(5.2) External force potential  $U_p$ : the negative value of virtual work done by the external force. Assume that the body force is  $B_i$  and the surface force is  $T_i$  on the stress boundary. The external force potential  $U_p$  is

$$U_p = -\left( \int_V B_i u_i dV + \int_{S_\sigma} T_i u_i dS \right)$$

(5.3) Total potential  $\Pi$ :

$$\Pi = U + U_p = \int_V w dV - \left( \int_V B_i u_i dV + \int_{S_\sigma} T_i u_i dS \right)$$

#### (5.4) Energy Release Rate $G$

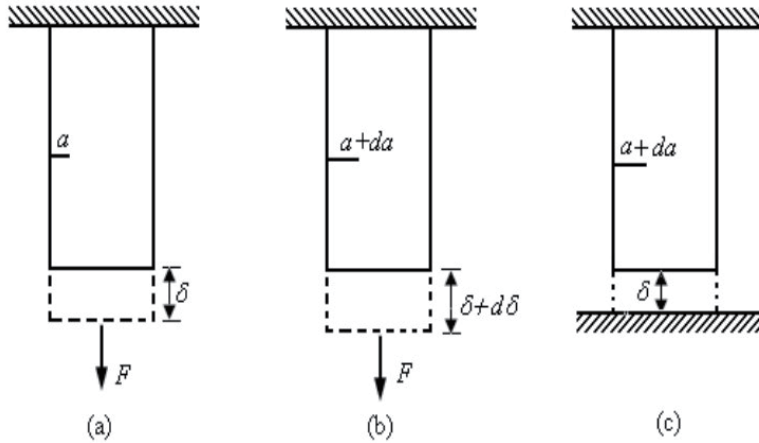
The body force  $B_i$ , the surface force  $T_i$  on  $S_\sigma$  and the displacement  $\bar{u}_i$  on  $S_u$  are given. Assume that the crack size is changed from  $a$  to  $a + \Delta a$ . Accordingly, the displacement, strain, stress, strain energy density, internal force potential, external force potential and total potential are also changed. The total potential  $\Pi$  is changed to  $\Pi + \Delta\Pi$ .  $\Delta\Pi$  is the increment caused by the crack growth  $\Delta a$ . Assume that the plate thickness is  $t$ .  $\Delta S = t \cdot \Delta a$  denotes the single surface area increment. The energy release rate  $G$  is defined as

$$G = - \lim_{\Delta a \rightarrow 0} \frac{\Delta\Pi}{\Delta S} = - \frac{d\Pi}{dS}$$

If the plate thickness  $t$  is a constant, the energy release rate  $G$  is

$$G = - \lim_{\Delta a \rightarrow 0} \frac{\Delta\Pi}{t \cdot \Delta a} = - \frac{1}{t} \frac{d\Pi}{da}$$

#### (5.5) Constant force and constant displacement conditions



##### Constant force condition:

A plate with a crack is applied by a constant force  $F$  as shown in Fig. 3.1(b). The external force virtual work  $W$  and external force potential  $U_p$ , respectively, are

$$W = F\delta, \quad U_p = -W = -F\delta$$

The total strain energy  $U$  (internal force potential) is

$$U = \frac{1}{2} F\delta$$

Then, the total potential  $\Pi$  is

$$\Pi = U + U_p = U - W$$



Now,  $W = 2U$  ,  $\Pi = -U$  . The energy release rate  $G$  under the constant force condition can be written as

$$G = -\frac{\partial \Pi}{\partial S} = \left(\frac{\partial U}{\partial S}\right)_F, \text{ for constant } F.$$

In this case,  $\partial U > 0$  , the strain energy in the body in fact increases rather than releases with the crack growth.  $G$  can not be called as the strain energy release rate.

Constant displacement condition:

After a displacement  $\delta$  occurs, the plate is clamped. This is the constant displacement condition as shown in Fig. 3.1(c). In this case, there is

$$W=0, \quad \Pi = U - W = U$$

$$G = -\frac{\partial \Pi}{\partial S} = -\left(\frac{\partial U}{\partial S}\right)_\delta, \text{ for constant displacement } \delta.$$

It is seen that only for the constant displacement condition,  $G$  can be called as the strain energy release rate. Since  $W=0$ , the energy needed by the crack growth comes from the release of strain energy stored in the body. That is the strain energy stored in the body decreases with the crack growth. For the constant force condition, the increment of external work is  $dW = Fd\delta$  in which a part is used to increase strain energy  $dU$  while the other part is used for crack growth.

However, the values of  $G$  for two cases are equal.

Constant force case:

$$U = \frac{1}{2} F\delta = \frac{F^2 C}{2}, \quad G = \left(\frac{\partial U}{\partial S}\right)_F = \frac{F^2}{2} \frac{\partial C}{\partial S}. \text{ C is the compliance of the plate.}$$

Constant displacement case:

$$U = \frac{1}{2} F\delta = \frac{\delta^2}{2C}, \quad G = -\left(\frac{\partial U}{\partial S}\right)_\delta = -\frac{\partial}{\partial S} \left(\frac{\delta^2}{2C}\right) = -\frac{\delta^2}{2} \frac{-1}{C^2} \frac{\partial C}{\partial S} = \frac{P^2}{2} \frac{\partial C}{\partial S}$$

It is seen that the values of  $G$  for two cases are equal.

# A mathematical study for mixed-mode loading crack problem in viscoelastic composite material

**Cheng Hua**

*Department of Aeronautics and Astronautics, Fudan University, Shanghai, China*



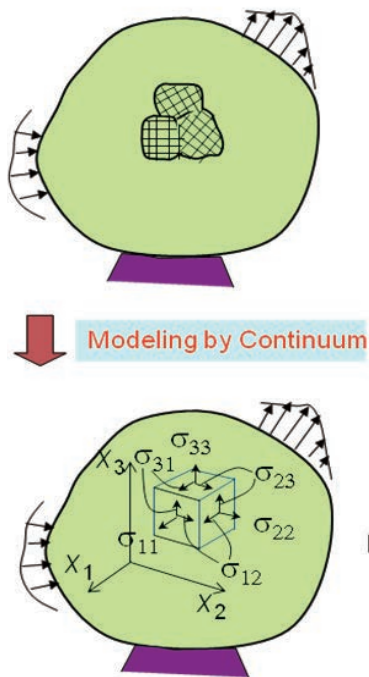
Practical inverse problems based on interdisciplinary and industry-academia collaboration  
Fukuoka, Japan, Oct. 24-28, 2017

## OUTLINE

Introduction of **CED** (Crack Energy Density) and Fracture Mechanics Based on **CED**

New path-independent integral for mixed-mode creep crack

# Summary of Mechanics of Materials



## Mechanics of Materials

Equilibrium equation

$$\frac{\partial \sigma_{11}}{\partial x_1} + \frac{\partial \sigma_{12}}{\partial x_2} + \frac{\partial \sigma_{13}}{\partial x_3} = 0$$

:

$$\sigma_{12} = \sigma_{21}, \dots$$

Relation between Displacement and strain

$$\epsilon_{11} = \frac{\partial u_1}{\partial x_1}, \dots$$

$$\epsilon_{12} = \frac{1}{2} \left( \frac{\partial u_1}{\partial x_2} + \frac{\partial u_2}{\partial x_1} \right)$$

:

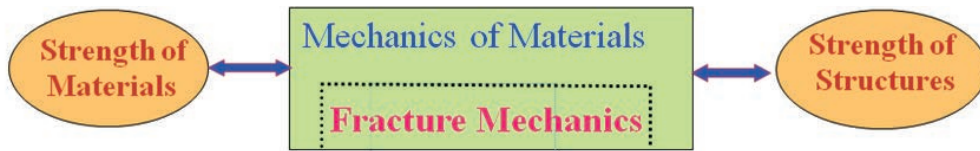
Stress-strain relation

Boundary condition  $T_i = \bar{T}_i$  on  $S_\sigma$   
 $u_i = \bar{u}_i$  on  $S_u$   
*(i=1,2,3)*

Continuum mechanics under small displacement

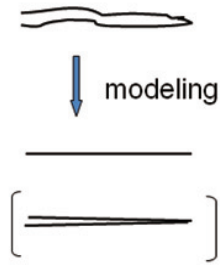
Mechanics of Materials

## Role of Fracture Mechanics



## Mechanics of Materials and Fracture Mechanics

# Crack Problem (Fracture Mechanics)



Stress, Strain, Strain energy density  $\rightarrow \infty$

other parameters are necessary

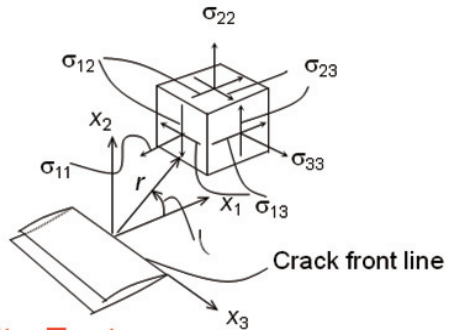
## Fracture Mechanics

### Stress around a crack tip

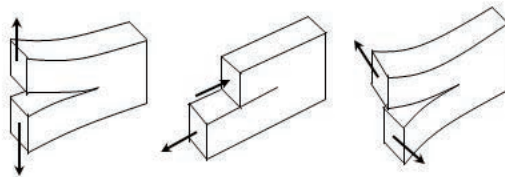
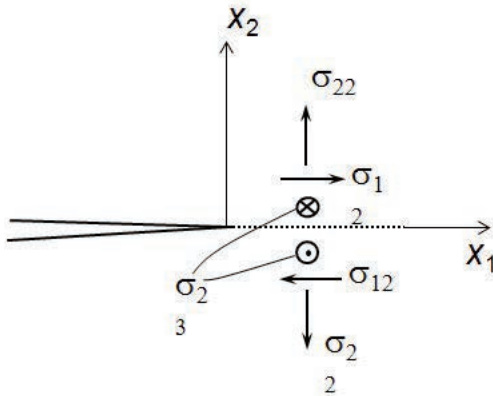
Linear Elasticity

$$\sigma_{ij} = \frac{A_1}{\sqrt{r}} f_{ij}^{(1)}(\theta) + A_2 f_{ij}^{(2)}(\theta) + A_3 \sqrt{r} f_{ij}^{(3)}(\theta) + \dots$$

$$K = \sqrt{2\pi} A_1 : \text{Stress Intensity Factor}$$



### Deformation mode around a crack tip



Mode I

Mode II

Mode III

### Mode I

$$\begin{Bmatrix} \sigma_{11} \\ \sigma_{22} \\ \sigma_{12} \end{Bmatrix} = \frac{K_I}{\sqrt{2\pi r}} \cos \frac{\theta}{2} \begin{Bmatrix} 1 - \sin \frac{\theta}{2} \sin \frac{3\theta}{2} \\ 1 + \sin \frac{\theta}{2} \sin \frac{3\theta}{2} \\ \sin \frac{\theta}{2} \cos \frac{3\theta}{2} \end{Bmatrix}$$

$$\begin{Bmatrix} u_1 \\ u_2 \end{Bmatrix} = \frac{K_I}{2G} \sqrt{\frac{r}{2\pi}} \begin{Bmatrix} \cos \frac{\theta}{2} \left( \kappa - 1 + 2 \sin^2 \frac{\theta}{2} \right) \\ \sin \frac{\theta}{2} \left( \kappa + 1 - 2 \cos^2 \frac{\theta}{2} \right) \end{Bmatrix}$$

### Mode II

$$\begin{Bmatrix} \sigma_{11} \\ \sigma_{22} \\ \sigma_{12} \end{Bmatrix} = \frac{K_{II}}{\sqrt{2\pi r}} \begin{Bmatrix} \sin \frac{\theta}{2} \left( 2 + \cos \frac{\theta}{2} \cos \frac{3\theta}{2} \right) \\ \sin \frac{\theta}{2} \cos \frac{\theta}{2} \cos \frac{3\theta}{2} \\ \cos \frac{\theta}{2} \left( 1 - \sin \frac{\theta}{2} \sin \frac{3\theta}{2} \right) \end{Bmatrix}$$

$$\begin{Bmatrix} u_1 \\ u_2 \end{Bmatrix} = \frac{K_{II}}{2G} \sqrt{\frac{r}{2\pi}} \begin{Bmatrix} \sin \frac{\theta}{2} \left( \kappa + 1 + 2 \cos^2 \frac{\theta}{2} \right) \\ -\cos \frac{\theta}{2} \left( \kappa - 1 - 2 \sin^2 \frac{\theta}{2} \right) \end{Bmatrix}$$

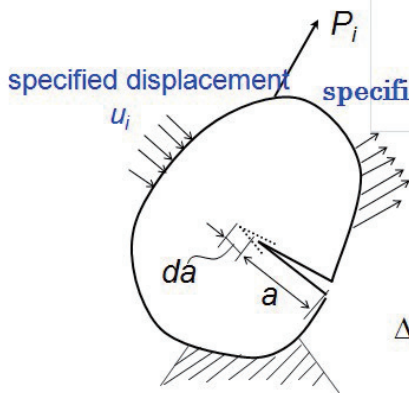
### Mode III

$$\begin{Bmatrix} \sigma_{13} \\ \sigma_{23} \end{Bmatrix} = \frac{K_{III}}{\sqrt{2\pi r}} \begin{Bmatrix} -\sin \frac{\theta}{2} \\ \cos \frac{\theta}{2} \end{Bmatrix} \begin{cases} \text{plane strain} \\ \kappa = 3 - 4\nu \end{cases}$$

$$u_3 = \frac{2K_{III}}{G} \sqrt{\frac{r}{2\pi}} \sin \frac{\theta}{2} \begin{cases} \text{plane stress} \\ \kappa = (3 - \nu)/(1 + \nu) \end{cases}$$

# Summary of Fracture Parameters

## Energy Release Rate



$$\sigma_{22}^{(a)} = \frac{K_I(a)}{\sqrt{2\pi x}} + \dots$$

$$u_2^{(b)} = \frac{\kappa+1}{2G} K_I(a+\Delta a) \sqrt{\frac{\Delta a - x_1}{\pi}} + \dots$$

$\Delta U =$  Work done by external force  $\Delta L$

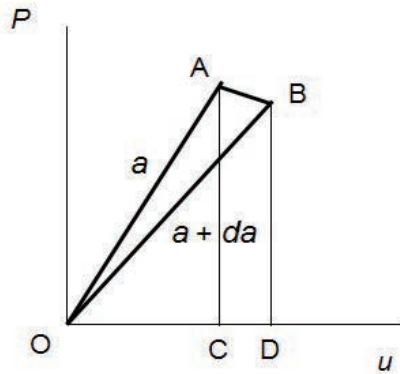
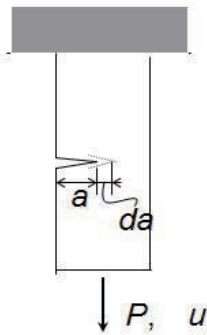
$$-2 \int_0^{\Delta a} \frac{1}{2} \sigma_{22}^{(a)} B u_2^{(b)} dx_1$$

$$\mathcal{G} = \lim_{\Delta a \rightarrow 0} \frac{2}{B \Delta a} \int_0^{\Delta a} \frac{1}{2} \sigma_{22}^{(a)} B u_2^{(b)} dx_1$$

$$= \frac{\kappa+1}{8G} (K_I^2 + K_{II}^2) + \frac{K_{III}^2}{2G}$$

$$\mathcal{G} = \frac{dL}{dA} - \frac{dU}{dA}$$

$$dA = B da$$



$$\mathcal{G} = \frac{dL}{dA} - \frac{dU}{dA} = \frac{1}{2} P^2 \frac{d\lambda}{B da} = \frac{\kappa+1}{8G} (K_I^2 + K_{II}^2) + \frac{K_{III}^2}{2G}$$

$$u = \lambda P$$

$\lambda$ : Compliance

$$U = \frac{1}{2} P u$$

# Elastoplastic Body

$n$  power law (deformation theory):

$$\left(\frac{\bar{\varepsilon}}{\varepsilon_0}\right) = \left(\frac{\bar{\sigma}}{\sigma_0}\right)^n \quad (n \geq 1)$$

$$\sigma_{ij} = K_\sigma r^{-1/(n+1)} \tilde{\sigma}_{ij}(\theta, n) + \dots$$

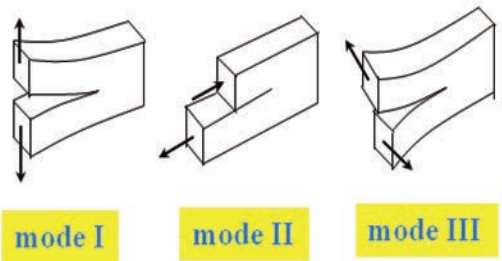
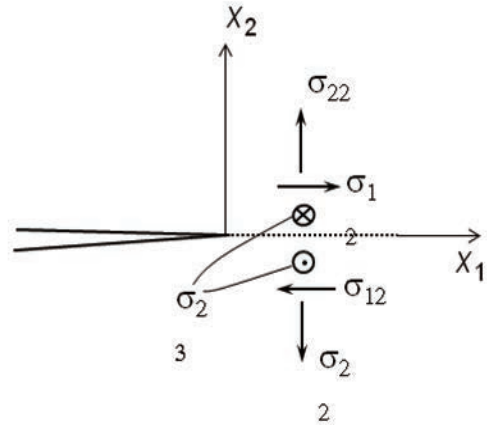
$$\varepsilon_{ij} = K_\varepsilon r^{-n/(n+1)} \tilde{\varepsilon}_{ij}(\theta, n) + \dots$$

: HRR singularity

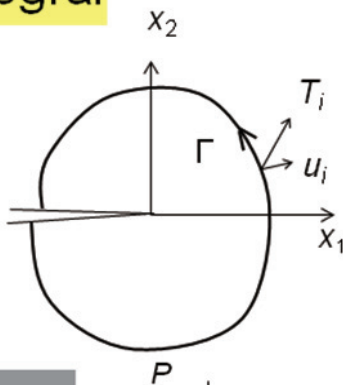
$K_\sigma$  : Plastic stress intensity factor

$K_\varepsilon$  : Plastic strain intensity factor

$$\frac{K_\varepsilon}{\varepsilon_0} = \left(\frac{K_\sigma}{\sigma_0}\right)^n$$



# J integral

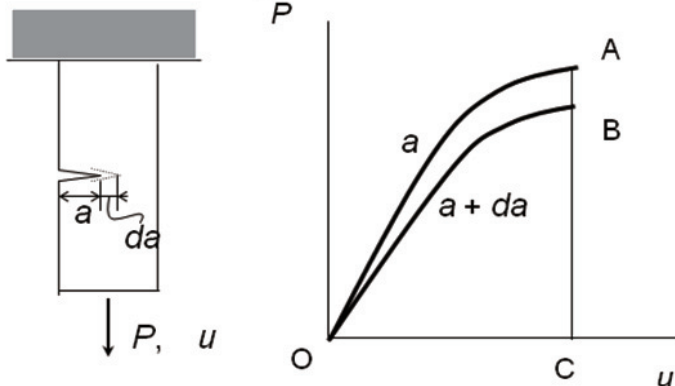


$$\sigma_{ij} = \frac{\partial W}{\partial \varepsilon_{ij}} = f_{ij}(\varepsilon_{11}, \varepsilon_{22}, \dots, \varepsilon_{31})$$

$W$  : Strain Energy Density  
(deformation theory)

Path Independent Integral

$$J = \int_{\Gamma} (W dx_2 - T_i u_{i,1} d\Gamma)$$



Load-Displacement Curves

Elastic Body  $\rightarrow$  Energy Release Rate

Linear Elastic Body

$$J = G = \frac{\kappa + 1}{8G} (K_I^2 + K_{II}^2) + \frac{K_{III}^2}{2G} = \frac{1}{2} P^2 \frac{d\lambda}{Bda}$$

Elastoplastic Body (deformation theory)

$n$  power law  $\rightarrow$  Meaning is not clear

$$J = \frac{I_n \varepsilon_0 K_\sigma^{n+1}}{\sigma_0^n} = I_n K_\sigma K_\varepsilon = \frac{I_n \sigma_0 K_\varepsilon^{(n+1)/n}}{\varepsilon_0^{1/n}}$$

$$\sigma_{ij} = K_\sigma r^{-1/(n+1)} \tilde{\sigma}_{ij}(\theta, n) + \dots$$

$$K_\sigma = \sigma_0 \left( \frac{J}{I_n \varepsilon_0 \sigma_0} \right)^{1/(n+1)}$$

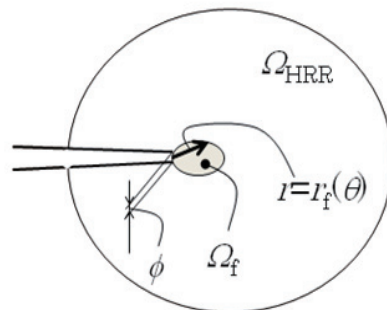
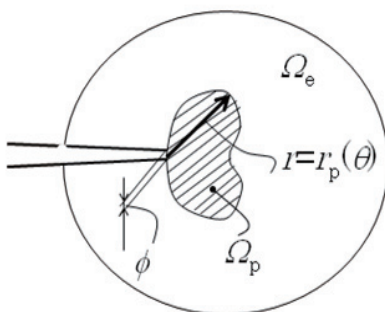
Stress Intensity Factor

Plastic Stress (Strain) Intensity Factor

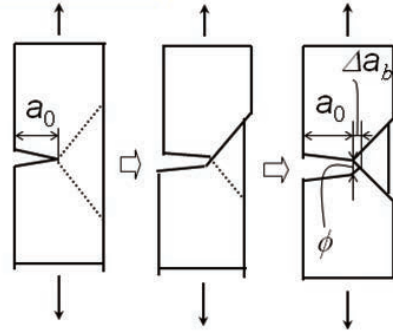
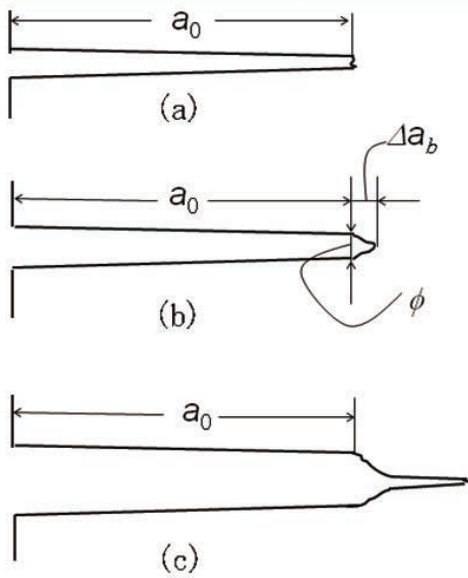
$$\begin{Bmatrix} \sigma_{11} \\ \sigma_{22} \\ \sigma_{12} \end{Bmatrix} = \frac{K_I}{\sqrt{2\pi r}} \cos \frac{\theta}{2} \begin{Bmatrix} 1 - \sin \frac{\theta}{2} \sin \frac{3\theta}{2} \\ 1 + \sin \frac{\theta}{2} \sin \frac{3\theta}{2} \\ \sin \frac{\theta}{2} \cos \frac{3\theta}{2} \end{Bmatrix}$$

$$\sigma_{ij} = K_\sigma r^{-1/(n+1)} \tilde{\sigma}_{ij}(\theta, n) + \dots$$

$$\varepsilon_{ij} = K_\varepsilon r^{-n/(n+1)} \tilde{\varepsilon}_{ij}(\theta, n) + \dots$$



## Actual Deformation around a Crack Tip



$\phi$  : COD  
( or CTOD )

$$\phi =$$

COD: Crack Opening Displacement

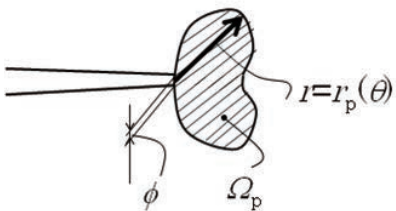
## Fracture Parameters and their availabilities

Stress Intensity Factor  
Energy Release Rate

**Linear Fracture Mechanics**

Plastic Stress Intensity Factor  
( Plastic Strain Intensity  
Factor )  
 $J$  integral  
COD

**Nonlinear Fracture Mechanics  
( Elastoplastic Fracture Mechanics )**



**Small Scale Yielding**  
 $r \ll a$

**Linear Fracture Mechanics**

**Large Scale Yielding**  
 $r \sim a$

**Nonlinear Fracture Mechanics**



## Applications to Fracture Phenomena

### Brittle Fracture (no plasticity)

$$K_I = K_{IC} \quad (\text{also for a stably growing crack})$$

or

$$G = G_{IC} = \frac{\kappa+1}{8G} K_{IC}^2 (= 2\gamma, \text{Griffith})$$

### Quasi-brittle Fracture (small scale yielding)

$$K_I = K_{IC} \quad (\text{also for a stably growing crack})$$

or

$$G = G_{IC} = \frac{\kappa+1}{8G} K_{IC}^2 (= 2\gamma, \text{Griffith - Orowan})$$

### Ductile Fracture (large scale yielding)

$$J = J_{IC} \quad (? \text{ for a stably growing crack})$$

## Brittle or Quasi-brittle Fracture

Stable

$$\frac{dK_I}{da} < 0 \quad (= \frac{dK_{IC}}{da})$$

Unstable

$$\frac{dK_I}{da} \geq 0 \quad (= \frac{dK_{IC}}{da})$$

## Ductile Fracture

Stable

$$\frac{dJ}{da} < \frac{dR}{da}$$

Unstable

$$\frac{dJ}{da} \geq \frac{dR}{da}$$

## Mixed Mode Fracture

Brittle or quasi-brittle fracture

criterion

Ductile fracture

?

## Fatigue Crack

$$\frac{da}{dN} = f(\Delta K)$$

## Creep Crack

$$\frac{da}{dt} = f(C^*) \quad \text{for stationary creep}$$

## Problems in Conventional Fracture Mechanics

1. The concept of energy release rate was considered successfully applied to elastoplastic fracture under small scale yielding. But, it failed to explain elastoplastic fracture under large scale yielding.
2. There exists no crack parameter that can be defined without depending on constitutive equation. Elastoplastic crack parameter  $J$  is defined just under deformation theory. It loses its meaning when unloading occurs and it is applicable just before the onset of crack growth. There is no way to deal with a growing elastoplastic crack.
3. There is no parameter for mixed mode elastoplastic crack.
4. Depending on phenomena, different parameters are required depending on phenomena.

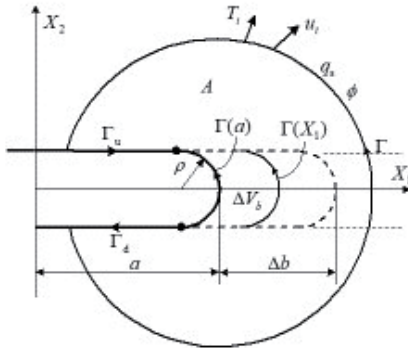
## Introduction of CED (Crack Energy Density)

"the work, expressed per unit area in the crack plane, done at the crack tip during deformation"

“き裂端が初期の状態から現在まで担ってきたエネルギーをき裂を含む面内の単位面積当たりで表したもの”

Continuum Model

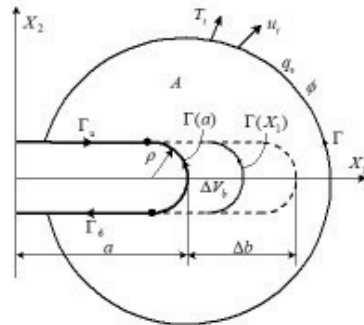
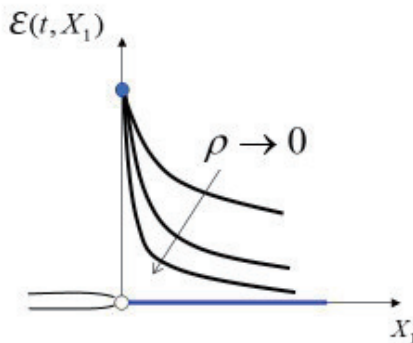
$$E = \lim_{\Delta b \rightarrow 0} \left( \int_{\Delta V_s} W dV \right) / \Delta b = \lim_{\Delta b \rightarrow 0} \int_a^{a+\Delta b} \left( \int_{\Gamma(X_1)} W dX_2 \right) dX_1 / \Delta b = \int_{\Gamma(a)} W dX_2$$



$$\text{When } \mathcal{E}(t, X_1) = \int_{\Gamma(X_1)} W dX_2,$$

$$\mathcal{E} = \mathcal{E}(t, a)$$

$$\text{Here } W = \int_0^t \sigma_{ij} \dot{\varepsilon}_{ij} d\tau$$



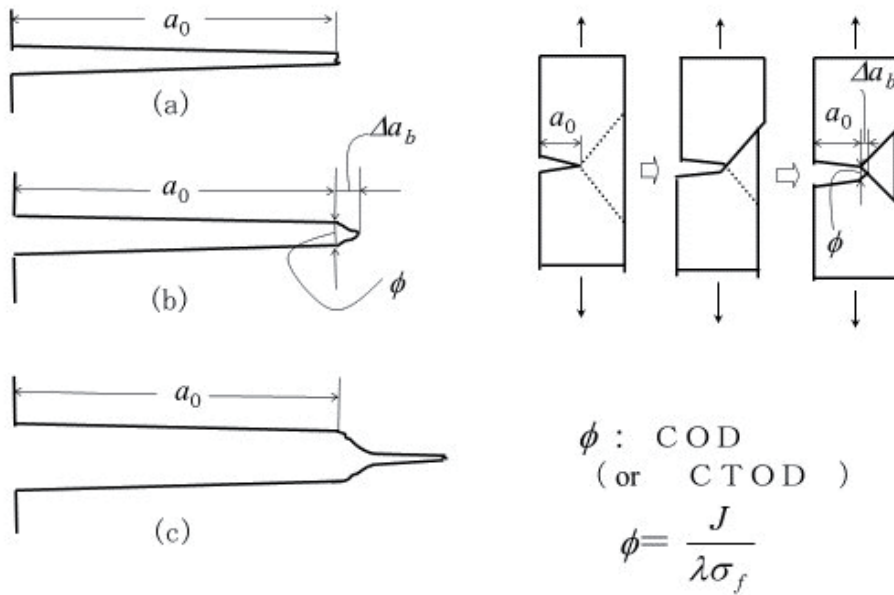
$$\text{For a crack of } \rho = 0 \quad \mathcal{E}^{(c)} = \lim_{\rho \rightarrow 0} \mathcal{E}(t, a) = \lim_{\rho \rightarrow 0} \int_{\Gamma(a)} W dX_2$$

$$\text{When } \sigma_{ij} = \frac{\partial W}{\partial \varepsilon_{ij}} = f_{ij}(\varepsilon_{11}, \varepsilon_{22}, \dots, \varepsilon_{31}), \quad \int_{\Gamma(a)} W dX_2 = \int_{\Gamma} (W dX_2 - T_i u_{i,1} d\Gamma)$$

$$\text{Therefore, } \mathcal{E}^{(c)} = J$$

$$\text{When } \rho \text{ is sufficiently small, } \mathcal{E}^{(c)} \cong \mathcal{E}(t, a) = \int_{\Gamma(a)} W dX_2$$

## Actual Deformation around a Crack Tip



Elastic Body  $\Rightarrow$  Energy Release Rate

Linear Elastic Body

$$J = G = \frac{\kappa + 1}{8G} (K_I^2 + K_{II}^2) + \frac{K_{III}^2}{2G} = \frac{1}{2} P^2 \frac{d\lambda}{Bda}$$

Elastoplastic Body (deformation theory)

$n$  power law  $\Rightarrow$  Meaning is not clear

$$J = \frac{I_n \varepsilon_0 K_\sigma^{n+1}}{\sigma_0^n} = I_n K_\sigma K_\varepsilon = \frac{I_n \sigma_0 K_\varepsilon^{(n+1)/n}}{\varepsilon_0^{1/n}}$$

$$\sigma_{ij} = K_\sigma r^{-1/(n+1)} \tilde{\sigma}_{ij}(\theta, n) + \dots$$

$$K_\sigma = \sigma_0 \left( \frac{J}{I_n \varepsilon_0 \sigma_0} \right)^{1/(n+1)}$$



## Small Scale Yielding

$$\mathcal{E}^{(c)} \cong J \cong \frac{\kappa + 1}{8G} (K_{\text{I}}^2 + K_{\text{II}}^2) + \frac{K_{\text{III}}^2}{2G}$$

## Large Scale Yielding

$$\mathcal{E}^{(c)} \cong J$$

## Creep Crack

When stationary creep is realized,

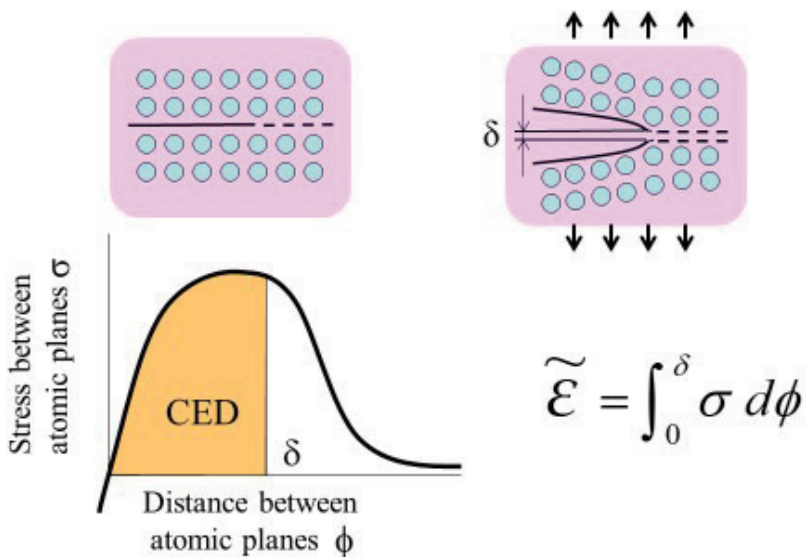
$$\dot{\mathcal{E}}^{(c)} = CC^* \quad (C : \text{const}, C^* = \int_{\Gamma} (W' dx_2 - T_i \dot{u}_{i,1} d\Gamma))$$

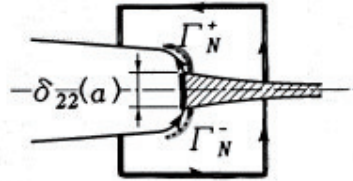
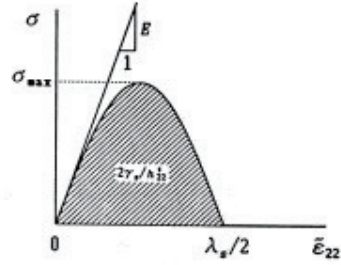
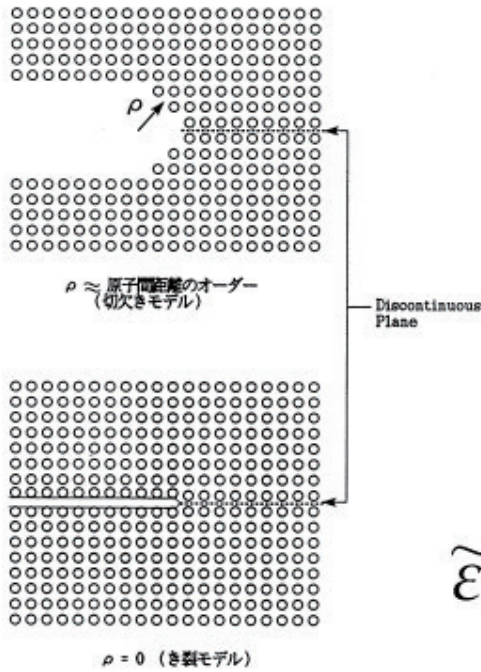
When Norton's rule  $\dot{\epsilon}^{cr} = A\sigma^n$  is employed,

$$C = \frac{n+1}{n}$$

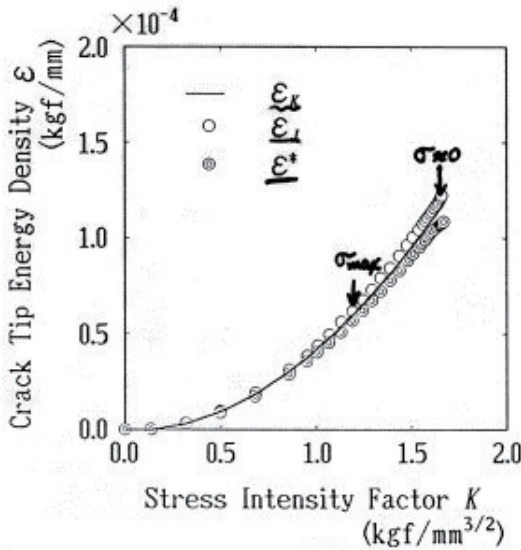
## CED for Atomic Array Model

*"the work, expressed per unit area in the crack plane, done at the crack tip during deformation"*





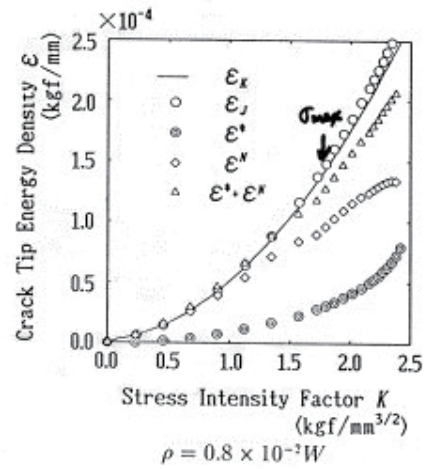
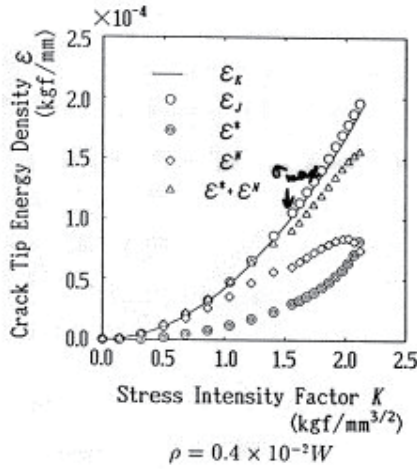
$$\tilde{\mathcal{E}} = \int_0^{\delta_{22}} \sigma d\phi + \int_{\Gamma_n} W dX_2$$



$$\tilde{\mathcal{E}} = \int_0^{\delta_{22}} \sigma d\phi$$

$$\mathcal{E}_K = \mathcal{E}^{(c)} = \frac{(\kappa+1)}{8G} K_I^2$$

$$\tilde{\mathcal{E}} \cong \mathcal{E}^{(c)}$$



$$\tilde{\mathcal{E}} = \int_0^{\delta_{22}} \sigma d\phi + \int_{\Gamma_n} W dX_2 \quad \mathcal{E}_K = \mathcal{E}^{(c)} = \frac{(\kappa + 1)}{8G} K_1^2$$

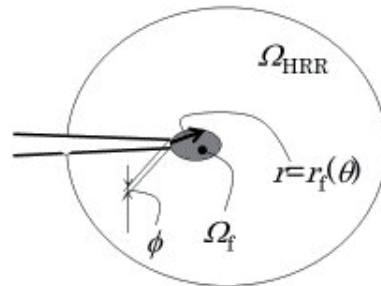
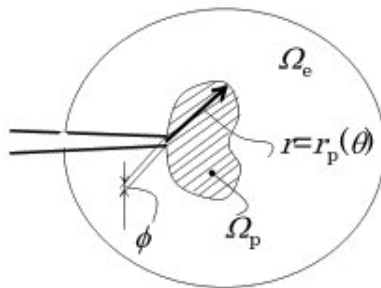
$$\tilde{\mathcal{E}} \cong \mathcal{E}^{(c)}$$

**Stress Intensity Factor**

**Plastic Stress (Strain) Intensity Factor**

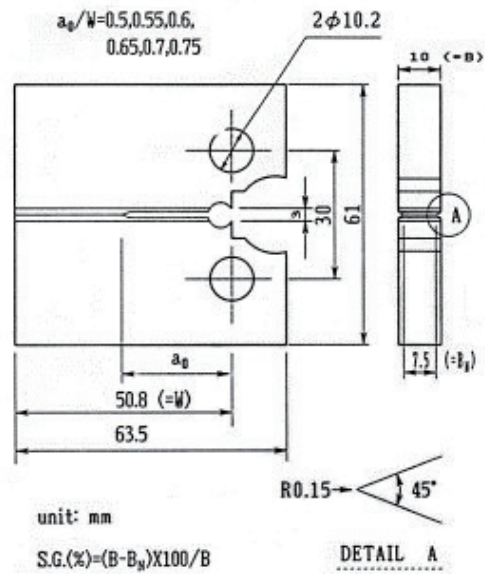
$$\begin{cases} \sigma_{11} \\ \sigma_{22} \\ \sigma_{12} \end{cases} = \frac{K_1}{\sqrt{2\pi r}} \cos \frac{\theta}{2} \begin{cases} 1 - \sin \frac{\theta}{2} \sin \frac{3\theta}{2} \\ 1 + \sin \frac{\theta}{2} \sin \frac{3\theta}{2} \\ \sin \frac{\theta}{2} \cos \frac{3\theta}{2} \end{cases}$$

$$\begin{aligned} \sigma_{ij} &= K_\sigma r^{-1/(n+1)} \tilde{\sigma}_{ij}(\theta, n) + \dots \\ \varepsilon_{ij} &= K_\varepsilon r^{-n/(n+1)} \tilde{\varepsilon}_{ij}(\theta, n) + \dots \end{aligned}$$

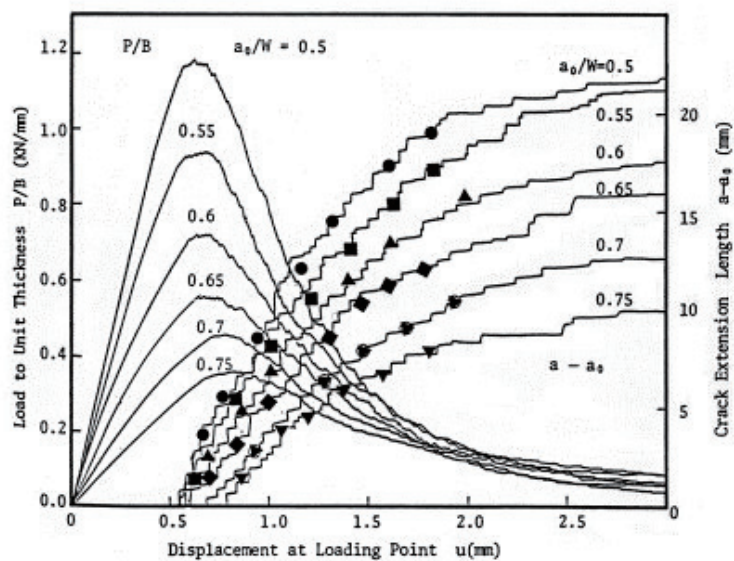




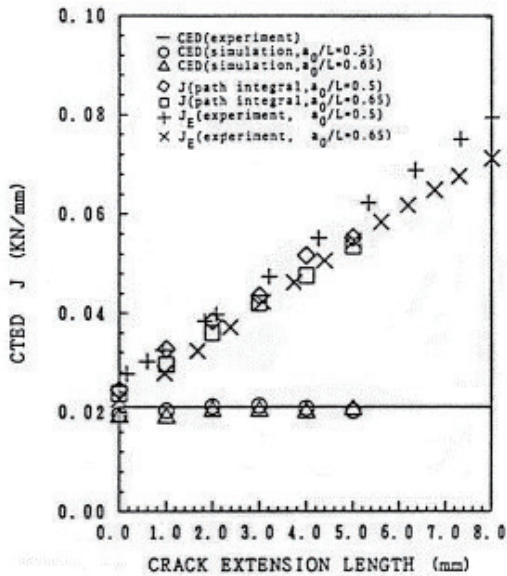
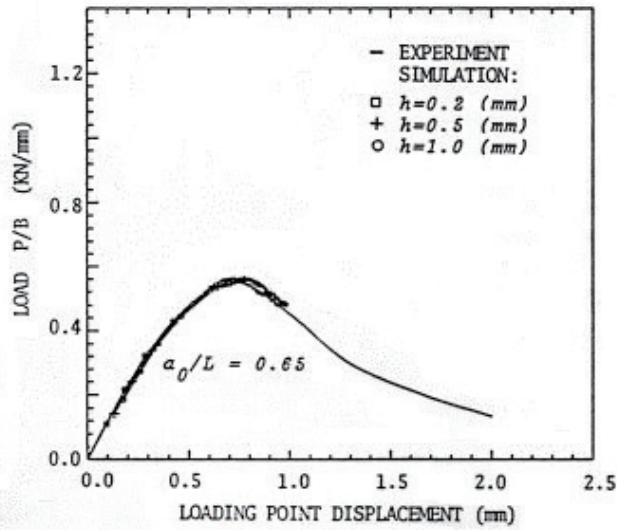
## Stable Growth of an Elastoplastic Crack



Load-Displacement and Crack Extension Length-Displacement curves



Comparison of Load-Displacement Curve from Generation Type FEM Crack Growth Simulation with Experimental Result



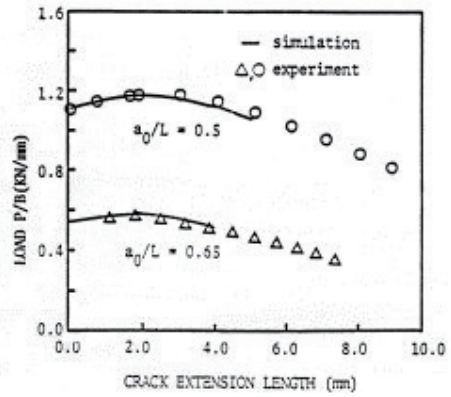
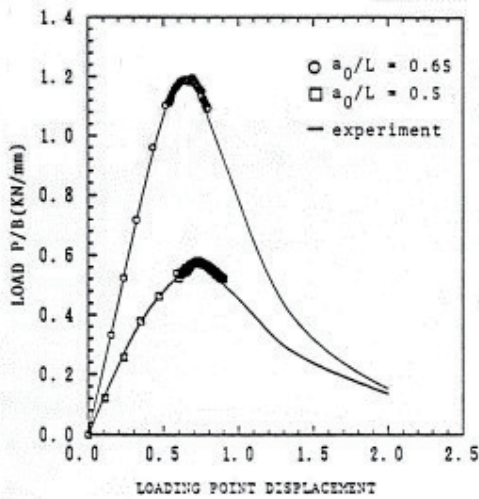
$$\mathcal{E} = \mathcal{E}_{IC} \cong J_{IC}$$

is always available.

$$J = J_{IC}$$

is available  
only as the onset condition

Application Type FEM Crack Growth Simulation  
Based on Crack Growth Criterion of  $\mathcal{E} = \mathcal{E}_{IC}$



Brittle or Quasi-brittle Fracture

Stable

$$\frac{dK_I}{da} < 0 \left( = \frac{dK_{IC}}{da} \right)$$

Unstable

$$\frac{dK_I}{da} \geq 0 \left( = \frac{dK_{IC}}{da} \right)$$

Ductile Fracture

$$\frac{dJ}{da} < \frac{dR}{da}$$

$$\frac{dJ}{da} \geq \frac{dR}{da}$$

Tearing modulus

$$T_J = \frac{E}{\sigma_f^2} \frac{dJ}{da}$$

$$T_J < T_{JC}$$

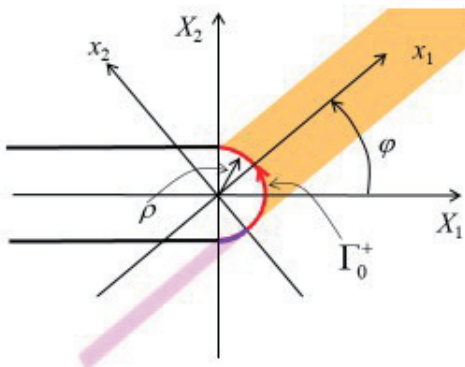
$$T_J \geq T_{JC}$$

## Brittle or Quasi-brittle Fracture

Stable	Unstable
$\frac{dK_I}{da} < 0 (= \frac{dK_{IC}}{da})$	$\frac{dK_I}{da} \geq 0 (= \frac{dK_{IC}}{da})$
or $\frac{d\mathcal{E}}{da} < 0 (= \frac{d\mathcal{E}_{IC}}{da})$	$\frac{d\mathcal{E}}{da} \geq 0 (= \frac{d\mathcal{E}_{IC}}{da})$
<b>Ductile Fracture</b>	
$\frac{d\mathcal{E}}{da} < 0 (= \frac{d\mathcal{E}_{IC}}{da})$	$\frac{d\mathcal{E}}{da} \geq 0 (= \frac{d\mathcal{E}_{IC}}{da})$
Tearing modulus	$T_{\mathcal{E}} = \frac{E}{\sigma_f^2} \frac{d\mathcal{E}}{da}$
$T_{\mathcal{E}} < 0$	$T_{\mathcal{E}} \geq 0$

## Mixed Mode Crack

### CED in an Arbitrary Direction



$$\mathcal{E}_{\varphi} = \int_{\Gamma_0^+} W dx_2$$

Here,  $W = \int_0^t \sigma_{ij} \dot{\epsilon}_{ij} d\tau$

For a crack of  $\rho = 0$

$$\mathcal{E}_{\varphi}^{(c)} = \lim_{\rho \rightarrow 0} \mathcal{E}_{\varphi}$$

Division into mode I, mode II and mode III contributions

$$\mathcal{E}_{\varphi}^{(c)} = \mathcal{E}_{\varphi}^{I(c)} + \mathcal{E}_{\varphi}^{II(c)} + \mathcal{E}_{\varphi}^{III(c)}$$

## Linear Elastic Body

$$\begin{aligned} \mathcal{E}_{\varphi}^{(c)} = \mathcal{E}_{\varphi}^{I(c)} + \mathcal{E}_{\varphi}^{II(c)} + \mathcal{E}_{\varphi}^{III(c)} &= \frac{K_I^2}{8G} \sin^2 \frac{\varphi}{2} (\kappa + \cos \varphi) + \frac{K_{II}^2}{8G} \cos^2 \frac{\varphi}{2} (\kappa - 3 \cos \varphi + 4) \\ &\quad + \frac{K_I K_{II}}{8G} \sin \varphi (-\kappa - 2 \cos \varphi - 1) + \frac{K_{III}^2}{2G} \cos^2 \frac{\varphi}{2} \end{aligned}$$

$$\mathcal{E}_{\varphi}^{I(c)} = \frac{K_I^2}{8G} \cos^4 \frac{\varphi}{2} (\kappa + \cos \varphi) + \frac{K_{II}^2}{8G} 3 \sin^2 \frac{\varphi}{2} (\kappa + 2 + 3 \cos \varphi) + \frac{K_I K_{II}}{8G} 2 \sin \frac{\varphi}{2} \cos^3 \frac{\varphi}{2} (-2\kappa - 1 - 3 \cos \varphi)$$

$$\mathcal{E}_{\varphi}^{II(c)} = \frac{K_I^2}{8G} \sin^2 \frac{\varphi}{2} \cos^2 \frac{\varphi}{2} (\kappa + \cos \varphi) + \frac{K_{II}^2}{8G} \sin^2 \frac{\varphi}{2} (3 \cos^2 \frac{\varphi}{2} - 2)(\kappa - 2 + 3 \cos \varphi) + \frac{K_I K_{II}}{8G} \sin \frac{\varphi}{2} (\kappa \cos \varphi + 1 - \frac{3}{2} \sin^2 \varphi)$$

$$\mathcal{E}_{\varphi}^{III(c)} = \frac{K_{III}^2}{2G} \cos^2 \frac{\varphi}{2}$$

When  $\varphi = 0^\circ$ ,

$$\mathcal{E}_{\varphi}^{I(c)} = \frac{\kappa + 1}{8G} K_I^2$$

$$\mathcal{E}_{\varphi}^{II(c)} = \frac{\kappa + 1}{8G} K_{II}^2$$

$$\mathcal{E}_{\varphi}^{III(c)} = \frac{K_{III}^2}{2G}$$

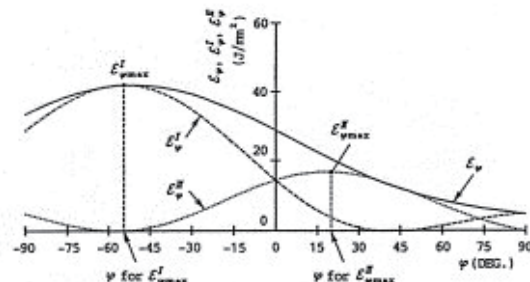


図4  $\mathcal{E}_{\varphi}$ ,  $\mathcal{E}_{\varphi}^I$ ,  $\mathcal{E}_{\varphi}^{II}$  と  $\varphi$  の関係  
( $K_{II}/K_I = 1.0$ )

## Fracture Criterion

▪  $\mathcal{E}_{\varphi \max}^I$  criterion :

When  $\mathcal{E}_{\varphi \max}^I = \mathcal{E}_{IC} \cong J_{IC}$ ,

mode I fracture occurs in the

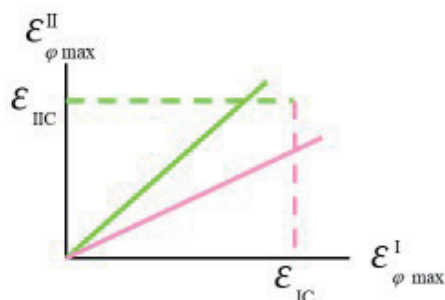
direction of  $\mathcal{E}_{\varphi \max}^I$ .

▪  $\mathcal{E}_{\varphi \max}^{II}$  criterion :

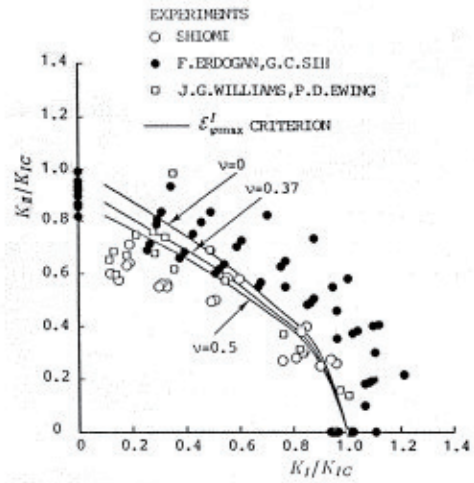
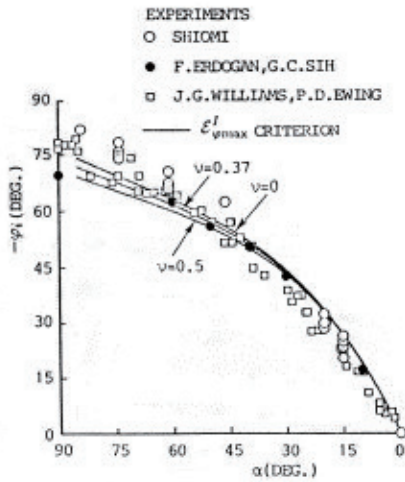
When  $\mathcal{E}_{\varphi \max}^{II} = \mathcal{E}_{IIC}$ ,

mode II fracture occurs in the

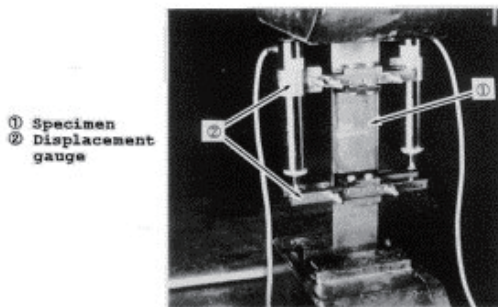
direction of  $\mathcal{E}_{\varphi \max}^{II}$ .



## Brittle Fracture under Mixed Mode Load

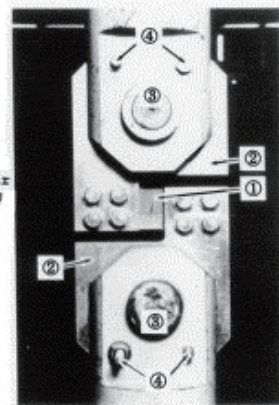


## Ductile Fracture Test under Mixed Mode



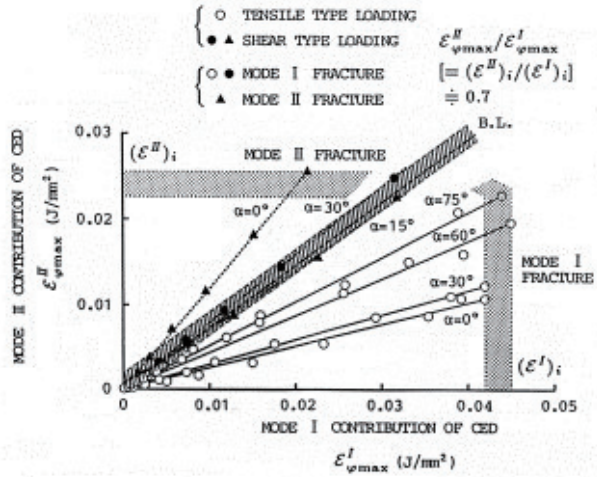
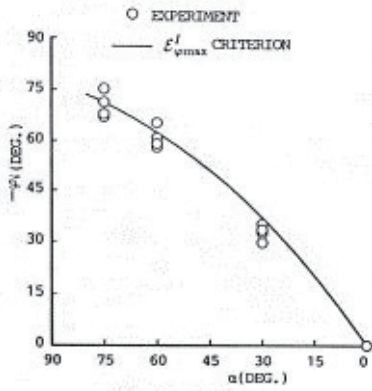
(a) under tensile type loading

- ① Specimen  
② Jig for shear type loading  
③ Chuck pin  
④ Bolt

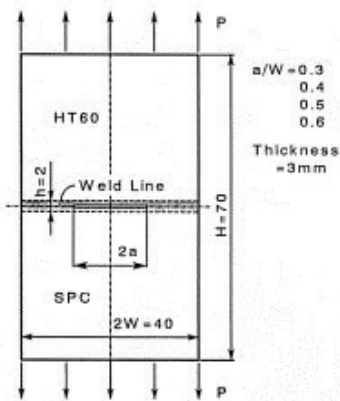


(b) under shear type loading

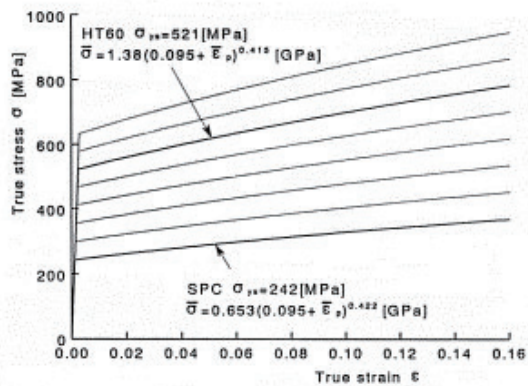
Experimental configurations



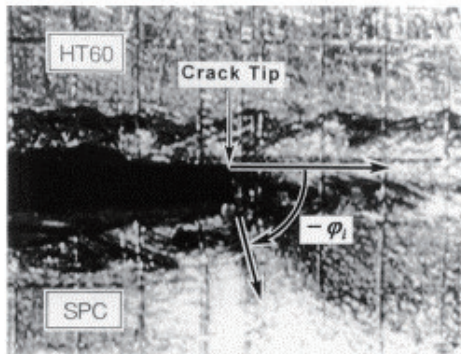
$(\epsilon^{\text{I}})_i$  : Critical value for mode I fracture  
 $(\epsilon^{\text{II}})_i$  : Critical value for mode II fracture  
 ▨ : Boundary across which the fracture mode changes



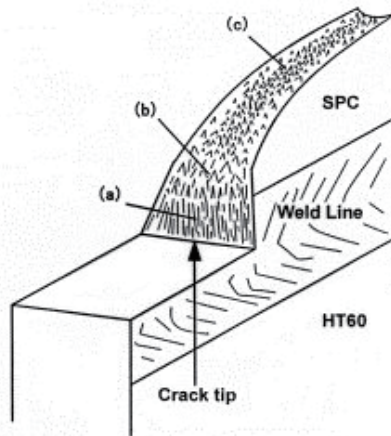
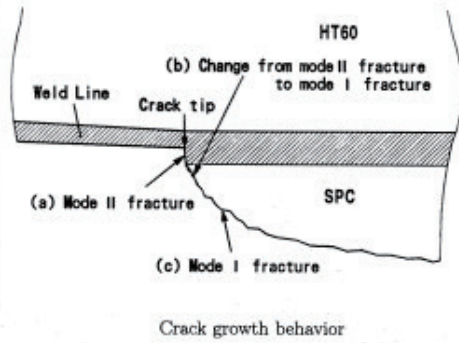
Specimen configuration



Stress-strain curves

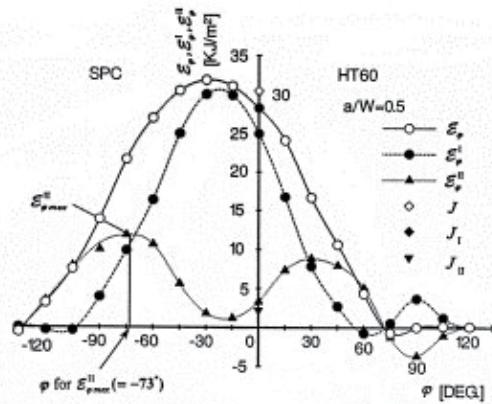


Direction of crack growth



Schematic fracture surface





Distributions of  $\mathcal{E}_\varphi$ ,  $\mathcal{E}_\varphi^I$  and  $\mathcal{E}_\varphi^{II}$  versus  $\varphi$  at the onset of crack growth ( $a/W = 0.5$ )

$\varphi_i$ ,  $\varphi$  for  $\mathcal{E}_{\varphi\max}^I$  and  $\mathcal{E}_{\varphi\max}^{II}$  at the onset of crack growth

Specimen	$a/W=0.3$	$a/W=0.4$	$a/W=0.5$	$a/W=0.6$
$\varphi_i$ (Experiment)	-76°	-72°	-77°	-75°
$\varphi$ for $\mathcal{E}_{\varphi\max}^{II}$	-74°	-73°	-73°	-72°
$\mathcal{E}_{\varphi\max}^{II}$	10.8kJ/m <sup>2</sup>	11.6kJ/m <sup>2</sup>	11.8kJ/m <sup>2</sup>	11.9kJ/m <sup>2</sup>

## Conventional Fracture Mechanics

Brittle Fracture (no plasticity)

$$K_I = K_{IC} \text{ (also for a stably growing crack)}$$

or

$$\mathcal{G} = \mathcal{G}_{IC} = \frac{\kappa+1}{8G} K_{IC}^2 \text{ (= } 2\gamma, \text{ Griffith)}$$

Quasi-brittle Fracture (small scale yielding)

$$K_I = K_{IC} \text{ (also for a stably growing crack)}$$

or

$$\mathcal{G} = \mathcal{G}_{IC} = \frac{\kappa+1}{8G} K_{IC}^2 \text{ (= } 2\gamma, \text{ Griffith - Orowan)}$$

(?)

Ductile Fracture (large scale yielding)

$$J = J_{IC} \text{ (? for a stably growing crack)}$$

## CED-based Fracture Mechanics

Always,

$$\mathcal{E} = \mathcal{E}_{IC} \cong J_{IC}$$

Linear elastic

$$\mathcal{E}^{(e)} = \frac{\kappa+1}{8G} K_I^2 = \mathcal{G}$$

Small Scale Yielding

$$\mathcal{E}^{(e)} \cong \frac{\kappa+1}{8G} K_I^2 \neq \mathcal{G}$$

In these cases, the fracture condition above can be expressed also by

$$K_I = K_{IC}$$

### Mixed Mode Fracture

Brittle or quasi-brittle fracture

$\sigma_{\theta \max}$  criterion

Ductile fracture

?

### Fatigue Crack

$$\frac{da}{dN} = f(\Delta K)$$

### Creep Crack

$$\frac{da}{dt} = f(C^*)$$

for stationary creep

### Mixed Mode Fracture

$$\epsilon_{\phi \max}^I = \epsilon_{IC} \cong J_{IC}$$

or

$$\epsilon_{\phi \max}^{II} = \epsilon_{IIC}$$

### Fatigue Crack

$$\frac{da}{dN} = f(\Delta \epsilon)$$

### Creep Crack

$$\frac{da}{dt} = f(\dot{\epsilon})$$

$\epsilon$ : Cumulative Damage

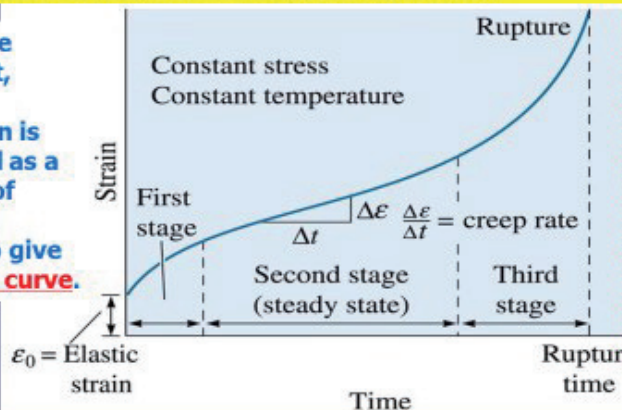
## ➤ Summary of Creep Fracture Parameters (Mode-I)

### Evaluation of Creep Behavior:

**Creep**- a time dependent, permanent deformation at high temperature, occurring at constant load or constant stress.

**Creep rate** - The rate at which a material deforms when a stress is applied at a high temperature.

During the creep test, strain or elongation is measured as a function of time and plotted to give the **creep curve**.



The resulting curve shows three stages. During the first stage, dislocations climb and break free from whatever was pinning them. **The second stage of creep is characterized by a steady rate of strain.** In the third stage, necking and failure occur.

## ➤ Summary of Creep Fracture Parameters (Mode-I)

### Creep Crack ( $C^*$ parameter)

Analogy to Elastoplastic Problem under **Deformation Theory** (全ひずみ理論)

Elastoplastic

$$\sigma_{y,j} = 0$$

$$\varepsilon_{ij} = \frac{1}{2}(u_{i,j} + u_{j,i})$$

$$\sigma_{ij} = \frac{\partial W}{\partial \varepsilon_{ij}}$$

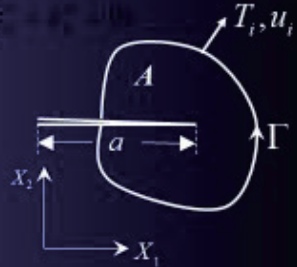
Hoff

Stationary Creep

$$\sigma_{y,j} = 0$$

$$\dot{\varepsilon}_{ij}^{cr} = \frac{1}{2}(\dot{u}_{i,j} + \dot{u}_{j,i})$$

$$\sigma_{ij} = \frac{\partial W}{\partial \dot{\varepsilon}_{ij}^{cr}}$$



$$J = \int_{\Gamma} (W dx_2 - T_i u_{i,1} d\Gamma)$$

$$C^* = \int_{\Gamma} (W \cdot dx_2 - T_i \dot{u}_{i,1} d\Gamma)$$

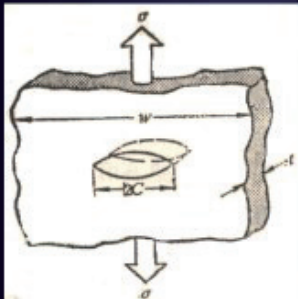
**n power law**  $\left(\frac{\bar{\varepsilon}}{\varepsilon_0}\right) = \left(\frac{\bar{\sigma}}{\sigma_0}\right)^n$

**Norton's rule**  $\dot{\varepsilon}^{cr} = A \sigma^n$

$$\sigma_{ij} = \sigma_0 \left( \frac{J}{I_n \varepsilon_0 \sigma_0} \right)^{1/(n+1)} r^{-1/(n+1)} \tilde{\sigma}_{ij}(\theta, n) + \dots$$

$$\sigma_{ij} = \sigma_0 \left( \frac{C^*}{I_n A} \right)^{1/(n+1)} r^{-1/(n+1)} \tilde{\sigma}_{ij}(\theta, n) + \dots$$

### Background



#### Fracture Parameter

- J-integral
- Path-independent

#### Creep (high temp property)

- $C^*$  parameter
- Steady state creep conditions



Mixed-mode

# The analysis method

## Energy variation method

– The principal aspect of crack analysis

Basic Model: A crack in a two-dimensional deformation field

+

Auxiliary Model: Due to the difference of initial crack



An arbitrary integration path surrounding the crack

A new path-independent integral



Creep Analogy

Steady-state creep crack problem

# The Creep Analogy

-HOFF

Plastic Deformation Theory

Steady-state Creep

displacement  $u_i$



displacement velocity  $\dot{u}_i$

strain  $\varepsilon_{ij}$



strain rate  $\dot{\varepsilon}_{ij}$

$$\sigma_{ij} = \frac{\partial W}{\partial \varepsilon_{ij}}$$

Strain energy density



$$\sigma_{ij} = \frac{\partial W'}{\partial \dot{\varepsilon}_{ij}}$$

Strain energy rate density

Power law

$$\varepsilon = \varepsilon_0 \left( \frac{\sigma}{\sigma_0} \right)^n$$



Norton rule

$$\dot{\varepsilon} = \dot{\varepsilon}_0 \left( \frac{\sigma}{\sigma_0} \right)^n$$

$$J = \int_{\Gamma} (W n_1 - T_i u_{i,1}) d\Gamma$$



$$C^* = \int_{\Gamma} (W' n_1 - T_i \dot{u}_{i,1}) d\Gamma$$

## The Previous Conditions

- A two-dimensional crack in a homogeneous, elastic-plastic body
- A sharp (not necessarily straight) crack
- A stationary crack/stable crack growth before final fracture
- Simple loading conditions

8

## J-integral – as a fracture criterion parameter

$$J = \int_{\Gamma} (Wn_1 - T_i u_{i,1}) d\Gamma$$

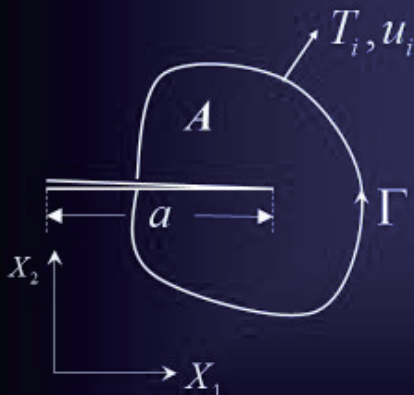


Fig. 1 An arbitrary integration path surrounding a crack

### Properties

- Avoid concentrated stresses and strains in the vicinity of a crack tip
- Arbitrary integration path
- Path-independent

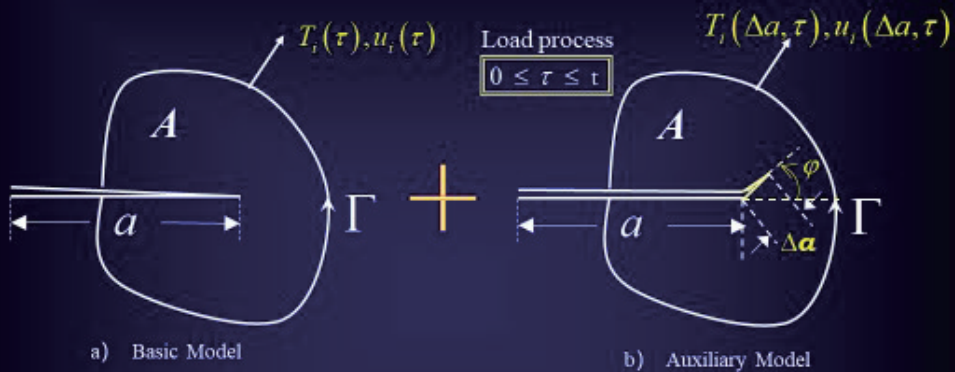
### Conditions

- Small strain deformation
- Deformation Plasticity
- No body force
- Homogeneous, at least in  $x_1$
- Straightforward Crack

An Arbitrary Direction

9

## A New Path-independent Integral



$$\int_{\Gamma} \int_0^{\tau} \left( \dot{T}_i \frac{\partial u_i}{\partial a} - \dot{u}_i \frac{\partial T_i}{\partial a} \right) d\tau d\Gamma$$



Path-independent

Under a kind of boundary conditions

10

## Analysis Methods

### 1. Comparison of two cracked bodies differing in geometry

- Identical shape
- Identical composition
- Identical loading by displacements
- Differing in crack size only

### 2. A study of energy variations ...

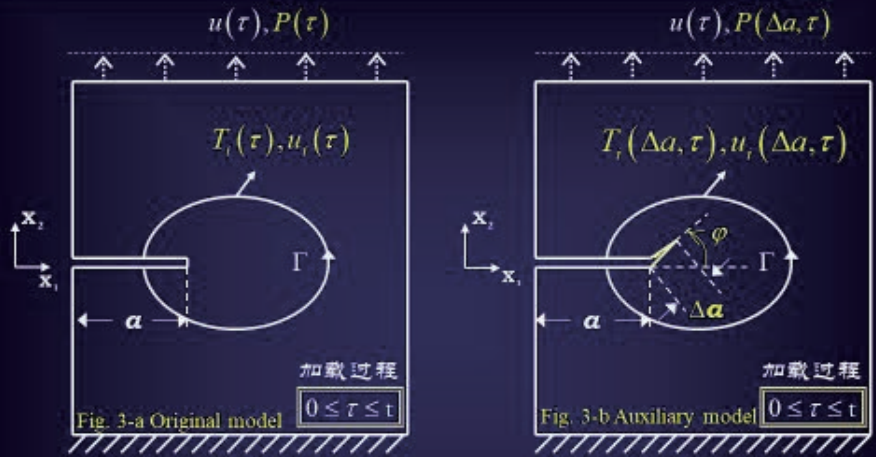
- A crack in an arbitrary structure
- Contour  $\Gamma$  is common to both bodies
- Plastic deformation theory or nonlinear elastic behavior

### 3. Treatments of potential energy difference and path independence ...



11

Two specimens with a different initial crack lengths



- Fig.3-a and Fig.3-b Comparison of two cracked bodies of identical shape, composition, and loading by displacements, except the crack of body 1-b is longer by an amount  $\Delta a$  in an arbitrary direction  $\varphi$

Load-displacement  $P$ - $u$  curves

on any arbitrary common contour  $\Gamma$   
Traction-displacement  $T_i$ - $u_i$  curves

Load-displacement  $P$ - $u$  curves

on any arbitrary common contour  $\Gamma$   
Traction-displacement  $T_i$ - $u_i$  curves

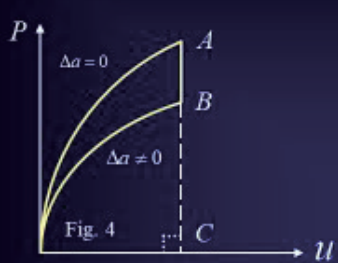


Fig.4 : Difference between potential energies of 1-a and 1-b

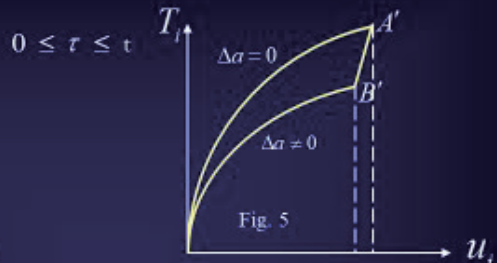


Fig.5 : Area between Traction-displacement curves when loading is by displacements alone

Potential energies of both models :

$$U(a) = \int_0^t P(a, \tau) u d\tau$$

$$U(a + \Delta a) = \int_0^t P(a + \Delta a, \tau) u d\tau$$

Difference between potential energies :

$$\Delta U = U(a + \Delta a) - U(a)$$

In the special case of  $\varphi=0^\circ$

# J contour integral

## A Straightforward J-integral

$$J = - \lim_{\Delta a \rightarrow 0} \frac{\Delta U}{\Delta a}$$

$\Delta U$  : Difference between potential energies

Rate of potential energy decrease for two bodies differing in crack length by an infinitesimal amount

Energy release rate  
can be interpreted as Crack driving force

$$= \int_{\Gamma} (Wn_1 - T_i u_{i,1}) d\Gamma$$

Conventional definition of J integral

$$= \int_{\Gamma} T_i \frac{\partial u_i}{\partial a} d\Gamma - \int_A \frac{\partial W}{\partial a} dA$$

Referred to virtual crack extension force

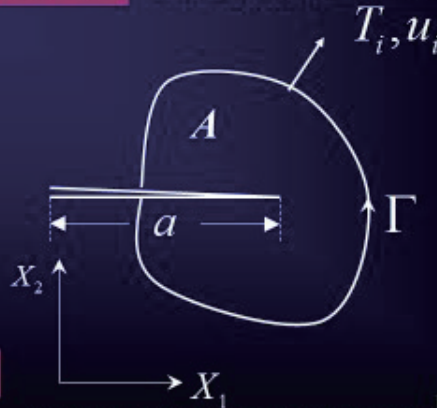


Fig. 1 An arbitrary integration path surrounding a crack

In the general case of  $\varphi \neq 0^\circ$

# Load-displacement and Traction-displacement curves

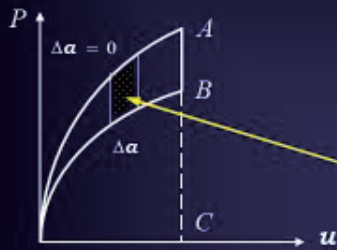


Fig. 6 Load-displacement curves

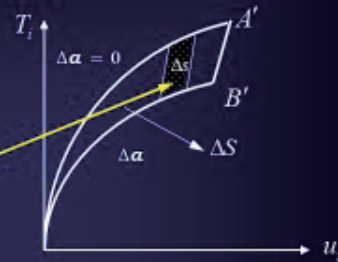


Fig. 7 Traction-displacement curves

Increment  $\Delta s$  :

$$\Delta s = \begin{vmatrix} u_i & T_i & 1 \\ u_i + \frac{\partial u_i}{\partial a} \Delta a & T_i + \frac{\partial T_i}{\partial a} \Delta a & 1 \\ u_i + \dot{u}_i \Delta \tau & T_i + \dot{T}_i \Delta \tau & 1 \end{vmatrix} = \left( \dot{T}_i \frac{\partial u_i}{\partial a} - \dot{u}_i \frac{\partial T_i}{\partial a} \right) \Delta a \Delta \tau$$

Area between traction-displacement curves for the two bodies :

$$\Delta S = \int_{\Gamma} Area(O'A'B') d\Gamma = \Delta a \int_{\Gamma} \int_0^{\tau} \left( \dot{T}_i \frac{\partial u_i}{\partial a} - \dot{u}_i \frac{\partial T_i}{\partial a} \right) d\tau d\Gamma$$



**Traction-displacement curves within  $\tau \square \tau + \Delta\tau$**

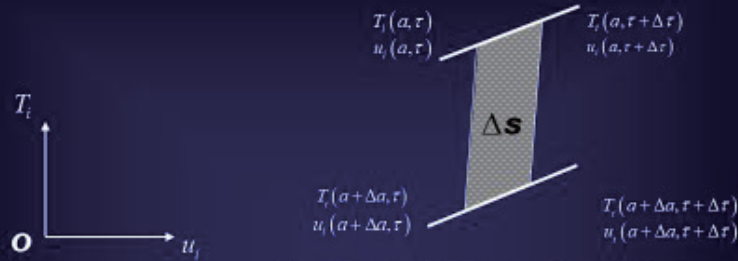


Fig. 7 Traction-displacement curves within  $\Delta\tau$

*based on Calculus and Analysis geometry*

**Increment  $\Delta s$  (as indicated by the shaded area in Fig.7) :**

$$\Delta s = \begin{vmatrix} u_i & T_i & 1 \\ u_i + \frac{\partial u_i}{\partial a} \Delta a & T_i + \frac{\partial T_i}{\partial a} \Delta a & 1 \\ u_i + \dot{u}_i \Delta \tau & T_i + \dot{T}_i \Delta \tau & 1 \end{vmatrix} = \left( \dot{T}_i \frac{\partial u_i}{\partial a} - \dot{u}_i \frac{\partial T_i}{\partial a} \right) \Delta a \Delta \tau$$

**In the general case of  $\varphi \neq 0^\circ$**

**New Contour Integral :**

**D-Integral**

$$D = \lim_{\Delta a \rightarrow 0} \frac{\Delta S}{\Delta a} = \int_{\Gamma} \int_{\theta}^{\tau} \left( \dot{T}_i \frac{\partial u_i}{\partial a} - \dot{u}_i \frac{\partial T_i}{\partial a} \right) d\tau d\Gamma$$



*Creep Analogy*

**For Steady-state creep crack problem**

**A New Path-independent Integral :**

**D'-Integral**

**D-Integral**  $\int_{\Gamma} \int_0^t \left( \dot{T}_i \frac{\partial u_i}{\partial a} - \dot{u}_i \frac{\partial T_i}{\partial a} \right) d\tau d\Gamma$  *Somewhat like Betti's reciprocal work theorem*

$$\begin{aligned} & \int_{\Gamma} \int_0^t \left( \dot{T}_i \frac{\partial u_i}{\partial a} - \dot{u}_i \frac{\partial T_i}{\partial a} \right) d\tau d\Gamma \\ &= \int_{\Gamma} \int_0^t \left( \dot{T}_i \frac{\partial u_i}{\partial a} + T_i \frac{\partial \dot{u}_i}{\partial a} \right) d\tau d\Gamma - \int_{\Gamma} \int_0^t \left( \dot{u}_i \frac{\partial T_i}{\partial a} + T_i \frac{\partial \dot{u}_i}{\partial a} \right) d\tau d\Gamma \\ &= \int_{\Gamma} T_i \frac{\partial u_i}{\partial a} d\Gamma - \int_{\Gamma} \left( \frac{\partial}{\partial a} \int_0^t T_i \dot{u}_i d\tau \right) d\Gamma \\ &= \int_{\Gamma} T_i \frac{\partial u_i}{\partial a} d\Gamma - \int_V \frac{\partial W}{\partial a} dV \end{aligned}$$

**Notice:**

$$\begin{aligned} \int_V \frac{\partial W}{\partial a} dV &= \int_V \left( \frac{\partial}{\partial a} \int_0^t \sigma_{ij} \dot{\epsilon}_{ij} d\tau \right) dV \\ &= \int_{\Gamma} \left( \frac{\partial}{\partial a} \int_0^t T_i \dot{u}_i d\tau \right) d\Gamma \end{aligned}$$

*Similar to Virtual crack extensive force*

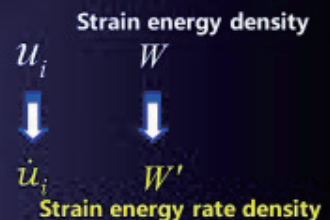
18

**D-Integral**  $= \int_{\Gamma} \int_0^t \left( \dot{T}_i \frac{\partial u_i}{\partial a} - \dot{u}_i \frac{\partial T_i}{\partial a} \right) d\tau d\Gamma$

$$= \int_{\Gamma} T_i \frac{\partial u_i}{\partial a} d\Gamma - \int_V \frac{\partial W}{\partial a} dV$$

**Creep Analogy**

$$\int_{\Gamma} T_i \frac{\partial \dot{u}_i}{\partial a} d\Gamma - \int_V \frac{\partial W'}{\partial a} dV$$



**Notice:**

$$\begin{aligned} \int_V \frac{\partial W'}{\partial a} dV &= \int_V \left( \frac{\partial}{\partial a} \int_0^t \sigma_{ij} \dot{\epsilon}_{ij} d\tau \right) dV = \int_{\Gamma} \left( \frac{\partial}{\partial a} \int_0^t T_i \dot{u}_i d\tau \right) d\Gamma \\ &= \int_{\Gamma} \left( \int_0^t \frac{\partial T_i}{\partial a} \dot{u}_i d\tau + T_i \frac{\partial \dot{u}_i}{\partial a} \right) d\Gamma \end{aligned}$$

## A New Contour Integral :



### *D'*-Integral

$$D' = - \int_{\Gamma} \int_0^{\dot{u}_i} \frac{\partial T_i}{\partial a} d\dot{u}_i d\Gamma$$

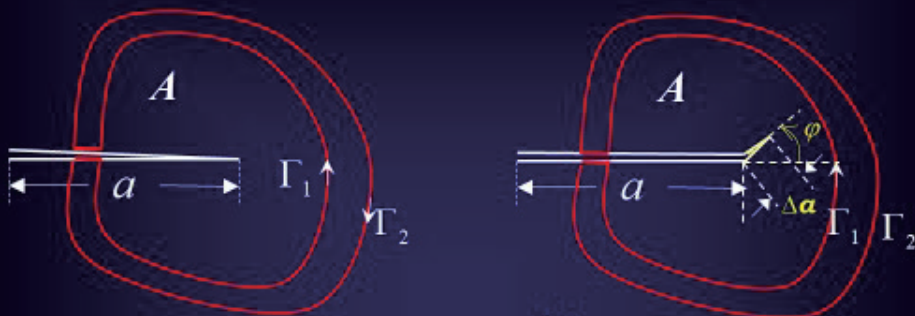
1. Path-independent Integral ?

In the special case of  $\varphi=0^\circ$

2. *D'*-Integral = C\*-Integral ?

20

### *D'*-Integral: Path-independent



a) Basic Model  $\Gamma_c = \Gamma_1 + \Gamma_2 + \text{crack faces}$  b) Auxiliary Model

where  $\Gamma_1, \Gamma_2$  are two arbitrary contours,  $\Gamma_c$  is a closed path

*D'*-integral can be concluded that

$$\begin{aligned} \int_{\Gamma_c} \int_0^{\dot{u}_i} \frac{\partial T_i}{\partial a} d\dot{u}_i d\Gamma &= \int_{\Gamma_c} \left( \frac{\partial}{\partial a} \int_0^{\dot{u}_i} T_i d\dot{u}_i - T_i \frac{\partial \dot{u}_i}{\partial a} \right) d\Gamma \\ &= \frac{\partial}{\partial a} \int_V \int_0^{\dot{\epsilon}_{ij}} \sigma_{ij} d\dot{\epsilon}_{ij} dV - \int_V \sigma_{ij} \frac{\partial \dot{\epsilon}_{ij}}{\partial a} dV = \int_V \left( \frac{\partial W'}{\partial a} - \sigma_{ij} \frac{\partial \dot{\epsilon}_{ij}}{\partial a} \right) dV = 0 \end{aligned}$$

Therefore, the *D'*-integral is path-independent

21

In the special case of  $\varphi=0^\circ$

## 2. $D'$ -Integral = $C^*$ -Integral

$$\frac{\partial}{\partial a} \quad \text{Partial derivative in } OX_1X_2$$

$$\frac{\partial'}{\partial a} \quad \text{Partial derivative in } OX_1x_2$$

Then

$$\frac{\partial}{\partial a} = \frac{\partial'}{\partial a} - \frac{\partial}{\partial X_1}$$

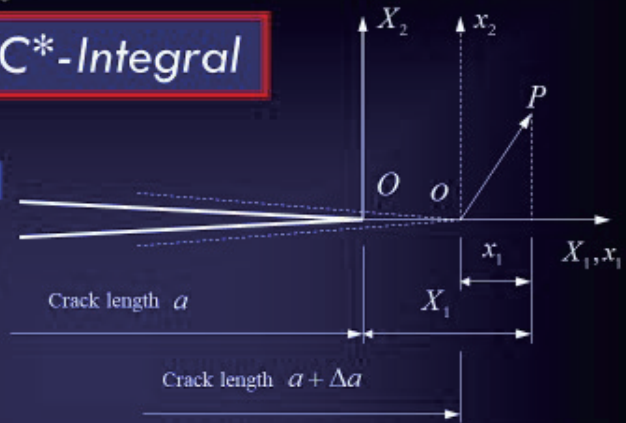


Fig.8 Coordinate system move with the crack tip

In the special case

$$\begin{aligned} D'_{(\varphi=0^\circ)} &= -\int_{\Gamma} \int_0^{\dot{u}_i} \frac{\partial T_i}{\partial a} d\dot{u}_i d\Gamma = \int_{\Gamma} \int_0^{\dot{u}_i} \frac{\partial T_i}{\partial X_1} d\dot{u}_i d\Gamma - \int_{\Gamma} \int_0^{\dot{u}_i} \frac{\partial' T_i}{\partial a} d\dot{u}_i d\Gamma \\ &= \int_{\Gamma} \left( \frac{\partial}{\partial X_1} \int_0^{\dot{u}_i} T_i d\dot{u}_i - T_i \frac{\partial \dot{u}_i}{\partial X_1} \right) d\Gamma - \int_{\Gamma} \left( \frac{\partial'}{\partial a} \int_0^{\dot{u}_i} T_i d\dot{u}_i - T_i \frac{\partial' \dot{u}_i}{\partial a} \right) d\Gamma \end{aligned}$$

the first term

$$\int_{\Gamma} \left( \frac{\partial}{\partial X_1} \int_0^{\dot{u}_i} T_i d\dot{u}_i \right) d\Gamma = \frac{\partial}{\partial X_1} \int_V \int_0^{\dot{\epsilon}_{ij}} \sigma_{ij} d\dot{\epsilon}_{ij} dV = \int_V \frac{\partial W'}{\partial X_1} dV = \int_{\Gamma} W' n_1 d\Gamma$$

the last term

$$\begin{aligned} \int_{\Gamma} \left( \frac{\partial'}{\partial a} \int_0^{\dot{u}_i} T_i d\dot{u}_i - T_i \frac{\partial \dot{u}_i}{\partial a} \right) d\Gamma &= \frac{\partial'}{\partial a} \int_V \int_0^{\dot{\epsilon}_{ij}} \sigma_{ij} d\dot{\epsilon}_{ij} dV - \int_V \sigma_{ij} \frac{\partial' \dot{\epsilon}_{ij}}{\partial a} dV \\ &= \int_V \left( \frac{\partial' W'}{\partial a} - \sigma_{ij} \frac{\partial' \dot{\epsilon}_{ij}}{\partial a} \right) dV = 0 \end{aligned}$$

then,  $D'$ -Integral becomes

$$D'_{(\varphi=0^\circ)} = \int_{\Gamma} \left( W' n_1 - T_i \frac{\partial \dot{u}_i}{\partial X_1} \right) d\Gamma = C^*$$

Therefore, in the special case  $D'$ -Integral =  $C^*$ -Integral

## *Conclusion and and Expectation*

- 1. On the basis of Energy variation between two cracked bodies differing in geometry, a new path-independent contour integral was obtained.*
- 2. The path-independent integral is expected to be used as a new creep fracture parameter, determining the mixed-mode for creep crack problems.*
- 3. The CED in an arbitrary direction can be evaluated and calculated by the new path-independent integral in next lecture.*

24

**Thank You Very Much!**

**DEPARTMENT OF AERONAUTICS AND ASTRONAUTICS  
FUDAN UNIVERSITY**



# Richardson's law and the concentration of Cs-137 in Fukushima

Yuko Hatano

Department of Risk Engineering, Tsukuba University, Japan

email: *hatano@risk.tsukuba.ac.jp*

---

In the diffusion theory of tracers in the atmosphere, the Richardson's 4/3 law is well known. It says that the mean square of the distances between two particles in the turbulent atmosphere will increase in time as  $t^3$  [1,2]. On the other hand, we have been observing that the concentration of Cs-137 in the air, measured at several fixed sites in Fukushima, seems decreasing in time asymptotically as  $t^{-4/3}$ . We examine the Richardson's theory to find out its connection to the observations.

## Reference

[1] Richardson, L.F., Atmospheric Diffusion shown on a distance-neighbor graph. Proc. Roy. Soc. London Ser.A, 110, 709-737, 1926.

[2] Kanatani, K. et al., The self-similar telegraph model of relative dispersions in turbulence, RIMS Kokyuroku 1543, 118-127, 2007 (in Japanese).

# Reference material

(This material is not the slide of the talk in this workshop)

## Richardson's law and the concentration of Cs-137 in Fukushima

Yuko Hatano, University of Tsukuba

研究背景

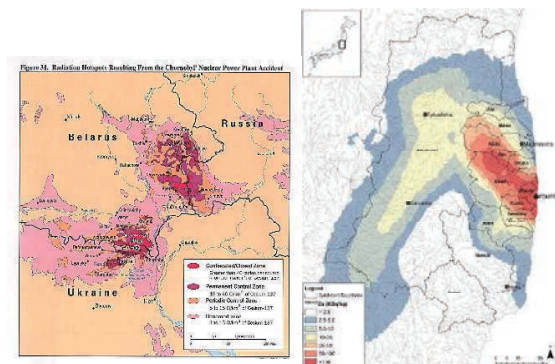
2

### 原子力発電所事故による汚染

1987年  
チェルノブイリ原子力発電所  
2011年  
福島第一原子力発電所

→ 国際原子力評価尺度(INES)  
レベル7(深刻な事故)

大量の放射性物質が広域に飛散  
大気中から様々な移動を行う



放射性物質飛散範囲  
(左)チェルノブイリ(1996)  
(右)福島県周辺(2015)

移動を考える前提として、大気中の濃度を把握する必要

## 大気中放射性物質の移動予測

### 短期的予測

粉塵プルームに含まれる，半減期の短い $^{131}\text{I}$ などを対象とした分析  
例：緊急時迅速放射能予測ネットワークシステム(W-SPEEDI)

### 長期的予測

半減期の長い $^{137}\text{Cs}$ ,  $^{129}\text{I}$ などを対象とした分析  
自然への吸収の働き，再飛散による大気汚染

### 本研究

$^{137}\text{Cs}$ を対象とした，**長期的**な推移の予測

## 大気中の物質移動モデル

### 移流方程式によるモデル

$$\frac{\partial C}{\partial t} + v \frac{\partial C}{\partial x} = 0$$

C : 物質量    t : 時間変数

v : 移流速度    x : 位置変数

支配方程式の設定

$$\frac{\partial C}{\partial t} + v_i \frac{\partial C}{\partial x_i} + \lambda_{\text{env}}(t)C + \lambda_{\text{phy}}C = \delta(x_1)\delta(x_2)\delta(t)$$

C : 大気中放射性物質濃度

$v_i(t)$  : i方向の移流速度

$\lambda_{\text{env}}(t)$  : 流出,植物の取り込みを表す項

$\lambda_{\text{phy}}$  : 核種の物理崩壊定数

( $=\alpha/t$ )

t : 経過時間



# 小林によるモデル

## 小林モデル

$$C(t) = A \exp(-\lambda_{\text{phy}} t) t^{-\alpha}$$

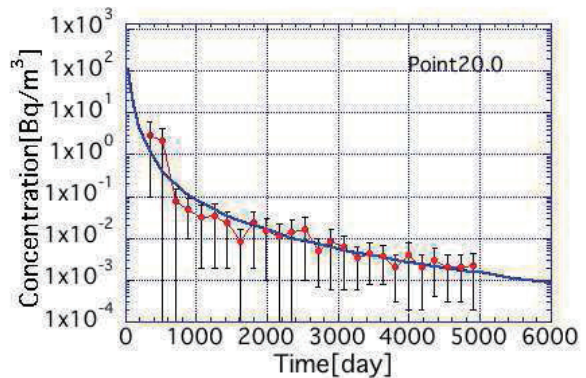
A : 初期飛散量

$\alpha$  : 拡散の度合いを示す係数

$\lambda_{\text{phy}} = 6.31 \times 10^{-5}$  ( $^{137}\text{Cs}$ )

データから推定すべき

パラメータは2つ



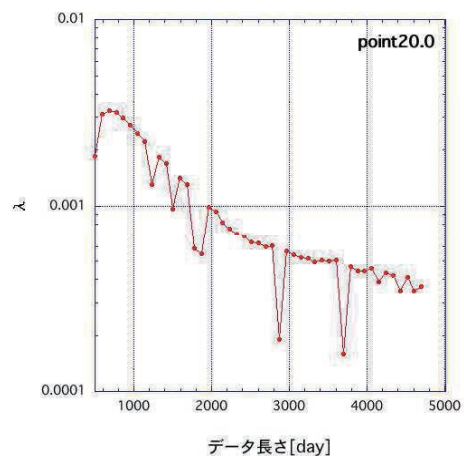
チェルノブイリ測定データに対する  
小林モデル当てはめ(2011)

# 小林モデルの問題点

## 佐藤による検証

対象のデータ範囲を変化させ、  
推定されるパラメータを比較

データ範囲を伸ばすにつれ、  
 $\lambda$ の値が減少する



パラメータ $\lambda$ の時間依存性(2013)

$\lambda$ の時間依存性



仮定に対する矛盾

## 佐藤によるモデルの改善

支配方程式の見直し

$$\lambda_{\text{phy}} = \lambda_{\text{decay}} + \lambda_{\text{new}}(t) \quad \lambda_{\text{decay}} : \text{崩壊定数}$$

$\lambda_{\text{new}}$  の設定

$$\lambda_{\text{new}}(t) = B \exp(-\beta/t)$$

新しい $\lambda$ を導入した支配方程式

$$\begin{aligned} \frac{\partial C}{\partial t} + v_i \frac{\partial C}{\partial x_i} + \lambda_{\text{env}}(t)C + \lambda_{\text{decay}}C + \lambda_{\text{new}}(t)C \\ = \delta(x_1)\delta(x_2)\delta(t) \end{aligned}$$

## 佐藤モデル

佐藤モデル

$$C(t) = A \exp(-B e^{-\beta/t} - \lambda t) t^{-\alpha}$$

$\lambda$  : 物理崩壊定数

$B$  : 初期の浸透量

$\beta$  : 初期の浸透率

推定すべきパラメータ数は4

**二重指数の項**を導入することで、初期の急激な減少を表現

# ボックスモデル

## ボックスモデル(完全混合ボックスモデル)

- 対象区域を箱に見立て、内部の物質収支をモデル化

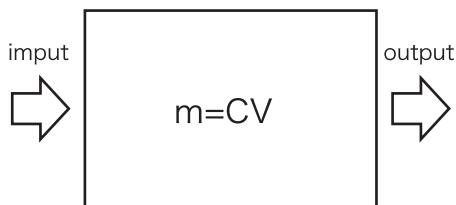
$$\frac{dm}{dt} = \frac{d(VC)}{dt} = (\text{input rate}) - (\text{output rate})$$

単一のボックスの場合、

$$\frac{dC}{dt} = -\lambda C$$

$$C(t) = e^{-\lambda t}$$

指数関数の形をとる



1次ボックスモデル模式図

# 複数ボックスモデル

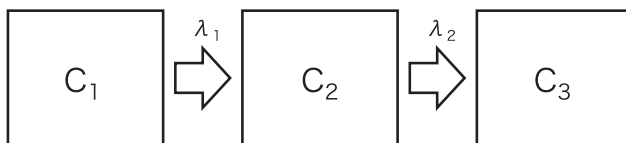
空間的に連続した複数のボックスを想定  
例: 3次

それぞれのボックスにおける収支表現式は、

$$\frac{dC_1}{dt} = -\lambda_1 C_1$$

$$\frac{dC_2}{dt} = \lambda_1 C_1 - \lambda_2 C_2$$

$$\frac{dC_3}{dt} = \lambda_2 C_2$$



3次ボックスモデル模式図

# 3次ボックスモデル

各ボックスについての解

$$C_1(t) = e^{-\lambda_1 t}$$

$$C_2(t) = \frac{\lambda_1 \lambda_2}{\lambda_2 - \lambda_1} (e^{-\lambda_1 t} - e^{-\lambda_2 t})$$

$$C_3(t) = \frac{\lambda_1 \lambda_2}{\lambda_2 - \lambda_1} \left( -\frac{e^{-\lambda_1 t}}{\lambda_1} + \frac{e^{-\lambda_2 t}}{\lambda_2} \right)$$

複数のボックスが連なったモデルは、指数関数の和で表される

## 本研究の目的

### モデル式導出

ボックスモデルによるアプローチ

### パラメータ推定手順

Back and forward methodによる、効率的なパラメータ推定

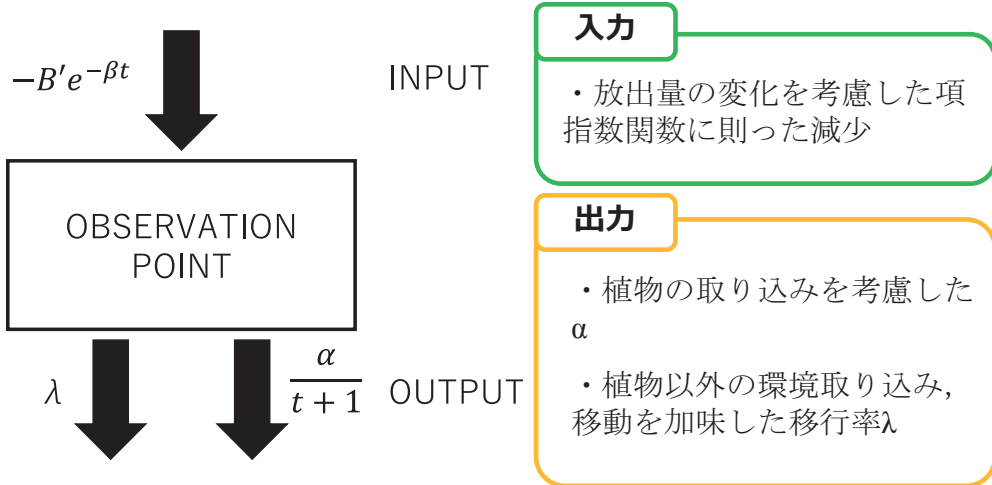


- ・初期値，初期変動を重視した推定
- ・長期的な変動推定

**両立**

**モデルと導出手順**を組み合わせた提案とその検証

## 提案するボックスモデル



## モデル式の導出

微分方程式による収支の表現

$$\frac{dC}{dt} = (-B'e^{-\beta t})C - \left(\lambda t + \frac{\alpha}{t+1}\right)C$$

$$\log C = Be^{-\beta t} - \lambda t - \alpha \log(t+1) \quad B' = B\beta$$

初期値に関するパラメータ $c_0$ を導入して、以下のモデルになる

新しい長期予測モデル  $C(t) = C_0 \exp(Be^{-\beta t} - \lambda t)(t+1)^{-\alpha}$   
 初期値  $C(0) = C_0 e^B$


## 新モデル

### パラメータの条件

パラメータ数は5 ( $\alpha, \lambda, B, \beta, C_0$ )  
0より大きい自由パラメータ

### モデル式の特徴

$$C(t) = C_0 \frac{e^{Be^{-\beta t}}}{e^{-\lambda t}} (t+1)^{-\alpha}$$

 急速に1に漸近する

推定の段階付けの提案  **Back and forward method**

## Back and forward method

### Step0

推定の対象となるデータで、二重指数項が1となるまでの十分な時間 $t_p$ を定める

### Step1

対象データの $t_p$ より後のデータより、近似式のパラメータ推定

$$C(t) = Dt^{-\alpha} e^{-\lambda t}$$

推定されたパラメータのうち、 $\alpha$ と $\lambda$ を利用、Dは破棄する

## Back and forward method(2)

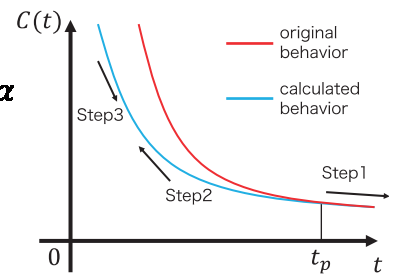
### Step2

$\alpha$ ,  $\lambda$  を用いて,  
 $t_p$  より前のデータから残りのパラメータ  
 を求める

$$C(t) = C_0 \exp(Be^{-\beta t} - \lambda t)(t + 1)^{-\alpha}$$

### Step3

より正確な初期値の推定  
 同時に、長期的な予測を行う



Back and forward method

同時に求めるパラメータ数を3にすることで、  
 数値計算の効率化、短縮化を見込める

## $t_p$ の決定

実際に二重指数項が1になる時間を考える

$$e^{Be^{-\beta t}} = 1$$

$$\frac{B}{e^{\beta t}} = 0$$

解析的に求めることができない

$t_p$  の値をいくつかに変化させ、  
 それぞれのパラメータを比較することで推定を行う

## 対象データ

### チェルノブイリ原子力発電所由来

- ・ 日本原子力研究所発行  
“Environmental monitoring data around chernobyl nuclear power plant used in the cooperative research project between JAERI and CHESCIR(UKRAINE)(Cooprative Research)” 掲載データ
- ・ 測定期間：1987年～1999年

### 福島第一原子力発電所由来

- ・ 東京都市大学原子力研究所(原発より南東に245km)
- ・ 測定期間：2011年3月～2014年3月(週次測定)

## 解析概要

- ・ Back and forward method に則った手順
- ・ マルカール法を用いた非線形最小二乗法による推定

### チェルノブイリ

- ・ 2000日までのデータを利用
- ・  $t_p (< 2000[\text{day}])$ が、600,800,1000,1200,1400の場合の計算を行い、パラメータを比較

### 福島

- ・  $t_p$ はデータより判断
- ・ 2000日程度までの予測を行う



## 解析概要

### 経過時間の取り扱い

日数を年に換算して計算

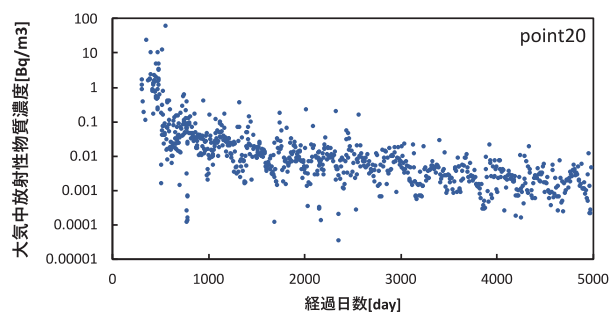
・モデル中(t+1)

測定週の間は濃度が一定であると仮定し、  
補正を7[day]≒1/52[year]として計算

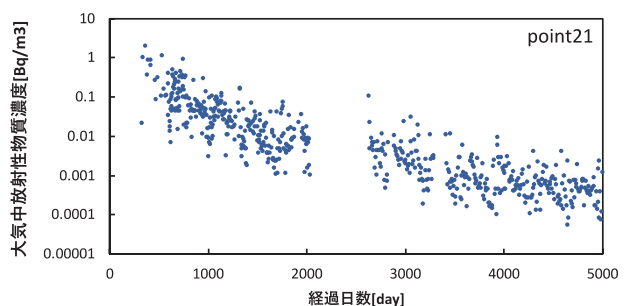
$$C(t) = C_0 \exp(Be^{-\beta t} - \lambda t) \left(t + \frac{1}{52}\right)^{-\alpha}$$

## 対象データ

・地点20  
発電所敷地内  
4号炉(爆発地点)より  
北1km

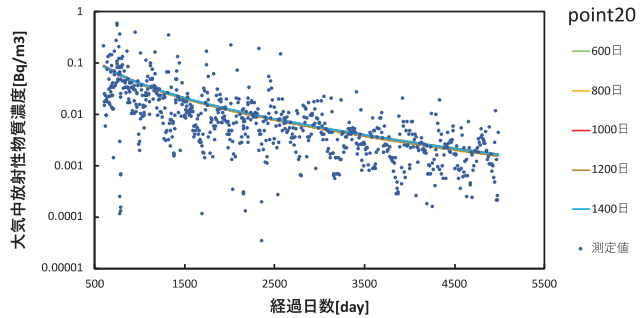


・地点21  
発電所敷地内  
4号炉より南西2km

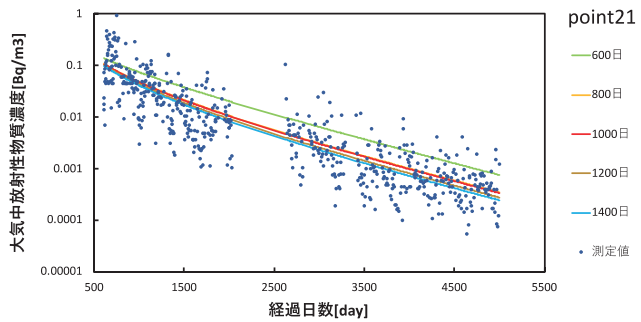


# パラメータ推定結果(Step1)

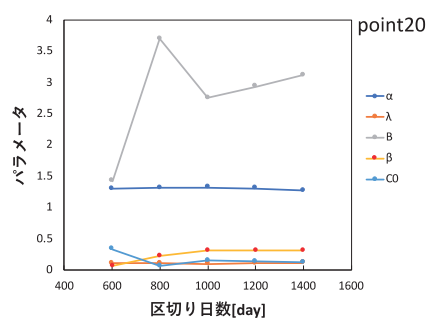
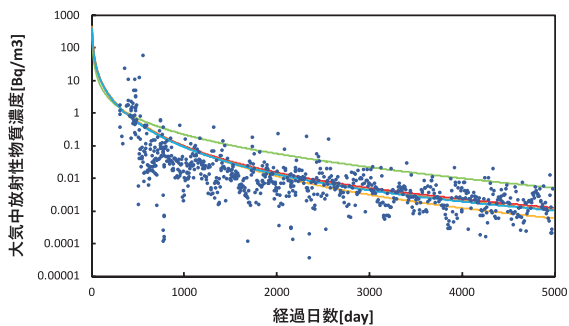
地点20では $\alpha, \lambda$ に大きな変化なし



地点21ではデータ範囲に起因する差を確認



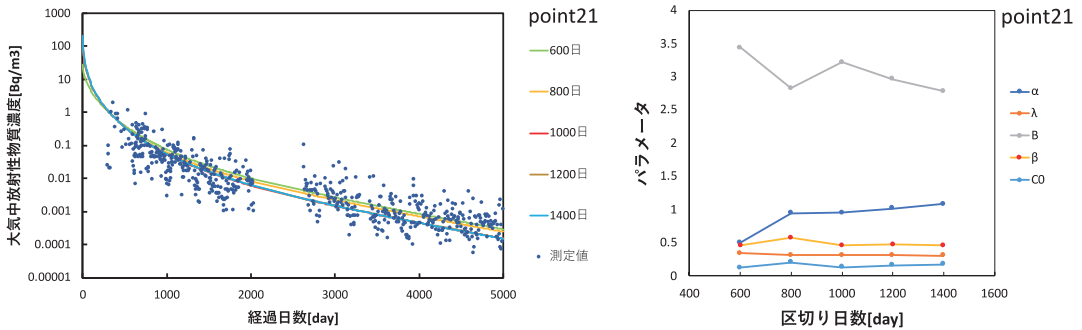
# パラメータ推定結果(Step2)



$t_p$	600	800	1000	1200	1400
初期値	224.3	449.5	429.4	432.9	392.0

- ・参照データによる影響は、 $t_p$ が小さい場合に大きく現れた
- ・ $t_p \geq 1000$ ではほとんど差がない

# パラメータ推定結果(Step2)



$t_p$	600	800	1000	1200	1400
初期値	28.2	146.1	142.3	173.6	209.7

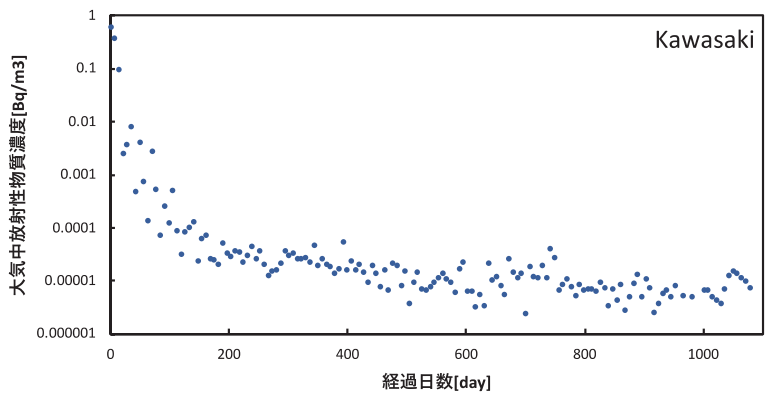
$t_p$ を大きくした場合の測定に誤差が生じた初期減衰の影響を過大評価した可能性

# 福島事故に対するパラメータ推定

測定値のレンジが小さいので、対数をとって計算を行う

$$(\text{残差}) = \log(y_i) - \log(F(x_i)) = \log\left(\frac{y_i}{F(x_i)}\right)$$

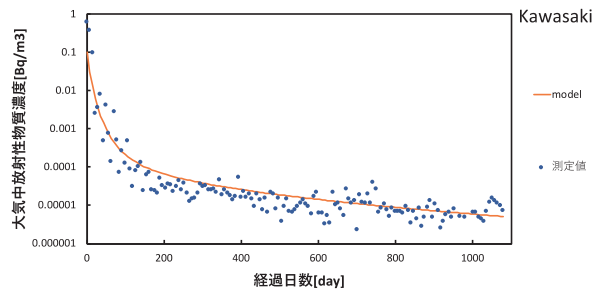
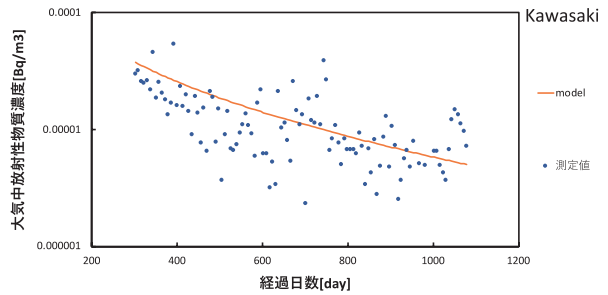
$t_p=300[\text{day}]$ とする



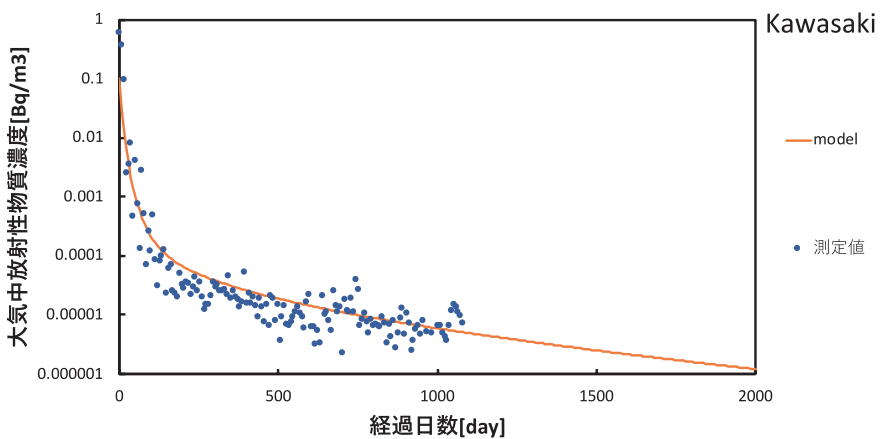
# パラメータ推定結果

$\alpha$	$\lambda$
1.063	0.313
B	$\beta$
3.810	8.027
C0	初期値
$4.10 \times 10^{-5}$	$9.86 \times 10^{-2}$

実際の初期値は  
0.597[Bq/m<sup>3</sup>]であった



# モデルによる長期予測



2000日までの予測により、およそ**1500日**程度で  
**1/10に減衰**するという結果を得られた

## まとめ

長期予測モデル

$$C(t) = C_0 \exp(Be^{-\beta t} - \lambda t)(t + 1)^{-\alpha}$$

及び、パラメータ推定の手順に関して  
Back and forward methodの提案を行った

チェルノブイリ事故の測定データでは、約6年分のデータから、13年程度の濃度変動の予測、初期減衰の影響期間、初期飛散量の推定を行った。

同じ手法を用いて福島事故の測定データを解析し、濃度予測を行った。結果、その地点では、1000日以降、1500日程度で濃度が10分の1になるように減衰すると予測できた

## 画像出典

Univewsity of Texas Libraries, 2018 1月確認.  
<https://legacy.lib.utexas.edu/maps/belarus.html>

O. Evrard, J. P. Laceby, H. Lepage, Onda, Y., O. Cerdan, S. Ayrault,  
"Radiocesium transfer from hillslopes to the Pacific Ocean after the Fukushima Nuclear Power Plant accident: A review", Journal of Environmental Radioactivity, 148, 92-110,2015.

Kobayashi, K.,  
長期的物質輸送モデルの開発及びチェルノブイリ原発事故と桜島火山の事例による検証, 筑波大学大学院 システム情報工学研究科 修士論文, March 2011.

Sato, M.,  
大気中放射性核種濃度の長期予測モデルの提案と福島事故への適用に向けたパラメータ収束性評価, 筑波大学大学院 システム情報工学研究科修士論文, March 2013.











「マス・フォア・インダストリ研究」シリーズ刊行にあたり

本シリーズは、平成 23 年 4 月に設立された九州大学マス・フォア・インダストリ研究所 (IMI) が、平成 25 年 4 月に共同利用・共同研究拠点「産業数学の先進的・基礎的共同研究拠点」として、文部科学大臣より認定を受けたことにもない刊行するものである。本シリーズでは、主として、マス・フォア・インダストリに関する研究集会の会議録、共同研究の成果報告等を出版する。各巻はマス・フォア・インダストリの最新の研究成果に加え、その新たな視点からのサーベイ及びレビューなども収録し、マス・フォア・インダストリの展開に資するものとする。

平成 26 年 10 月  
マス・フォア・インダストリ研究所  
所長 福本康秀

**Practical inverse problems based on interdisciplinary and  
industry-academia collaboration**

マス・フォア・インダストリ研究 No.8, IMI, 九州大学

ISSN 2188-286X

発行日 2018 年 2 月 20 日

編集 藤原宏志, 滝口孝志

発行 九州大学マス・フォア・インダストリ研究所

〒819-0395 福岡市西区元岡 744

九州大学数理・IMI 事務室

TEL 092-802-4402 FAX 092-802-4405

URL <http://www.imi.kyushu-u.ac.jp/>

印刷 社会福祉法人 福岡コロニー

〒811-0119 福岡県糟屋郡新宮町緑ヶ浜 1 丁目 11 番 1 号

TEL 092-962-0764 FAX 092-962-0768

## シリーズ既刊

Issue	Author / Editor	Title	Published
マス・フォア・インダストリ 研究 No.1	穴田 啓見 安田 貴徳 Xavier Dahan 櫻井 幸一	Functional Encryption as a Social Infrastructure and Its Realization by Elliptic Curves and Lattices	26 February 2015
マス・フォア・インダストリ 研究 No.2	滝口 孝志 藤原 宏志	Collaboration Between Theory and Practice in Inverse Problems	12 March 2015
マス・フォア・インダストリ 研究 No.3	笈 三郎	非線形数理モデルの諸相：連続，離散，超離散， その先 (Various aspects of nonlinear mathematical models : continuous, discrete, ultra-discrete, and beyond)	24 March 2015
マス・フォア・インダストリ 研究 No.4	穴田 啓見 安田 貴徳 櫻井 幸一 寺西 勇	Next-generation Cryptography for Privacy Protection and Decentralized Control and Mathematical Structures to Support Techniques	29 January 2016
マス・フォア・インダストリ 研究 No.5	藤原 宏志 滝口 孝志	Mathematical Backgrounds and Future Progress of Practical Inverse Problems	1 March 2016
マス・フォア・インダストリ 研究 No.6	松谷 茂樹 佐伯 修 中川 淳一 上坂 正晃 濱田 裕康	結晶のらせん転位の数理	10 January 2017
マス・フォア・インダストリ 研究 No.7	滝口 孝志 藤原 宏志	Collaboration among mathematics, engineering and industry on various problems in infrastructure and environment	1 March 2017



Institute of Mathematics for Industry  
Kyushu University

九州大学マス・フォア・インダストリ研究所

〒819-0395 福岡市西区元岡744  
URL <http://www.imi.kyushu-u.ac.jp/>